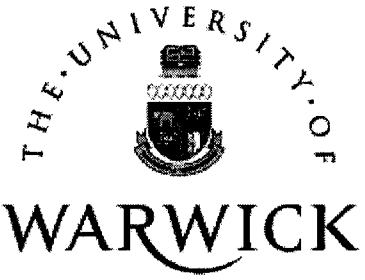

AN EXPERIMENTAL STUDY OF SOME SILICATE BASED GLASSES

by

Julian Francis Bent

supervised by

Dr.D.Holland and Dr.A.C.Hannon

A thesis submitted to the university of Warwick, England
for admission to the degree of
DOCTOR OF PHILOSOPHY

Physics Department June 1999

This work is dedicated to Hannah and Ruby.

LIST OF CONTENTS

LIST OF TABLES

LIST OF FIGURES

LIST OF ABBREVIATIONS

BO	bridging oxygen
CSA	Chemical Shift Anisotropy
C_Q	Quadrupolar coupling constant
DAS	Dynamic Angle spinning
DOR	Double Orientation Rotation
D(r)	Differential correlation function
δ	Isotropic chemical shift
EDX	Energy Dispersive Xrays
efg	electric field gradient
EXAFS	Extended X-ray absorption fine structure
FSDP	First Sharp Diffraction Peak
FT	Fourier Transform
FWHM	Full Width Half Maximum
i(Q)	Distinct scattering function
I(Q)	differential cross section
LAD	Liquid and Amorphous Diffractometer
MAS	Magic Angle Spinning
η	quadrupolar asymmetry parameter
NBO	Non-Bridging Oxygen
NMR	Nuclear Magnetic Resonance
PPM	Parts Per Million
P(r)	TOF neutron diffraction peak function
TCE	Thermal Coefficient of Expansion
T(r)	Total correlation function
TOF	Time Of Flight
TMS	Tetra Methyl Silane
SEM	Scanning Electron Microscope
XRD	X-Ray Diffraction
XRF	X-Ray Fluorescence
XANES	X-ray Absorption Near Edge Structure
ZAF	Atomic number, Absorption and Fluorescence

ACKNOWLEDGEMENTS

I would like to thank; Diane Holland for her excellent supervision of this project, Alex Hannon for his help with this neutron diffraction study (particularly the simulation study), all members of the NMR group at Warwick (both past and present), all members of the Glass-Ceramics group at Warwick (both past and present), Steve York for his help in making the SEM-EDX measurements, Ron Hardy at Durham Univeristy for his help in making the XRF measurements, all the technical staff in the Physics Department at Warwick and finally EPSRC and the Rutherford Appleton Laboratory for their financial support.

DECLARATION

The work presented here was carried out at the Physics Department, Warwick University and at the Rutherford Appleton Laboratory under the supervision of Dr. D.Holland and Dr. A.C.Hannon between October 1995 and September 1998. The results are the product of my own independent research, unless otherwise stated in the text, and have not been submitted for any other degrees. Some of this work has been published as:

J.F.Bent, A.C.Hannon, D.Holland and M.M.A.Karim, *J.Non-Cryst.Solids* **232-234** (1998) 300

It is anticipated that more of this work will be submitted for publication in the future.

ABSTRACT

TOF neutron diffraction and multinuclear MAS NMR data are combined to investigate the local structure of three silicate based glass forming systems. The effects of experimental resolution on the structural parameters obtained from neutron diffraction data are considered using simulated correlation functions.

The Gaussian fit parameters to a peak in T(r) report a smaller peak width and area than that of the Gaussian broadening. This is due to the contribution of the real-space resolution function. This effect is most dramatic for small values of $\langle u^2 \rangle^{1/2}_{thermal}$ and Q_{max} but is negligible for typical values.

The experimental uncertainty in measuring Q is considered for TOF neutron diffraction data. ΔQ is considered constant for data measured at several scattering angles. Some of the scattering intensity is transferred to a tail on the low r side of each peak, the magnitude of which increases with ΔQ. The peak fit parameters (position, width and area) change with increasing ΔQ, both before and after removing the gradient at low r. The Q-space resolution at a fixed scattering angle is considered by broadening i(Q) with a Gaussian of width $\Delta Q/Q$=constant. The peak fit parameters change with increasing $\Delta Q/Q$ but not significantly at the resolution quoted for the high angle detectors on LAD.

The interpretation of experimental data in terms of glass structure is greatly dependant upon an accurate knowledge of the glass composition. It is considered necessary to determine the concentration of all the cation species by a single or combination of techniques.

TOF neutron diffraction and ^{17}O MAS NMR data are reported for several $(SnO)_x(SiO_2)_{1-x}$ glasses and a partially crystallised $(SnO)(SiO_2)$ sample. ^{29}Si, ^{119}Sn MAS NMR and a powder X-ray diffraction data are also presented for the partially crystallised sample. The tin is present as Sn^{2+} and is three co-ordinated to oxygen at all compositions. The $(SnO)_x(SiO_2)_{1-x}$ glasses are thought to consist of a network of $SnO_{3/3}$ and $SiO_{4/2}$ polyhedra. The tin polyhedra may form pairs or chains. The local order in the crystalline phase is thought to be similar to that in the glasses. There are

two tin and two silicon sites in the crystal phase of approximate composition $(SnO)_4(SiO_2)$. It has not been possible to refine the crystal structure.

^{29}Si MAS NMR data are presented for $(Li_2O)_x(SnO)_{1-x}(SiO_2)$, $(Na_2O)_x(SnO)_{1-x}(SiO_2)$ and $(K_2O)_x(SnO)_{1-x}(SiO_2)$ glasses and TOF neutron diffraction data for $(K_2O)_x(SnO)_{1-x}(SiO_2)$. The tin is present as Sn^{2+} and is three co-ordinated at all compositions. Replacing the tin with modifier oxide reduces the ^{29}Si NMR chemical shift. The modifier cation is thought to depolymerise the tin silicate network, associating with the tin to maintain charge neutrality.

^{29}Si and ^{31}P MAS NMR and TOF neutron diffraction data are presented for $(K_2O\text{-}4SiO_2)_x(P_2O_5)_{1-x}$, $(K_2O\text{-}2SiO_2)_x(P_2O_5)_{1-x}$ and $(SiO_2)_x(P_2O_5)_{1-x}$ glasses. Each glass contains Si^{IV} and Si^{VI} species, the potassium tetrasilicate-P_2O_5 glasses also contain Si^{V} species. The proportion of silicon species changed with thermal history. Each glass is thought to consist of a modified phosphosilicate network. The potassium disilicate-P_2O_5 glasses are thought to consist of a continuous network of $Si(OP)_3(OSi)$, $Si(OP)_4(OSi)_2$, $(P\text{-}Q^2)^-$ and $(P\text{-}Q^4)^+$ species. The alkali-free phosphosilicate and potassium tetrasilicate-P_2O_5 glasses are thought to have similar structures but it is not possible to define the phosphate species. It was not possible to distinguish the different species by neutron diffraction. The phosphosilicate network is thought to be more disordered than modified phosphate and modified silicate networks.

CHAPTER 1

INTRODUCTION

1.1 GLASS STRUCTURE

The study of glass structure is fundamental to the understanding of the material and its properties. Glasses are important materials and have many industrial applications, particularly since their physical, chemical and electrical properties can be manipulated by composition and thermal history. In order to understand and control these material properties a knowledge of the relationship between glass composition and glass structure is required [1].

The complete goemetric structure of a glass cannot be defined by symmetry elements or solved by a single diffraction experiment because the long range order is not periodic. No single technique or combination of several techniques can completely define the structure of a glass. Instead, the experimental study of glass structure requires a combination of data from several techniques to obtain complementary structural information.

This study primarily reports time of flight neutron diffraction and multinuclear NMR data and combines this with physical property and Mössbauer data as reported by collaborative projects [2-3]. XPS [4] and EXAFS [5] are also considered powerful techniques and are commonly used to study glass structure but are not included in the present study.

1.2 DEFINITION OF GLASS

Glasses possess most of the macroscopic and thermodynamic properties of the crystalline state but have the structural disorder and isotropic behaviour of the liquid state. Glasses can be defined by two distinguishing characteristics;

1. no long range atomic structure and
2. a region of glass transformation behaviour.

The region of glass transformation is the temperature range over which the material transforms from a liquid to a solid, without crystallising. This can be observed as a change in the rate of change of enthalpy with temperature [6].

1.3 THE AMORPHOUS NETWORK

The glasses used in this study were prepared by cooling from a melt. The structure of these glasses are considered in terms of a vitreous network, as first proposed by Zachariasen [7]. Zachariasen considered the atomic arrangement in glass with repect to empirical observations of inorganic, oxide glasses. He stated that 'an oxide glass may form if;

1. the sample contains a high percentage of cations which are surrounded by oxygen tetrahedra or by oxygen triangles,
2. the tetrahedra or triangles share only corners with each other and
3. some oxygen atoms are only connected to two such cations and do not form bonds with any other cations.'

These three statements are considered necessary to describe a continuous, open network. Zachariasen considered non-network cations to fill holes within the network, the size of the holes being determined by the size of the cation on cooling from the melt. The structural roles of different oxides have since been categorized as;

network formers - oxides that readily form glasses,

network intermediates - oxides that do not independently form glasses but which will act within an amorphous network by substituting for a network former and

network modifiers - oxides that disrupt the network by breaking dihedral bonds.

The network can be considered a cross linking of chains which continue in all directions. Network intermediate cations replace network cations within the chains without disrupting the continuity of the network. In fact, network intermediate oxides can be added to introduce cross linking and to remove chain end groups. These chain ends are called 'non-bridging oxygens'. Network modifier oxides introduce non-bridging oxygens by breaking the network chains. Consequently there is a limit to the amount of modifier that can be accommodated within a continuous network. This behaviour has been well documented for simple oxide glasses such as alkali and alkaline-earth aluminosilicate glasses [8].

A continuous amorphous network requires strong directional bonding. This provides a kinetic barrier to structural rearrangement and crystallisation. The network forms, on cooling from the melt, by minimising the *local* free energy. This is dominated by the Coulombic and steric contributions of each atom species. The

local structural unit is often well defined. Disorder is introduced into the network by variations in the bond angles between structural units.

The majority of structural studies have focused on defining the local order. This is because the disordered nature of the network inhibits the observation of glass structure at longer distances. This study concentrates on defining the local order about each atom species and then considers the connectivity of these structural units in terms of an amorphous network. Alternative models of glass structure are described in the literature [9-11] but the oxide glasses used in this study are considered to consist of a continuous amorphous network

1.4 SILICATE GLASSES

Silicate based glasses constitute a large proportion of commercially available glasses. Hence, their structure is of great interest. The majority of 'real' glasses consist of many atom species for which the interpretation of experimental data is extremely difficult [9]. It is necessary to develop structural models for simple, single component glasses and to then extend this model to more complicated multi-component glasses.

Silicate glasses are predominantly based upon a network of $SiO_{4/2}$ tetrahedra. The $SiO_{4/2}$ tetrahedra link to different tetrahedra at all four corners to form a continuous, three-dimensional network [10]. The presence of modifier cations disrupts the network such that the tetrahedra do not link to other network cations at all four corners. Lippmaa et al. developed a Q^n notation to describe the nature of the tetrahedra in modified silicates. The Q indicates that the species is tetrahedral and the superscript indicates the number of dihedral bonds, as shown in figure 1.1.

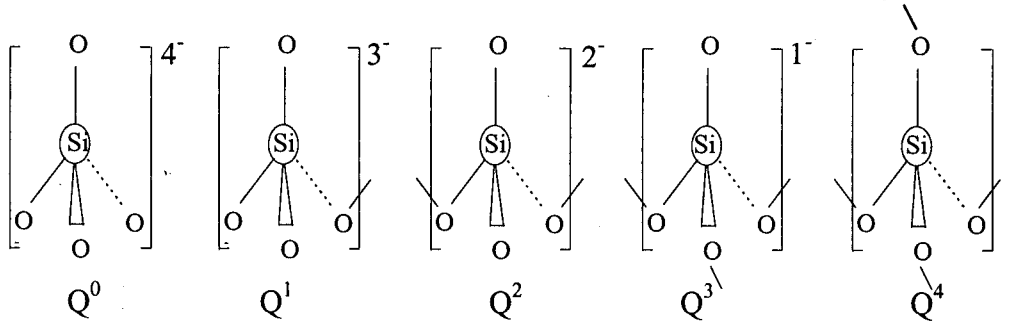

Figure 1.1 A schematic representation of $SiO_{4/2}$ Q^n species.

The distribution of different Q^n species within modified silicate glasses is still a matter of discussion in the literature [8]. A single model of cation distribution cannot be used to describe the behaviour of all modified silicate glasses, particularly for less polarising modifier cations.

1.5 PHOSPHATE GLASSES

Phosphate based glasses are used in many applications [11-14] despite the volatiliy of P_2O_5 at high temperatures and their high reactivity with water. Phosphorus is pentavalent but both crystalline and amorphous phosphates consist of tetrahedral $PO_{4/2}$ structural units. The ν-P_2O_5 network consists of $PO_{4/2}$ tetrahedra linked at three corners whilst the fourth oxygen atom forms a double bond with the phosphorus atom. The double bond is shorter than the dihedral bonds and is susceptible to attack from modifier cations and/or water. In fact modified phosphate glasses are more resistant to attack from water because the modifier cation removes the double bond. On further increasing the modifier content dihedral bonds are broken to disrupt the network.

A Q^n nomenclature, similar to that used to describe silicate glasses, can be used to describe the $PO_{4/2}$ structural units, as shown in figure 1.2. This was first formalised by Van Wazer [15] and confirmed by structural studies which have been reviewed by Martin [16], Eckert [17] and Kirkpatrick [18].

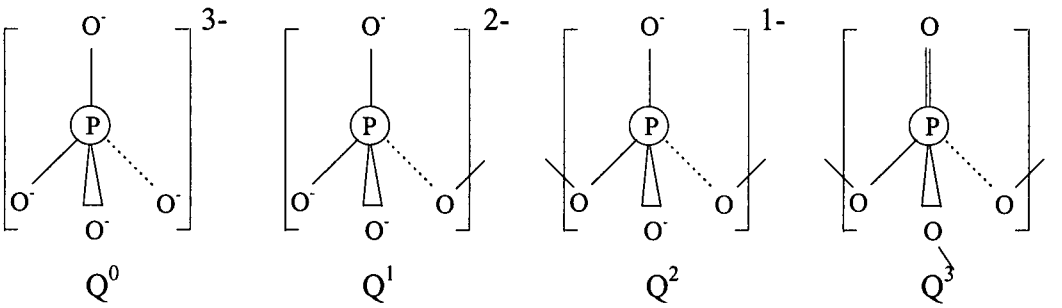

Figure 1.2 A schematic representation of PO_4 Q^n species.

1.6 THESIS PLAN

The contents of this thesis are divided as follows:

Chapter 1 introduces the motivation for this study of glass structure. A definition of glass and details of the amorphous network model of glass structure is given. The Q^n nomenclature is introduced to describe the structural units in silicate and phosphate glasses.

Chapter 2 describes the theoretical background necessary to understand the total scattering neutron diffraction technique used in this study.

Chapter 3 describes the theoretical background necessary to understand the NMR techniques used in this study.

Chapter 4 introduces the other experimental techniques used in this study; powder X-ray diffraction, SEM-EDX, XRF and density measurements.

Chapter 5 presents several effects of experimental resolution upon the structural parameters obtained from fitting T(r). This considers fitting experimental data with a Gaussian function instead of the analytically correct function (real space resolution) and also the effect of the experimental uncertainty in measuring Q for a TOF diffractometer. The data were simulated on the VAX computers at RAL using FORTRAN routines.

Chapter 6 presents neutron diffraction data for a series of $(SnO)_x(SiO_2)_{1-x}$ glasses, where $0.16 \leq x \leq 0.64$. The structural units are defined and a model of a possible glass structure is proposed. A sample of the metastable crystalline tin silicate phase is prepared by heat treating a $(SnO)(SiO_2)$ glass. Neutron diffraction, X-ray diffraction and ^{29}Si MAS NMR data are presented for this partially crystallised sample. ^{17}O MAS NMR data are presented for three glasses and one partially crystallised sample.

Chapter 7 presents neutron diffraction and ^{29}Si MAS NMR data for a series of glasses of the composition $(K_2O)_x(SnO)_{1-x}(SiO_2)$, where $0 \leq x \leq 0.2$ and ^{29}Si MAS

NMR data for $(Na_2O)_x(SnO)_{1-x}(SiO_2)$, where $0 \leq x \leq 0.3$. The structural units are defined and a model of a possible glass structure is proposed.

Chapter 8 presents neutron diffraction, ^{29}Si and ^{31}P MAS NMR data for a series of potasium disilicate-P_2O_5, potassium tetrasilicate-P_2O_5 and an alkali-free phosphosilicate glass. The glasses of identical composition were cooled at different rates to produce glasses with different proportions of silicate species.

Chapter 9 considers the general conclusions of the project and the conclusions and thoughts for future work for each series of glasses.

REFERENCES

[1] S.R.Elliott, 'Physics of amorphous materials', 2nd Ed. (Longman, 1990)

[2] A.Sears, PhD thesis, Warwick University 1998.

[3] P.Appleyard, PhD thesis, John Moores University

[4] C.G.Pantano in 'Experimental techniques in glass science', ed C.J.Simmons and O.H.El-Bayoumi, The American Ceramic Society 1993

[5] R.Pettifer in 'Glasses and Glass-ceramics', ed.M.H.Lewis, Chapman & Hall, London 1989

[6] J.E.Shelby, 'Introduction to Glass Science and Technology' RSC 1997.

[7] W.H.Zachariasen, *J.Am.Chem.Soc.* **54** (1932) 3841

[8] R.Dupree and D.Holland in 'Glasses and Glass-ceramics', ed.M.H.Lewis, Chapman & Hall, London 1989

[9] M.M.A.Karim, 'A study of tin oxides in silicate based glasses' PhD thesis, Warwick University 1995

[10] A.C.Wright, *J.Non-Cryst.Solids* **179** (1994) 84

[11] M.W.G.Lockyer, 'High resolution multinuclear nuclear magnetic resonance studies of oxide glasses', PhD thesis, Department of Physics, University of Warwick, September 1993

[12] J.A.Wilder, *J.Non-Cryst.Solids* **38/9** (1980) 879

[13] T.Minami, Y.Takuma and M.Tanaka, *J.Electrochem.Soc.* **124** (1977) 1659

[14] D.Ehrt, C.Fuchs and W.Vogel, *Silikattechnik* **35** (1984) 6

[15] J.Van Wazer, 'Phosphorus and its compounds', Vols 1 and 2, Interscience, New York 1951

[16] S.W.Martin, *J.Am.Ceram.Soc.* **74** (1991) 1767

[17] H.Eckert, *Progress in NMR spectroscopy* **24** (1992) 159

[18] R.J.Kirkpatrick and R.K.Brow, *S.S.Nuc.Mag.Res.* **5** (1995) 9

CHAPTER 2

NEUTRON DIFFRACTION

2.1 INTRODUCTION

Neutron scattering can be used to probe nuclear and magnetic structures and dynamics of condensed matter. It is an expensive but extremely powerful experimental technique. This study reports the total scattering by the sample nuclei. This technique measures all the scattered neutrons, regardless of final energy, and assumes that the scattering is elastic because the incident energy is much larger than the excitation energies of the sample. This assumption is known as the static approximation [1]. The total diffraction pattern depends upon the geometric positions of the atoms in the sample and can be used to measure the atomic structure.

The total scattering diffraction technique can be used to probe the structure of both crystalline and amorphous materials. The diffraction pattern for a crystalline material consists of a series of Bragg peaks which can be indexed and refined to obtain the crystal structure [2]. The diffraction pattern for an amorphous material does not consist of Bragg peaks because the structure is disordered. The peaks are broad but relate to a sum of partial correlation functions between atoms in the sample, by Fourier transform [3].

The information obtained from neutron diffraction is complementary to that obtained by either X-ray or electron diffraction but has the added advantage that the non-magnetic scattering of neutrons is governed by weak, short range interactions with the sample nuclei. Hence, the neutron diffraction pattern describes the positions of the nuclei in the bulk of the material. This is different to both X-ray or electron diffraction which measure electron density distribution and has the advantage that it not as dependent upon the nature and type of the bonding between atoms. It is also possible to study samples containing both light and heavy elements, as the neutron scattering length is not simply proportional to the atomic number.

2.2 THEORY

The quantity measured in a total scattering neutron diffraction experiment is the differential cross section. This is a measure of the scattered neutron flux with respect to the incident neutron flux and can be defined as;

$$\frac{d\sigma}{d\Omega} = \frac{\begin{pmatrix}\text{number of neutrons of wavelength } \lambda \text{ scattered per unit} \\ \text{time into a small solid angle } d\Omega \text{ at a scattering angle } 2\theta\end{pmatrix}}{N\Phi(\lambda)d\Omega} \qquad (2.1)$$

where N is the number of atoms in the sample and $\Phi(\lambda)$ is the incident neutron flux at wavelength λ [4].

The scattering process can be described by considering the neutrons as waves [5]. The incident neutron can be considered as a plane wave and the scattered neutron as a spherical wave centred on the scattering nucleus. The relative position of each nucleus determines the phase shifts between the scattered waves and these determine the intensity fluctuations in the resulting interference pattern. The differential cross section is a sum of the waves from many scattering processes. For total scattering diffraction this provides a 'snapshot' of the instantaneous structure [1].

Assuming that the incident neutron energy is large compared with the energy of any sample nuclear motion (the static approximation) and that the detectors are equally efficient at all neutron energies, then the total scattering by an amorphous material can be described by equation 2.2;

$$\frac{d\sigma}{d\Omega} = \left\langle \left| \sum_R b_R \exp\left[i(\mathbf{k}_0 - \mathbf{k}_1)\cdot \mathbf{R}(t) \right] \right|^2 \right\rangle_t \qquad (2.2)$$

in which b_R is the scattering length of the atom at position $\mathbf{R}$, $\mathbf{k_0}$ is the incident wavevector and $\mathbf{k_1}$ the scattered wave vector [6]. The vector difference between $\mathbf{k_0}$ and $\mathbf{k_1}$ is called the scattering vector, $\mathbf{Q}$. The magnitude of $\mathbf{Q}$ is defined, for elastic scattering at an angle 2θ, in equation 2.3.

$$Q = |\mathbf{k}_0 - \mathbf{k}_1| = \frac{4\pi\sin\theta}{\lambda} \qquad (2.3)$$

The amorphous and polycrystalline samples used in this study are assumed to be isotropic, for which only the magnitude of the scattering vector Q is important.

It is conventional to write the total scattering in terms of the self scattering, $I^S(Q)$, and the distinct scattering ,i(Q).

$$\frac{d\sigma}{d\Omega} = I(Q) = I^S(Q) + i(Q) \tag{2.4}$$

The self scattering is the interference between scattered waves from the same nucleus. This can be calculated and subtracted from the total scattering to reveal the distinct scattering, which contains the structural information. The self and distinct scattering can be defined by equations 2.5 and 2.6;

$$I^S(Q) = \sum_l \frac{c_l \sigma_l^{scatt}}{4\pi}\left(1 + P_l(Q,\theta)\right) \tag{2.5}$$

$$Qi(Q) = \int_0^\infty D(r)\sin(Qr)dr \tag{2.6}$$

where the summation l is taken over elements in the sample, c_l is the atomic fraction for element l, σ_l^{scatt} is the total bound scattering cross section and r is the distance from an arbitrary nucleus in real space. $P_l(Q,\theta)$ represents a correction for inelasticity effects due to the use of the static approximation.

The distinct scattering is the interference between neutron waves scattered from different nuclei and can be related to the real space differential correlation function D(r) by Fourier transform, as described by equation 2.7.

$$D(r) = \frac{2}{\pi}\int_0^\infty Qi(Q)M(Q)\sin(rQ)dQ \tag{2.7}$$

A modification function M(Q) is applied to the data before calculating the Fourier transform. This has the effect of reducing the termination ripples in D(r) by smoothing the discontinuity at Q_{max}. The Lorch modification function was used during this study. It is a slowly decaying function, described by equations 2.8 and 2.9. This slightly broadens the features in D(r) but dramatically reduces the termination ripples.

$$M(Q) = \frac{\sin(Q\Delta r)}{Q\Delta r} \qquad \text{for } Q < Q_{max} \tag{2.8}$$

$$M(Q) = 0 \qquad \text{for } Q > Q_{max} \tag{2.9}$$

The data in this study are presented as the total correlation function, T(r). T(r) is calculated from D(r), as defined by equation 2.10. $T^0(r)$ is defined by equation 2.11, in which g^0 is the macroscopic number density of atoms.

$$T(r) = D(r) + T^0(r) \tag{2.10}$$

$$T^0(r) = 4\pi r g^0 \left(\sum_l c_l \bar{b}_l \right)^2 \qquad (2.11)$$

The magnitude of the elastic scattering from an atom is determined by its coherent scattering length. Table 2.1 summarises the average coherent scattering length for the natural isotopic distribution for each of the elements used in this study.

	Si	P	K	O	Sn
$\bar{b}$ (fm)	4.1534	5.13	3.67	5.803	6.225

Table 2.1 Average (natural abundance) coherent neutron scattering lengths [8].

2.3 EXPERIMENTAL METHOD

2.3.1 TIME OF FLIGHT DIFFRACTION

The data presented in this study were measured by the time of flight (TOF) diffraction technique on the Liquids and Amorphous Diffractometer (LAD) at ISIS, RAL. The pulses of neutrons, generated by a spallation process, are undermoderated. This produces neutrons with a wide range of energies, including high energy (short wavelength) neutrons, which makes possible the high real space resolution of the measurements [9].

The differential cross section is measured as a function of TOF, at a constant scattering angle 2θ. The neutrons travel from the moderator to the sample and on to the detector. As they travel the total flight path, neutrons become separated in time as a function of their wavelength. TOF neutron diffraction is a dispersive technique. Assuming the neutrons leave the moderator at the same time and that the scattering is elastic then the time at which the neutron is detected can be related to its wavelength by equation 2.12;

$$t = \frac{m_n}{h} L\lambda \qquad (2.12)$$

where m_n is the neutron mass, h is Planck's constant and L is the total flight path.

The total scattering is measured for each pulse at each detector angle. Subsequent pulses are summed to obtain suitable counting statistics.

LAD consists of detectors at seven different scattering angles. as shown in figure 2.1. The data at different angles can then be combined to yield data over the range $0.3 < Q < 50\text{Å}^{-1}$.

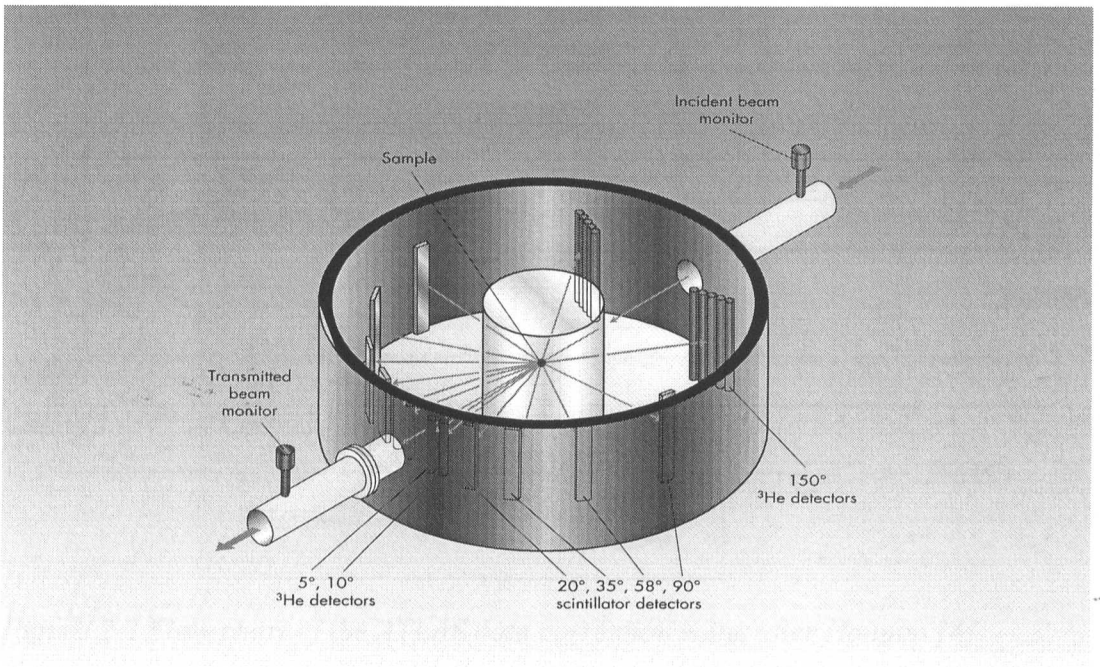

Figure 2.1The LAD diffractometer [10]

2.3.2 DATA ACQUISITION

TOF data were acquired for a vanadium rod, an empty can, the empty spectrometer and each sample during each experiment. The sample, empty can and vanadium rod were sequentially rotated into the neutron beam using a mechanical sample changer. Data were acquired for each in several hundred μAhr increments. This averaged the drift in detector efficiency and incident flux shape during the experiment between each of the data sets. The sample changer and data acquisition were controlled remotely, using the LAD computer as described in the 'LAD Experimenter's Manual' [10].

2.3.3 DATA CORRECTION

The data presented in this study were processed from the total scattering to the total correlation function using the ATLAS suite of software at RAL, as shown in

figure 2.2 [4].The routines were run either in batch mode or as a FORTRAN routine within genie, as described in reference [11].

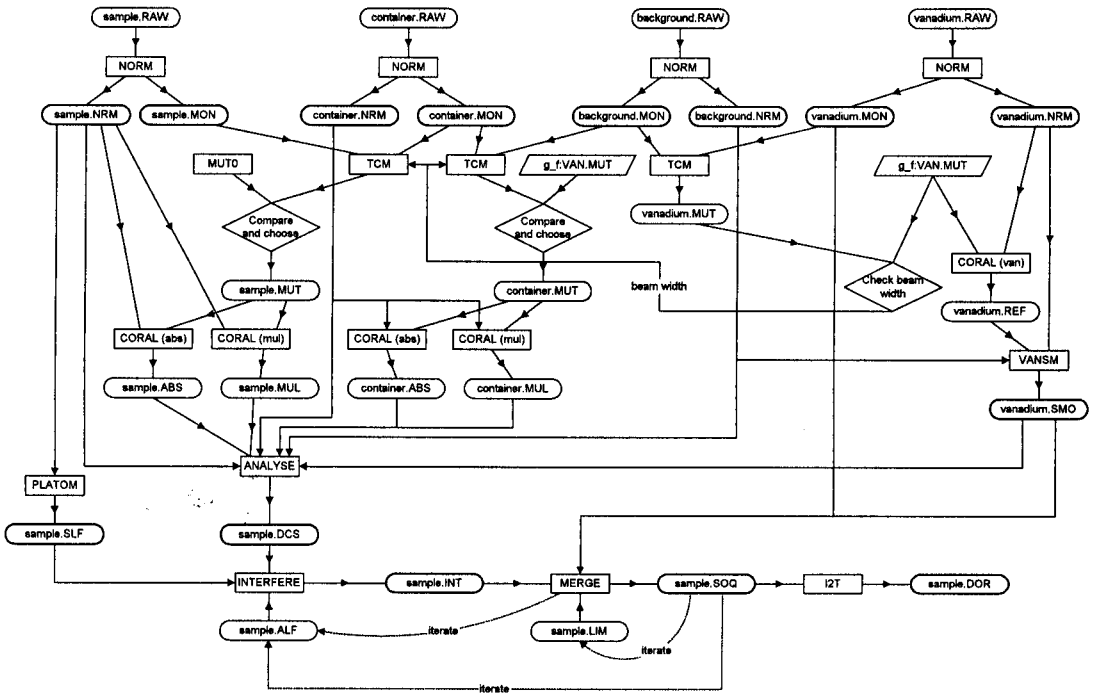

Figure 2.2 Flow chart of the ATLAS data correction suite, after Hannon [4].

The data were checked for consistency between sample, can, rod or empty spectrometer runs using the 'g_f:nq' routine within genie. This was a necessary check that the correct sample, vanadium rod or empty can was in the neutron beam.

The data for each sample (empty can, vanadium rod or empty spectrometer) were then combined, corrected for detector deadtime and normalised to $\Phi(\lambda)$ using the NORM routine. Several data sets were recorded for each sample and each normalised to the incident neutron flux (measured by the incident beam monitor detector) to account for any change in the flux shape due to a change in moderator conditions. The deadtime correction was applied for each detector bank, as the time after detecting a neutron that the detector is unable to detect another neutron is dependent upon the type of detector. The NORM routine also reduces the data set size by combining data from similar scattering angles within each detector bank and converting the data from TOF to a Q-scale.

The transmission spectrum, measured by the downstream monitor, was used to calculate the wavelength dependent cross section and hence the absorption and multiple scattering corrections. The wavelength dependence of the attenuation and

the multiple scattering for the sample and can (and also the vanadium rod) were calculated numerically using the 'g_f:coral' routine.

The program VANSM was used to fit the vanadium data with a low order Chebyshev polynomial. This removed the small Bragg peaks and filtered out the background noise to produce a slowly varying spectrum. VANSM also applied the attenuation and multiple scattering corrections, previously calculated by 'g_f:coral', and a standard inelasticity correction for vanadium.

The sample and can absorption and multiple scattering corrections were applied and the differential cross section was normalised to the vanadium spectrum using the ANALYSE routine. This subtracted the background spectrum (empty can or empty spectrometer), divided by the smoothed vanadium spectrum, applied the attenuation and multiple scattering corrections and finally scaled by a factor to provide an absolute normalisation. This factor was calculated from the effective density and beam dimensions, using the routine 'g_f:ana_const', to normalise to the number of scattering units in the beam.

The sample scattering was normalised to the vanadium scattering to remove its dependence on the flux distribution $\Phi(\lambda)$ arising from the moderator. Vanadium is used for this purpose because its scattering is almost completely incoherent (the Bragg peaks are very small) and hence its scattering is closely related to the incident flux $\Phi(\lambda)$.

The PLATOM routine was used to calculate the self scattering for each detector bank. This used the Placzek approach and a fit to the incident flux to calculate the inelastic deviation from the static approximation [6].

The distinct scattering i(Q) was then obtained by subtracting the self scattering $I^S(Q)$ from the measured differential cross section I(Q) using the 'g_f:interfere' routine. It was generally found that the distinct scattering at each scattering angle did not oscillate about zero. This was partly due to the uncertainty associated in calculating the amount of sample in the beam. A renormalisation factor α_j (of approximately one) was applied to the total scattering at each detector bank prior to subtracting the self scattering, as shown in equation 2.13. This correction was slightly different for each detector bank, as indicated by the subscript j.

$$i_j(Q) = \alpha_j I_j(Q) - I_j^S(Q) \qquad (2.13)$$

The distinct scattering $i_j(Q)$ for different detector banks was then combined using the 'g_f:merge' routine. This weighted each $i_j(Q)$ with the intensity with which it was measured, as calculated from the corrected vanadium data. The high angle scattering was considered accurate between 12 and 50Å^{-1}. The lower angle scattering were combined with this, over ranges of Q in which the data were consistent. Care was taken to ensure that the overlap of data from different detector banks was consistent and no discontinuities were introduced to the data. In practise, 'g_f:interfere' and 'g_f:merge' were used iteratively to correct the normalisation and combine the data to i(Q). This combination of data from different scattering angles improved the counting statistics and increased the Q-range relative to that measured at just one scattering angle. The ranges over which data were typically combined are summarised in table 2.2.

2θ	5°	10°	20°	35°	60°	90°	150°
Q_{min}	0.14	1.00	2.30	3.10	5.20	8.60	12.40
Q_{max}	1.20	3.20	7.10	12.00	15.30	22.00	50.00

Table 2.2 Typical Q-limits for data at scattering angle 2θ.

The low Q limit, measured by the 5° detectors, was then extended to zero by fitting i(Q) between approximately 0.14 and 0.3Å^{-1} with a function $y = a + bQ^2$. This was performed using the genie transform 'lowq', and the low Q data replaced with the fit. This was necessary to extend i(Q) to the low Fourier transform limit, see equation 2.7.

The corrected i(Q) was then transformed to D(r) by fast Fourier transform using the 'g_f:i2t' routine. This was performed before and after smoothing i(Q) with the genie transform 'g_f:3p_spline' to ensure that the smoothing process did not noticeably broaden the resulting correlation function.

D(r) was often found not to oscillate about $T^0(r)$ at low r. This was due to slight errors in the normalisation of the data. This was corrected by fitting D(r) with a straight line at low r using the 'lfit' genie transform and then scaling D(r) to $T^0(r)$. $T^0(r)$ was then added to D(r) to obtain T(r).

Further details of the ATLAS suite of software can be found in the ATLAS Manual [11] and details of the software used to display the data can be found in the Punch Genie Manual [12].

2.4 EXTRACTING STRUCTURAL INFORMATION

2.4.1 THE DISTINCT SCATTERING

Structural information can be obtained directly from the distinct scattering. The detail at low Q is thought to be a measure of the intermediate range order. The first sharp diffraction peak (FSDP) is due to the longest period real space correlations. Wright interprets the FSDP in silica to be due to the periodicity of the boundaries between a succession of cages within a three-dimensional silica network [13]. Alternative interpretations are also given in the literature [14]. The magnitude of the intermediate range periodicity can be calculated using equation 2.15. This can be derived from Braggs law, equation 2.14, and the definition of Q, equation 2.3.

$$\lambda = 2d \sin\theta \tag{2.14}$$

$$d = \frac{2\pi}{Q} \tag{2.15}$$

The FSDP is also often the sharpest peak in the diffraction pattern. This indicates that it contains contributions from many slowly decaying correlations. Its origin cannot be universally defined for all glass systems, but changes in its behaviour can be used to indicate changes in intermediate range order with composition within a glass system.

2.4.2 THE TOTAL CORRELATION FUNCTION

The total correlation function is defined by equation 2.16. It is the weighted sum of the partial correlation functions, which are defined by equation 2.17;

$$T(r) = \sum_{ll'} c_l \bar{b}_l \bar{b}_{l'} t_{ll'}(r) \tag{2.16}$$

$$t_{ll'}(r) = 4\pi r g_{ll'}(r) \tag{2.17}$$

where c_l is the atomic fraction for element l, $\bar{b}_l$ and $\bar{b}_{l'}$ are the coherent scattering lengths for elements l and l' and $g_{ll'}(r)$ is the average number density of atoms of element l' a distance r from an atom of element l [15].

The contribution to $t_{ll'}(r)$ due to a single interatomic distance is broadened by the thermal motion of the atoms, as shown in equation 2.18

$$t_{ll'}(r) = \frac{n_{ll'}}{r_{ll'}\left(2\pi\left\langle u_{ll'}^2\right\rangle\right)} \exp\left(-\frac{(r - r_{ll'})^2}{2\left\langle u_{ll'}^2\right\rangle}\right) \tag{2.18}$$

where $\left\langle u_{ll'}^2\right\rangle$ is the mean square variation in the distance $r_{ll'}$ between atoms l and l' and $n_{ll'}$ is the average number of l' atoms at a distance $r_{ll'}$ from a l atom [16].

The shape of a peak in T(r) (assuming static order is absent) is given by the convolution of the real-space resolution function, P(r), and a Gaussian thermal distribution (assuming the harmonic approximation) [17]. P(r) is given by the cosine transform of the modification function as shown in equation 2.19;

$$P(r) = \left(\frac{1}{\pi}\right)\int_0^\infty M(Q)\cos(rQ)dQ \tag{2.19}$$

The position of a peak in T(r) is equal to the interatomic separation of the atoms contributing to the peak. The bond angle between adjacent structural units in the glass can be calculated from the positions of the nearest and next nearest neighbours, assuming only these atoms contribute to these peaks.

The co-ordination number of atoms contributing to the peak can be calculated from the area of a peak in T(r) as described by equation 2.20;

$$n_{ll'} = \frac{r_{ll'}A_{ll'}}{c_{ll'}} \tag{2.20}$$

where $A_{ll'}$ is the area under the peak and $c_{ll'}$ is the coefficient in the expansion of equation 2.16 multiplied by 0.01 (to scale the units from fm^2 to barns).

The area of the peak in $t_{ll'}(r)$ is related to the zero Q limit of the related Fourier component in the distinct scattering [18 & 19]. The accuracy of the co-ordination number obtained from fits to the data is dependent upon the accuracy to which the low Q scattering is measured. The accuracy of the co-ordination numbers is also dependent upon the normalisation of the data and greatly dependent upon $c_{ll'}$, which is calculated from the sample composition.

The calculation of co-ordination numbers from neutron diffraction data is discussed further in chapter 5.

REFERENCES

[1] A.C.Hannon, 'Neutron diffraction theory' in 'Encyclopedia of spectroscopy and spectrometry', eds. J.Lindon, G.Tranter and J.Holmes, Academic Press 1999, in press.

[2] M.F.C.Ladd and R.A.Palmer, 'Structure Determination by X-ray Crystallography', Plenum Press, 2nd Edition 1985

[3] A.C.Wright, A.G.Clare, D.I.Grimley and R.N.Sinclair, *J.Non-Cryst.Solids* **112** (1989) 33

[4] A.C.Hannon, W.S.Howells and A.K.Soper, *IOP Conf.Series* **107** (1990) 193

[5] G.E.Bacon, 'Neutron diffraction' 3rd Edition, Oxford Clarendon Press 1975

[6] C.G.Windsor, 'Pulsed neutron scattering', Taylor and Francis Ltd., 1981

[7] A.C.Wright and R.N.Sinclair, *J.Non-Cryst.Solids* **76** (1985) 351

[8] V.F.Sears, *Neutron News* **3** #3 (1992) 26

[9] A.C.Hannon, 'Neutron diffraction instrumentation' in 'Encyclopedia of spectroscopy and spectrometry', eds. J.Lindon, G.Tranter and J.Holmes, Academic Press 1999, in press.

[10] A.C.Hannon and W.S.Howells, 'The LAD Experimenter's Manual'1996

[11] A.K.Soper, W.S.Howells and A.C.Hannon, RAL-89-046

[12] W.I.F.David, M.W.Johnson, K.J.Knowles, C.M.Moreton-Smith, G.D.Crosbie, E.P.Campbell, S.P.Graham and J.S.Lyall, RAL-86-102

[13] A.C.Wright, *J.Non-Cryst.Solids* **179** (1994) 84

[14] S.R.Elliott, *Nature* **254** (1991) 445

[15] A.C.Wright, *J.Non-Cryst.Solids* **106** (1988) 1

[16] A.C.Hannon, D.I.Grimley, R.A.Hulme, A.C.Wright and R.N.Sinclair, *J.Non-Cryst.Solids* **177** (1994) 299

[17] A.C.Wright and A.J.Leadbetter, *Phys.Chem.Glasses* **17** #5 (1976) 122

[18] P.A.V.Johnson, A.C.Wright and R.N.Sinclair, *J.Non-Cryst.Solids* **58** (1983) 109

[19] D.I.Grimley, A.C.Wright and R.N.Sinclair, *J.Non-Cryst.Solids* **119** (1990) 49

CHAPTER 3

NUCLEAR MAGNETIC RESONANCE

3.1 INTRODUCTION

Nuclear magnetic resonance (NMR) is a non-destructive, site specific probe of the environment around non-zero spin nuclei. It is a particularly good probe of the amorphous state because it is sensitive to short range structure (≤5Å). It can detect changes in bond length, bond angle, connectivity and co-ordination up to the third co-ordination sphere [1]. The NMR spectrum contains information from several interactions, the combination of which is difficult to predict but which can be interpreted by comparison with spectra of similar crystalline samples and related to glass structure with knowledge of the sample composition. Recently developed experimental NMR techniques can extract further, more detailed information. However this study only uses basic, well established techniques, as outlined below.

3.2. THEORY

Nuclei with a non-zero nuclear spin, **I**, have a magnetic moment, μ, equation 3.1, in which γ, the gyromagnetic ratio, is characteristic of the nucleus.

$$\mu = \gamma \hbar \mathbf{I} \qquad (3.1)$$

The nuclei have 2I+1 possible degenerate energy states, which correspond to the possible magnitude and orientation of the moment. When placed in a static magnetic field the moments align with (lower energy) or against (higher energy) B_0. The moments then occupy 'Zeeman split' energy levels separated by ΔE,

$$\Delta E = \gamma \hbar B_0 \qquad (3.2)$$

The alignment of nuclear moments to an equilibrium magnetisation is called 'spin lattice relaxation'. The moments align with a small excess of nuclei in the lower energy state; 1 in 100000 for ^{29}Si at 300K when B_0 = 8.45T, [2]. This population difference can be descibed with Boltzman statistics and the rate at which it recovers from a random distribution can be described by the 'spin-lattice' relaxation time, T_1,

$$M(t) = M_0 (1-\exp(-t / T_1)) \qquad (3.3)$$

This relaxation to thermal equillibrium requires the transfer of energy to rotations, vibrations and translations of the matrix surrounding the nuclei. The transition between energy states has to be stimulated by fluctuating fields at the nuclei. In liquids, these are caused by rapid molecular motion, and so T_1 can be short (~ms). However, in glasses T_1 can be of the order of days. This restricts the NMR experiment. Doping with paramagnetic impurities provides the moments with a mechanism to relax. All the glasses used in this study are doped with ~ 0.05 mol.% Fe_2O_3, reducing T_1 to less than a minute, without distorting the energy levels, [3].

The dominant interactions between nuclei and their environment distort the energy levels as they stimulate relaxation. Their combined effect can be measured, and related to the bulk local structure, by exciting the nuclei with an oscillating rf field of energy $h\nu$ ($h\nu = \Delta E$) and observing the resonant transitions. Three basic relaxation mechanisms, relevent to this study, are outlined below.

3.2.1. THE CHEMICAL SHIFT INTERACTION

Nuclei are screened from B_0 by the electrons around them. This changes the energy level separation and shifts the resonant frequency by a factor $(1-\sigma)$

$$h\nu = \gamma \hbar B_0 (1-\sigma) \qquad (3.2)$$

σ is a second order tensor which is sensitive to the number and type of nearest neighbours, the bond angle and the type of next nearst neighbour. It combines the diamagnetic shielding, σ_d, due to closed electron shells and the paramagnetic shielding, σ_p, which is a measure of the covalency of the bonding and dominates when the shell is not closed. Fields due to electron spins (hyperfine splitting) and conduction electrons (Knight shift) do not contribute to the shifts observed in this study.

The isotropic chemical shift is measured relative to an accepted reference material and quoted as δ in ppm ($\delta = h\nu/B_0$). However, the isotropic chemical shift is not always easy to observe because non-uniform shielding of the nuclei can produce a spread in resonant frequency and a broadening of the resonant lineshape. The Sn^{2+}, see figure 6.8.4, and similarly Pb^{2+} lineshapes are broadened by the anisotropic shielding of their non-bonding pair of electrons, such that it is difficult to observe an

undistorted resonance in a single experiment. This is not a problem with the other nuclei used in this study (^{29}Si, ^{31}P, ^{27}Al and ^{1}H).

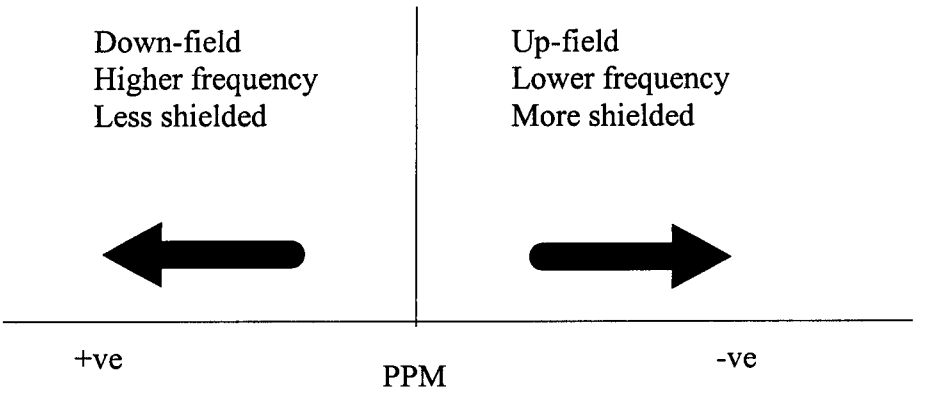

Figure 3.1 The chemical shift changes with the shielding of the nuclei.

The chemical shift (δ) is sensitive to the combination of several sources of oscillating field felt at the nucleus. The net effect of these oscillating fields can be related to the local environment about the nuclei by comparing the shift to those reported for similar structures. Figure 3.1 illustrates the shift in the resonant frequency caused by a change in the shielding of the nuclei [4]. The ^{29}Si and ^{31}P MAS NMR presented in this study primarily relates the chemical shift to the co-ordination about and the connectivity of the probed nuclei. This provides useful structural information which can be compared to that from other techniques, notably the sample composition, but which is only as accurate as the comparison to the similar structures.

3.2.2. THE DIPOLE-DIPOLE INTERACTION

There is a spread in the magnetic field felt at a nucleus due to the time varying magnetic fields of neighbouring nuclei and the static inhomogeneity in B_0. Both effects stimulate relaxation. The latter is a small effect which can be removed by experimental technique, see section 3.3, whilst the former contains structural information of the environment of the excited nuclei. 'Spin-spin relaxation' is the dominant relaxation mechanism between spin $^1/_2$ nuclei in solids and has a characteristic time constant T_2,

$$M(t) = M_0 \exp(-\tau / T_2) \qquad (3.5)$$

where τ is the time elapsed after exciting the nuclei. The interaction between an isolated pair of nuclei can be considered analogous to the classical through-space interaction of two dipoles, separated by a distance r and at an angle θ with B_0.

$$B = B_0 \pm \frac{3}{4}\left(\frac{\mu_0}{4\pi}\right)\frac{\hbar\gamma}{r^3}\left(1-3\cos^2\theta\right) \qquad (3.6)$$

Dipolar coupling between two nuclei produces a splitting of the resonant line from which the internuclear separation can be measured. The dipolar interaction between many spins produces a spread in the local magnetic field and hence a spread in resonant frequencies, the width of which can be related to the internuclear separation, [5]. It can, however, mask other structural information such as the chemical shift and the symmetry of the lineshape.

Magic angle spinning techniques remove the dipolar broadening by spinning the sample at 54°44'8'' relative to B_0, such that $(1-3\cos^2\theta)$ is zero. MAS has been used in this study at frequencies faster than the dipolar broadening so that the width of the resonance is a measure of the site disorder.

3.2.3. THE QUADRUPOLE INTERACTION

The quadrupolar interaction is the dominant broadening mechanism for $I > {}^1/_2$ nuclei in non-cubic environments. It is a perturbation of the Zeeman split energy levels, see figure 3.2. This results from the coupling between the non-spherical nuclear charge distribution and the electric field gradient (efg) felt at the nucleus due to the surrounding non-symmetric electron charge distribution and/or charges on nearby atoms or ions. This can be a large effect which hides the effects of chemical shielding and dipolar coupling and is not completely removed by spinning at the magic angle. The quadrupolar coupling does, however, offer two further probes of the local order. The departure of the efg from cylindrical symmetry (the asymmetry parameter, η) and the magnitude of the efg at the nucleus (the quadropole coupling constant, C_Q) can be extracted by simulating the experimental lineshape, varying these quadrupolar parameters.

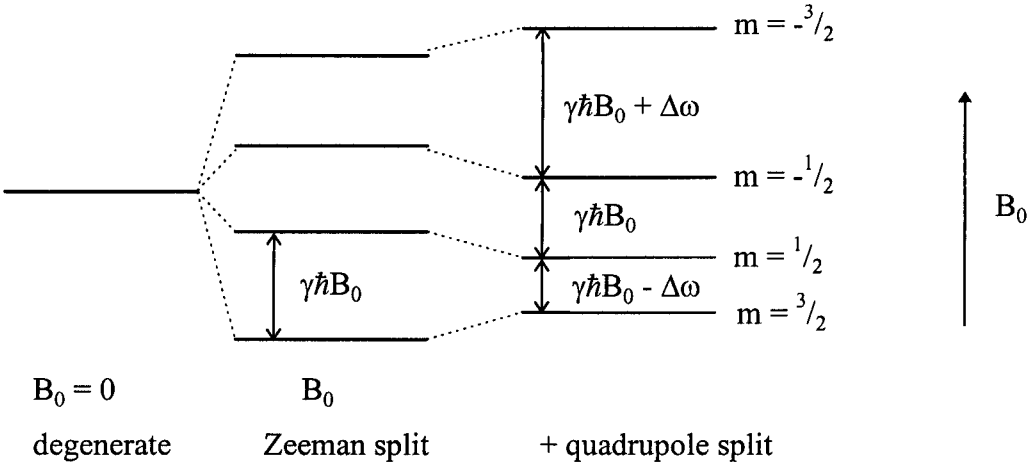

Figure. 3.2 Zeeman and quadrupole energy level splitting for nuclei I = $^3/_2$, when $C_Q \neq 0$ is small.

The quadrupolar coupling for I = $^3/_2$ nuclei, as shown in figure 3.2, increases the energy of the spin - $^3/_2$ states and decreases the energy of the spin + $^3/_2$ states. This shifts the resonant freqency. When C_Q is large the $^1/_2 \rightarrow -^1/_2$ transition is also shifted, so that the split lineshape is also distorted. Spinning at the magic angle can reduce the first and third order components of the quadrupolar coupling if the broadening is not much larger than the spinning speed. DOR and DAS techniques, spinning about two axes, can also reduce the second order component of the quadrupolar coupling, but these techniques were not used in this study.

3.3. EXPERIMENTAL METHOD

The glass samples were powdered and carefully packed into spinners, in a dry glove box when necessary (notably the phosphosilicate glasses presented in chapter 8) and then spun at the 'magic angle' with dry gas (nitrogen or air) at a frequency higher than the resonant broadening from internal interactions. A Bruker 4mm MAS probe, spinning the sample at 6 ~ 10 kHz, was used for most samples with the exception of the potassium phosphodisilicates, presented in chapter 8, which required a larger sample volume spinner to improve the S/N ratio.

The sample was spun inside and excited by a coil in a tunable LC circuit. The probe positioned the sample in the large, static field B_0 and a set of 'shim' coils inside the bore of the superconducting magnet were used to improve the homogeneity of the field. The experiments, summarised in table 3.1 were automated and the data collected by the spectrometer. Most experiments were carried out on the MSL 360 although the tin spectra were collected at a lower field (to reduce the

chemical shift anisotropy) and the ^{17}O ($I = {}^{5}/_{2}$) experiments were performed on the CMX-600 to improve the resolution and the S/N ratio.

	Spin (I)	Isotopic abundance (%)	reference material	ν (MHz) CMX-300	ν (MHz) MSL-360	ν (MHz) CMX-600
^{1}H	1/2	99.985	H_2O		360[2,4]	
^{17}O	5/2	0.037	H_2O			81.342[1]
^{27}Al	5/2	100	α-Al_2O_3		93.84[4]	
^{29}Si	1/2	4.7	T.M.S.		71.54[1,2,3,4]	
^{31}P	1/2	100	85% H_3PO_4		145.78[4]	
^{119}Sn	1/2	7.61	SnO_2	88.75[1]		

Table 3.1 Natural abundance, reference materials and spectrometers used to probe nuclei at their resonant frequency ν (MHz). The superscripts indicate: [1] tin silicates (chapter 6), [2] sodium and potassium tin silicates (chapter 7) and [4] potassium phosphosilicates (chapter 8).

3.3.1. PULSED FOURIER TRANSFORM NMR

The nuclei are excited by a sequence of square rectangular pulses of radio frequencies applied perpendicular to the static field B_0. These produce an oscillating field B_1 orthogonal to the static field which can be considered to tip the magnet moment from its equilibrium position by an angle θ_P;

$$\theta_P = \gamma B_1 t_P \qquad (3.7)$$

where γ is the gyromagnetic ratio of the nuclei, B_1 is the oscillating field generated by the pulse and t_P is the length of the pulse. The length of the pulse is inversely proportional to the range of frequencies irradiated, as shown in figure 3.3. The square rectangular pulse in the time domain and the sinc function in the frequency domain are a Fourier pair related by a Fourier transform.

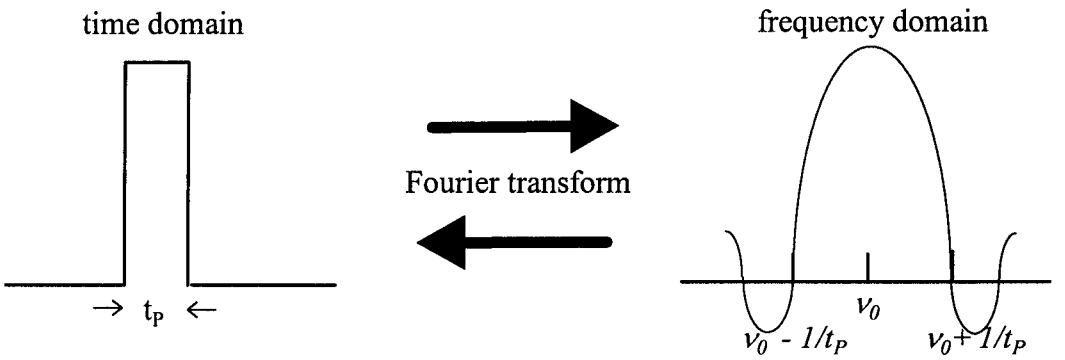

Figure 3.3 The relationship between the time and frequency domains of a square rectangular pulse of frequency v and length t_P.

It is important to irradiate all the nuclei in the sample uniformly. The square wave can be considered the sum of all the frequencies up to the inverse of its width [6]. So short pulses are used, particularly when the resonance is broad and/or when nuclei have very different local environments.

A $^{\pi}/_{2}$ pulse in a NMR experiment excites all of the small excess of nuclei in the lower energy state and observes the decay of the nuclei back to thermal equilibrium. This effect is best observed about the resonant frequency of the nuclei. The same coil which excited the nuclei records the envelope of frequencies which decay with time. This envelope of frequencies is called the field induced decay (FID). The FID is related to the frequency response of the nuclei (the NMR spectrum) by Fourier transform.

Before applying the Fourier transform each FID was first multiplied by an exponential function to damp the noise. This is equivalent to replacing each point in the NMR spectrum by a Lorentzian function. Care was taken to ensure that this did not change the shape of the spectrum.

3.3.2. PULSE SEQUENCES

A 1-pulse sequence excites the nuclei with a single square rectangular pulse, records the FID, waits for the nuclei to return to thermal equilibrium and then pulses again. The FIDs from each pulse are summed to obtain a suitable S/N ratio. Two phase sensitive detectors in quadrature (90° out of phase with each other) detect the FID and are then summed. This improves the S/N ratio which saves acquisition time. The phase of subsequent pulses is cycled to remove detector artifacts.

The FID is a complex frequency response which consists of a combination of absorption and dispersion mode components. The detectors are set to measure the absorption mode of the FID. However, if the weighting of the components in the FID is offset from that of the detectors then the Fourier transform introduces a frequency-independent offset to the lineshape. The NMR lineshape, the absorption mode component, can be obtained by changing the weighting of the two components. This is known as 'zeroth order' phase correction.

A 'first order' phase correction is also often necessary, largely because the front end of the FID is truncated when using a 1-pulse sequence. This is because the probe 'rings' for a short time after the pulse, so the first ~5μs of the FID is not recorded. This offset in t=0 from the centre of the pulse introduces a frequency dependent phase error which can be removed by a linear phase correction to the absorption mode of the resonance [6]. When the phase shift is not significant the baseline of the spectrum can be fitted by a polynomial and subtracted, without changing the resonant lineshape [7].

A 1-pulse sequence is the simplest pulse sequence to use but requires an excellent static field homogeneity such that the FID decays with the decay constant T_2 (characteristic of the sample) and not with T_2^* (characteristic of the static field). Inhomogeneity in B_1 causes a variation in flip angle across the sample, this distorts the FID. Also, a 1-pulse sequence is not suitable when the FID is short (the spectrum is broad). Instead a spin echo pulse sequence is used to remove the FID from the ringing coil deadtime, see figure 3.4.

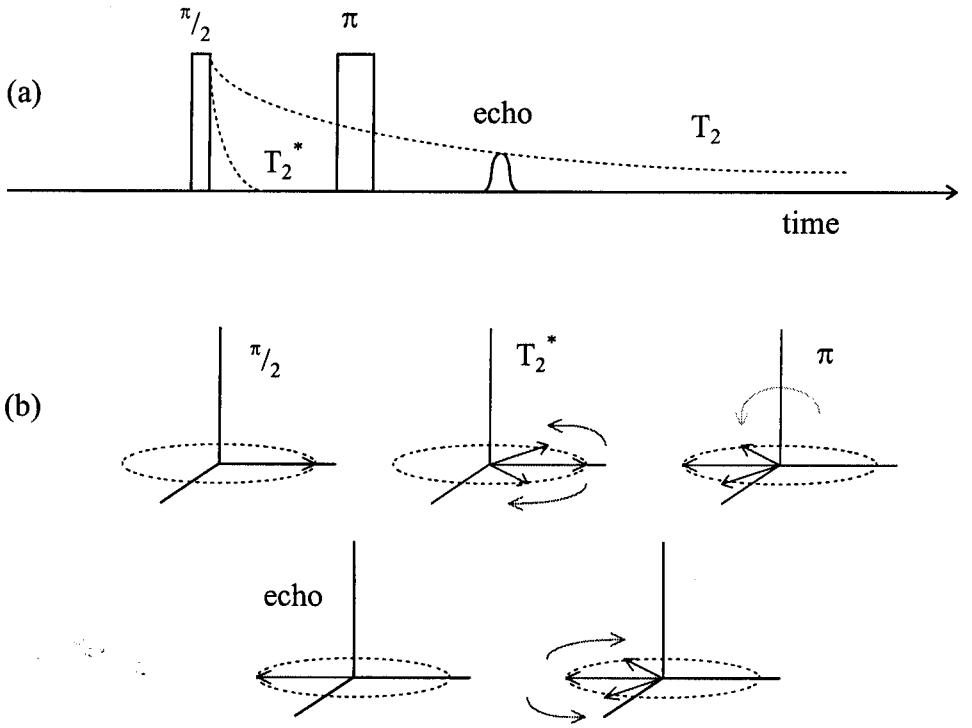

Figure 3.4 (a) The spin echo pulse sequence and (b) the response of the moments .

The spin echo pulse sequence is best considered classically in the rotating frame of the moment. A $^{\pi}/_{2}$-pulse (when $\theta_P = 90°$) tips the moments into the x-y plane. The moments dephase and the net magnetisation decays with a time constant T_2^*. Then a π-pulse (when $\theta_P = 180°$), after a time τ, flips the moment 180° such that the moments rephase after a time 2τ. This rephasing and subsequent dephasing again forms an 'echo' of two FIDs back to back. The characteristic dipole-dipole decay constant T_2 can be (but not in this study) measured from the decay of the echo with τ.

The spin echo pulse sequence can also be used to sample the magnetisation after a saturation comb to measure the spin lattice relaxation time T_1. The saturation comb is a series of short pulses which remove the net magnetisation. The spin echo sequence, using a short τ, can then sample the rate at which the magnetisation recovers. T_1 is not reported for any glasses in this study but the pulse train repetition times were estimated ~$3T_1$, to prevent saturation of the spins.

3.3.3 ^{29}Si NMR

T_1 can often be very long in silicates (up to days) because ^{29}Si is a spin $^1/_2$ nucleus and has a low natural abundance (so active nuclei are well separated). Hence, the number and strength of relaxation mechanisms are limited. The Fe^{3+} added to the glasses in this study act as 'spin sinks', providing an oscillating field to stimulate the relaxation back to thermal equilibrium. This reduced the acquisition time such that an adequate S/N ratio could be acquired for each glass.

Care was taken to ensure that the pulse repetition time was not too fast and that the magnetisation had sufficient time to relax so that the proportion of different species remained quantitative. Short pulses (~2μs) were used to reduce θ_P and to irradiate a large spectral width, as nuclei in different local environments resonate at very different resonant frequencies.

The ^{29}Si chemical shift was used to identify the type and connectivity of silicate species by comparison with δ for crystalline and amorphous systems in the literature, see figure 3.5. The number of nearest neighbours (co-ordination number) has a large effect on δ whilst the connectivity to and type of next nearest neighbours has a lesser effect. The resonances of different tetrahedral species overlap to produce a single resonance, the width and position of which changes with the proportion of species. It is possible to distinguish between Q^n species, as described in chapter 1, but the comparison is only accurate with similar characterised crystalline and amorphous systems and becomes more ambiguous with the number and type of different nuclei.

Structural information can also be obtained from the width of the resonance. The FWHM, when completely narrowed by MAS, is indicative of the site disorder and can be compared with similar systems. Maekawa reported the FWHM as ~12ppm (Q^4) and ~10ppm (Q^2 and Q^3) in alkali silicates [8]. Devine reported the FWHM in ν-SiO_2 as 11ppm [9].

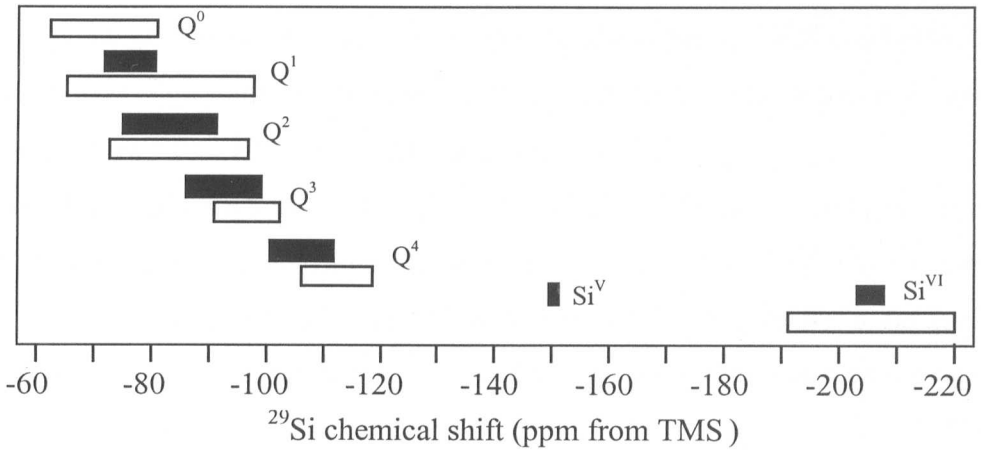

Figure 3.5 The reported shift ranges for silicate polyhedra with different degrees of polymerisation in crystalline silicates (white) from [10] and [11], and amorphous silicates (black) from [4] and [12]. Shifts relative to TMS.

3.3.4 ^{31}P NMR

Static ^{31}P NMR spectra are typically very broad (~300ppm). This is largely due to dipolar broadening which can be removed by MAS experiments. The MAS spectra can resolve different Q^n species [13], see figure 3.6. The ^{31}P nuclei are less shielded (γ shifts down-field (becomes less negative)) as the network is depolymerised. However, the type of next nearest neighbours also has a significant effect on the shielding of the ^{31}P nuclei. The assignment of Q^n species from ^{31}P NMR requires a careful comparison with characterised phosphates.

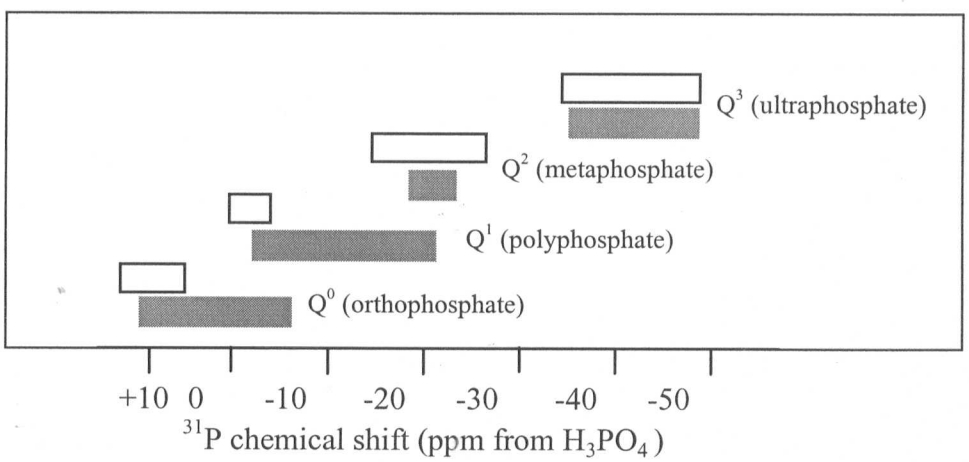

Figure 3.6. The reported shift ranges for crystalline (white) [14] and amorphous (shaded) [15] phosphates with different tetrahedral arrangements.

The phosphate glasses in this study, see chapter 8, were spun at ~9kHz and pulsed with short pulses (2μs) every 10 seconds. Each spectrum only required ~2hrs acquisition time, as ^{31}P is 100% naturally abundant.

The static lineshape can help to identify ^{31}P-Q^n species as Q^3 is axially symmetric about its double bond and Q^1 about its bridging oxygen. Q^2 and Q^0 have lower symmetry [14]. Figure 3.7 shows typical, unbroadened lineshapes for a random orientation (relative to B_0) of axially symmetric and lower symmetry phosphate groups.

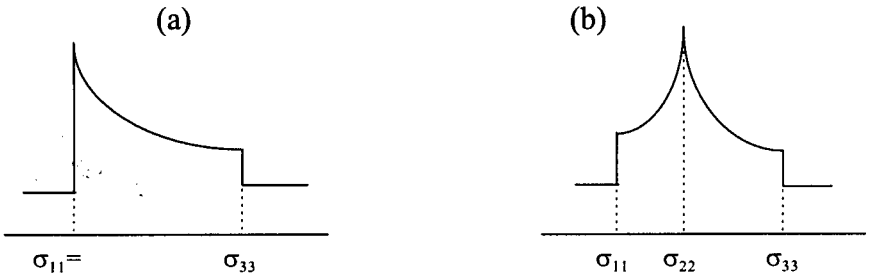

Figure 3.7 Powder pattern linshapes for (a) axially symmetric and (b) lower symmetry sites.

REFERENCES

[1] R.K.Harris, Nuclear Magnetic Resonance Spectroscopy, Longman Scientific and Technical 1986

[2] M.W.G.Lockyer, 'High resolution mltinuclear magnetic resonance studies of oxide glasses' PhD thesis, Physics Department, Warwick University, September 1993.

[3] M.G.Mortuza, 'A nuclear magentic resonance investigation of the structure of some alkali silicate glasses' PhD thesis, Physics Department, Warwick University, September 1989.

[4] R.Dupree and D.Holland, in 'Glasses and Glass Ceramics' ed. M.H.Lewis, Chapman and Hall 1989

[5] J.H.Van Vleck, *Phys.Rev.* **74** #9 (1948) 1168

[6] E.Fukushima and S.B.W.Roeder, 'Experimental pulse NMR', Addison Wesley 1981

[7] personal correspondance with Dr.A.P.Howes, Warwick University.

[8] H.Maekawa, T.Maekawa and K.Kawurma, J.Non-Cryst.Solids 127 (1991) 53

[9] R.A.B.Devine, R.Dupree, I.Farnan and J.J.Capponi, *Phys.Rev.B* **35** (1987) 2305

[10] A.R.Grimmer, F.Von.Lampe, M.Mägi, *Chem.Phys.Lett.*, **132** (1986) 549

[11] J.S.Frye and G.E.Maciel, *J.Magn.Reson.*, **48** (1982) 125

[12] X.Xue, J.F.Stebbins, M.Kanzaki, P.F.McMillan and B.Poe, *Am. Min.* **76** (1991) 8

[13] H.Eckert, *Prog.Nucl.Magn.Reson.Spectrosc.* **24** (1992) 159

[14] R.K.Brow, R.J.Kirkpatrick and G.L.Turner, *J.Non-Cryst.Solids* **116** (1990) 39

[15] S.W.Martin, *Eur.J.Solid State Inorg.Chem.*, **28** (1991) 163

[16] R.J.Kirkpatrick and R.K.Brow, *Solid State NMR* **5** (1995) 9-21

CHAPTER 4

OTHER EXPERIMENTAL TECHNIQUES

4.1 POWDER X-RAY DIFFRACTION

Powder X-ray diffraction is a well established technique for the structural characterisation of crystalline materials [1-3]. It was used to confirm that each glass sample was amorphous and also to identify crystalline phases in the devitrified samples. Crystalline phases were identified with reference to JCPS diffraction files [4]. The diffraction pattern for each glass sample was diffuse as they, by definition, lack long range periodicity. X-ray diffraction patterns for c-SiO_2 and v-SiO_2 are shown in figure 4.1.

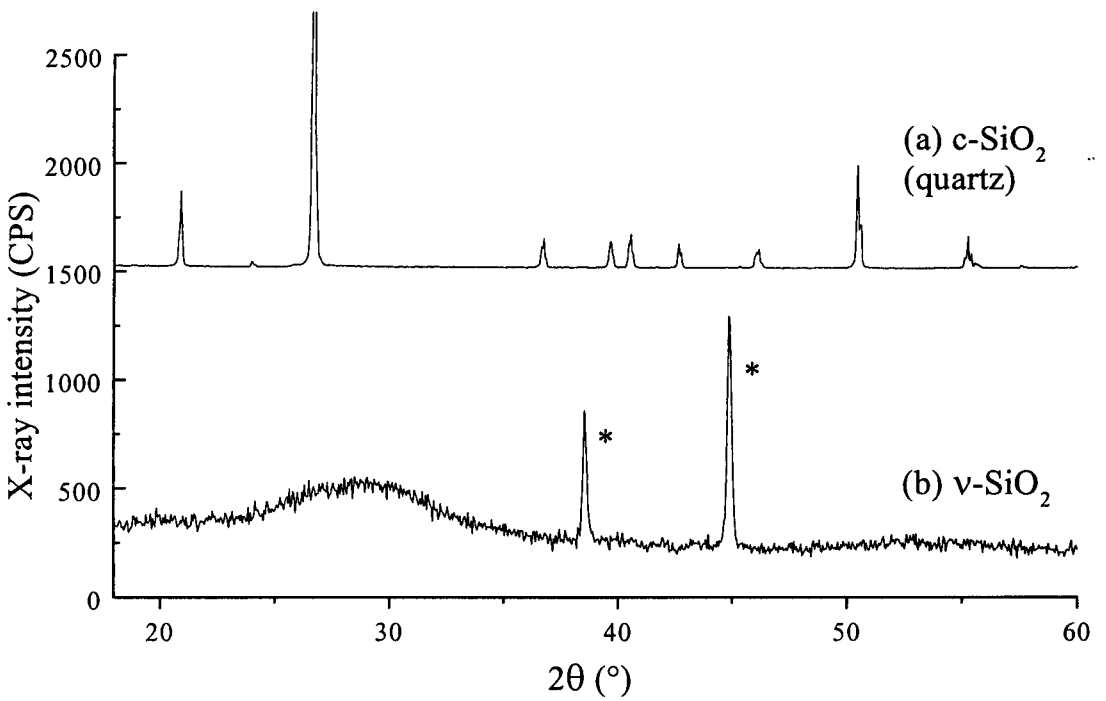

*Figure 4.1 X-ray diffraction patterns for (a) quartz and (b) silica. The * indicate diffraction peaks from the aluminium slide.*

The diffraction pattern can be considered as a series of summed partial reflections from planes in a periodic lattice. The intensity of each reflection is related to the type of atoms in the plane and the sum dependent upon the phase shift between the reflections [5]. The diffraction pattern is related to the sample structure by Bragg's law, as described by equation 4.1;

$$n\lambda = 2\,d\sin\theta \qquad (4.1)$$

where n is the order of the reflection (=1), λ the wavelength of the radiation, θ is the incident angle and d the interplanar separation.

The samples were powdered using an agate pestle and mortar and flattened into a recess in an aluminium slide. The sample and slide were then positioned in the diffractometer and rotated through an angle θ as the diffraction pattern was measured at an angle 2θ. θ - 2θ scans were performed on each powdered sample using Cu K_α radiation (λ = 1.54178Å). The detector was swept at typically $2°min^{-1}$ in 0.01° steps between 10° and 70° and the diffraction pattern recorded on an Acorn 3020.

4.2 ENERGY DISPERSIVE X-RAYS

Energy dispersive X-ray analysis using a scanning electron microscope (SEM-EDX) is routinely used to determine the chemical composition of glasses [6-8]. The electron beam is used to irradiate and excite the atoms in the glass and the resulting X-rays are detected using a solid state detector [9]. The energy and intensity of the X-rays are characteristic of the type and concentration of the excited atoms in the sample.

Quantitative SEM-EDX analysis was used to determine the composition of the sodium tin silicate glasses presented in chapter 7. Pieces of glass (~ $0.1cm^3$) were mounted in bakelite and polished to a flat surface with oil based diamond solutions. These were then coated with a thin film of carbon to prevent surface charging in the electron beam. A JEOL 6100 SEM was used to measure the X-ray emission spectra for each sample with ISIS analytical software [10]. A low energy, 10keV, electron beam was used to excite the sample electrons (Na^K, Si^K and Sn^L). This accelerating voltage was chosen to excite the atoms $\leq 10\mu m$ from the sample surface whilst minimising the charge induced migration of species, notably Na [11]. The energy scale was calibrated by recording a spectrum for a manganese standard. The working distance and sample and detector angles were kept constant. EDX measurements for several sodium tin silicate glasses of unknown composition and similar glasses of known composition [12] were made on the same date under identical conditions.

It is possible to calculate and apply ZAF corrections to the recorded X-ray emission spectrum. These correct for the effect of atomic number, absorption and

fluorescence of each atom species on all the emitted X-rays. However all these corrections are calculated with reference to a characterised internal standard. The ISIS software [10] uses elemental tin, silicon and sodium as internal standards to calculate the ZAF corrections for Sn^{2+}, Si^{4+} and Na^{+} X-ray emissions. The ZAF behaviour of these standards are not thought to relate to the species in these glasses. So, the raw (pre ZAF corrected) atom specific X-ray intensities were used to determine the unknown sample compositions by comparison with those for samples of known composition. It is assumed that the matrix effects are comparable between glasses of similar compositions. The background X-ray intensity was removed using a top hat digital filter [10].

4.3 X-RAY FLUORESCENCE.

X-ray fluorescence is commonly used to determine the composition of glasses. It is considered to be more sensitive than SEM-EDX analysis because the excitation efficiency is higher whilst the background noise is lower [9]. White X-rays irradiate the sample, the atoms fluoresce and emit characteristic series of X-rays.

The composition of the phosphosilicate glasses, presented in chapter 8, were determined by X-ray fluorescence (XRF) measurements. The samples and reference mixtures of analytical grade K_2CO_3, SiO_2 and P_2O_5 were weighed and mixed in a pestle and mortar under dry argon and were kept dry in an evacuated glove box until use. Each sample (or reference mixture) was presented in a modified holder using a 6μm Mylar membrane. Wavelength dispersive XRF measurements were made using a Phillips PW1400 at the Geological Science Department, Durham University. The intensity of the background and the major fluorescent line for each atom species (K^K, Si^K, P^K) were selected with a LiF crystal and measured at an angle 2θ. An α-based correction system, Phillips X40 software package was used to calibrate and correct the data. The K, Si and P content of the glasses were determined by interpolating between the raw X-ray intensities of the reference mixtures. It is assumed that the matrix effects in the glass samples and reference mixtures are similar.

4.4 DENSITY MEASUREMENTS

The density of a material can be defined as

$$\rho = \frac{mass}{volume} \tag{4.2}$$

The volume of non-regular pieces of glass can be measured by 'Archimedes method' displacing a liquid [12] or more accurately by displacing a gas. Gas can penetrate pores in a solid and avoids 'surface wetting' problems. The volume of solid pieces of glass were measured using a Quantachrome micropycnometer, displacing helium [13].

The micropycnometer measures the change in pressure when a known volume of gas, under pressure, is allowed to flow from a reference volume into a sample cell. The initial state of the sample cell, when isolated from the reference volume but open to atmospheric pressure, P_a, can be defined as

$$P_a\left(V_c - V_p\right) = n_a R T_a \tag{4.3}$$

where V_c is the cell volume, V_p the sample volume, n_a the number of moles of gas, R the gas constant and T_a the ambient temperature. The state of the reference volume, V_R , pressurised to ~ 17 pounds per square inch , P_1, can also be defined as

$$P_1 V_R = n_1 R T_a \tag{4.4}$$

The pressure drops to P_2 when the valve between the reference and sample volumes is opened and gas flows between the sample cell and the pressurised reference volume. The state of the combined system can be written as

$$P_2\left(V_c - V_p + V_R\right) = n_a R T_a + n_1 R T_a \tag{4.5}$$

This can be rewritten as

$$P_2\left(V_c - V_p + V_R\right) = P_a\left(V_c - V_p\right) + P_1 V_R \tag{4.6}$$

P_a , the ambient pressure, is initially set to zero such that the sample volume can be expressed as

$$V_p = V_c - V_R\left(\left(P_1 / P_2\right) - 1\right) \tag{4.7}$$

V_c and V_R are known from calibrating the micropycnometer with two stainless steel spheres of known volume. The volume of ~ 1cm^3 of solid phosphosilicate glass was measured to an accuracy of ±0.02 cm^3 by repeating this method. The stability of the values obtained was improved by initially purging the sample and sample cell with helium for ~ 5 minutes. This removed air and moisture from the sample surface.

REFERENCES

[1] B.E.Warren, 'X-ray Diffraction', Addison Wesley, 1969.

[2] H.P.Klug and L.E.Alexander, 'X-ray Diffraction Procedures for Polycrystalline and Amorphous Materials', 2nd Ed. Wiley, 1974.

[3] D.W.L.Hukins, 'X-ray Diffraction by Disordered and Ordered Systems' Oxford-Pergamon, 1981.

[4] PDF-2 Database Sets 1-41, International centre for diffraction data 1991.

[5] A.M.Glazer, 'The structures of crystals', IOP Publishing Ltd. 1987.

[6] J.G.Spray and D.A.Rae, Canadian Mineralogist 33 #2 (1995) 323

[7] D.T.Bowron, G.BushnellWye, R.J.Newport, B.D.Rainford and G.A.Saunders *J.Phys.Cond.Mat.* **8** #19 (1996) 3337

[8] M.D.Norman, W.L.Griffin, N.J.Pearson, M.O.Garcia and S.Y.O'Reilly, *J.Analytical Atomic Spectroscopy* **13** #5 (1998) 477

[9] P.J.Goodhew and F.T.Humphreys, 'Electron microscopy and analysis', 2nd ed. Taylor and Francis 1992.

[10] 'The Oxford guide to Xray microanalysis', Oxford instruments plc 1997.

[11] Personal correspondance with Steve York.

[12] A.Sears, PhD Thesis, Physics Department, Warwick University, 1998

[13] 'Quantachrome micropycnometer handbook', Quantachrome Corporation, 1995.

CHAPTER 5

THE SIMULATION OF RESOLUTION EFFECTS ON THE STRUCTURAL PARAMETERS OBTAINED FROM NEUTRON DIFFRACTION DATA

5.1 INTRODUCTION

The standard approach used to probe glass structure by neutron diffraction is to Fourier transform the data and to fit the peaks in the real space correlation function. The peak position represents an interatomic separation, the peak width indicates the variation in the interatomic separation and the peak area is proportional to the co-ordination number. However, the parameters obtained from fitting the correlation function are affected by experimental inaccuracies. Two such sources of experimental uncertainty are considered in this study.

5.2 REAL SPACE RESOLUTION

It is common practice to fit the peaks in the real space correlation function with a Gaussian function. However, this is not the analytically correct function with which to fit the peaks in T(r). This simulation study considers the the peaks in T(r) to be broadened resolution functions. There are two factors which contribute to the broadening: the static disorder in the sample and the thermal motion of the atoms. The static disorder may be asymmetric and is often very small for oxide glasses. Hence static disorder is neglected for the purpose of this simulation. The thermal broadening is Gaussian in T(r), as described in equation 2.18 [1].

The real space resolution function, P(r), represents the experimental condition that the scattering cannot be measured to $Q = \infty$ but only up to a finite value Q_{max}. The discontinuity at Q_{max} introduces termination ripples in the Fourier transform. It is common practice to apply a modification function to the diffraction data to damp these termination ripples, but this broadens the resulting real space resolution function.

This study simulates the resolution function for both Lorch and step modification functions. Each resolution function is broadened with a Gaussian function, to simulate the thermal broadening, and then fitted by an unbroadened Gaussian function. The results are presented to quantify the error introduced into the peak fit parameters by fitting with the wrong function.

5.2.1 REAL-SPACE SIMULATION DETAILS

The resolution function is the cosine transform of the modification function, as described by equation 2.19. The Lorch modification function is defined by equations 2.8 and 2.9. The step modification function is described by equations 5.1 and 5.2;

$$M_{step}(Q) = 1 \quad \text{for} \quad Q \le Q_{max} \tag{5.1}$$

$$M_{step}(Q) = 0 \quad \text{for} \quad Q > Q_{max} \tag{5.2}$$

The resolution function can be evaluated analytically for $M_{step}(Q)$, as described by equation 5.3, but does not have an analytical form for $M_{Lorch}(Q)$.

$$P_{step}(r) = \frac{Q_{max}}{\pi} \frac{\sin(rQ_{max})}{rQ_{max}} \tag{5.3}$$

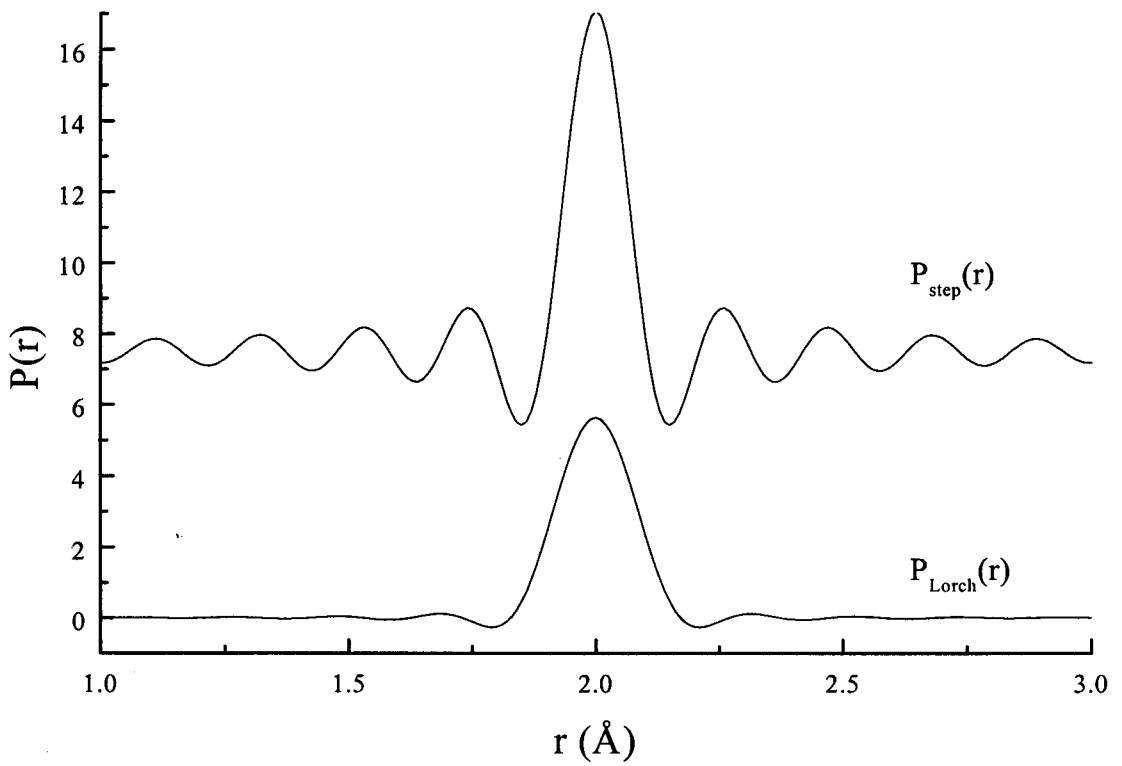

Figure 5.1 $P_{LORCH}(r)$ and $P_{STEP}(r)$ for $Q_{max}=30Å^{-1}$.

P(r) was calculated numerically using the 'g_f:pori_plus' and g_f:por_step_plus' FORTRAN routines available at RAL. The routines were run as genie load routines. Each routine required an empty file called dummy.dat in the working directory. $P_{step}(r)$ and $P_{lorch}(r)$ calculated with a Q_{max} of $30Å^{-1}$ are shown in figure 5.1.

The central peak in $P_{step}(r)$ is narrow but the associated termination ripples are large. The termination ripples in $P_{lorch}(r)$ are much smaller but the central peak is broader. The width of the central peak in each resolution function is related to Q_{max} by equations 5.4 and 5.5.

$$FWHM_{step} = \frac{3.791}{Q_{max}} \tag{5.4}$$

$$FWHM_{Lorch} = \frac{5.437}{Q_{max}} \tag{5.5}$$

The broadening of the resolution function was simulated using the genie load routine 'g_f:tprime'. As previously, an empty file called dummy.dat was required in the working directory. This routine replaces each point in P(r) with a Gaussian of width $\langle u^2 \rangle^{1/2}_{thermal}$, as defined by equation 2.18, and sums the intensity of each.

The central peak in the broadened resolution function was then fitted with a Gaussian function using the ffit_g routine. This was repeated for values of Q_{max} between 12 and $50Å^{-1}$ and for $\langle u^2 \rangle^{1/2}_{thermal}$ between 0 and 0.3Å, for both $M_{Lorch}(Q)$ and $M_{step}(Q)$.

5.2.2 REAL-SPACE SIMULATION RESULTS AND DISCUSSION

Figures 5.2 and 5.3 show simulated T(r)s for both Q_{max} = 20 and $40Å^{-1}$ using $M_{Lorch}(Q)$ and $M_{step}(Q)$ respectively. Each simulated T(r) consists of P(r) broadened by a Gaussian. The Gaussian fit to each peak is shown as a dotted line. The fit was restricted to the region over which the central peak was positive. This was considered to be a typical approach that might be used in fitting real experimental data. The fitting process was repeated several times for each peak and the final fit to each peak is considered acceptable. However, it is clear in these diagrams that there are discrepancies between the simulated peak and the peak fit.

Fitting the central region of the simulated T(r) with a Gaussian reports the correct peak position but not the correct peak width and does not include the contribution to

the area contained within the termination ripples. The effect of these discrepancies varies with the type of modification function, the value of Q_{max} and the width of the broadening Gaussian.

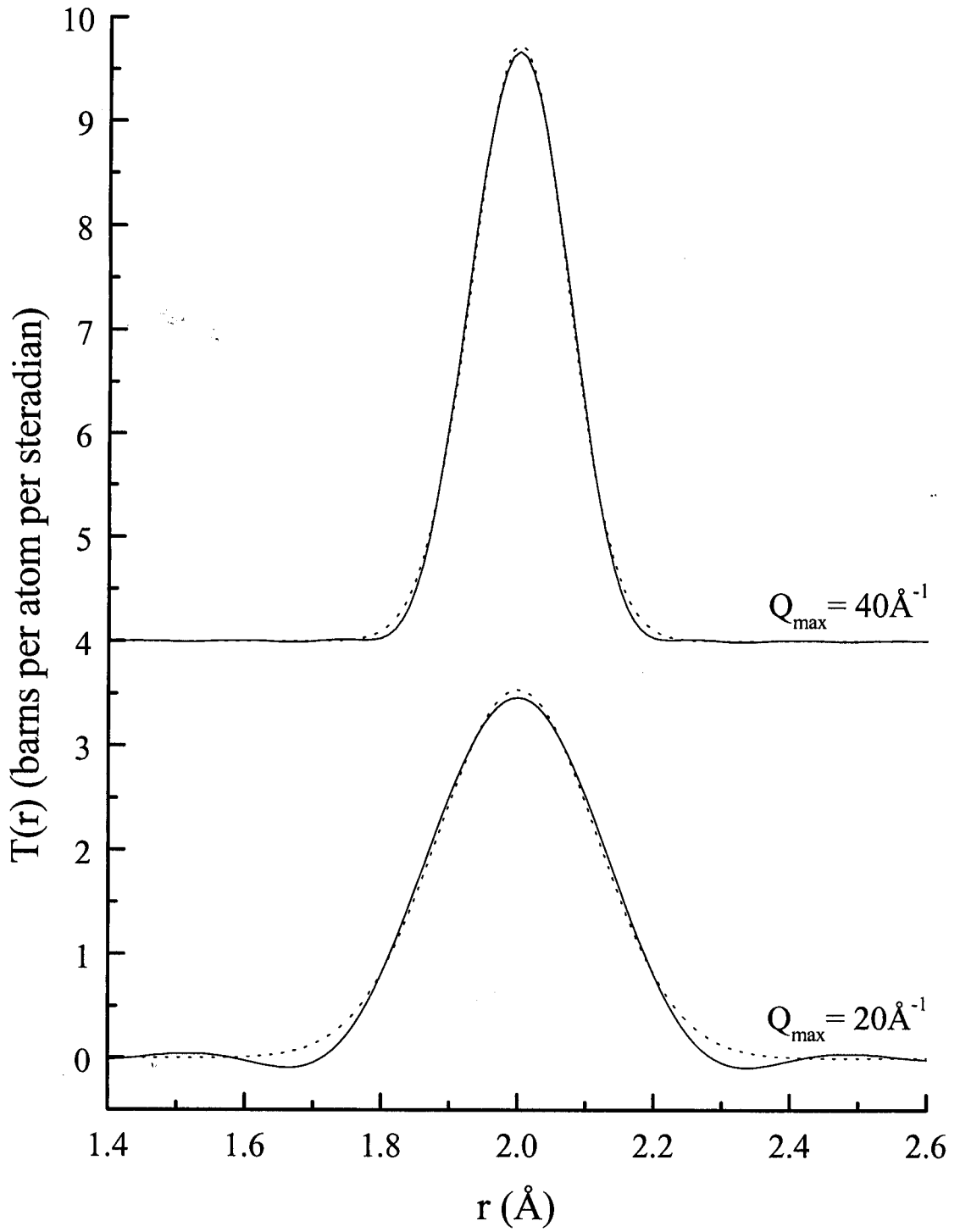

Figure 5.2 $T_{LORCH}(r)$ for Q_{max}=20 and 40Å^{-1}, broadened with a Gaussian of width $\langle u^2 \rangle^{1/2}_{thermal}$ = 0.05Å. The Gaussian peak fit is shown as a dotted line.

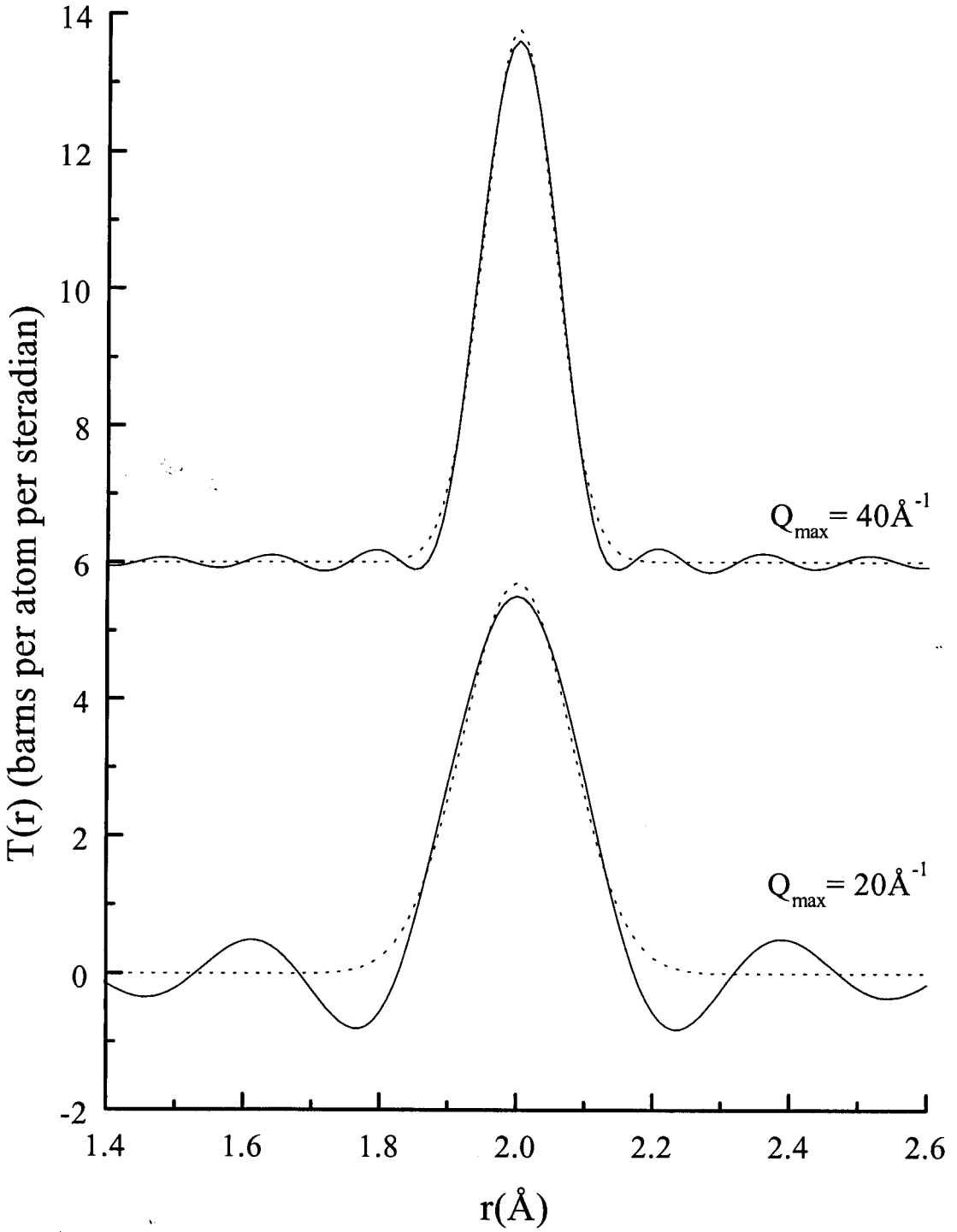

Figure 5.3 $T_{STEP}(r)$ for Q_{max}=20 and 40Å^{-1}, broadened with a Gaussian of width $\langle u^2 \rangle^{1/2}_{thermal}$ = 0.05Å. The Gaussian peak fit is shown as a dotted line.

5.2.2a THE WIDTH OF THE GAUSSIAN PEAK FIT

If two Gaussian functions are convoluted then the resulting function is also a Gaussian. The width of the resulting Gaussian, $\langle u^2 \rangle^{1/2}_{T(r)}$, is given by adding in quadrature the widths of the two input Gaussians, $\langle u^2 \rangle^{1/2}_{thermal}$ and $\langle u^2 \rangle^{1/2}_{P(r)}$ [2]. If all the functions used in these simulations are assumed to approximate Gaussian functions then;

$$\langle u^2 \rangle_{T(r)} = \langle u^2 \rangle_{thermal} + \langle u^2 \rangle_{P(r)} \qquad (5.6)$$

However, P(r) is not Gaussian and the deviation from this behaviour increases as $\langle u^2 \rangle^{1/2}_{thermal}$ and Q_{max} decrease. This can be seen for $T_{Lorch}(r)$ and $T_{step}(r)$ in figures 5.4 and 5.5.

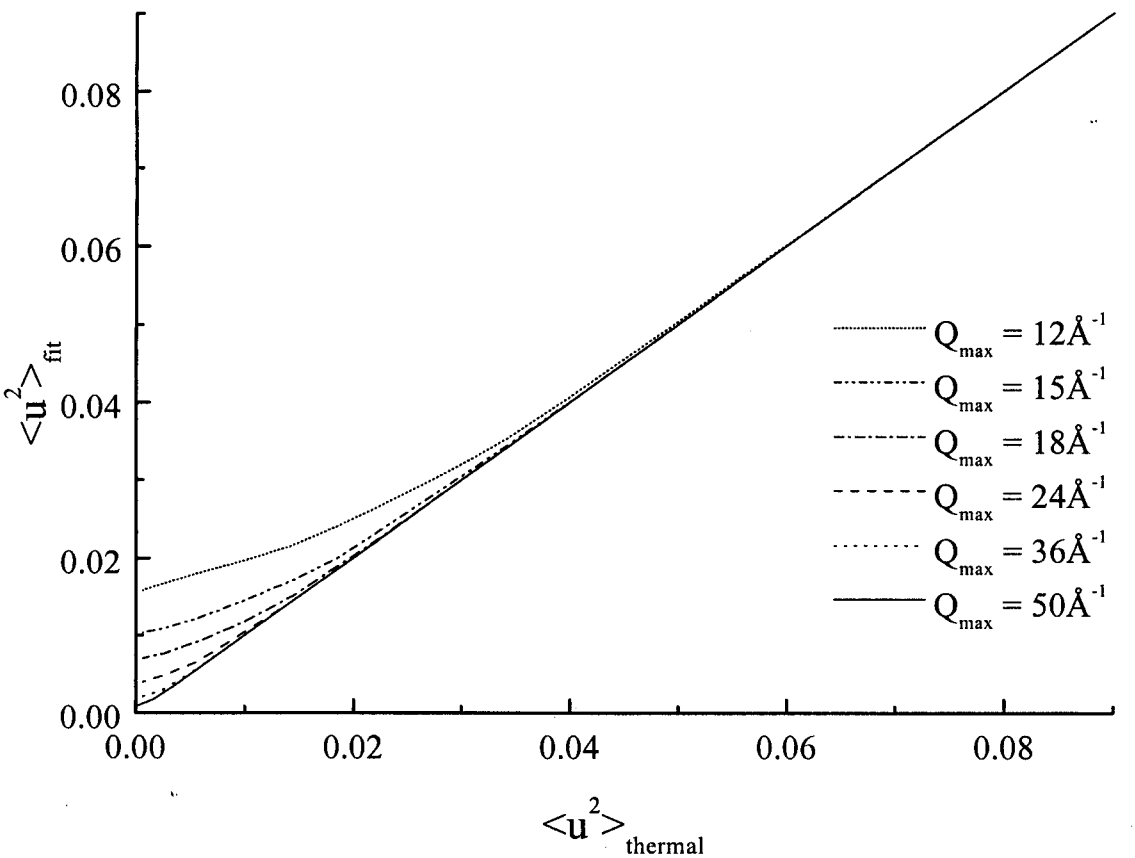

Figure 5.4 The change in $\langle u^2 \rangle_{fit}$ *of the Gaussian peak fit to* $T_{step}(r)$ *with respect to* $\langle u^2 \rangle_{thermal}$.

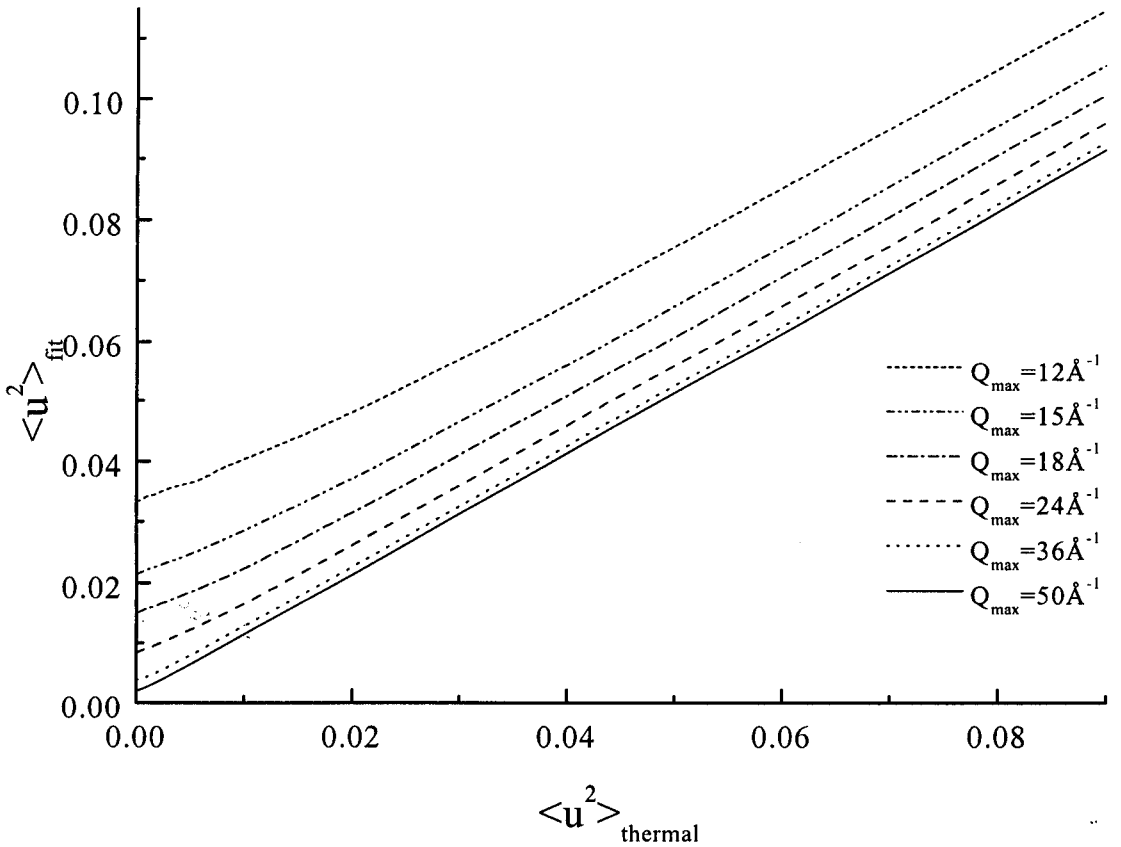

Figure 5.5 The change in $\langle u^2 \rangle_{fit}$ *of the Gaussian peak fit to* $T_{Lorch}(r)$ *with respect to* $\langle u^2 \rangle_{thermal}$.

The deviation from the linear relationship in equation 5.6 is due to the contribution of P(r) to the width of T(r). At small $\langle u^2 \rangle^{1/2}_{thermal}$ and at low Q_{max}, the non-Gaussian function P(r) makes a proportionately greater contribution to the full width of T(r), and hence to the departure from the summation by quadrature as described by equation 5.6.

The width of the Gaussian fit to data simulated using $P_{step}(r)$ and a high Q_{max} is dominated by $\langle u^2 \rangle^{1/2}_{thermal}$. The relationship between $\langle u^2 \rangle_{thermal}$ and $\langle u^2 \rangle_{fit}$ is linear, hence the Gaussian peak fit width directly reflects the width of the broadening Gaussian. This is not true for data simulated using $P_{Lorch}(r)$ until high Q_{max} (50Å^{-1}) This is due to the greater contribution of $P_{Lorch}(r)$ to the width of $T_{Lorch}(r)$.

These results are summarised, in figure 5.6, by combining data for all simulated values of $\langle u^2 \rangle^{1/2}_{thermal}$ and Q_{max}. It is possible to use this data to obtain $\langle u^2 \rangle^{1/2}_{thermal}$ from $\langle u^2 \rangle^{1/2}_{fit}$ and remove the broadening effect of P(r). However, this approach assumes that all the broadening of T(r) is Gaussian (like that due to thermal motion).

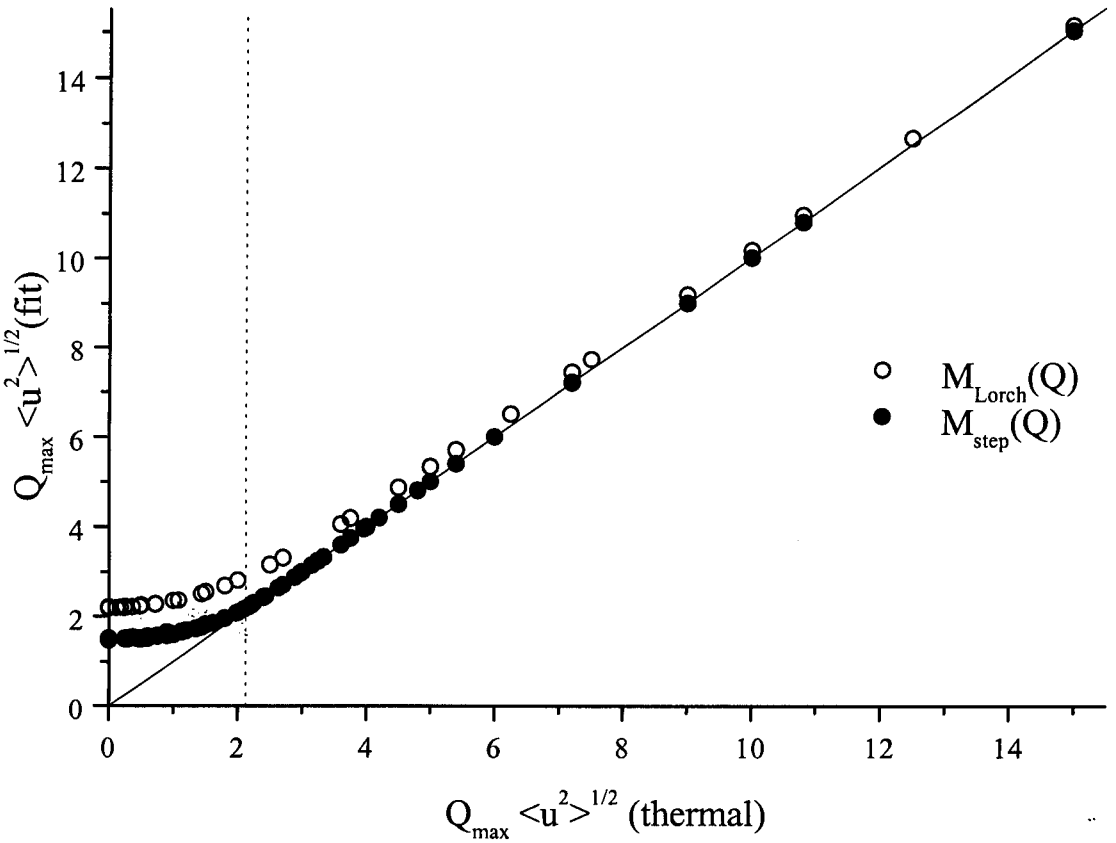

Figure 5.6 The change in Q_{max} $\langle u^2 \rangle_{fit}^{1/2}$ with Q_{max} $\langle u^2 \rangle_{thermal}^{1/2}$. The product of Q_{max} and $\langle u^2 \rangle_{thermal}^{1/2}$ reported by Grimley et al. [3] for the Si-O peak in v-SiO_2 is shown as a dotted vertical line.

The Si-O peak width in v-SiO_2, measured with a $Q_{max} = 45.2Å^{-1}$ and fitted with the correct function, is reported to be 0.047Å [3]. This simulation study suggests that a Gaussian fit to the same data broadened by a Lorch modification function would produce a broader fit width, as indicated in figure 5.6. This is due to the contribution of $P_{Lorch}(r)$ to the width of the peak in T(r). It is evident from this simulation study that $P_{lorch}(r)$ significantly changes the shape of the peaks in T(r) and that fitting with a Gaussian introduces a larger error as Q_{max} decreases.

5.2.2b THE AREA OF THE GAUSSIAN PEAK FIT

A co-ordination number can be obtained from the area under a peak in T(r), as described by equation 2.19. However, a Gaussian fit to T(r) does not include the contribution to the area from the termination ripples. Most significantly, it does not include the first trough either side of the central peak. This is the largest of the termination ripples and as a result of this, the Gaussian fit area is larger than the area

defined in the simulation of T(r). The error in area is presented as the % error in area against Q_{max} $\langle u^2 \rangle^{1/2}_{thermal}$ in figure 5.7. These data can be used to correct an experimental Gaussian fit area, assuming that the $\langle u^2 \rangle^{1/2}_{thermal}$ obtained from the fit width, using figure 5.6, is accurate.

The error in area is larger for Gaussian fits to $T_{step}(r)$ than $T_{Lorch}(r)$. This is because the termination ripples are larger in $T_{step}(r)$ than in $T_{Lorch}(r)$.

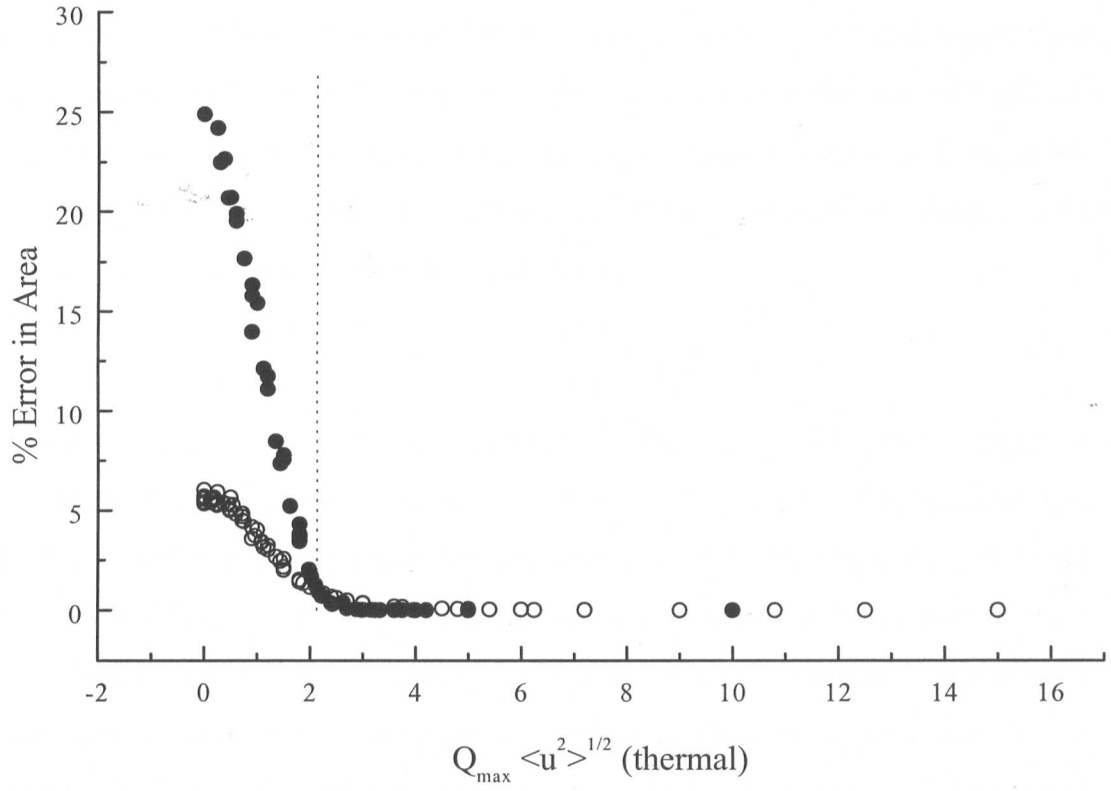

Figure 5.7 % error in area obtained from a Gaussian fit to T(r).

The error in the peak fit area, introduced by fitting with a Gaussian function, becomes less important for data measured up to high Q. This is because the non-Gaussian P(r) contributes a smaller width to the peak shape for T(r) as Q_{max} increases.

A Gaussian fit to the Si-O correlation reported for ν-SiO_2 by Grimley et al. [3] would report a larger peak fit area than that reported by fitting with the correct function. This is indicated by a dotted vertical line in figure 5.7. The effect is small in this instance because the data were measured to high Q_{max}. The % error in area becomes more significant for data measured to a lower Q_{max}. This, however, contradicts the finding that n_{SiO} calculated from neutron diffraction data is usually

less than four [4]. This suggests that fitting peaks in T(r) with a Gaussian function is not the dominant source of uncertainty in obtaining co-ordination numbers from neutron diffraction data.

5.3 Q-SPACE RESOLUTION

The accuracy to which Q can be measured in a diffraction experiment is restricted by a combination of the moderator size, the sample size and the acceptance angle of the detector. The Q-space resolution of the time of flight technique is also dependent upon uncertainty in the flight path, ΔL, and the uncertainty in the time of flight, Δt. The different sources of uncertainty may be highly dependent upon each other, but for a simple discussion of Q-space resolution the combination of effects can be expressed in terms of independent parameters as;

$$\frac{\Delta Q}{Q} = \frac{\Delta d}{d} = \left[\left(\cot\theta \Delta\theta \right)^2 + \left(\frac{\Delta L}{L} \right)^2 + \left(\frac{\Delta t}{t} \right)^2 \right]^{1/2} \qquad (5.7)$$

The expression for the angular uncertainty is obtained by differentiating equation 2.3, where the semi-angle θ is expressed in radians. The uncertainty in the flight path is due to the finite sizes of the moderator, sample and detector whilst the uncertainty in the time of flight is due to the time that the neutron spends in the moderator. Each contribution can be approximated by a Gaussian. The relative importance of each contribution changes with scattering angle. At low and medium scattering angles the angular contribution tends to dominate whilst at high scattering angles the time of flight uncertainty is more significant.

The Q-space resolution for each detector bank on LAD is shown in figure 5.8. The Q-range shown for each detector bank is typical of that used in this experimental study, detailed in chapters 6, 7 and 8. The $\Delta Q/Q$ resolution of each detector bank is taken from the ISIS User Guide [5].

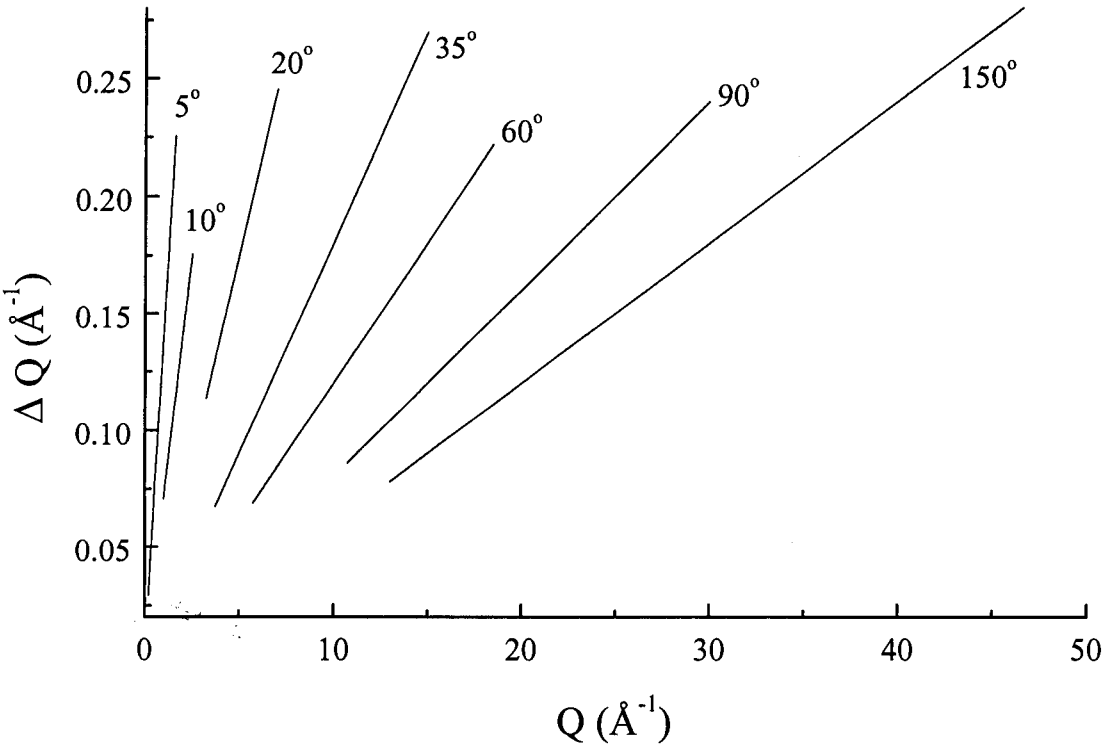

Figure 5.8 The Q-space resolution of each detector bank on LAD.

The data from the detector banks are usually merged to improve the statistical accuracy and increase the Q-range, so the Q-resolution of LAD follows a saw-tooth function across the diffraction pattern. This can be approximated to a combination of two models of Q-space resolution;

5.3a ΔQ=constant;

The combination of the Q-space resolution for several detectors can be considered as broadening the diffraction data with a Gaussian function of constant width.

5.3b $\Delta Q/Q$= constant;

The Q-space resolution for a single detector can be considered as broadening the diffraction pattern with a Gaussian function, the width of which is proportional to Q. This is most significant for the backward scattering angle (2θ = 150°) on LAD. The scattering measured at high Q is only measured by the 150° detectors and greatly contributes to the first few peaks in the real space correlation function.

Grimley et al. consider the Q-space Gaussian broadening of i(Q) to be equivalent to a damping of the real space correlation function by a Gaussian function centred at r=0 [3]. This qualitatively reduces the magnitude and hence the co-ordination numbers obtained from the peaks in D(r). However, this approach applies the convolution theorem, which requires the integrand of the Fourier transform to be

i(Q). This is not the case. The integrand of the Fourier tansform is Qi(Q)M(Q). This greatly complicates an analytical approach to the problem and hence this simulation study uses numerical methods.

5.3.1 Q-SPACE SIMULATION DETAILS

The distinct scattering for an ideal $SiO_{4/2}$ tetrahedron (r_{SiO}=1.61Å) was calculated using the 'g_f:debeqn_l' routine. This numerically calculated the distinct scattering for a single $SiO_{4/2}$ tetrahedron according to the Debye equation, equation 5.8;

$$i(Q) = \exp\left(\frac{-\langle u^2\rangle Q^2}{2}\right)\sum_{j=1}^{N}\sum_{k=1}^{N}\bar{b}_j\,\bar{b}_k\,\frac{\sin(Qr_{jk})}{Qr_{jk}} \qquad (5.8)$$

where the summations j and k are over the N atoms in the model (excluding j=k), r_{jk} is the magnitude of the vector $\mathbf{r}_{jk}$ from atom j to atom k and $\bar{b}_j$ is the coherent neutron scattering length for atom j. The values for $\bar{b}_{Si}$ and $\bar{b}_O$ are given in table 2.1.

The distinct scattering was then damped for the effect of the thermal motion of the atoms by applying a Debye-Waller factor, as defined by equation 5.9;

$$\text{D.W. factor} = \exp\left(\frac{-\langle u^2\rangle Q^2}{2}\right) \qquad (5.9)$$

For simplicity, $\langle u^2\rangle^{1/2}$ was defined as 0.05Å for all the atoms in the simulation. This value was chosen with reference to that reported for $\langle u^2\rangle^{1/2}$ in ν-SiO_2 [3]. The Debye-Waller factor was calculated using the 'g_f:model:dw' genie function routine. The Gaussian, centred about Q=0 was then multiplied by the distinct scattering (this is equivalent to convoluting P(r) with a Gaussian in real space).

The Q-space resolution broadening was then applied to the distinct scattering using the 'g_f:broad' routine. This routine replaced each point in the distinct scattering with, and then summed the intensity of, Gaussian functions of constant width (ΔQ=constant) or of a width which varied with Q ($\Delta Q/Q$=constant). Several values of Q-space broadening were applied within the ranges; $0 \le \Delta Q \le 0.3$ and $0 \le \Delta Q/Q \le 0.2$.

Real-space correlation functions were obtained by applying $M_{Lorch}(Q)$, truncating the data at 50Å^{-1} and numerically calculating the Fourier transform of the broadened scattering functions using the 'g_f:i2t' routine. The scattering from a single

tetrahedron can be considered to have a macroscopic sample density of zero, such that T(r) was equivalent to D(r). Each T(r) consisted of two peaks; one arising from the Si-O correlation, centred about 1.61Å, and the second due to the O-O intratetrahedral correlation, centred about 2.63Å. The parameters for both these peaks were obtained by fitting with the convolution of P(r) and a Gaussian, using the 'pfit' routine.

5.3.2 Q-SPACE SIMULATION RESULTS AND DISCUSSION

5.3.2a ΔQ = CONSTANT RESOLUTION

The shape of the peaks in the real space correlation functions changes with increasing ΔQ=constant Q-space broadening, as shown in figure 5.9. Some of the scattering intensity of each peak is transferred to a wing on the low r side. The magnitude of this increases with Q-space broadening.

These simulations make several assumptions (that the broadening effects are independent, that the saw-tooth function approximates to ΔQ=constant broadening and that each peak is still described by P(r) convoluted with a Gaussian). However, the intention of this simulation study is to examine the effects of Q-space broadening with regards to experimental data. If an experimental T(r) were found to have a non-zero gradient at low r it is considered reasonable to assume that this is due to an error in normalising the data with respect to the sample density. Some of the experimental data presented in chapters 6, 7 and 8 were corrected for non-zero behaviour at low r. These corrections were small and considered an acceptable stage of the data processing.

T(r) was corrected for non-zero behaviour at low r by by scaling D(r) to oscillate about $T^0(r)$. However, as noted previously, the sample density in these simulations is zero. D(r) was calculated by subtracting $T^0(r)$, calculated for ν-SiO_2. D(r) was then scaled to oscillate about $T^0(r)$ before adding $T^0(r)$ to calculate the corrected T(r). Each simulated T(r) was fitted before and after this correction for non-zero behaviour at low r.

The peak position, r_{SiO}, shifts to low r with increasing Q-space broadening. The shift to low r is small for an average broadening of the detectors on LAD, as shown

in figure 5.8. The correction for non-zero behaviour at low r does not have a significant effect on the peak fit position but the accuracy of the fit decreases at larger Q-space broadening, as shown in figure 5.10.

The peak fit width deviates from the applied Gaussian broadening with increasing Q-space broadening. However, it is curious to note that the peak fit width decreases on correcting T(r) for non-zero behaviour at low r.

The Si-O co-ordination number, n_{SiO}, was calculated from the peak fit area, according to equation 2.19. n_{SiO} decreases with increasing Q-space broadening, as area is transfered from the peak to low r. This effect accounts for a decrease in n_{SiO} from 4 to 3.95 for an average Q-space broadening on LAD. However, the correction for non-zero behaviour at low r increases n_{SiO}. At large ΔQ, the peak shape is distorted such that the areas obtained from the peak fit have a large associated uncertainty.

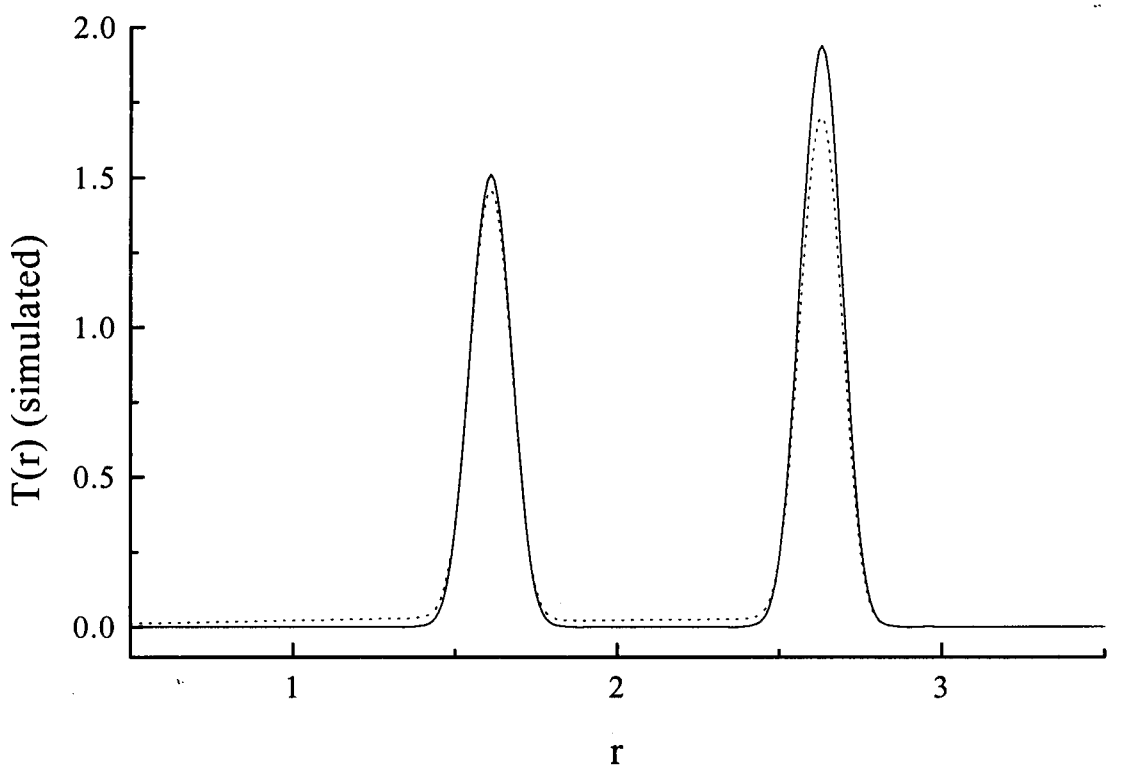

Figure 5.9 T(r) simulated using ΔQ = 0.2 (dotted line) and ΔQ = 0 (solid line).

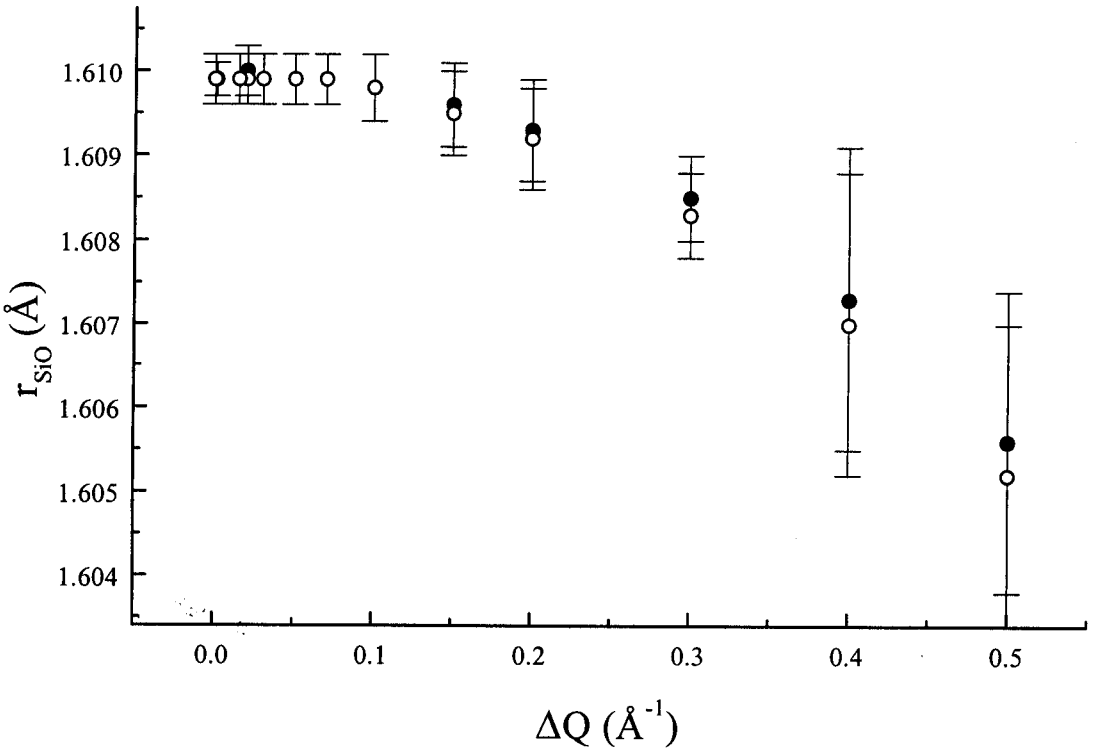

Figure 5.10 The change in r_{SiO} with ΔQ = constant broadening, before (solid circle) and after (hollow circle) low r correction. The error bars indicate the accuracy of the fit.

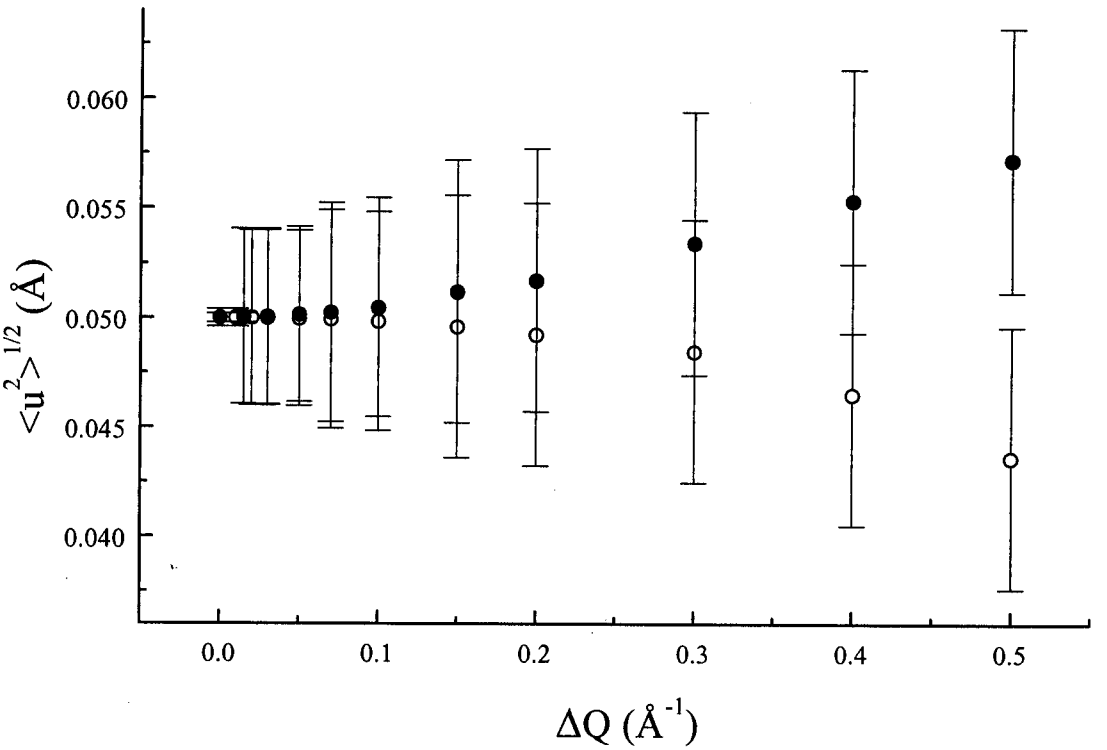

Figure 5.11 The change in the Si-O $\langle u^2 \rangle_{fit}^{1/2}$ with ΔQ = constant broadening, before (solid circle) and after (hollow circle) low r correction. The error bars indicate the accuracy of the fit.

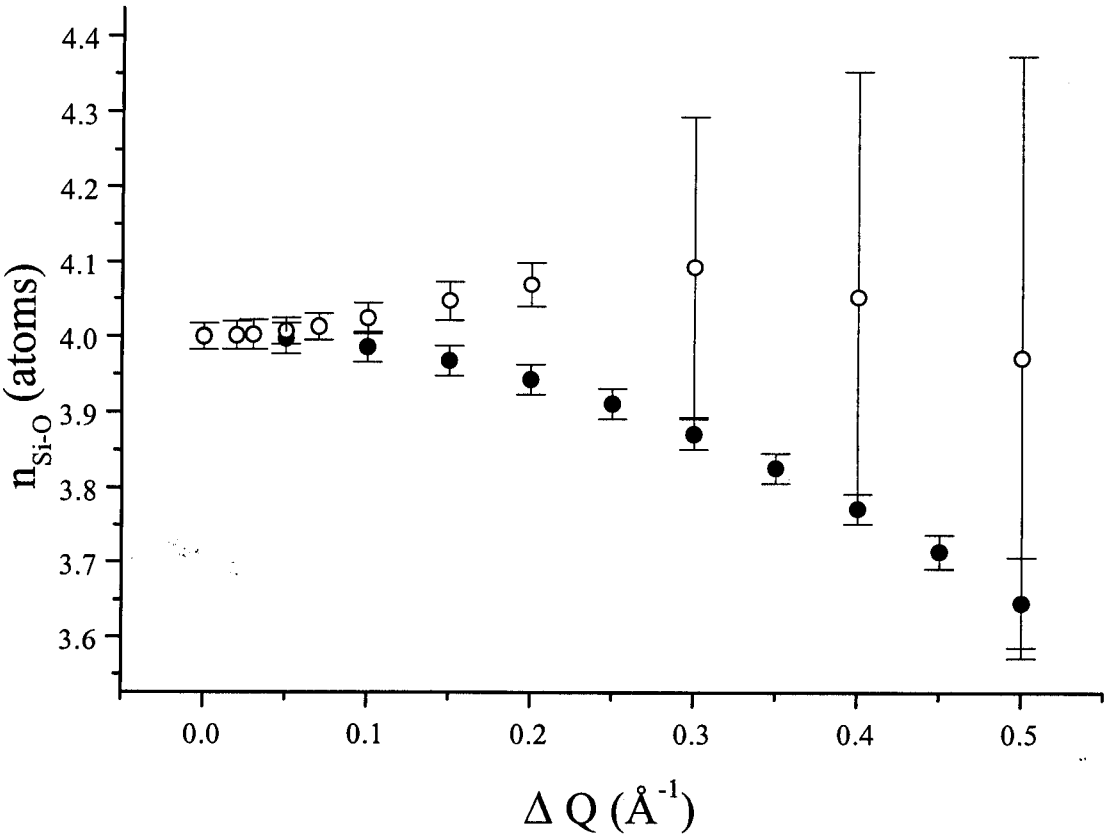

Figure 5.12 The change in n_{SiO} with ΔQ = constant broadening, before (solid circle) and after (hollow circle) low r correction. The error bars indicate the accuracy of the fit.

5.3.2b ΔQ/Q = CONSTANT RESOLUTION

The Q-space resolution of each detector bank is shown in figure 5.8. The values, taken from reference [6], are also summarised in table 5.1 In a typical diffraction experiment on LAD the data from the detector banks are combined. However, the high Q scattering is only measured by the backward angle detectors. The resolution of the 150° detectors is very high, but this simulation study calculates T(r) for ΔQ/Q up to 0.2 because the approximation that ΔQ=constant oversimplifies the effects of Q-space resolution.

	5°	10°	20°	35°	60°	90°	150°
ΔQ/Q	0.14	0.07	0.035	0.018	0.012	0.008	0.006

Table 5.1 The Q-space resolution of each detector bank on LAD, after [6] .

The shape of the peaks in T(r) changes with increasing ΔQ/Q broadening. This is shown for several values of ΔQ/Q broadening in figure 5.13. Both the Si-O and the O-O peaks were fitted with the 'pfit' routine and the structural parameters obtained for the Si-O peak are detailed below. The quality of the fit deteriorated with increasing broadening, as indicated by the size of the error bars in figure 5.14, 5.15 and 5.16.

The peak position, r_{SiO}, decreased with increasing ΔQ/Q broadening, as shown in figure 5.14. The shift to low r is dramatic for large broadening but no change in r_{SiO} was found by applying ΔQ/Q=0.006 (the value for the LAD 150° detectors).

The peak fit width increases with ΔQ/Q broadening, as shown in figure 5.15. The Si-O peak is slightly broader after broadening with a Gaussian of width ΔQ/Q=0.06, but this is no greater than the uncertainty in the fit.

The Si-O co-ordination number decreases with increasing ΔQ/Q broadening, as shown in figure 5.16. The decrease in n_{SiO} is dramatic for large values of ΔQ/Q but a value of 3.98 ± 0.05 is reported after broadening with a Gaussian of width ΔQ/Q=0.06.

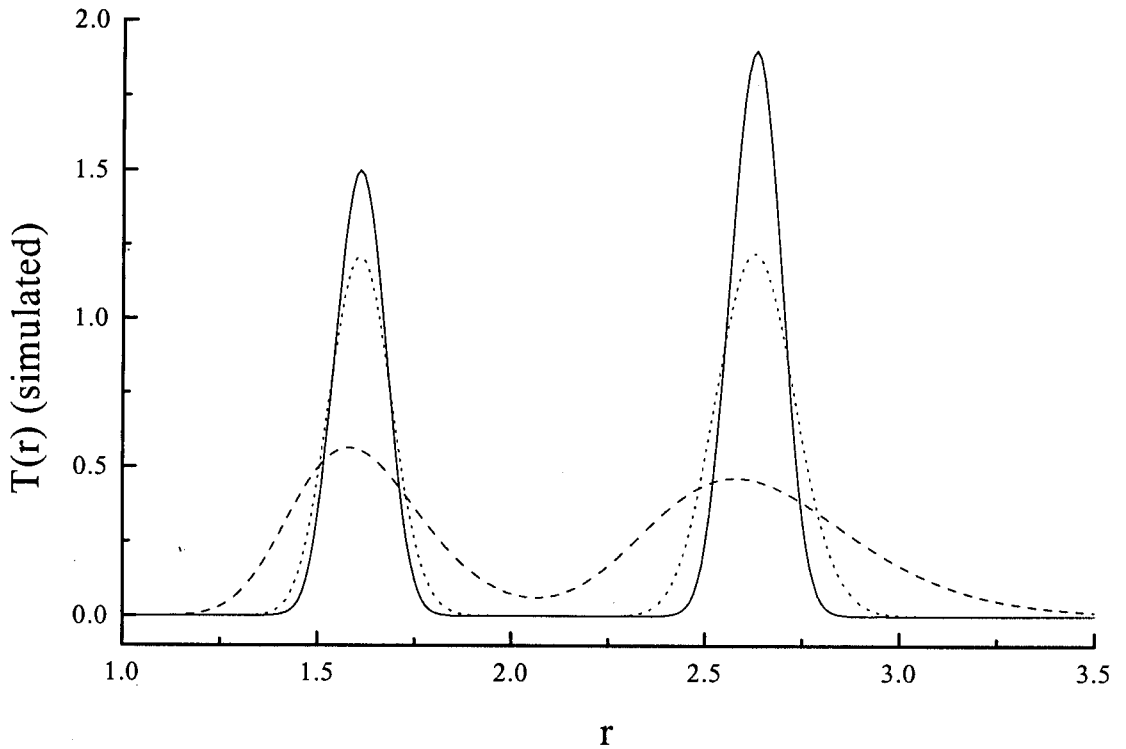

Figure 5.13 T(r) simulated using ΔQ/Q = 0.1 (dashed line), ΔQ/Q = 0.03 (dotted line) and ΔQ = 0 (solid line).

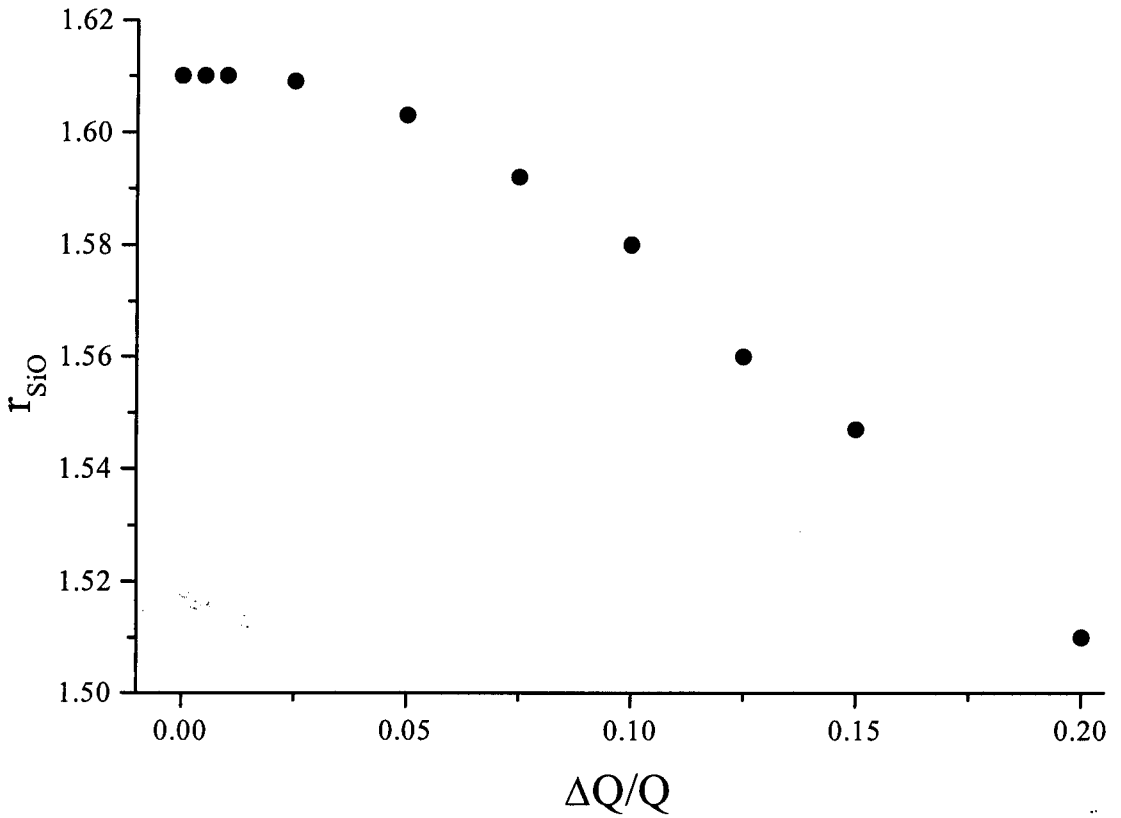

Figure 5.14 The change in r_{SiO} with ΔQ/Q = constant broadening.

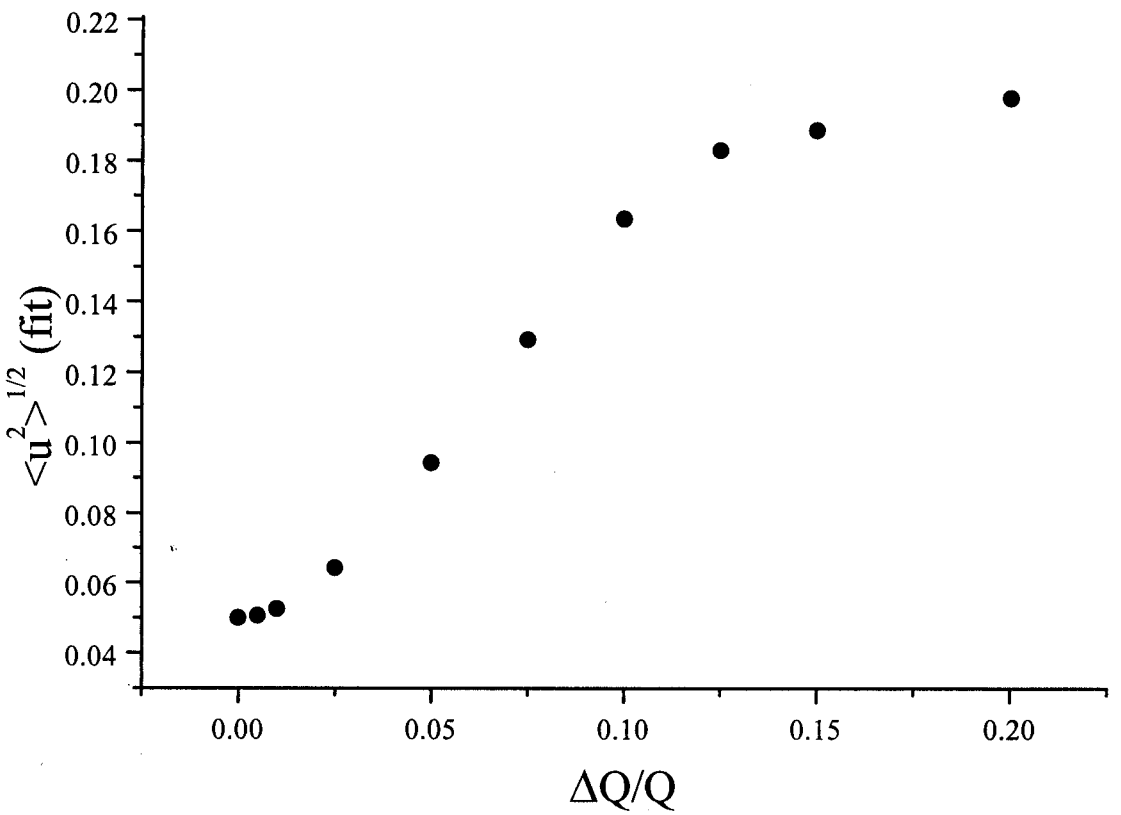

Figure 5.15 The change in the Si-O $\langle u^2 \rangle_{fit}^{1/2}$ with ΔQ/Q = constant broadening.

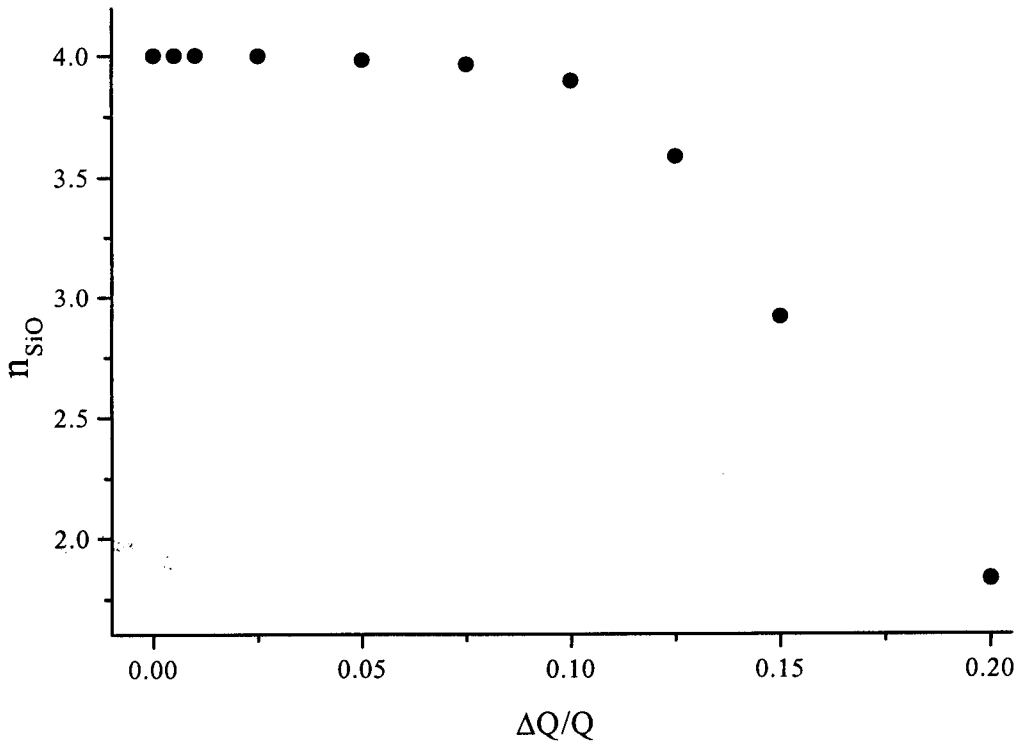

Figure 5.16 The change in n_{SiO} with $\Delta Q/Q$ = constant broadening

5.4 CONCLUSIONS AND FUTURE WORK

The effects of real space resolution and reciprocal space resolution on the structural parameters obtained from fits to the peaks in T(r) is small for values typical of the detectors on LAD. However, it should be noted that these simulations assume that the broadening parameters are independent, and that this is not wholly realistic.

The real space simulation study suggests that if a Gaussian function is used to fit the peaks in T(r) then a step modification function should be used to obtain co-ordination numbers from data measured using a low Q_{max} The choice of modification function proves to be less significant for data measured up to a high Q_{max}. Universal plots have been obtained by combining data from several values of $\langle u^2 \rangle^{1/2}_{thermal}$ and Q_{max}. It is possible to use these plots to relate the width of the Gaussian fit to the width of the thermal broadening and the % error in area. However, the inaccuracies introduced by fitting the peaks in T(r) with Gaussian

functions are not significant for data using a high Q_{max} and for realistic values of $\langle u^2 \rangle^{1/2}_{thermal}$.

The reciprocal space broadening of i(Q) simulations indicate that the correction of D(r) for errors in normalising the data should be prudent. Scaling D(r) to $T^0(r)$ does change the structural parameters obtained from fitting the data.

The results of this simulation study suggest that the source of experimental uncertainty, particularly the depression of n_{SiO} from 4 to 3.8, is not due to resolution broadening. Grimley et al. consider the extrapolation of the scattering function to Q = 0 to limit the accuracy to which the diffraction data is quantitative [3]. This may be improved by the larger detector area at low angles on GEM, which is currently replacing LAD. GEM also has an increased detector area at high scattering angles. It is expected that GEM will be capable of measuring i(Q) to an even higher Q_{max} than was possible on LAD.

The study of experimental effects on the structural parameters obtained by fitting neutron diffraction data could be continued by considering the effect of individual stages of the data processing. This could involve obtaining good statistics for a well characterised sample and varying the correction for absorption and multiple scattering, merging the detectors, extrapolating the data to Q = 0 and defining the sample density.

REFERENCES

[1] A.C.Hannon, D.I.Grimley, R.A.Hulme, A.C.Wright and R.N.Sinclair, *J.Non-Cryst.Solids* **177** (1994) 299

[2] J.F.James, 'A students guide to Fourier transforms' Cambridge University Press 1995

[3] D.I.Grimley, A.C.Wright and R.N.Sinclair, *J.Non-Cryst.Solids* **119** (1990) 49

[4] A.C.Wright, *J.Non-Cryst.Solids* **179** (1994) 84

[5] A.K.Soper, W.S.Howells and A.C.Hannon, 'Analysis of time-of-flight diffraction data from liquid and amorphous samples' 1989.

[6] B.Boland and S.Whapham, 'ISIS User Guide-Experimental Facilities', 1992.

CHAPTER 6

TIN SILICATE

6.1 INTODUCTION TO SYSTEM

Small quantities of tin can improve the chemical, mechanical, thermal and optical properties of glass. Stannous oxide is added in very small quantities to increase the solubility of gold, copper and selenium in ruby glasses [1], and to glass surfaces to increase the adhesion of metal films [2]. A tin compound is applied to the surface of glassware during manufacture to increase the mechanical strength of the glass [3] and stannosil glass, silica containing up to 0.8mol% SnO_2, has a low thermal expansion and absorbs short-wave ultra-violet radiation [4]. The most common example of tin in glass results from diffusion into the surface of float glass. About 85% of the flat sheet soda-lime-silica glass in the world is produced by the float glass process [5]. The diffusion of tin into the float glass surface depends upon the melt temperature and the contact time. The tin distribution is best described by two intersecting exponential decays from the contact surface, which can contain up to 22mol% tin [6]. The tin has been found to improve the weatherability of the glass in cyclic humidity tests, but causes 'blooming' (clouding) on subsequent heat treatment [7]. It also affects the homogeneity of other elements in the glass [8]. Interpreting the structural role of tin in such a multicomponent glass is complicated by the presence of Sn^0, Sn^{2+} and Sn^{4+} at different concentrations at different depths [9]. The problem can be simplified by restricting the number of components and studying, at first, alkali-free glasses in which the solubility of SnO_2 is very low.

Paul et al. studied binary $(SnO)_x(B_2O_3)_{1-x}$ glasses containing $12 \leq SnO \leq 58$ mol% and less than 0.1 mol% SnO_2 by infrared and ^{119}Sn Mössbauer spectroscopy [10]. The infrared spectra were interpreted as showing an increase in non-bridging oxygens with SnO content. The Mössbauer spectra were interpreted as showing a smooth decrease in the ionicity of the Sn-O bonds with increasing SnO content. A ^{119}Sn Mössbauer study of three $(SnO)_x(GeO_2)_{1-x}$ glasses also observed larger chemical shifts and quadrupolar splittings than in tetragonal SnO [11]. The Sn-O bonding was interpreted as being more ionic and distorted than in crystalline SnO.

Carbo Nover and Williamson [12] studied the crystallisation and decomposition of $(SnO)_x(SiO_2)_{1-x}$ glasses containing $28 \leq SnO \leq 59$ mol%. The glasses were prepared as first described by Keysselitz [13] and subsequently heated in tube furnaces open to the atmosphere. Glasses containing more than 42mol% SnO and particularly about the metasilicate composition partially crystallised to form a metastable crystalline phase which decomposed to metallic Sn, SnO_2 and SiO_2 above 700°C. The X-ray diffraction pattern of the 'stannous metasilicate' crystalline phase was not successfully indexed but likened to blue-black SnO.

Ishikawa and Akagi studied $(SnO)_x(SiO_2)_{1-x}$ glasses containing $32 \leq SnO \leq 57$ mol% using density, X-ray radial distribution and infrared absorption measurements [14]. The radial distribution functions were calculated from the combined scattered intensity of monochromatic Cu K_α and Mo K_α X-rays. The peak positions in the normalised X-ray intensity curves became more like the powder diffraction pattern of the metastable '$SnSiO_3$' with increasing tin content. The infrared spectra of the glasses also became more like that for the crystalline '$SnSiO_3$' with increasing tin content. The radial distribution functions all consisted of broad peaks due to the poor real-space resolution ($Q_{max} \sim 12 Å^{-1}$). The most prominent peak at 3.7Å and a small peak at 7Å both increased in magnitude with increasing SnO content and were interpreted as first and second nearest Sn-Sn correlations. The density was seen to increase with increasing tin content.

Karim and Holland reported an increase in density and thermal expansion coefficient with increasing tin content in $(SnO)_x(SiO_2)_{1-x}$ glasses containing $17 \leq SnO \leq 72$ mol% [15]. The thermal expansion coefficient increased, indicating a decrease in the strength of crosslinking and cation-oxygen bond strength, with tin content. They conclude that this requires Si-O-Sn linkages which become more covalent with increasing tin content. They also report discontinuities in the changes of both density and thermal expansion coefficient with tin content at 30~35 mol% SnO and interpret these to indicate a sudden change in the role of the tin from modifier to network intermediate. However, these discontinuities are not dramatic and could result from what appear to be conservative estimates of the experimental uncertainties.

^{119}Sn and ^{29}Si NMR and ^{119}Sn Mössbauer spectra have been reported for the same $(SnO)_x(SiO_2)_{1-x}$ glasses containing $17 \leq SnO \leq 72$ mol% [16]. Only one, static ^{119}Sn

NMR spectrum is presented. This consists of a broad lineshape (fwhm ~ 900ppm) which is typical of axially symmetric Sn^{2+} sites and a small symmetric peak due to less than 1 mol% Sn^{4+} The Sn^{2+} isotropic chemical shift is reported to increase with tin content but spectra for different glasses are not reported. This shift up-field is interpreted to indicate a decrease in the ionicity of the Sn^{2+} cation with tin content but may in fact indicate the formation of Sn-O-Sn linkages, as later discussed in terms of ^{207}Pb.

The ^{29}Si MAS NMR spectra shift downfield with increasing tin content but the shift range is much narrower than that for alkali silicate glasses. Gaussian fits to the spectra indicate that the number of different Q-species increases with tin content. At low tin content the Q-species distribution is best described by a binary model. This is typical of a depolymerised network in a low field strength alkali silicate glass [17]. At tin contents in excess of 30mol%, the Q-species distribution can better be described by a statistical model. At 70mol% SnO mainly isolated $(SiO_4)^{4-}$ groups exist within a Sn-O matrix. It is concluded that Sn^{2+} cations depolymerise the silicate network but not as much as alkali metal cations. In fact the 'non-bridging' oxygens may form Si-O-Sn linkages which are more ionic than Si-O-Si linkages but not part of a depolymerised silicate network.

An increase in the ionicity of the tin, with increasing tin content in these glasses, has been reported by Williams et al. [18]. Karim [16] reported a decrease in the ^{119}Sn Mössbauer isomer shift with increasing tin content having corrected for the temperature dependence of the shift. Williams then further corrected the shift for the decrease in molar volume and found the isomer shift to increase with increasing tin content. This increase in the isomer shift and a decrease in the quadrupolar splitting was interpreted as indicating a decrease in the covalency of the Sn-O bonds with increasing tin content.

The Sn^{2+} ^{119}Sn NMR lineshape is typical for nuclei in an axially symmetric environment and comparable to that for SnO [19]. The tin atoms in crystalline SnO each bond to four oxygen atoms which are repelled to one side by its lone pair of electrons. These $SnO_{4/4}$ square based pyramids share edges to form a layered structure, see figure 6.1.

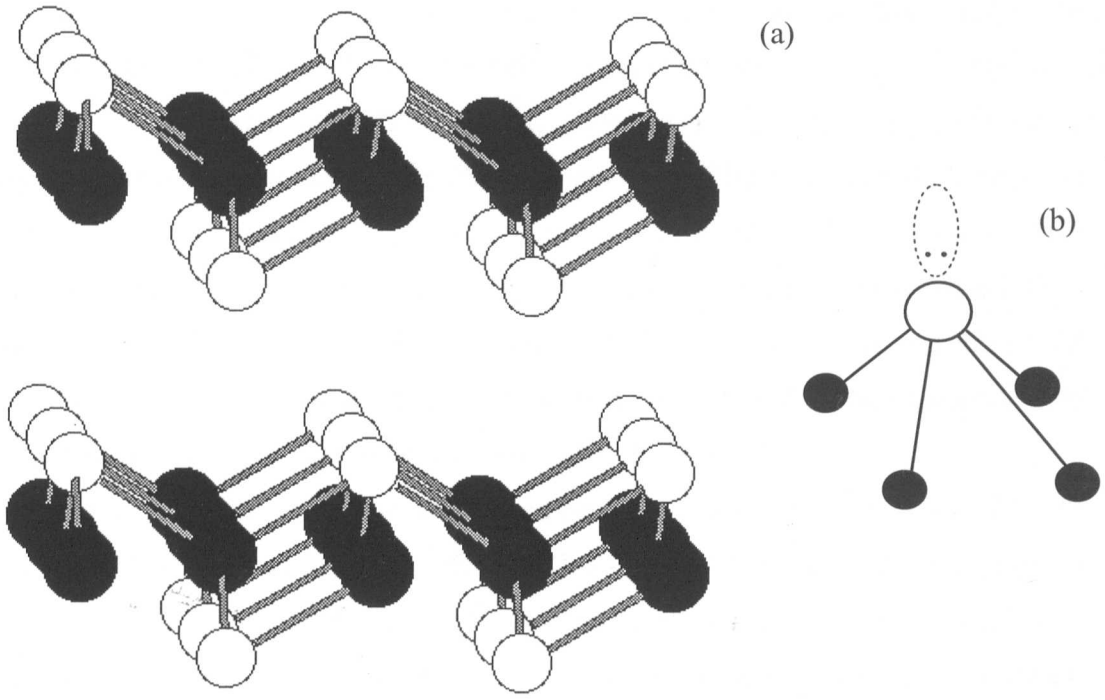

Figure 6.1 (a) The crystal structure of SnO and (b) The local order about the tin attom. Black circles represent oxygen atoms, white circles represent tin atoms and the two dots represent the inert pair of electrons.

Ion	Ionic radius (Å)	Coordination number with respect to oxygen	Dietzel's field strength ($Å^{-2}$) (valency/interatomic distance^2)
Si^{4+}	0.39	4	1.56
Sn^{4+}	0.69	4	1.13
Sn^{4+}	0.69	6	1.01
Sn^{2+}	0.93	4	0.46
Sn^{2+}	0.93	6	0.41
Pb^{2+}	1.18	6	0.31
Na^{+}	1.02	6	0.18

Table 6.1 The ionic radius, coordination number with respect to oxygen and field strength of silicon, tin, lead and sodium, after Karim [16].

The SnO crystal structure is similar to that for PbO. Lead, like tin, is a group IV element which exhibits the lone pair effect in its bivalent state, Pb^{2+} [20]. It is also possible to form the $(PbO)_x(SiO_2)_{1-x}$ glasses past the orthosilicate composition. The

literature contains several structural studies of lead silicate glasses which are worth considering with reference to the structure of tin silicate glasses.

The ^{29}Si NMR spectra for $(PbO)_x(SiO_2)_{1-x}$ glasses consists of a single peak which shifts downfield with increasing PbO content [21]. The chemical shift range is greater than in $(SnO)_x(SiO_2)_{1-x}$ glasses but less than in alkali silicate glasses. This can be explained in terms of the glass structure according to the Dietzel field strength of each cation, see table 6.1. Network forming cations have a high field strength, network modifying cations a low field strength and network intermediate cations have a field strength between the two [4].

The co-ordination of the lead by oxygen has been studied by ^{207}Pb NMR [22], Pb L_{III} EXAFS [24], Raman spectroscopy [24] X-ray [25-26] and neutron diffraction [27]. Fayon et al. reported ^{207}Pb NMR spectra in $(PbO)_x(SiO_2)_{1-x}$ glasses [22] with respect to crystalline lead compounds [23]. The glass spectra consist of a single resonance with a large chemical shift anisotropy (CSA) (~1200ppm). This was reported to be typical of predominantly covalent lead compounds but it was not possible to distinguish between sites in which the Pb^{2+} sits at the apex of tetragonal or trigonal pyramids. The lineshapes suggest that more than one site and/or distorted pyramids are present at low lead contents. The resonance shifts upfield to a value previously reported for Pb-O-Pb linkages [23] and the number of sites and/or their distortion decreases with increasing lead content.

EXAFS and Raman spectra of $(PbO)_x(SiO_2)_{1-x}$ glasses were reported similar to that for PbO, which consists of edge sharing PbO_4 tetragonal pyramids [24]. The spectra did not change with sample composition.

Morikawa et al. reported an X-ray radial distribution function for amorphous $(PbO)_2(SiO_2)$ as showing PbO_4 zig-zag chains interconnected by PbO_6 and various silicate groups, [25].This interpretation has since been questioned by Imaoka et al. [26] who prefer a model consisting of corner sharing PbO_3 and silicate chains. Imaoka et al. report two inequivalent Pb-O correlations within the PbO_3 unit at 2.25 and 2.45Å.

Yamada et al. report static structure factors for $(PbO)_x(SiO_2)_{1-x}$ ($0<x<0.66$) by pulsed neutron diffraction [27]. These offer an improved real-space resolution over the X-ray studies, using a Q_{max} of $30Å^{-1}$, and are not dominated by Pb-Pb interactions because the Pb, Si and O neutron scattering lengths are more similar

than their X-ray form factors. The area of the Pb-O correlation at 2.3Å corresponds to a Pb-O co-ordination of three. But a coexistence of different Pb-O environments are reported by comparison with the pair distributions in $PbSiO_3$ and $Pb_3Si_2O_7$. The short range order in these crystals contain two PbO_4 and one PbO_3 and two PbO_3 and one PbO_6 species respectively.

It is possible to compare the Pb-O interatomic separation reported by Yamada et al. with values calculated considering the valence and co-ordination of the two ions. These calculations are based upon empirical values for characterised crystalline structures [28]. The bond valence calculations for Pb-O interatomic separations, based upon the Pb-O separation in c-PbO, are summarised in table 6.2. The Pb-O correlation reported at 2.3Å is slightly larger than that calculated for three co-ordinated lead. This could suggest that $(PbO)_x(SiO_2)_{1-x}$ glasses contain a mix of PbO_3 and PbO_4 pyramids. However these calculations are only a guide to the relationship between interatomic separation and co-ordination number.

	PbO_3	PbO_4	PbO_6
Pb-O (± 0.02) (Å)	2.26	2.37	2.52

Table 6.2 Pb-O bond lengths calculated with reference to crystalline PbO_2.

The structural studies of $(PbO)_x(SiO_2)_{1-x}$ glasses described above make use of the related lead silicate crystal structures. This is not possible in the structural study of $(SnO)_x(SiO_2)_{1-x}$ glasses as there are no known stable tin silicate crystal structures. The purpose of this study is to probe the $(SnO)_x(SiO_2)_{1-x}$ glass structure by neutron diffraction, ^{17}O MAS NMR and further study the metastable '$SnSiO_3$' crystal phase structure.

6.2 EXPERIMENTAL DETAILS

6.2.1 SAMPLE PREPARATION

The $(SnO)_x(SiO_2)_{1-x}$ glasses used in the neutron diffraction experiment were prepared in alumina crucibles by Karim [16]. Subsequent samples were prepared by the same method (first used by Keysselitz [13]) but using silica crucibles. Stannous oxalate, Wacomsil quartz and 0.1mol% Fe_2O_3 were first mixed for several hours then compressed into pellets and heated to temperature (see table 6.3) at 9°Cmin^{-1}. The stannous oxalate decomposed, see equation 6.1, creating a reducing atmosphere which subsequently restricted the decompostion and disproportionation of SnO, see equation 6.2. The silica crucibles were covered with an alumina crucible to maintain the reducing atmosphere.

$$SnC_2O_4 \rightarrow SnO + CO_2 + CO \qquad (6.1)$$

$$2SnO \rightarrow Sn + SnO_2 \qquad (6.2)$$

The glass formed between a crust of SnO_2 at the surface and metallic tin at the bottom of the crucible. This prevented pouring the glass. The crucible was removed from the furnace at temperature, the crucible shattered or was smashed on cooling, and the yellow/orange tin silicate glass was separated from the crucible, tin and SnO_2. A small amount (~1g) of each sample was used to check amorphicity by powder X-ray diffraction, see chapter 4.1.

The reagents to prepare 50g of nominal composition $(SnO)_3(SiO_2)_2$ glass were prepared and heated as described above. Solid fragments of this glass were subsequently heated at 570°C for 35 minutes and then slowly cooled at one end of the tube furnace, through which argon flowed at ~1cm^{3}min^{-1}. These conditions were chosen with reference to a previous study of the crystallisation of $(SnO)_x(SiO_2)_{1-x}$ glasses, where x = 0.4, 0.5 and 0.7, at different temperatures and in air [16]. Further fragments of this glass were heated for longer periods and XRD used to identify the extent of the crystallisation and/or decomposition.

20% ^{17}O enriched SiO_2 was prepared by Yildrem [29] by the method described by Geissberger [30] and $(SnO)_x$-$(SiO_2)_{1-x}$ glasses, in which x nominally = 0.35, 0.45 and 0.6, were prepared as described previously but in smaller silica crucibles. Solid fragments of the nominal $(SnO)_3(SiO_2)_2$ glass were subsequently heated at 570°C for 35 minutes, as previously described.

6.2.2 SAMPLE COMPOSITION

The composition of the glass samples used in the neutron diffraction experiment were determined by Karim [16]. The compositional analysis obtained the SnO content by wet chemistry, Al_2O_3 by quantitative NMR and SiO_2 by difference.

The composition of the nominal $(SnO)_3(SiO_2)_2$ glass used for subsequent heat treatment was estimated from previous work which found this nominal composition to yield an approximately $(SnO)(SiO_2)$ analysed composition.

The composition of each ^{17}O enriched glass was deduced by comparing its density with those previously reported by Karim [16] and Sears [6]. Sample volumes and related sample masses were measured using a micropycnometer and a digital balance, at RAL, as described in section 4.4. The volume was measured repeatedly until settling at a value within the uncertainty associated in measuring the sample cell pressure.

6.2.3 NEUTRON DIFFRACTION

TOF neutron diffraction measurements were made for four tin silicate glasses on the LAD at RAL. Solid fragments of each glass were loaded into 8mm diameter cylindrical, vanadium cans which were mounted onto a mechanical sample changer, as was an empty can and a vanadium rod. Data was collected for each sample for approximately 2000μAhrs in 200μAhr increments, on the vanadium rod for 2000μAhrs, the empty can for 1500μAhrs and the empty spectrometer for 500μAhrs. The data were corrected using the ATLAS suite software, as outlined in chapter 2. The theoretical transmission cross-sections were used to calculate the absorption and multiple scattering corrections as the downstream monitor detector was not working.

TOF neutron diffraction measurements were later made on LAD at RAL for the heat treated '$SnSiO_3$' sample. Data was also collected for an empty can, vanadium rod and empty spectrometer and corrected using the ATLAS suite of software, as described in chapter 2.

6.2.4 X-RAY DIFFRACTION

A powder X-ray diffraction pattern of the heat treated '$SnSiO_3$' sample was recorded using a θ-2θ scan, referenced to a silicon standard, on a Bruker AXS D5005 X-ray diffractometer, as described in section 4.1.

6.2.5 ^{29}Si MAS NMR

^{29}Si MAS NMR spectra were recorded on a CMX-300 spectrometer for TS7 and the heat treated '$SnSiO_3$' sample using a 1-pulse sequence with various delay times between 2μs (< $^{\pi}/_{2}$) pulses. Each spectrum was acquired for ~48hrs using a Bruker 7mm probe spinning at 3kHz. 50Hz line broadening was applied to each FID.

6.2.6 ^{119}Sn MAS NMR

^{119}Sn MAS NMR spectra were acquired for the heat treated '$SnSiO_3$' sample on a CMX-300 by Yildrem [29]. The sample was spun at several spinning speeds (~11 and 13kHz) to distinguish between the isotropic peaks and their associated spinning sidebands. Each spectrum was acquired for ~2hrs.

6.2.7 ^{17}O NMR

^{17}O MAS NMR spectra were acquired for each ^{17}O enriched $(SnO)_x(SiO_2)_{1-x}$ glass and the heat treated '$SnSiO_3$' sample on a CMX-600 by Yildrem [29]. A pulse delay of 2 seconds was used between 0.9μs (π/2) pulses in an Oldfield echo pulse sequence. The samples were spun at ~15kHz and each spectrum acquired for ~24hrs.

6.3 RESULTS AND DISCUSSION

6.3.1 SAMPLE COMPOSITION

The composition of the glasses used in the neutron diffraction experiment, see table 6.3, are those reported by Karim [16]. The Al_2O_3 content was determined by quantitative NMR, the tin content by wet chemistry and the silicon content by difference.

	Nominal SnO content (mol%)	Melt temperature (°C)	Analyzed composition SnO (chemical ±1.6%)	SiO_2 (by difference)	Al_2O_3 (NMR ± 0.16%)
TS1	20	1600	16.8	83.0	0.2
TS2	32	1350	28.2	71.2	0.6
TS7	60	1150	49.4	50.4	0.2
TS10	75	1200	64.0	27.4	1.1

Table 6.3 The nominal and analysed composition of the $(SnO)(SiO_2)_{1-x}$ glasses used in the neutron diffraction experiment, after Karim [16]

Quantitative ^{29}Si NMR was not performed because of the long acquisition times. Quantitative ^{119}Sn NMR was not performed because it was not possible to uniformly irradiate all the ^{119}Sn nuclei due to their large chemical shift anisotropy. It was not possible to prepare the samples for inductively coupled plasma spectroscopy (ICP) analysis and other analytical techniques (SEM-EDX and XRF) were not used due to the difficulty in obtaining standards which reflect the matrix effects of the glass, see sections 7.3.1 and 8.3.1. The experimental uncertainties, reported by Karim, appear conservative. Nevertheless they dominate the uncertainty in interpreting this experimental data, particularly the co-ordination numbers obtained from the neutron diffraction data.

The heat treatment of the nominal $(SnO)_3(SiO_2)_2$ glass, described in section 6.2.1, partially crystallised the glass, changing the colour from orange to brown. The θ-2θ X-ray diffraction patterns for samples heat treated for 35 minutes and 2 hours show that the crystalline phase decomposes with time, see figure 6.2. The peaks at 29.9° and 33.3° 2θ are typical of SnO. These are only present in the sample heated for two hours. The sample heat treated for 35 minutes was subsequently used in this study.

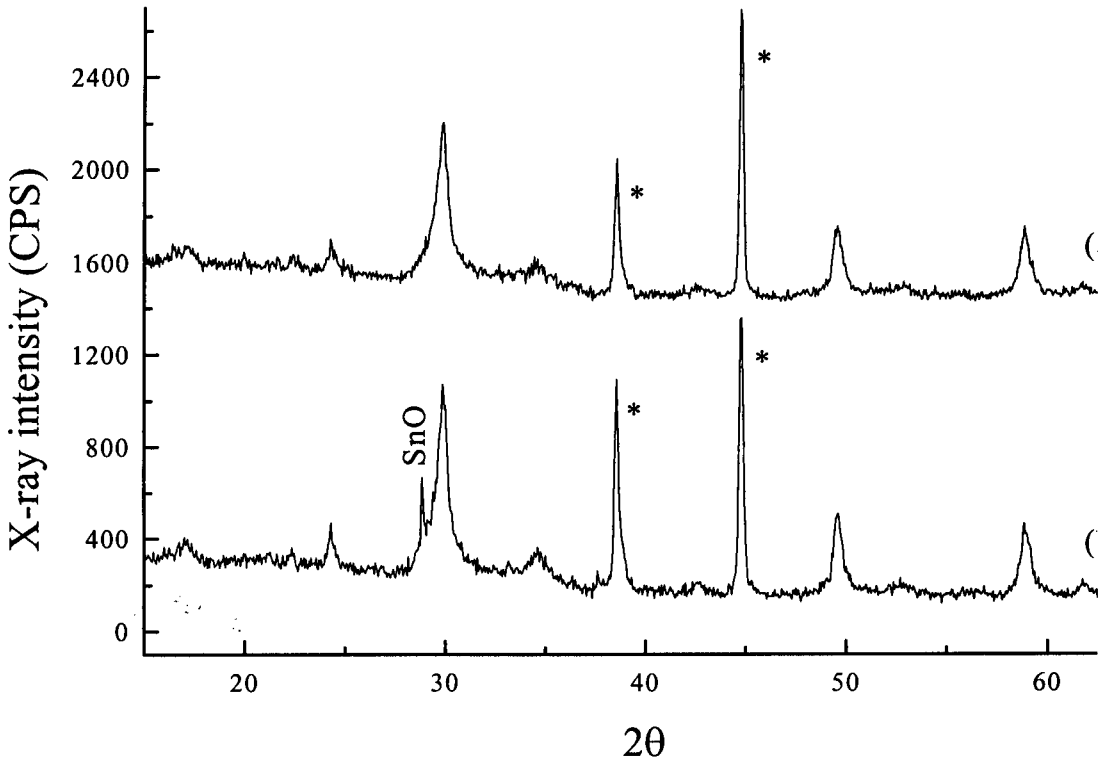

*Figure 6.2 Powder θ-2θ X-ray diffraction pattern for nominal $(SnO)_3(SiO_2)_2$ glasses heat treated treated at 570℃ for (a) 35minutes and (b) 2 hours. The * indicate Bragg peaks from the aluminium sample holder.*

The ^{17}O enriched samples were not chemically analysed because of the high cost of the isotropic enrichment. Instead their compositions were determined by comparing their density with that for similar samples of known composition. Figure 6.3 shows the glass density for subsequent measurements. The measured value settles to the reported value after (typically) 5 measurements. Figure 6.4 shows the measured density of the ^{17}O enriched samples and reported density of several tin silicate glasses.

Karim reported that the density increased with tin content in ten tin silicate glasses containing 16mol%<SnO<72mol% [16]. Sears also reports the density of five alumina-free tin silicate glasses containing 32mol%<SnO<70mol% [6]. The tin contents of the alumina-free glasses were analysed by XRF and the silica content by difference. On preparing all these glasses tin was lost by disproportionation, as eq.6.2. Therefore, the tin content in each glass is expected to be less than the nominal tin content in the mixture of reagents. However the composition of the ^{17}O enriched nominal $35SnO\text{-}65SiO_2$ glass was deduced from the density measurements as $39SnO\text{-}61SiO_2$. This suggests that either the wet chemistry [16] and XRF

measurements [6] over-estimate the tin content or that comparison between glass densities is not satisfactory. Nevertheless, the composition of the ^{17}O enriched samples are deduced in this manner and summarised in table 6.4.

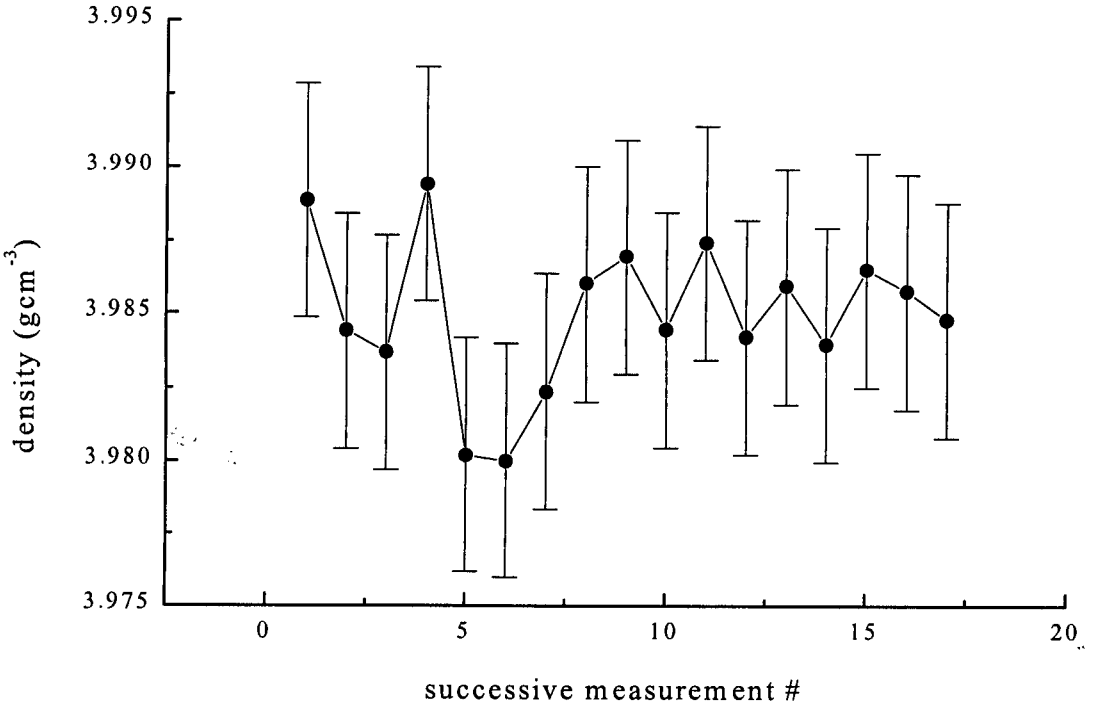

Figure 6.3 The measured density of the nominal $(SnO)_3(SiO_2)_2$ glass settled at 3.99±0.05gcm^{-3} after purging with helium and several measurements.

nominal composition	density (gcm^{-3})	SnO content (mol%)	SiO_2 content (mol%)
60SnO-40SiO_2	3.99 ± 0.05	54 ± 2	46 ± 4
45SnO-55SiO_2	3.60 ± 0.05	42 ± 2	58 ± 4
35SnO-65SiO_2	3.52 ± 0.09	39 ± 4	61 ± 6

Table 6.4 The measured density and inferred composition of ^{17}O enriched $(SnO)_x(SiO_2)_{1-x}$ glasses.

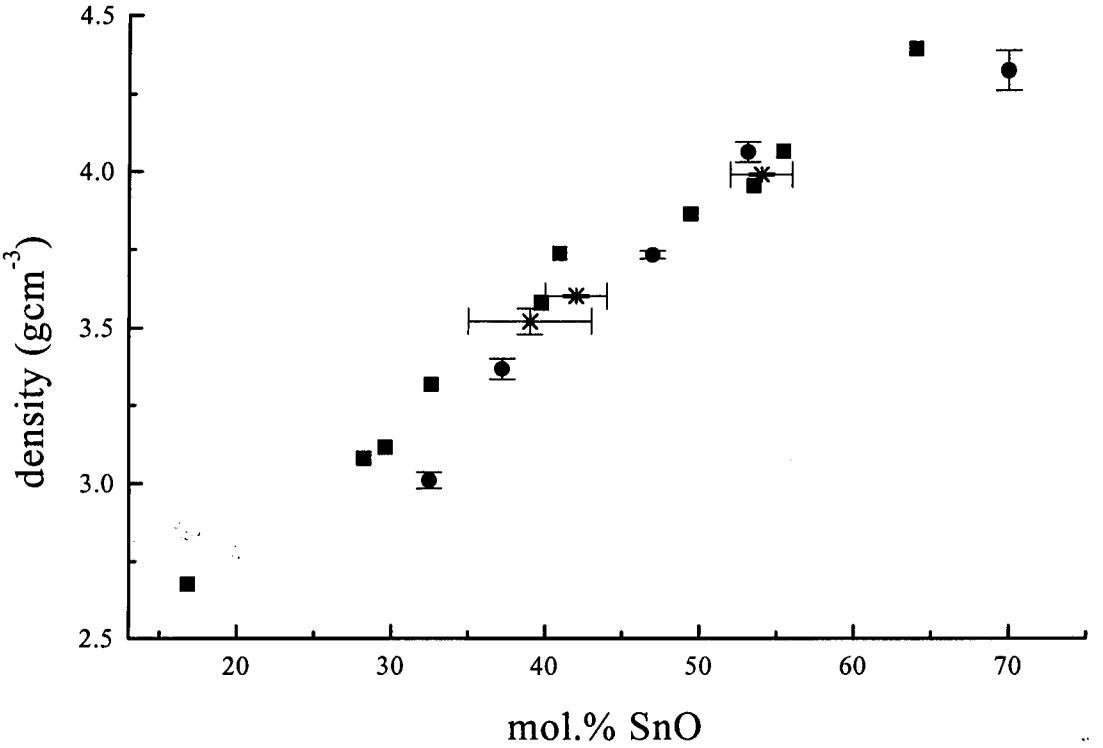

Figure 6.4 The bulk density of the ^{17}O enriched (asterix symbol) and the density of $(SnO)_x(SiO_2)_{1-x}$ glasses previously reported by Karim [16] (solid square symbols) and Sears [6] (solid circle symbols) vs. sample composition.

6.3.2 NEUTRON DIFFRACTION

The sample scattering function is discernible to 50Å^{-1} in i(Q) for the heat treated '$SnSiO_3$' sample and particularly in the low tin content glasses. However, the corresponding total correlation functions using a Q_{max} of 50Å^{-1} contain an additional feature at 1.78Å for all the glasses (but not the heat treated sample), see figure 6.6. This is not considered to be due to scattering from the sample. It is thought to be due to a problem with the Q-scale calibration of LAD at high Q [31], as previously reported for a shoulder at the base of the high r side of the first B-O peak in B_2O_3 [32]. This problem is only apparent in this data because i(Q) contains information up to high Q and is removed by truncating the data at 30Å^{-1}. No such peak was later observed in the '$SnSiO_3$' data, measured in March 1997. It is assumed that the detectors were recalibrated sometime between May 1994 and March 1997.

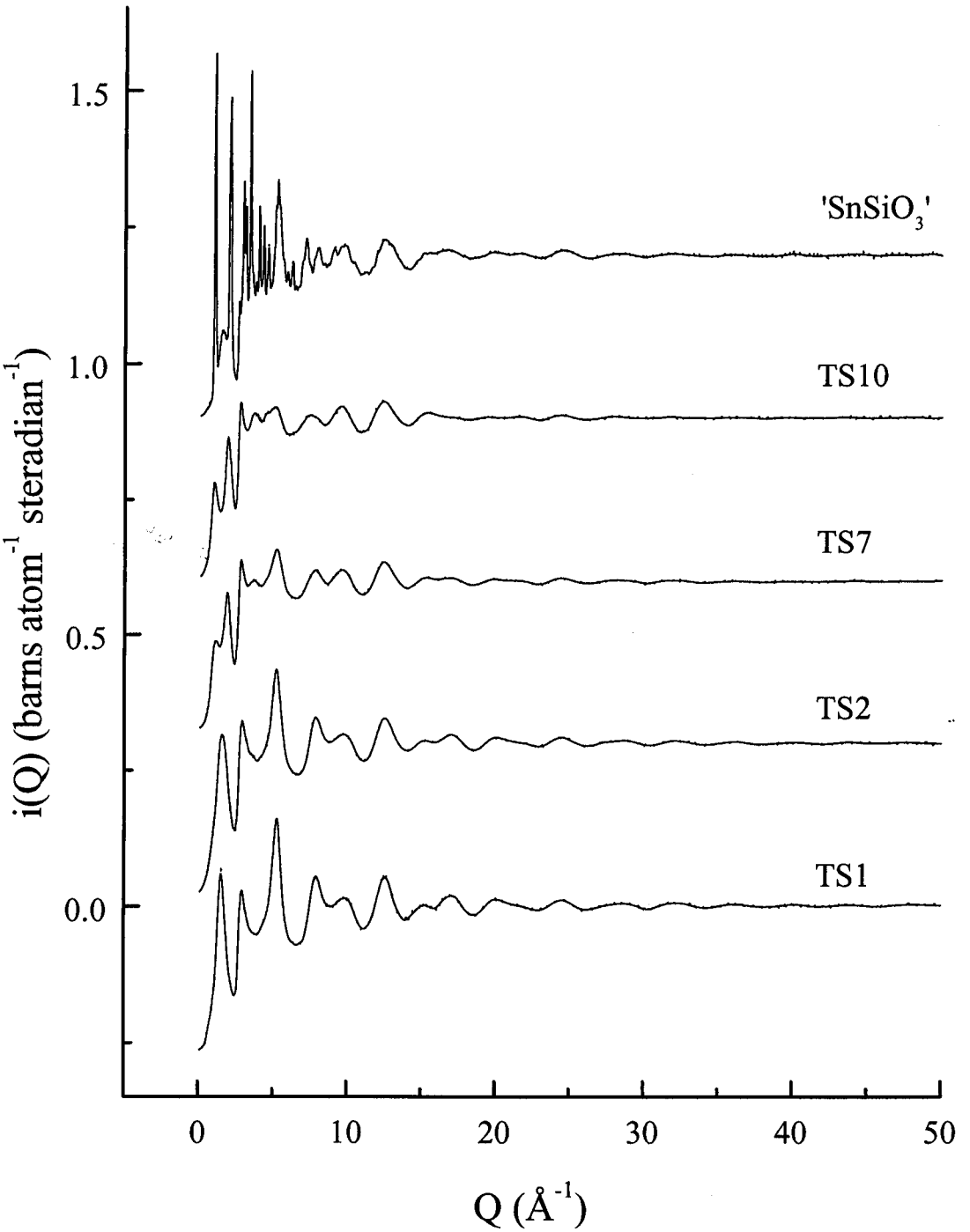

Figure 6.5 The distinct scattering, i(Q), for each tin silicate sample.

The distinct scattering functions show an increase in detail at low Q with increasing tin content. The two low tin content glasses (TS1 and TS2) are similar to that reported for silica at low Q [31], see table 6.5. The first sharp diffraction peak (FSDP) is at lower Q in the high tin content glasses (TS7 and TS10). This change in the position of the FSDP indicates a change in the extended range order of these glasses with tin content. The FSDP is thought to indicate periodicity in real space of

the order of $2\pi/Q$ [33]. The shift to low Q on adding tin indicates an increase in the period of the intermediate range order [34].

	ν-SiO_2	TS1	TS2	TS7	TS10	'$SnSiO_3$'
Q-FSDP ($Å^{-1}$) (± 0.05)	1.53	1.52	1.59	1.11	1.02	1.04
r-intermediate order (Å) (±0.15)	4.11	4.13	3.95	5.66	6.16	6.04

Table 6.5 The position of the FSDP in ν-SiO_2 [34] and the tin silicate i(Q)s.

The total correlation functions using a Q_{max} of $30Å^{-1}$ are shown in figure 6.7. The reduction in Q-resolution caused by truncating the data at 30 $Å^{-1}$ is not significant in this glass system as the peaks in T(r) are well separated. With reference to accepted bond lengths, the interatomic distances and the measured change in peak area with composition, the three peaks in the total correlation functions at ~1.6, ~2.1 and ~2.6Å can be assigned as Si-O, Sn-O and O-O correlations, respectively. The relative size of the peak at 2.1Å increases with tin content and the positions of the peaks at 1.6 and 2.6Å are typical Si-O and O-O distances in $SiO_{4/2}$ tetrahedra [34]. The O-O correlations within the SnO_n polyhedra are also thought to be coincident with those within SiO_4 at 2.6Å.

The data in the range $1.43 < r < 2.76$Å were fitted by three peaks, each of which was described by the convolution of a Gaussian and P(r) as described in chapter 2. The peak fits and residual between the fits and the data are shown in figure 6.7 and the fit parameters are summarised in table 6.6.

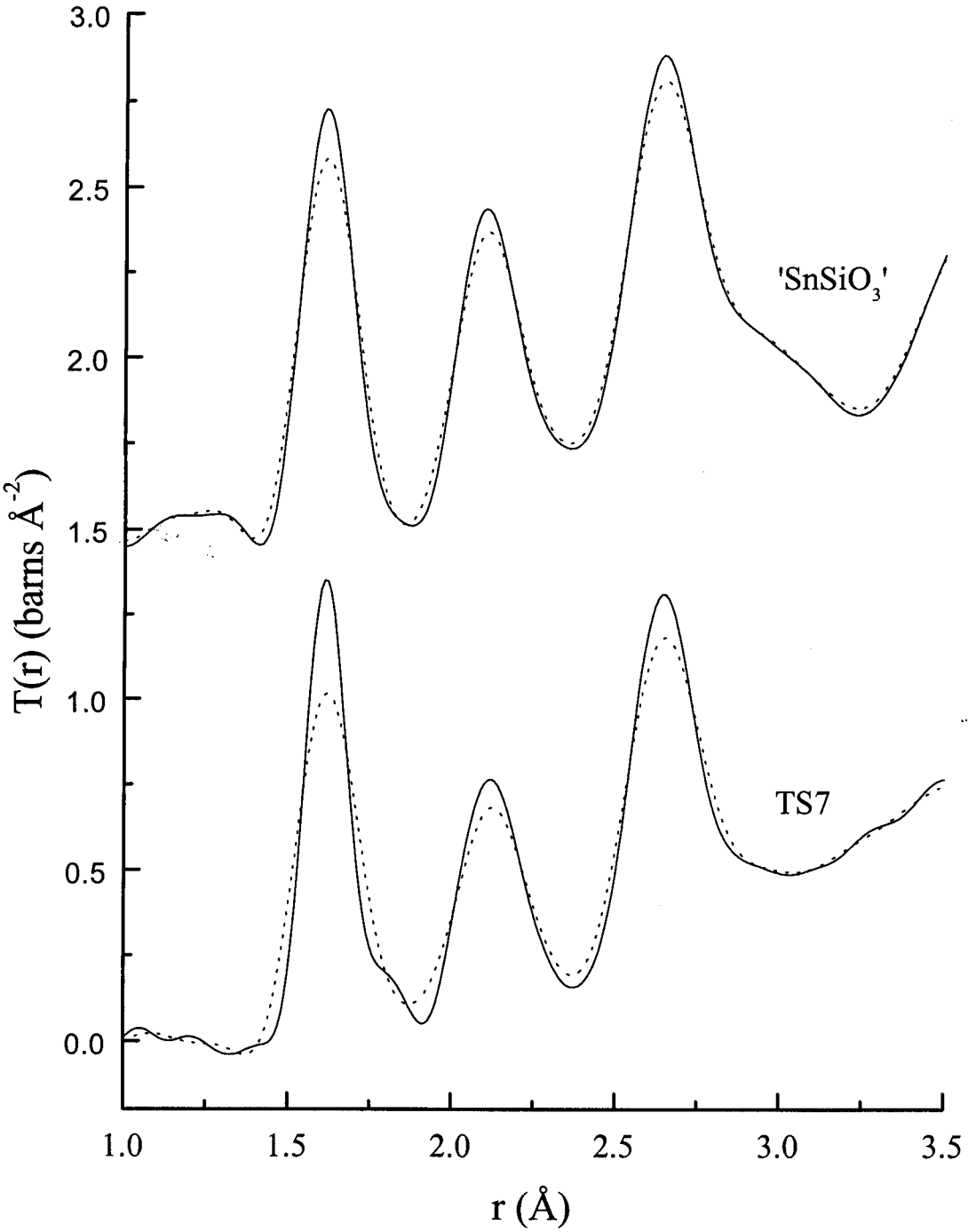

Figure 6.6 The total correlation function, T(r), between 1 and 3.5Å for TS7 using a Q_{max} of 50Å^{-1} (dotted line) and a Q_{max} of 30Å^{-1} (solid line).

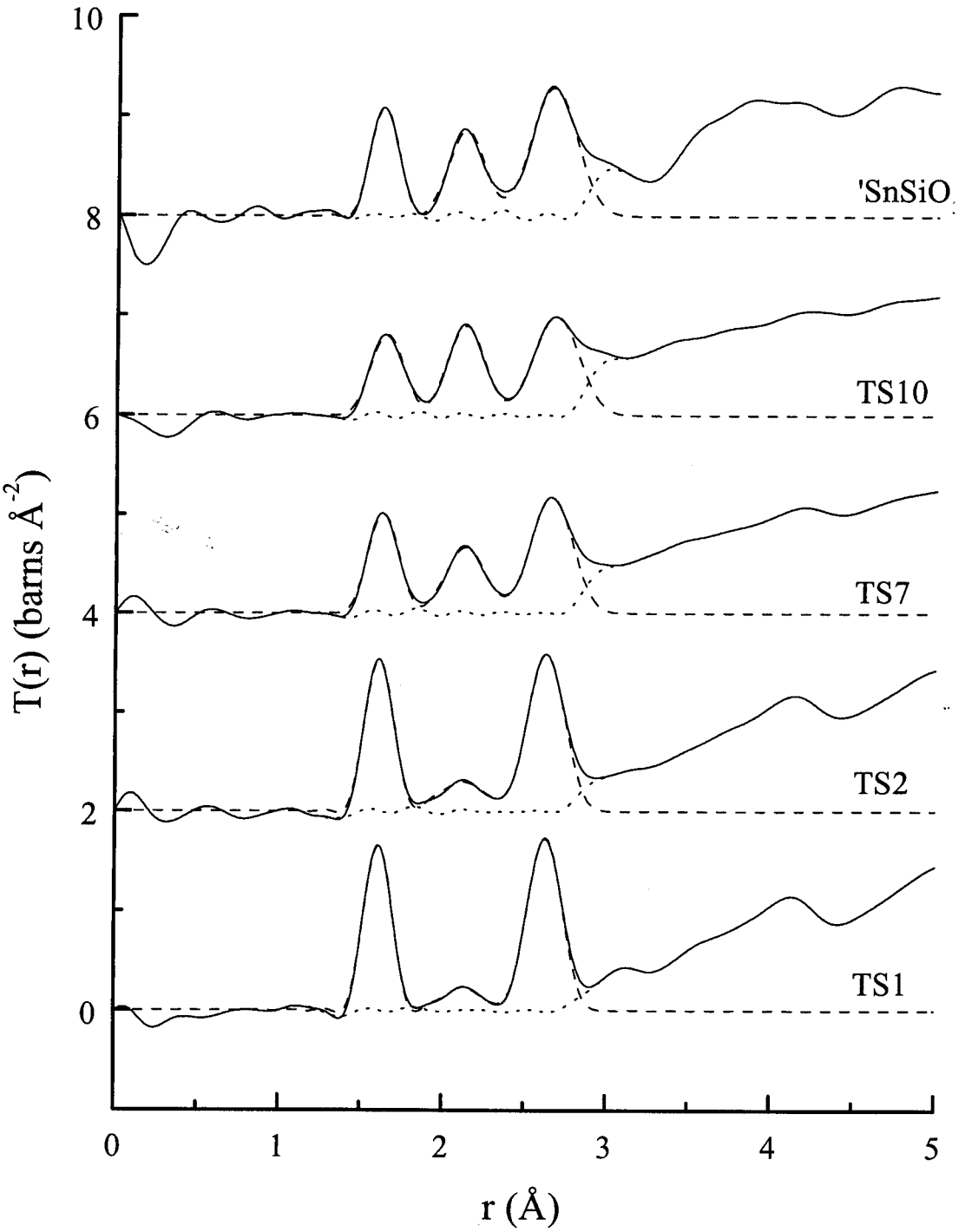

Figure 6.7 The total correlation function, T(r) (solid line), the peak fit (dashed line) and the residual (dotted line) for each tin silicate sample, using a Q_{max} of 30Å^{-1}.

	Peak	$r_{ll'}$ (Å)	$\langle u_{ll'}^2 \rangle^{1/2}$ (Å)	Area
TS1	Si-O	1.6088 (3)	0.0457 (5)	0.340 (1)
	Sn-O	2.128 (3)	0.098 (3)	0.067 (1)
	O-O	2.6284 (4)	0.0811 (6)	0.451 (2)
TS2	Si-O	1.6103 (4)	0.0496 (7)	0.321 (1)
	Sn-O	2.120 (3)	0.129 (4)	0.106 (2)
	O-O	2.6313 (6)	0.0902 (9)	0.441 (2)
TS7	Si-O	1.6257 (6)	0.063 (1)	0.231 (1)
	Sn-O	2.129 (1)	0.103 (2)	0.201 (2)
	O-O	2.655 (2)	0.109 (2)	0.374 (4)
TS10	Si-O	1.6433 (9)	0.075 (1)	0.200 (2)
	Sn-O	2.1255 (9)	0.091 (1)	0.249 (2)
	O-O	2.677 (2)	0.121 (2)	0.339 (5)
heat treated TS7	Si-O	1.6179 (3)	0.048(1)	0.225(1)
	Sn-O	2.1190 (3)	0.087(1)	0.230(1)
	O-O	2.653 (2)	0.121(1)	0.441(3)

Table 6.6 Fit parameters (uncertainty in the fit in parenthesis) for the total correlation functions T(r) for each tin silicate sample using data up to 30Å^{-1}.

The three peak fits shown in figure 6.7 and summarised in table 6.6 partially include but do not describe the scattering intensity on the high r side of the O-O correlation. The scattering intensity centred about 2.85Å increases with tin content, as shown in figure 6.8. This figure shows each T(r) and three difference correlation functions which were calculated by scaling the intensity of the Si-O correlation in each T(r) to that in TS1 and then subtracting TS1 from each scaled T(r). It is assumed that this removes the scattering due to the O-O correlation within the $SiO_{4/2}$ polyhedra. The O-O correlation in each difference plot is centred about 2.85 ± 0.02Å. This is thought to be due to the O-O correlation within the $SnO_{3/3}$ polyhedra.

It did not prove possible to obtain an accurate four peak fit, with reasonable peak widths, to even the highest tin content T(r). This is thought to be due the overlap of correlations to high r. Hence, it is not possible to obtain accurate O-O co-ordination numbers for the different types of polyhedra.

It is possible to calculate the O-Sn-O bond angle by considering an isosceles triangle with sides of length r_{SnO} , r_{SnO} and r_{OO}. The average O-Sn-O bond angle in these glasses calculated using r_{SnO} = 2.85Å and r_{OO} = 2.12Å is 84.2 ± 0.7°. This is larger than the O-Sn-O bond angles of 77.1°, 77.1° and 79° reported for $SnS_{3/3}$ [35]. This indicates that the $SnO_{3/3}$ trigonal pyramid is more squat and that the lone pair has a reduced p contribution to the sp^3 hybrid than in the $SnS_{3/3}$ trigonal pyramid.

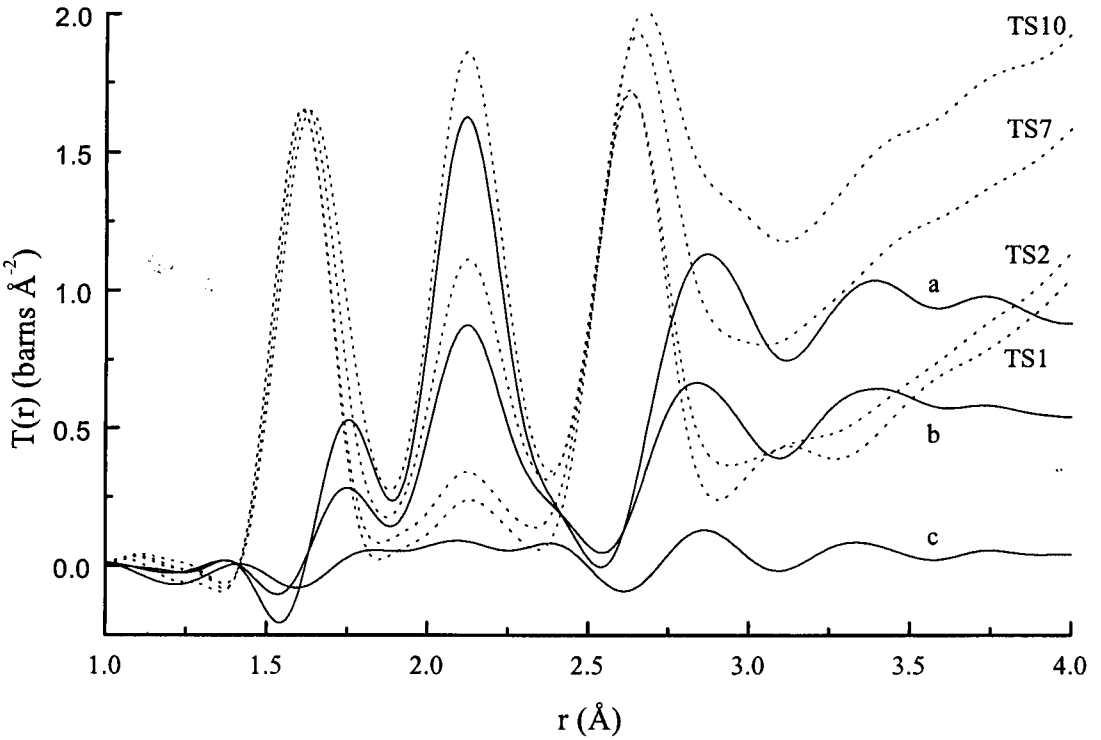

Figure 6.8 The total correlation function for each tin silicate glass (dotted lines) scaled to the Si-O peak in TS1 and the difference plots between (a) TS10-TS1, (b) TS7-TS1 and (c) TS2-TS1 (solid lines).

The distance ratios, r_{OO}/r_{SiO}, are consistent with that for a regular tetrahedron (1.633) at all compositions, see table 6.7. The SiO_4 tetrahedra are not distorted, within the uncertainty associated with each peak position, on increasing tin content.

	TS1	TS2	TS7	TS10	'$SnSiO_3$'
r_{SiO}	1.613 (5)	1.613 (5)	1.621 (5)	1.642 (5)	1.613 (5)
r_{SnO}	2.13 (1)	2.12 (1)	2.123 (5)	2.122 (5)	2.111 (5)
r_{OO}	2.63 (1)	2.63 (1)	2.65 (1)	2.67 (1)	2.64 (1)
r_{OO}/r_{SiO}	1.63 (1)	1.63 (1)	1.63 (1)	1.63 (1)	1.64 (1)

Table 6.7 Visual peak positions and distance ratio r_{OO}/r_{SiO} (errors in parenthesis).

Figure 6.9 shows the variation in position and width of the first three peaks in T(r) with tin content. The vertical bars correspond to the FWHMs of the fits summarised in table 6.6.

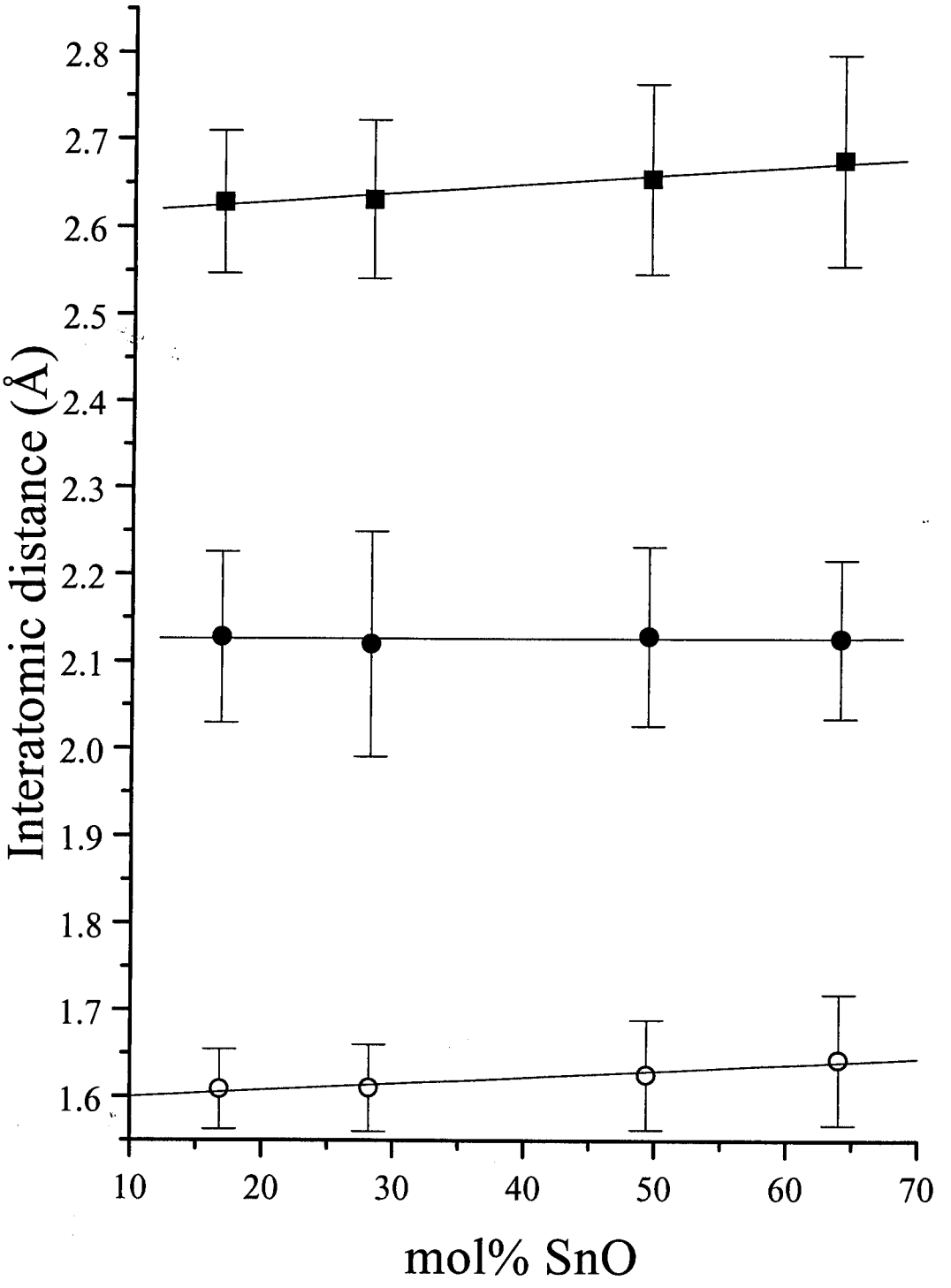

Figure 6.9 The positions and widths (indicated by the error bars) of the Si-O (hollow circles), Sn-O (solid circles) and O-O (solid squares) peaks in T(r) for each tin silicate glass.

The Si-O and O-O peaks both move to larger r and become broader as tin is added. The increase in Si-O and O-O bond lengths corresponds to a stretching of the SiO_4 tetrahedra due to the steric requirements of incorporating tin into the network. Although, it should be noted that the increase in the scattering intensity at 2.85Å does contribute to the increase in the increase in r_{OO}. The increase in Si-O and O-O peak widths is thought to be due to an increase in the static disorder arising from an increase in the distribution of Si-O bond lengths. This is comparable to the increase in the average Si-O and O-O bond lengths and peak widths with increasing alkali content in alkali silicate glasses [36].These changes are thought to be due to a decrease in the NBO bond length but an increase in the remaining BO bond lengths. In this respect the Sn^{2+} can be considered to act as a network modifier.

The Sn-O peak remains unchanged in both position and width. This result for the Sn-O distance contradicts an earlier X-ray diffraction study [14] with low real space resolution (Q_{max} ≈12Å^{-1}) which reported that the bond length decreases with increasing tin content.

The Si-O co-ordination numbers (n_{Si-O}) calculated as described in chapter 2, are close to 4 except that for TS10 which is larger than expected. The Si-O peak fit for TS10 is thought to include area from the Sn-O peak. This overlap is only apparent in the sample containing most tin, when the Sn-O peak is largest. The fit defines an Si-O bond length larger than the visual peak position and the calculated Sn-O co-ordination number (n_{SnO}) is smaller than in all the other samples. If an excess area is removed from the Si-O peak fit, such that n_{SiO} = 4, and transfered to the Sn-O peak fit area, then the larger Sn-O peak area relates to a n_{SnO} of 2.9. This is in good aggreement with the slight decrease in tin co-ordination with tin content, see table 6.8.

	TS1	TS2	TS7	TS10	'$SnSiO_3$'
N_{SiO} (atoms) (±0.3)	3.9	4.0	3.9	4.5	3.7
N_{SnO} (atoms) (±0.1)	3.3	3.2	3.0	2.7	3.4
N_{OO} (atoms) (±0.1)	5.4	5.4	4.9	4.7	5.8

Table 6.8 Co-ordination numbers N_{ij}, calculated from the peak postions in table 6.7 and the peak areas in table 6.6 (errors in parenthesis).

The gradual decrease in the calculated Sn-O co-oordination number (n_{SnO}) from 3.3 to 2.9 suggests that, whilst three co-ordinated tin predominates there may be

some four co-ordinated tin at low tin contents. However, the Sn-O peak remains symmetric with a FWHM of ~ 0.24Å and the peak position remains constant about 2.12Å at all compositions. This is comparable to that calculated for three co-ordinated Sn^{2+} by a bond valence formalism for metal oxides [28], see table 6.9.

$N_{II'}$ (atoms)	2	3	4	5	6
r_{SiO} (Å)	1.37	1.52	1.62	1.71	1.77
r_{SnO} (Å)	1.98	2.13	2.24	2.32	2.39

Table 6.9 Bond valence calculations for Si-O and Sn-O interatomic separations.

It is possible to consider the effects of adding SnO to a $SiO_{4/4}$ network in terms of changes in the oxygen co-ordination (n_{OO}) [37]. However, n_{OO} is not considered sufficiently accurate to warrant this. The O-O peak fit at 2.6Å is overlapped by correlations at higher r. The residual between the fit and the data shows a peak at ~3Å which increases with tin content. This is thought to be due to O-O correlations within the $SnO_{3/3}$ trigonal based pyramid, but it is not possible to extract any further information from this data above 2.7Å. The first Sn-Sn peak was reported at 3.7Å by Ishikawa [14] and the first Si-Si peak is expected about 3.1Å [34].

6.3.3 PROPOSED STRUCTURAL MODEL

It is possible to suggest several models of glass structure in which three co-ordinated tin can be incorporated into a tetrahedral silicate network. Two possible average structures are illustrated in figures 6.10 and 6.11. It is not possible to distinguish between the two, or the possible variation in connectivity within each of the models, with the structural information to date. The major difference between these two models is that, on increasing the tin content, the chain model considers an increasing chain length whilst the pair model considers more edge sharing pairs of $SnO_{3/3}$ units.

The tin chain model, figure 6.11, suggests that there are two ends to each chain of tin atoms. There is no evidence for this from the Sn-O peak position and width in T(r). However, if the two ends of each chain join to form a ring then there need not be end members to each chain. The increase in the period of intermediate range order, see table 6.5, can be interpreted to support an increase in ring size with tin content. Infact, the pair model, figure 6.10, can be considered to represent a two membered ring in low tin content glasses. However, as stated previously, it is not

possible to conclusively distinguish between these two models with the information to date.

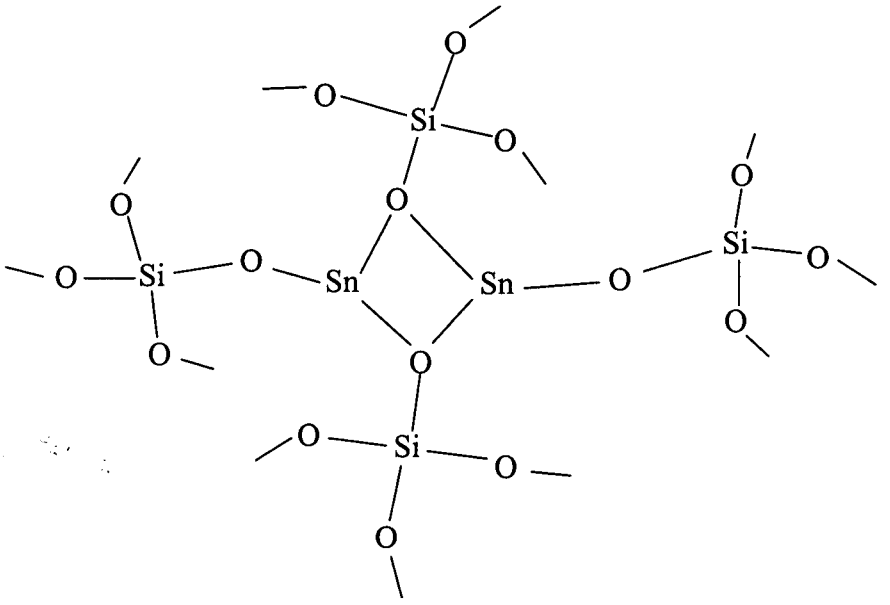

Figure 6.10 A model tin silicate glass structure which requires pairs of tin atoms.

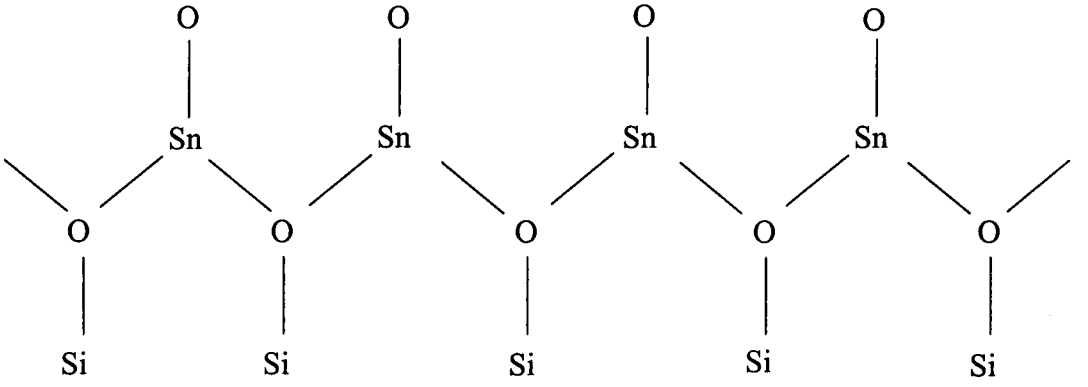

Figure 6.11 A model tin silicate glass structure which requires chains of tin atoms.

A three co-ordinated oxyen is required to charge balance each three co-ordinated Sn^{2+}. This contravenes one of Zachariasen's rules for glass formation [38], particularly at high tin content, but has previously been reported for bismuth and lead gallate glasses [39].

6.3.4 CRYSTALLINE TIN SILICATE

It is often useful to discuss glass structure in terms of related crystal structures. Yamada compared his neutron diffraction data for $(PbO)_x(SiO_2)_{1-x}$ glasses with that for related crystalline lead silicates. The tin silicate system contains only one, presently uncharacterised, metastable, crystalline phase. It is not possible to prepare a single phase '$SnSiO_3$' sample by crystalising tin silicate glass. Heating for 35 minutes, as described in section 6.2, causes a partial crystalisation which then decomposes on further heating. The sample used in this study consists of a mixture of '$SnSiO_3$' and remnant tin silicate glass.

6.3.4a NEUTRON AND X-RAY DIFFRACTION

The neutron diffraction data for the heat treated '$SnSiO_3$' sample was processed to i(Q) using absorption and multiple scattering corrections calculated for the initial glass sample TS7, assuming homogeneity and isotropy. The data from different detector banks were merged over a more restricted Q range than that for the glass sample data because the Bragg peaks were broadened by the Q-space resolution at each detector angle. It is not considered possible to directly compare the heat treated sample and each glass sample i(Q) as the Bragg peaks dominate the heat treated sample i(Q), see figure 6.5.

T(r) behaves well at low r, see figure 6.7. This suggests that the absorption and multiple scattering corrections were satisfactory. There is no systematic peak at 1.78Å in T(r) calculated using data up to $50Å^{-1}$. The first three peaks are at similar positions to but narrower than those for the $(SnO)_x(SiO_2)_{1-x}$ glasses, see table 6.6. The silicon is four co-ordinated and the tin is three co-ordinated with respect to oxygen. The r_{OO}/r_{SiO} distance ratio, see table 6.7, is within the experimental uncertainty of that for a regular SiO_4 tetrahedron. The partially crystallised tin silicate T(r) is comparable to those for the tin silicate glasses.

It is possible to convert i(Q) to a plot of neutron intensity against d-spacing using equation 2.15. Figure 6.12 shows both the neutron and X-ray diffraction patterns, X-ray intensity against d-spacing. The X-ray scattering is dominated by the tin atoms whilst the neutron scattering cross sections are similar for each atom species, as summarised in table 2.1. The offset between the two patterns is thought to be related

to the TOF calibration problem on LAD. This should be corrected if the data is to be used further to this study.

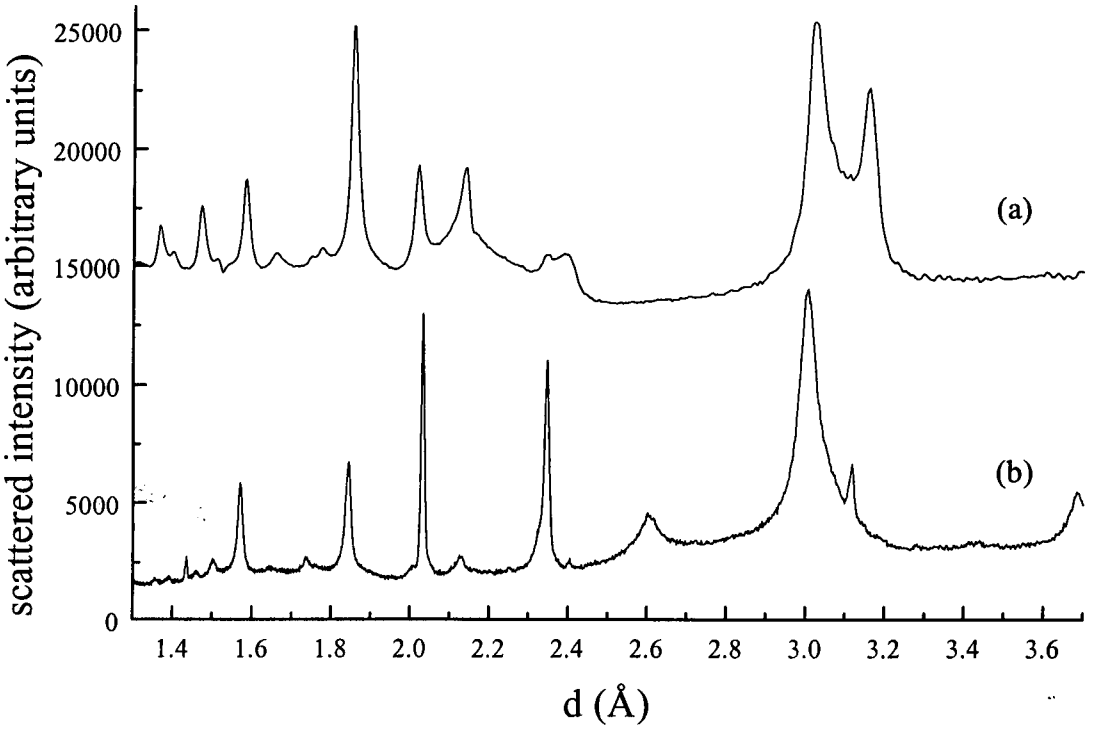

Figure 6.12 Scattered intensity vs. d-spacing for '$SnSiO_3$' measured by (a) neutron diffraction (150° detectors on LAD) and (b) X-ray diffraction.

It has not proved possible to characterise the '$SnSiO_3$' crystal structure from either the X-ray or neutron diffraction patterns. The Bragg peaks are broad (the crystallite size is small), the crystal phase composition is not known and the diffraction pattern is not similar to any other lead or tin compounds within a tetrahedral matrix ($PbSiO_3$, $PbGeO_3$ or $SnGeS_3$).

Carbo Nover suggests that the '$SnSiO_3$' crystal structure is similar to that for crystalline SnO, but with a larger unit cell [12]. This suggests that the '$SnSiO_3$' crystal structure consists of layers of SnO units. This is supported by the similarities between the '$SnSiO_3$'diffraction pattern and that for Pb_3GeO_5 but not with that for $PbSiO_3$. Pb_3GeO_5 consists of layers of square based $PbO_{4/4}$ pyramids connected by weakly deformed GeO_4 tetrahedra [41] whilst $PbSiO_3$ consists of zig-zag SiO_4 chains perpendicular to PbO_3 and PbO_4 screw chains [23].

Carbo Nover [12] and Karim [16] both report that the crystal phase grows as polycrystalline spherulites in the glass. This is a typical method of crystal growth when the crystal phase differs from the bulk composition [40]. The Si-O peak position in T(r) is more like TS2 than TS7 and the ^{29}Si MAS NMR data described

below also suggest that the crystalline stoichiometry is not $SnSiO_3$. This work is being continued [40] but not included within the scope of this study.

6.3.4b ^{29}Si MAS NMR

Carbo Nover [12] and Karim [16] describe the crystal phase as stannous metasilicate, '$SnSiO_3$'. However the ^{29}Si MAS NMR spectra indicates that only a small proportion of the silicon is in the crystal phase, see figure 6.13. The two narrow peaks at -68.6 and -74.6ppm are due to two crystallographically different silicon sites in the crystalline phase and the broad peak at -110ppm is due to silicon in the remnant glass. The relative intensity of the two narrow peaks with respect to the broad peak increases with pulse delay, see table 6.10. This is because the T_1 relaxation time is longer in the crystalline phase than in the remnant glass, possibly due to an exclusion of the Fe^{3+} impurity from the crystal phase. The increase in relative intensity is small with respect to the increase in pulse delay (from 1 to 100 seconds) so the spin system is not thought to be saturated in either spectrum. The relative intensities of the three peaks in spectrum acquired using a 100 second pulse delay is considered to approximately reflect the proportion of silicon atoms in two crystalline sites and the remnant glass.

	δ (ppm) (±0.2)	FWHM (ppm) (±0.5)	relative intensity (±1)
'$SnSiO_3$' pd=1s.	-68.6	2.7	4.5
	-74.6	2.6	2.5
	-110	16.3	93
'$SnSiO_3$'pd=100 s.	-68.5	3	9
	-74.6	9	5
	-110	15.5	86

Table 6.10 Gaussian fit parameters for ^{29}Si MAS NMR spectra of the heat treated '$SnSiO_3$' sample using 1 second and 100 seconds pulse delay.

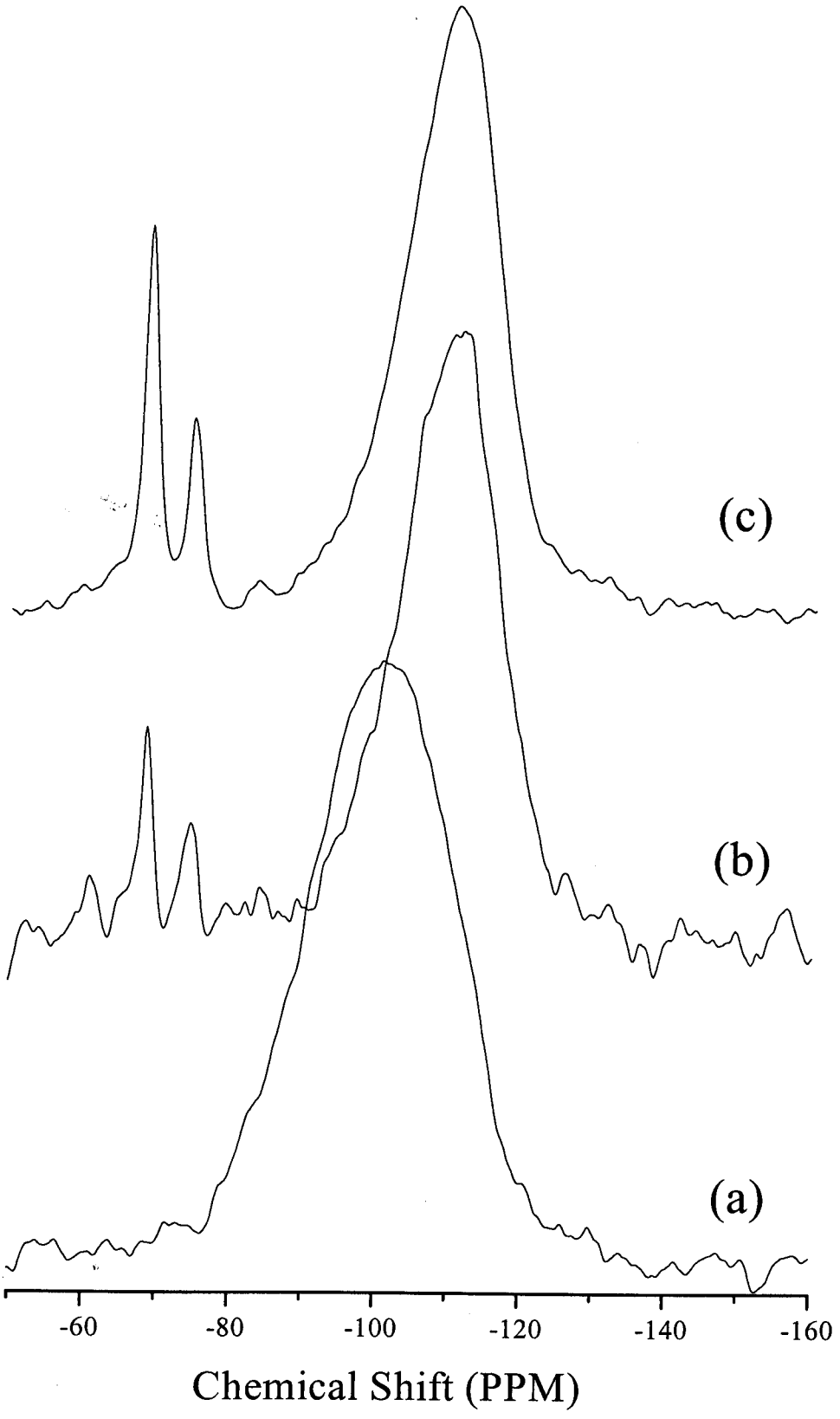

Figure 6.13 ^{29}Si MAS NMR spectra relative to T.M.S. for (a) the $50SnO\text{-}50SiO_2$ glass before heat treatment, (b) the heat treated '$SnSiO_3$' using a pulse delay of 1 second and (c) the heat treated '$SnSiO_3$' using a pulse delay of 100 seconds.

	δ (ppm) (±0.2)	FWHM (ppm) (±0.5)	relative intensity (±1)
TS0 (0mol%SnO)	-112	11.5	100
TS1 (16.8mol%SnO)	-110.6	13.9	100
TS2 (28.2mol%SnO)	-109.4	19.4	100
TS3 (29.6mol%SnO)	-107.1	19.6	100
TS4 (32.6mol%SnO)	-105.6	20.8	100
TS5 (39.7mol%SnO)	-103.3	23.6	100
TS6 (40.9mol%SnO)	-100.6	23.2	100
TS7 (49.4mol%SnO)	-97.6	22.2	100
TS8 (53.5mol%SnO)	-96.2	20.9	100
TS9 (55.4mol%SnO)	-92.2	19.4	100
TS10 (64.0mol%SnO)	-89.7	19.2	100
TS11 (71.5mol%SnO)	-87.7	28.9	100

Table 6.11 Gaussian fit parameters to ^{29}Si MAS NMR spectra of SnO-SiO_2 glasses, after Karim [16].

It is possible to estimate an approximate composition of the crystalline phase from the ^{29}Si MAS NMR spectrum. The position of the broad peak is typical for a glass containing 20mol% SnO, see tables 6.10 and 6.11. Hence, assuming the bulk sample contains 50mol% SnO then the crystalline phase contains approximately 30mol% SnO (±5mol%). The relative proportion of the crystalline and remnant glass resonances suggest that the crystalline phase contains 7mol% SiO_2. Therefore, the crystalline phase has an approximate composition of 4SnO-SiO_2. This has a higher tin content than previously reported.

6.3.4c ^{119}Sn MAS NMR

^{119}Sn MAS NMR spectra for this same heat treated '$SnSiO_3$' sample have been recorded by Yildrem [29], see figure 6.14. It is possible to identify two isotropic crystalline peaks and their associated spinning sidebands by spinning at different speeds. However, it is not considered possible to accurately determine the ratio of crystalline tin species with respect to that in the remnant glass because the narrow crystalline peaks are superimposed on and overlap the broad remnant glass resonance. The two isotropic peaks are reported at 553 and 640ppm relative to c-SnO_2. It is not possible to interpret these shifts in terms of crystal structure as there

are no related characterised crystal structures. Cossement et al. report δ_{iso} for c-SnO and c-SnO_2 (relative to a 5% solution of tetramethyltin in dichloromethane) as -208±2ppm and -603±2ppm, respectively [19]. Hence, the c-SnO δ_{iso} relative to c-SnO_2 is 395ppm. This is down-field of both δ_{iso} in the '$SnSiO_3$' sample, which suggests that the tin nuclei are less shielded in the metastable crystalline tinsilicate than in c-SnO.

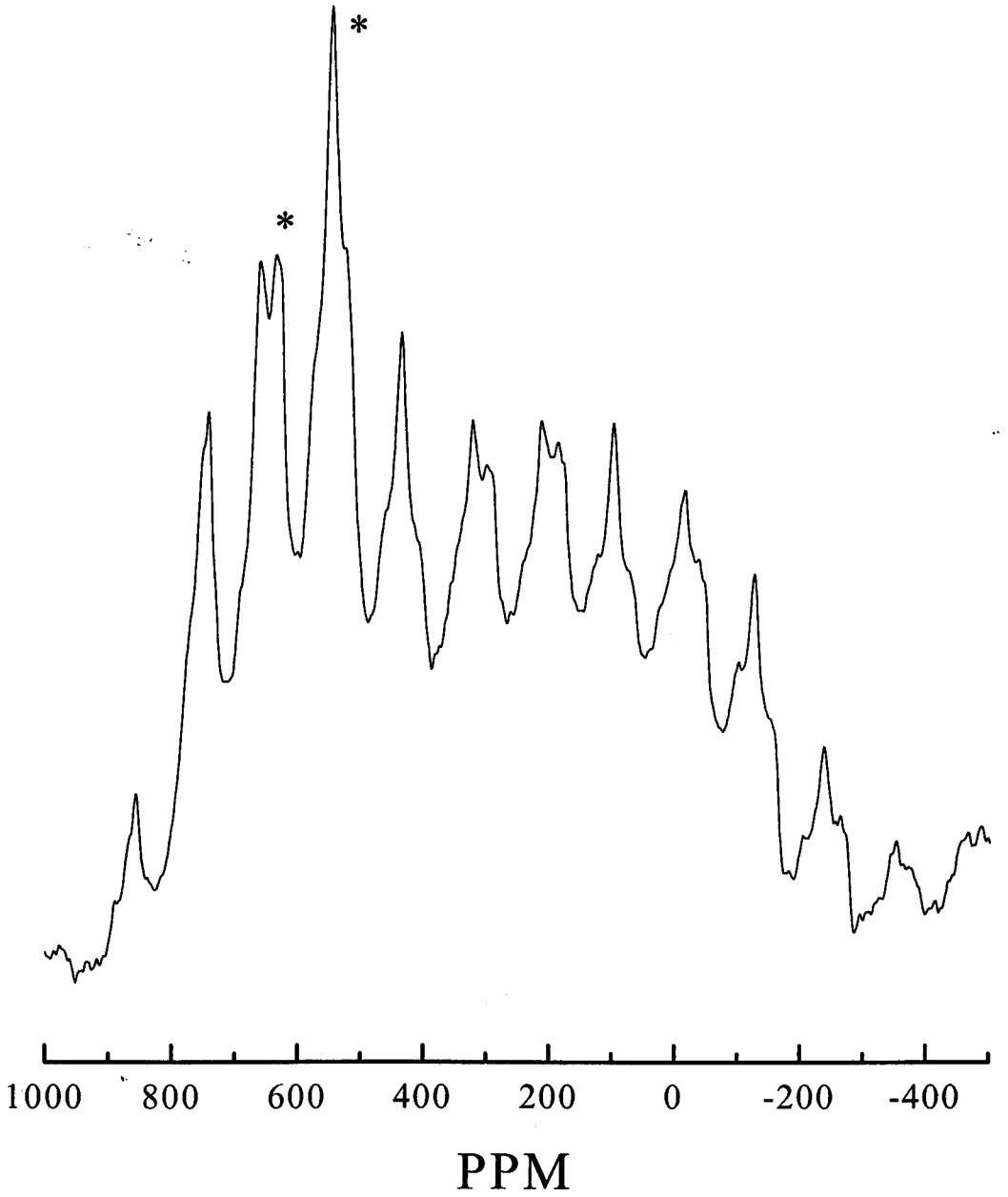

Figure 6.14 ^{119}Sn MAS NMR spectrum for heat treated '$SnSiO_3$' sample, after Yildrem [29]. Shift relative to c-SnO_2.

6.3.5 ^{17}O MAS NMR

^{17}O MAS NMR spectra for the ^{17}O enriched $(SnO)_x(SiO_2)_{1-x}$ glasses and heat treated '$SnSiO_3$' sample have been recorded by Yildrem [29], see figure 6.15. Each spectrum contains three featureless peaks at ~35, 110 and 200ppm which are thought to be due to oxygen within Si-O-Si, Si-O-Sn and Sn-O-Sn linkages, respectively. These peak assignments are made with reference to the ^{17}O chemical shifts reported for Sn-O-Sn and Si-O-Si. Bastow and Stuart report a single peak at 247ppm in crystalline SnO [42]. Jäger et al. report a broad second order quadropolar powder pattern centred about ~37ppm in ν-SiO_2 [43]. The Si-O-Sn peak may be expected to have an isotropic chemical shift somewhere between the Si-O-Si and Sn-O-Sn peaks.

The Si-O-Si peak in ν-SiO_2 has a well defined quadrupolar splitting. Geissberger and Bray report a large quadrupolar coupling constant ($C_Q \cong 5.8$MHz) and a low asymmetry parameter (η=0.2) [44]. The Si-O-Si peak in each of these $(SnO)_x(SiO_2)_{1-x}$ glasses and heat treated '$SnSiO_3$' sample does not have this quadrupolar lineshape. This could be due to a decrease in C_Q on increasing tin content, although a consistent reduction in the peak width is not seen on increasing tin content. The width of the peak is comparable to that in a tin-free hydrous silicate glass (in which the width is typically 41ppm) [45]. The reduction in C_Q could be due to either a reduction in the Si-O-Si bond angle [46] and/or the tin acting as a network modifier [47]. The peak width must then be largely dependent upon the chemical shift dispersion. This interpretation requires an increase in the distribution of Si-O-Si linkages as the electric field gradient (efg) at the oxygen nucleus decreases upon adding tin.

The Sn-O-Sn and Si-O-Sn peak intensities increase relative to the Si-O-Si peak with increasing tin content, see table 6.12. This supports the peak assignment described above. Also, the Sn-O-Sn and Si-O-Sn peak widths narrow more dramatically than the Si-O-Si peak, upon heat treatment. This supports the assignment of these peaks and the conclusion from the ^{29}Si NMR data, see section 6.3.4b, that the crystalline phase contains a high tin content.

However, the relative intensities of each peak do not agree with the structural model proposed in figures 6.10 and 6.11. The proposed incorporation of three co-ordinated tin into a tetrahedral silicate network in glasses of the form $(SnO)_x(SiO_2)_{1-x}$ requires x(Sn-O-Sn) linkages, x(Sn-O-Si) linkages and (2-3x)(Si-O-Si) linkages.

(In this description of figures 6.9 and 6.10 the oxygen atom in the Sn-O-Sn linkage is also bonded to a silicon atom.) The relative proportions of each oxygen environment, according to this proposed model, are summarised in table 6.11. The relative intensities of the peaks in the ^{17}O spectra are not in good agreement with this model. The relative intensity of the Si-O-Si peak is much greater than that predicted by this model. This could be due to the ^{17}O enriched glasses having a higher tin content than deduced from the density measurements described in section 6.3.1. However, the relative intensity of the peak at 110ppm is greater than the peak at 200ppm at all compositions whilst this model suggests that the proportion of Sn-O-Sn and Sn-O-Si linkages should be equivalent. This may require either redefinition of the proposed structural model or questioning the validity of the ^{17}O NMR spectra.

The glasses were prepared in small quantities (due to the high cost of the ^{17}O enrichment) and melted for a relatively short time (due to the disproportionation of SnO with time). It is considered possible that the ^{17}O is not distributed homogenously throughout the melt. The ^{17}O was added as enriched silica and whilst the sample composition is not known accurately; the Si-O-Si peak intensity is larger than expected and the Si-O-Sn and particularly the Sn-O-Sn peak is smaller than expected. The peak positions and peak shapes are considered typical of the tin silicate network but the relative intensity of the peaks is not considered to reflect the bulk sample.

The proportion of the peaks in the heat treated sample is not the same as in the 55mol%SnO glass from which it was prepared. The relative intensity of the Sn-O-Sn and Sn-O-Si peaks are less after heat treatment. The crystalline phase is thought to contain a high tin content and the ^{29}Si NMR data suggests that the paramagnetic impurity is not felt as strongly in the crystalline phase as in the glass. The ^{17}O spectra were acquired using a 2 second pulse delay which, particularly if the quadropolar coupling is reduced, may saturate the spins in the crystalline phase.

The long acquisition (24hrs) required to measure each spectrum restricted this study to a simple one dimensional MAS NMR study. A multiple quantum experiment would be very useful, to improve the resolution and to distinguish the connectivity of each oxygen species.

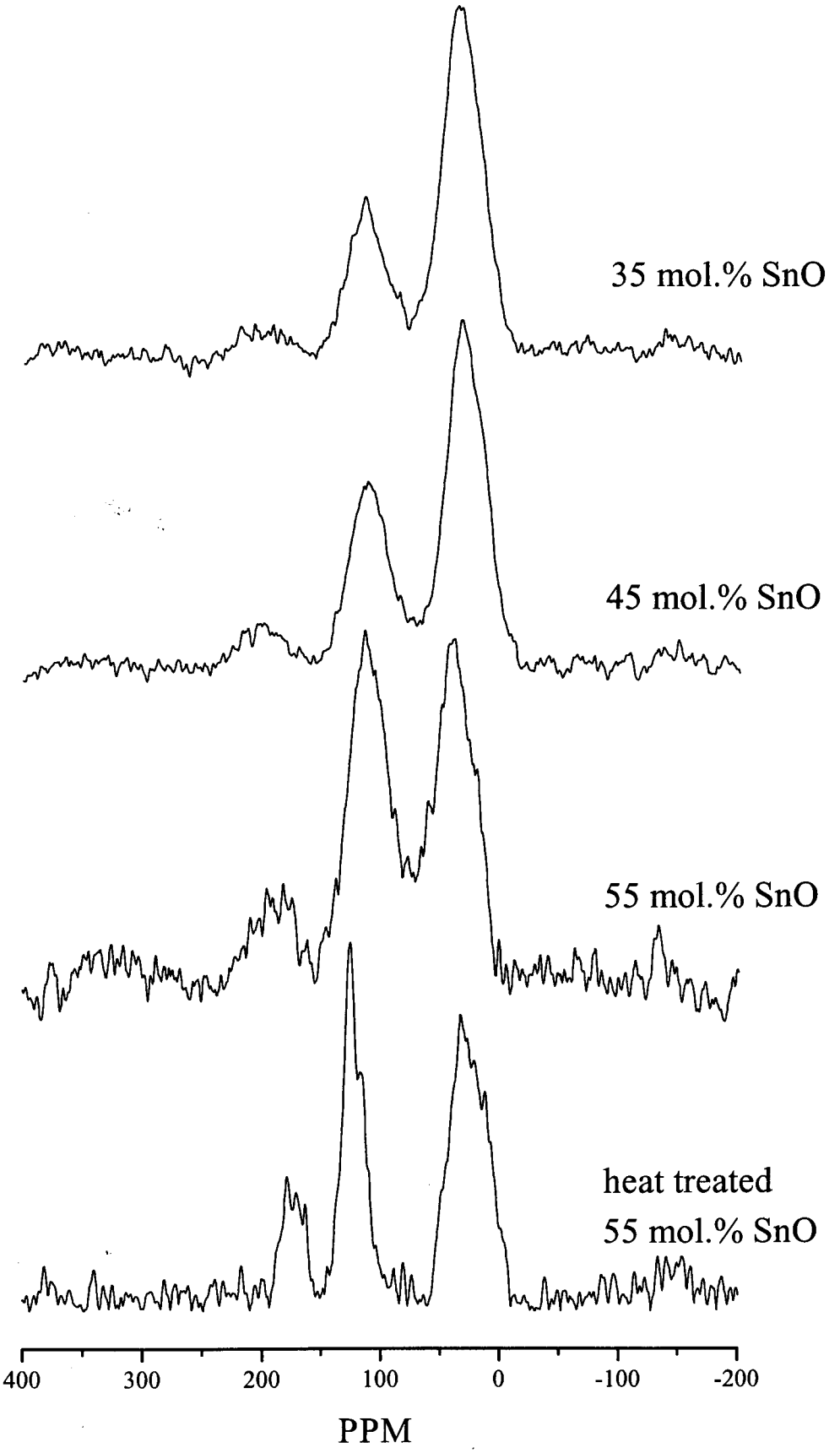

Figure 6.15 ^{17}O MAS NMR spectra for three tin silicate glasses and one partially crystallised tin silicate glass, relative to H_2O.

		δ (ppm) (±0.1)	fwhm (ppm) (±0.02)	relative intensity (%) (1.5%)	theoretical relative intensity (%)
39 mol%SnO	Si-O-Si	34.5	40.5	65.7	51.6
	Si-O-Sn	114.1	41.2	28.2	24.2
	Sn-O-Sn	201.3	48.2	6.1	24.2
42 mol%SnO	Si-O-Si	30.9	39.9	58.5	46.8
	Si-O-Sn	111.3	41.7	33.2	26.6
	Sn-O-Sn	200.7	45.4	8.3	26.6
54 mol%SnO	Si-O-Si	39.5	43.6	44.2	26.0
	Si-O-Sn	111.1	41.8	43.7	37.0
	Sn-O-Sn	190.4	45.1	12.1	37.0
heat treated 54 mol%SnO	Si-O-Si	26.4	36.8	52.2	26.0
	Si-O-Sn	123.8	21.9	35.6	37.0
	Sn-O-Sn	174.5	19.8	12.2	37.0

Table 6.12 Gaussian fit parameters to ^{17}O NMR spectra for glass samples and viasual peak parameters for the heat treated sample. Shifts relative to H_2O.

6.4 CONCLUSIONS AND FUTURE WORK

It is possible to prepare $(SnO)_x(SiO_2)_{1-x}$ glasses up to 71.5 mol% SnO. This requires a tin silicate network in which Sn^{2+} acts as a network intermediate or conditional network former. The change in ^{29}Si MAS NMR chemical shift with tin content, previously reported by Karim [16], suggests that the structural role of the tin changes at 30~35mol% SnO. The neutron diffraction data presented here does not support this.

The tin is three co-ordinated to oxygen at all compositions. This requires a three co-ordinated oxygen to charge balance each three co-ordinated tin atom. Two possible model structures which allow SnO_3 units within a SiO_4 network are presented. The pair model, see figure 9, can be considered the same as the chain model, see figure 6.10, when the chain is two tin atoms long and joins ends to form a ring. The increase in the period of intermediate range order with tin content could be used to support the chain/ring model but it is not possible to conclusively distinguish between the two models. The Si-O bond length increases with tin content. This is

also observed on depolymerising the network in alkali silicate glasses and could be interpreted to suggest that the Sn^{2+} acts as a network modifier. Alternatively tetrahedral $SiO_{4/2}$ network could expand as it incorporates the tin into the network, without depolymerisation as defined for a network modifier.

The peak positions and co-ordination numbers obtained from the fits to the neutron diffraction data are not accurate when the peaks overlap. This is only observed in TS10 but may be more significant in glasses in which the peaks are not clearly resolved in T(r). However, it should be noted that the accuracy of the calculated co-ordination numbers is largely restricted by the uncertainty in the sample composition.

The interpretation of experimental data for a series of glasses in terms of glass structure requires an accurate measure of the composition. This is a significant problem. It is important to quantify all the atom species to obtain a measure of the accuracy of the analysis. Several characterised materials of similar composition should be used as references in X-ray spectroscopic analysis.

The ^{29}Si MAS NMR identifies two non-equivalent silicon sites within a crystalline phase of higher tin content than reported previously [12 & 16]. An approximate composition of $(SnO)_4(SiO_2)$ is estimated from the position of the amorphous peak and the ratio of areas between the amorphous and crystalline peaks.

The crystalline tin silicate is thought to contain two non-equivalent tin sites. Two isotropic peaks and their associated spinning sidebands were identified by ^{119}Sn MAS NMR spectra, acquired at different spinning speeds.

The '$SnSiO_3$' diffraction pattern is reported but not in terms of a crystal structure. The diffraction pattern is not similar to that for $PbSiO_3$, $PbGeO_3$ or $SnGeS_3$ but does bear some resemblance to that for Pb_3GeO_5.

The ^{17}O MAS NMR study identified three oxygen sites, the relative intensity of which changed with sample composition. However, the compositional analysis of the ^{17}O enriched glasses is not considered accurate and the relative proportions of the three peaks are not in agreement with those calculated considering the proposed model. It is considered possible that the ^{17}O is not homogenously distributed throughout the sample.

A further diffraction experiment was performed on HRPD but the peaks were similarly broad. This suggests that the large peak widths in the '$SnSiO_3$' diffraction

pattern are due to particle size broadening and an overlapping with correlations in the remnant glass. It was also not possible to obtain a diffraction pattern from a single crystallite using a TEM with a cold stage because the crystallites decomposed in the electron beam.

The major finding of this work is that the tin is three co-ordinated within a tin silicate network. It may be possible to corroborate this by an EXAFS and/or XANES study of these samples. Otherwise the structural units are considered to be well defined, predominantly by neutron diffraction. Further work is considered necessary to study the interconnection of the structural units.

This work could be continued by studying;

- the structure of the metastable crystalline phase and
- continuing the ^{17}O NMR study by studying high tin content $(SnO)_x(SiO_2)_{1-x}$ glasses. An increase in the proportion of ^{17}O enrichment would reduce the acquisition time allow the use of a two dimensional technique. This could possibly yield an improved resolution and information on the connectivity of the oxygen species. The melt time could be varied (although this would effect the amount of disproportionation of SnO) and/or a series of pulse delays could be used to acquire an unsaturated spectrum for the crystallised sample.

REFERENCES

[1] A.E.Dodd, Dictionary of Ceramics, (1964) George Newnes Limited, London.

[2] W.A.Weyl, Coloured Glasses, (1967) Society of Glass Technology, England.

[3] A.S.Sanyal and J.Mukerji, Phys.Chem.Glasses 24 #4 (1982) 79

[4] M.B.Volf, Chemical Approach to Glass, (1984) Elsevier, Oxford.

[5] A.Pilkington, *Proc.R.Soc.London* **A314** (1969) 1

[6] A.Sears, 'The characterisation of stannosilicate glasses', PhD thesis, Department of Physics, University of Warwick, submitted December 1997.

[7] J.S.Sieger, *J.Non-Cryst.Solids* **19** (1975) 213

[8] F.Lamouroux, N.Can, P.D.Townsend, B.W.Farmery and D.E.Hole, *J.Non-Cryst.Solids* **212** (1997) 232

[9] J.Luo and C.Xu, *J.Non-Cryst.Solids* **119** (1990) 37

[10] A.Paul, J.D.Donaldson, M.T.Donoghue and M.J.K.Thomas, *Phys.Chem.Glasses* **18 #6** (1977) 125

[11] J.Silver, E.A.D.White and J.D.Donaldson, *J.Material Science* **12** (1977) 828

[12] J.Carbo Nover and J.Williamson, *Phys.Chem.Glasses* **8 #4** (1967) 164

[13] B.Keysselitz and E.J.Kohlmeyer, *Metall Erz.* **30** (1933) 172

[14] T.Ishikawa and S.Akagi, *Phys.Chem.Glasses* **19 #5** (1978) 108

[15] M.M.Karim and D.Holland, *Phys.Chem.Glasses* **36 #5** (1995) 206

[16] M.M.A.Karim, A study of tin oxides in silicate based glasses, PhD thesis, Department of Physics, University of Warwick, March 1995.

[17] H.Eckert, *Prog.Nuc.Mag.Res. Spec.* **24** #3 (1992) 159

[18] K.F.E.Williams, C.E.Johnson, J.A.Johnson, D.Holland and M.M.Karim, *J.Phys.Condens.Matter* **7** (1995) 9485

[19] C.Cossement, J.Darville, J.M.Gilles, J.B.Nagy, C.Ferdandez and J.P.Amoureux, *Mag.Res.Chem* **30** (1992) 263

[20] E.M.Rabinovich, *J.Materials Science* **11** (1976) 925

[21] R.Dupree, N.Ford and D.Holland, *Phys.Chem.Glasses* **28 #2** (1987) 78

[22] F.Fayon, C.Bessada, D.Massiot, I.Farnan and J.P.Coutures, *J.Non-Cryst.Solids* **232-243** (1998) 403

[23] F.Fayon, I.Farnan, C.Bessada, J.Coutures, D.Massiot and J.P.Coutures, *J.Am.Chem.Soc.* **119 #29** (1997) 6837

[24] P.P.Lottici, G.Antoniolo and A.Montenero, *Trans.ACA* **27** (1991) 309

[25] H.Morikawa, Y.Takagi and H.Ohno, *J.Non-Cryst.Solids* **53** (1982) 173

[26] M.Imaoka, H.Hasegawa, I.Yasui, *J.Non-Cryst. Solids* **85** (1986) 393

[27] K.Yamada, A.Matsumoto, N.Niimura, T.Fukunaga, N.Hayashi and N.Watanabe, *J.Phys.Soc.Japan* **55** #3 (1986) 831

[28] N.E.Brese and M.O'Keeffe, *Acta Cryst.* **B47** (1991) 192

[29] E.Yidrem, 'An ^{17}O NMR study of several silicate glasses', PhD thesis, Department of Physics, University of Warwick, in progess.

[30] A.E.Geissberger and P.J.Bray, *J.Non-Cryst.Solids* **54** (1983) 121

[31] D.I.Grimley, A.C.Wright and R.N.Sinclair, *J.Non-Cryst.Solids* **119** (1990) 49

[32] P.A.V.Johnson, A.C.Wright and R.N.Sinclair, *J.Non-Cryst.Solids* **50** (1982) 281

[33] P.H.Gaskell and D.J.Wallis, *Phys.Rev.Letters* **76** #1 (1996) 66

[34] A.C.Wright, *J.Non-Cryst.Solids* **179** (1994) 84

[35] J.D.Donaldson and D.C.Puxley, *Acta Cryst.* **B28** (1972) 864

[36] G.N.Greaves, C.R.A.Catlow, B.Vessal, J.Charnock, C.M.B.Henderson, R.Zhu, S.Qiao, Y.Wang, S.J.Gurman and S.Houde-Walter in; New Materials and their applications (1990) (Institute of Physics, Bristol 1990) p411

[37] J.F.Bent, A.C.Hannon, D.Holland and M.M.A.Karim *J.Non-Cryst.Solids* **232-234** (1998) 300

[38] W.H.Zachariasen, *J.Am.Ceram.Soc* **54** (1932) 3841

[39] F.Miyaji, T.Yoko, J.Jin, S.Sakka, T.Fukunaga and M.Misawa, *J.Non-Cryst.Solids* **175** (1994) 211

[40] D.Holland, personal correspondence

[41] S.A.Ivanov, N.V.Rannev, B.M.Shchedrin and Y.N.Venevtsev, *Sov.Phys.Dokl.* **23** #3 (1978)164

[42] T.J.Bastow and S.N.Stuart, *Chemical Physics* **143** (1990) 459

[43] C.Jäger, R.Dupree, S.C.Kohn and M.G.Mortuza, *J.Non-Cryst.Solids* **155** (1993) 95

[44] A.E.Geissberger and P.J.Bray, *J.Non-Cryst.Solids* **54** (1983) 121

[45] M.E.Smith, personal correspondance

[46] P.J.Grandinetti, J.H.Baltisberger, I.Farnan, J.F.Stebbins, U.Werner and A.Pines, *J.Phys.Chem.* **99** (1995) 12341

[47] K.E.Vermillion, P.Florian and P.J.Grandinetti, *J.Chem.Phys.* **108** #17 (1998) 7274

CHAPTER 7

ALKALI TIN SILICATE

7.1 INTRODUCTION

The structures of modified tin silicate glasses are of interest as an extension of the work presented in the previous chapter and as the next step to understanding the behaviour of tin in float glass. This work is part of a collaboration between several workers using complementary techniques to study these glasses [1-3]. Prior to these projects there have been very few studies of modified tin silicate glasses and no reports of modified tin silicate crystal structures.

A Mössbauer study of several sodium tin silicate glasses was reported by Dannheim et al. [4]. Both Sn^{2+} and Sn^{4+} were thought to act primarily as network intermediates. A change in co-ordination from 4 to 6 was observed, with reference to SnO, SnO_2 and SnS, on decreasing the Na_2O content and/or increasing the Sn^{2+}/Sn^{4+} ratio (by melting in a reducing atmosphere). This change in co-ordination was interpreted as a removal of first Sn^{2+} and eventually Sn^{4+} from the network to act as network modifiers.

A previous Mössbauer study of M_2O-SnO_2-SiO_2 glasses (where M = Li, Na and K) by Mitrofanov and Sidorov [5] did not observe any change in the ^{119}Sn chemical shift with composition. They assigned the tin to well defined sites, six co-ordinated with respect to oxygen. Similar results were reported for M_2O-SnO_2-B_2O_3 glasses (where M=Li, Na and K) by Eissa et al. [6]. An increase in the ^{119}Sn isomer shifts was interpreted as an increase in the ionicity of the Sn-O bond with increasing alkali ion radius (Li-Na-K). In all glasses the tin was assigned to be six co-ordinated to oxygen.

The most recent Mössbauer study of alkali tin silicates glasses did not observe any change in co-ordination with composition [3]. The glasses studied by Appleyard et al. were of the general composition $(R_2O)_x(SnO)_{1-x}(SiO_2)$ where R=Li, Na, K or Rb and x varied from $0 \leq x \leq 0.2569$. Small amounts of SnO_2 were quantifiable from the ^{119}Sn spectrum, but the glasses were prepared under reducing conditions so that the tin was largely present as Sn^{2+} [2]. Corrections were made, as previously by

Williams [7], for the molar volume and also for changes in bond angle [8]. The ^{119}Sn isotropic chemical shift decreased on replacing SnO with alkali oxide, see figure 7.1. The shift decreased at approximately the same rate in the sodium, potassium and rubidium tin silicate glasses but at a slower rate in the lithium tin silicates. These shifts indicate a decrease in the s-electron density at the ^{119}Sn nucleus on increasing alkali content. This was interpreted as an increase in the covalency of the ^{119}Sn on replacing SnO with alkali oxide. The decrease in chemical shift is accompanied by a decrease in quadrupolar splitting, see figure 7.2. This decrease in splitting is due to an increase in the isotropy of the magnetic field felt at the ^{119}Sn nucleus. This was interpreted as the ^{119}Sn environment being less distorted on replacing SnO with alkali oxide.

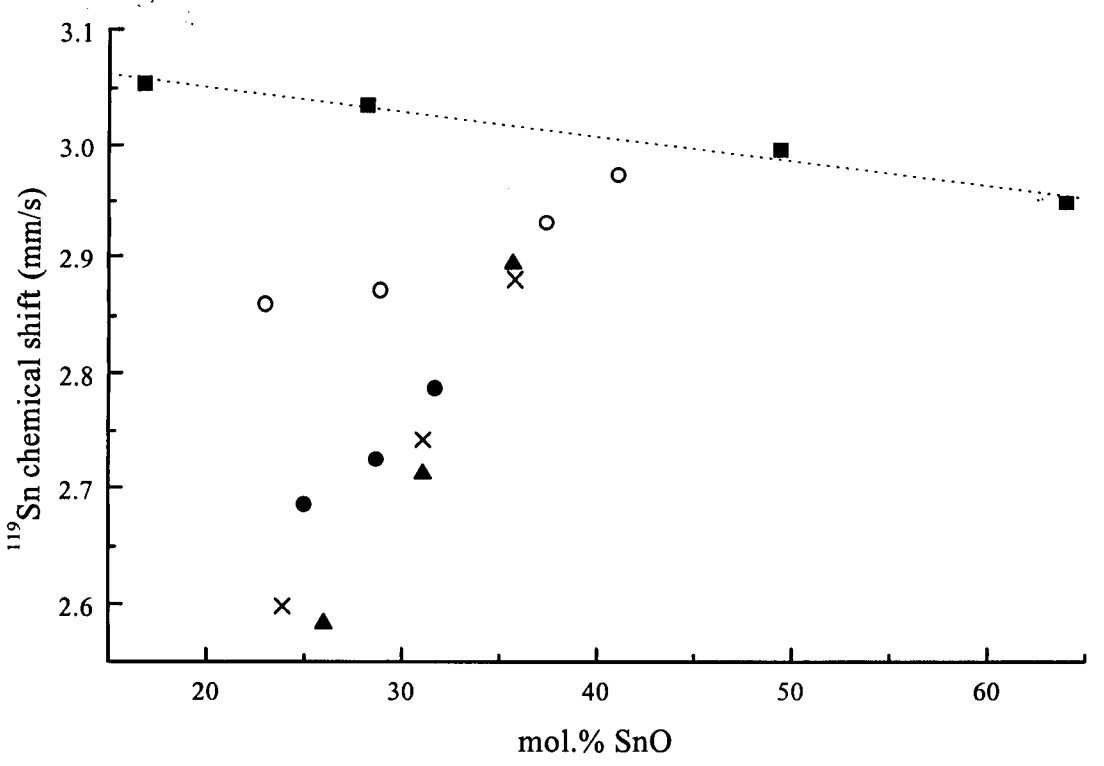

Figure 7.1 ^{119}Sn Mössbauer chemical shift vs mol% SnO in $(SnO)_x(SiO_2)_{1-x}$ glasses (solid square symbols) and $(R_2O)_x(SnO)_{1-x}(SiO_2)$ glasses where R is lithium (hollow circle symbol), sodium (solid cicle symbol), potassium (cross symbol) and rubidium (solid triangle symbol), after Appleyard [3]. Shifts referenced to c-$CaSnO_3$.

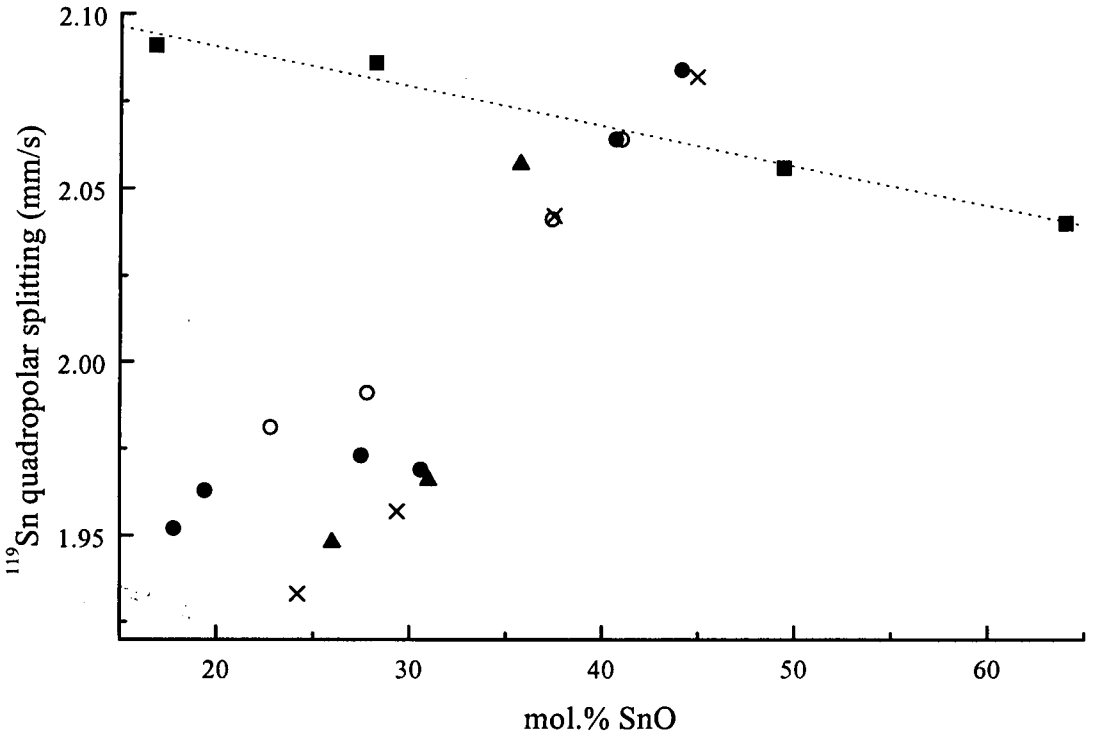

Figure 7.2 ^{119}Sn Mössbauer quadrupolar splitting vs mol% SnO in $(SnO)_x(SiO_2)_{1-x}$ glasses (solid square symbols) and $(R_2O)_x(SnO)_{1-x}(SiO_2)$ glasses where R is lithium (hollow circle symbol), sodium (solid circle symbol), potassium (cross symbol) and rubidium (solid triangle symbol), after Appleyard [3].

Some physical properties of the same glasses studied by Appleyard have been reported by Sears et al. [9]. The changes in molar volume (calculated from the sample density) with concentration of different modifiers are approximately linear, see figure 7.3. Replacement of SnO with Na_2O has little effect on the molar volume, replacement with K_2O and Rb_2O increases the molar volume, whilst replacement with Li_2O, MgO or CaO reduces the molar volume. These changes are representative of the volume of each of the ions and indicate that the steric requirements of Sn^{2+} are approximately equivalent to $2Na^+$.

Sears et al. also plot the change in molar volume with composition against the cube of the relevant ionic radius for $(R_2O)_x(SnO)_{1-x}(SiO_2)$ and $(R_2O)_x(SiO_2)_{1-x}$, see figure 7.4. The radius of a covalent, tetrahedral silicon atom lies on the straight line fit to the $(R_2O)_x(SnO)_{1-x}(SiO_2)$ data whilst the Sn^{2+} ionic radius lies on the straight line fit to $(R_2O)_x(SiO_2)_{1-x}$ data. This suggests that the tin in the binary glasses acts as Sn^{2+}. However, the tin is not thought to act as a simple network modifier within a $SiO_{4/2}$ network.

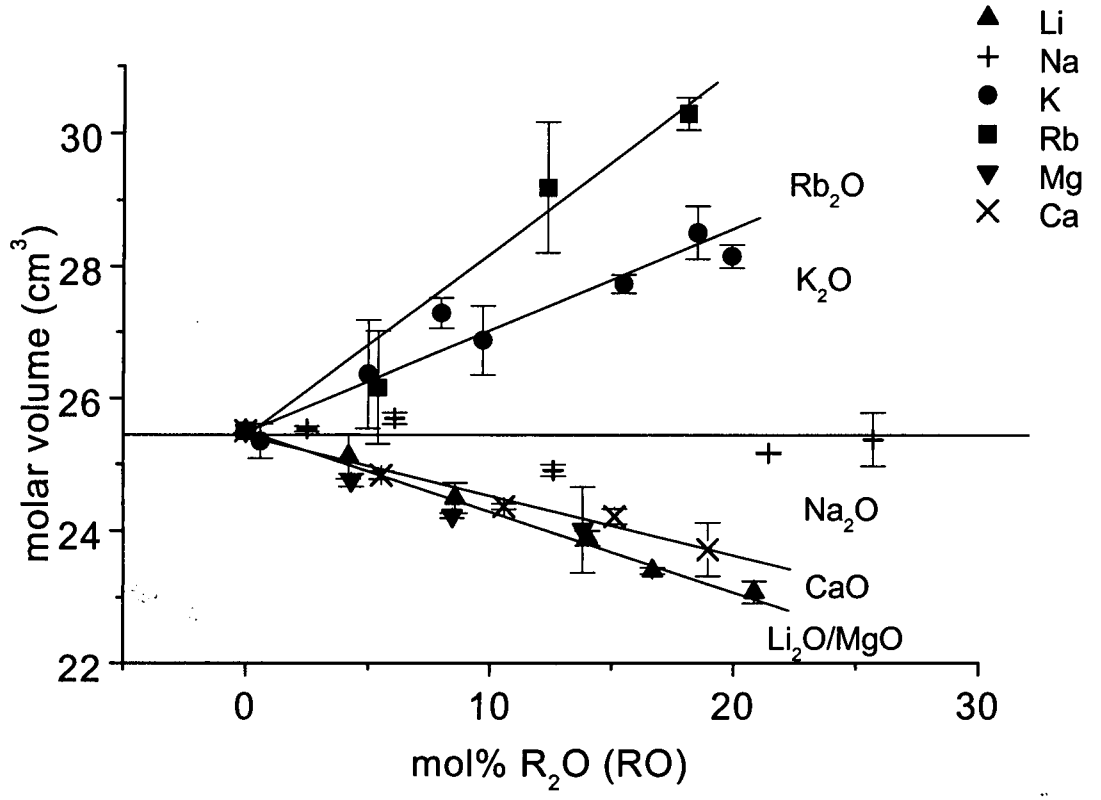

Figure 7.3 Changes in molar volume with R_2O (RO) content in $(R_2O)_x(SnO)_{1-x}(SiO_2)$ glasses, after Sears [9].

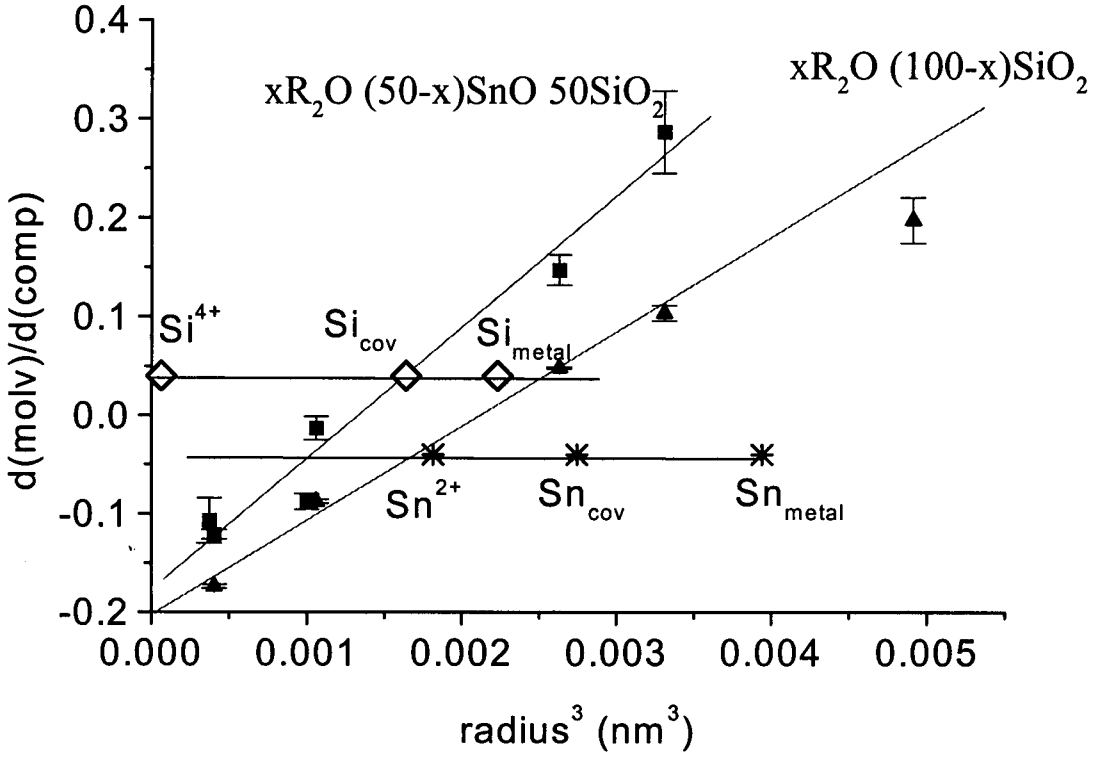

Figure 7.4 Rate of change of molar volume with modifier (R_2O or RO) content vs. the (ionic radius)^3, to represent the steric volume of the species, after Sears [9].

The thermal coefficient of expansion (TCE) of these glasses increases on replacement of SnO by alkali oxides (Rb, K, Na and less so for Li) but does not change on replacement with CaO and decreases on replacement by MgO. The TCE is a measure of the rate of change in volume with increasing temperature [10]. It indicates the strength of the bonding in the glass and the degree of cross linking within the network [9]. The TCE increases on replacing SnO by R_2O in v-$(R_2O)_x(SnO)_{1-x}(SiO_2)$, see figure 7.5. This disruption of the network is not as dramatic as replacing SiO_2 by R_2O in v-$(R_2O)_x(SiO_2)_{1-x}$ but more than replacing SiO_2 by SnO in v-$(SnO)_x(SiO_2)_{1-x}$. This is interpreted in terms of the strength of the bonding in the glasses. The Si-O-Sn bonding is not thought to be as strong as the Si-O-Si bonding but the v-$(SnO)_x(SiO_2)_{1-x}$ network is supported by cross linking via the three co-ordinated oxygen. Then replacing SnO with R_2O reduces this cross linking to form a more flexible modified tin silicate network.

Sears et al. also plot the rate of change of TCE with composition against the cation polarising power, see figure 7.6. The rate of change of TCE decreases with ionic radius (increasing Z/r) for both v-$(R_2O)_x(SiO_2)_{1-x}$ and v-$(R_2O)_x(SnO)_{1-x}(SiO_2)$. However, there is a displacement between the two general compositions and the Sn^{2+} lies amongst the ternary glasses. This contradicts the behaviour inferred from the molar volume data, see figure 7.4. The decrease of $d\alpha/dc$ with modifier ionic potential is interpreted as indicating a greater covalence of the R-O bond as the polarising power increases. The similarity of the point calculated for Sn^{2+} and the ternary glasses is interpreted as Sn^{2+} not being a simple ionic species with regard to its bonding to the network.

Differential thermal analysis studies of modified [9] and binary [11] tin silicate glasses indicate changes in T_g with composition. T_g is reported at a lower temperature in each $(R_2O)_x(SnO)_{1-x}(SiO_2)$ glass and at a higher temperature in each $(RO)_x(SnO)_{1-x}(SiO_2)$ glass than in its corresponding binary tin silicate glass. In all cases the data lie on lines which extrapolate to the values for v-SnO-SiO_2, v-R_2O-SiO_2 or v-RO-SiO_2, see figure 7.7. This suggests that the network reorganisation is controlled by the mobility of the R^+ or R^{2+}.

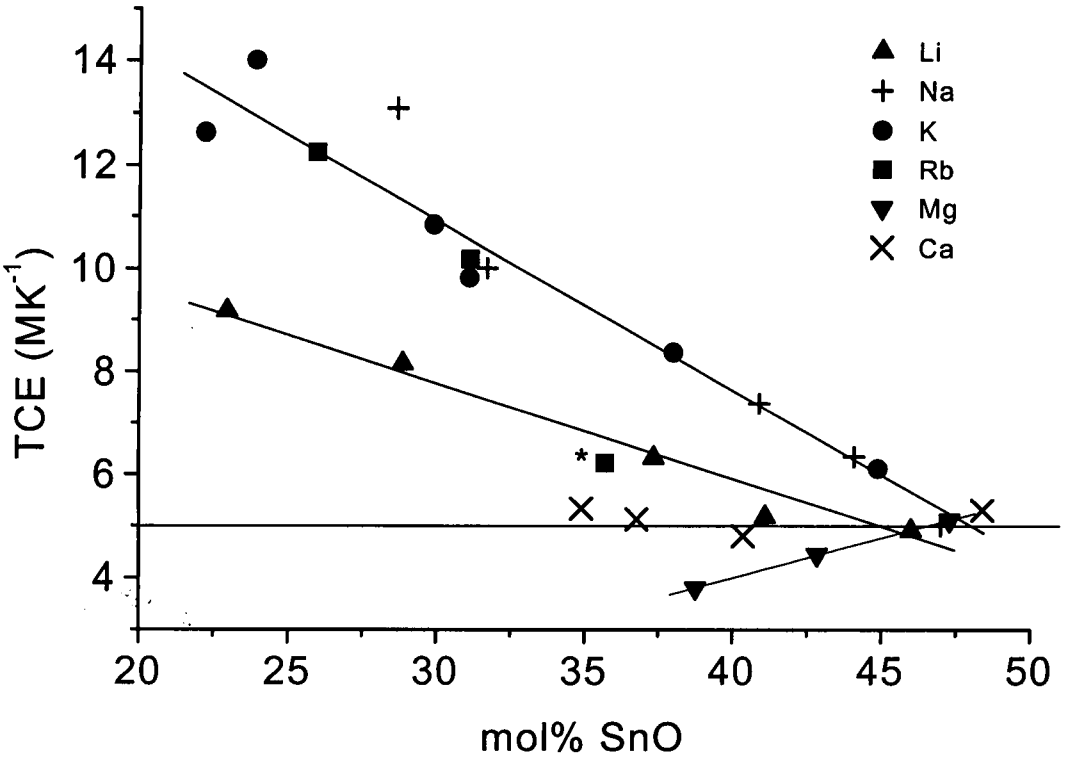

Figure 7.5 Changes in thermal expansion coefficient (TCE) when SnO is replaced by R_2O (RO) in $(R_2O)_x(SnO)_{1-x}(SiO_2)$ glasses. Errors in TCE are typically ±0.25MK^{-1}, after Sears [9].

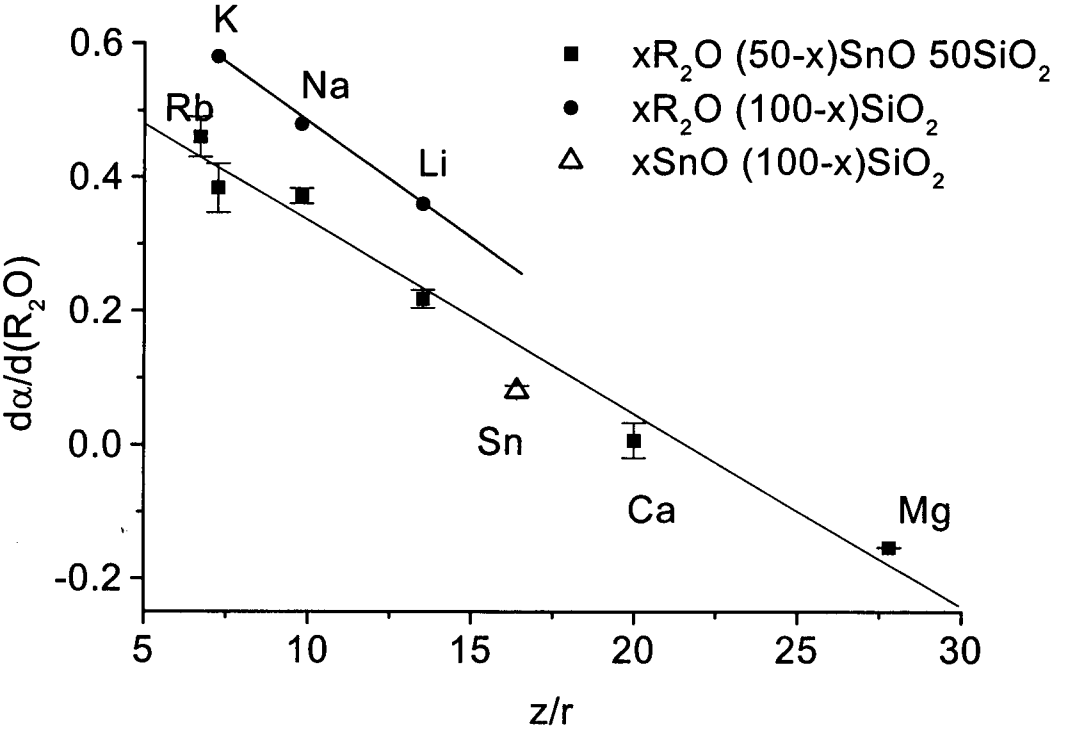

Figure 7.6 The rate of change of thermal expansion coefficient α with modifier (R_2O or RO) content plotted against ionic potential Z/r., after Sears [9].

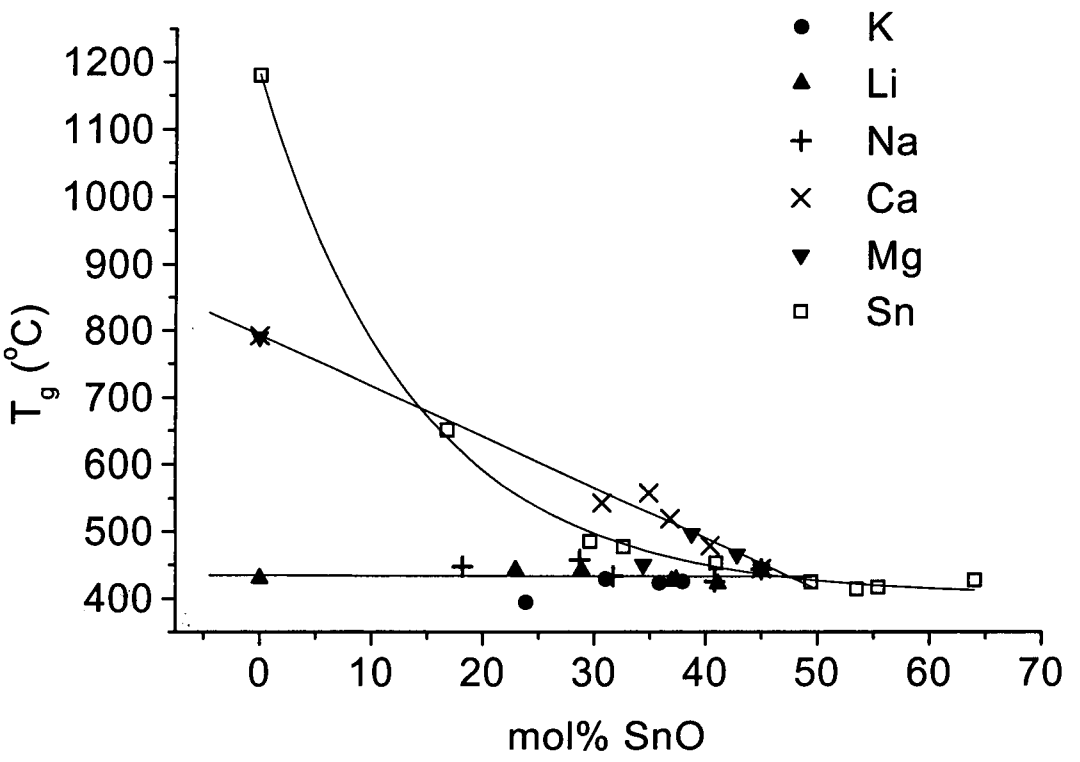

Figure 7.7 Glass transition temperature T_g plotted against SnO content in $(SnO)_x(SiO_2)_{1-x}$ and $(R_2O)_x(SnO)_{1-x}(SiO_2)$ glasses. The points at 0 mol% SnO represent pure SiO_2, 50:50 alkali metal or alkaline earth silicates, after Sears [9].

This chapter describes a study of $(K_2O)_x(SnO)_{1-x}(SiO_2)$, $(Na_2O)_x(SnO)_{1-x}(SiO_2)$ and $(Li_2O)_x(SnO)_{1-x}(SiO_2)$ glasses in which the modifier replaces tin whilst the silica content remains constant at ~50mol.%. The purpose of this study is to use neutron diffraction and ^{29}Si MAS NMR to probe the local environment about the tin and silicon atoms. This data can be combined with the information obtained using other experimental techniques, as outlined above, to propose a possible model of the glass structure.

7.2 EXPERIMENTAL DETAILS

7.2.1 SAMPLE PREPARATION

The potassium tin silicate glasses were prepared by Sears [2], the sodium tin silicate glasses by Fellows [12] and the lithium tin silicate glasses by Cao [21] by the same method used to prepare the binary $(SnO)_x$ $(SiO_2)_{1-x}$ glasses, see chapter 6. The modifier content was added to replace the tin, to prepare glasses of the nominal composition $(K_2O)_x(SnO)_{1-x}(SiO_2)$, $(Na_2O)_x(SnO)_{1-x}(SiO_2)$ and $(Li_2O)_x(SnO)_{1-x}(SiO_2)$. Wacomsil quartz, stannous oxalate, sodium (or potassium) carbonate and 0.1mol% Fe_2O_3 were mixed, pressed into pellets and heated in covered, silica crucibles at 1000~1200°C for 48 minutes [2]. The glass used for the subsequent studies was selected from the central region of each melt. The glasses were coloured, so it was possible to separate the glass from the crucible, unreacted reagents, SnO_2 and metallic Sn visually.

7.2.2 SAMPLE COMPOSITION

The composition of each lithium and potassium tin silicate glass was analysed by the Pilkington Analytical Division, Ormskirk [2]. The tin and potassium contents were determined by X-ray fluorescence (XRF) and the silica content was deduced by difference. The Sn^{2+}/Sn^{4+} ratio in each glass was determined by wet chemistry.

The composition of the series of sodium tin silicate glasses prepared by Mark Fellows [12] was studied using SEM-EDX. Sodium tin silicate glasses of 'known' composition were used as 'standards' with which to compare EDX data. These 'standards' were prepared by Adam Sears [2] and their composition analysed (like the lithium and potassium tin silicate glasses) by Pilkington Analytical Division.

A small piece (~0.1cm^3) of each glass (sample and 'standard') was mounted in conducting bakelite, polished to a flat surface and coated with a thin film of carbon. EDX measurements were made under identical conditions using Oxford Instruments software [13] on a JEOL6100, see section 4.2 for details. The raw Xray intensity (pre-ZAF corrections) of each atom species was measured for a period of 100 seconds and repeated on three different areas of the sample surface. The results reported below are the average of these measurements.

7.2.3 NEUTRON DIFFRACTION

TOF neutron diffraction measurements were made for three potassium tin silicate glasses on the LAD at RAL. Solid fragment of glass were loaded into 8mm diameter cylindrical, vanadium cans. These were mounted on the mechanical sample changer and data was collected in 500μAhr increments for a total acquisition time of 2000μAhrs for each sample. Data was also recorded for an empty can, a vanadium rod and the empty spectrometer.

7.2.4 ^{29}Si MAS NMR

^{29}Si MAS NMR spectra were recorded for four lithium tin silicate, nine sodium tin silicate and six potassium tin silicate glasses using a 1-pulse sequence with a 10 second delay between 2 μs ($< \pi/2$) pulses. The lithium tin silicate spectra were acquired by Cao [21]. The sodium tin silicate spectra were acquired in collaboration with Fellows [12]. Each spectrum was acquired for ~2hrs, spinning at 6kHz in a 4mm rotor. 100Hz line broadening was applied to each FID.

7.3 RESULTS AND DISCUSSION

7.3.1 RESULTS AND DISCUSSION OF THE SAMPLE COMPOSITION

The composition of each lithium tin silicate and potassium tin silicate glass, as analysed by Pilkngton Analytical, are summarised in table 7.1. The quoted experimental uncertainty (±1.6mol.%) is considered optimistic in the light of the EDX data presented and discussed below.

	% Li_2O/K_2O	% SnO	% SnO_2	% SiO_2
litinsil5	4.20	41.10	-	54.58
litinsil10	8.58	37.35	-	54.02
litinsil15	16.68	28.86	-	54.35
litinsil20	20.84	22.95	-	54.58
pottinsil0	-	46.94	-	52.94
pottinsil06	0.6	44.85	-	54.43
pottinsil5	4.99	35.85	1.0	58.03
pottinsil10	9.69	31.06	1.3	57.82
pottinsil15	15.47	29.91	-	54.51
pottinsil20	19.89	23.89	0.3	55.88

Table 7.1 The composition of the lithium tin silicate and potassium tin silicate glasses, after Sears [2].

A typical EDX spectrum for sodtinsil15 is shown in figure 7.8. The Brehmstraulung background radiation was removed using a top hat function digital filter [13]. The total number of X-rays for the series of lines for each atom species were recorded without making any ZAF corrections. These results are presented in figures 7.9, 7.10 and 7.11. The y-axis error bars shown in these figures are calculated from an average of three measurements made on different areas of each glass and indicate the homogeneity of the glass.

The raw X-ray intensities for each sample were used for comparison with those for known sodium tin silicate glasses because the quantitative Oxford Instruments software [13] uses elemental tin, sodium and silicon to make the ZAF corrections and calculate the composition. These internal standards neglect the matrix effects of the glass structure.

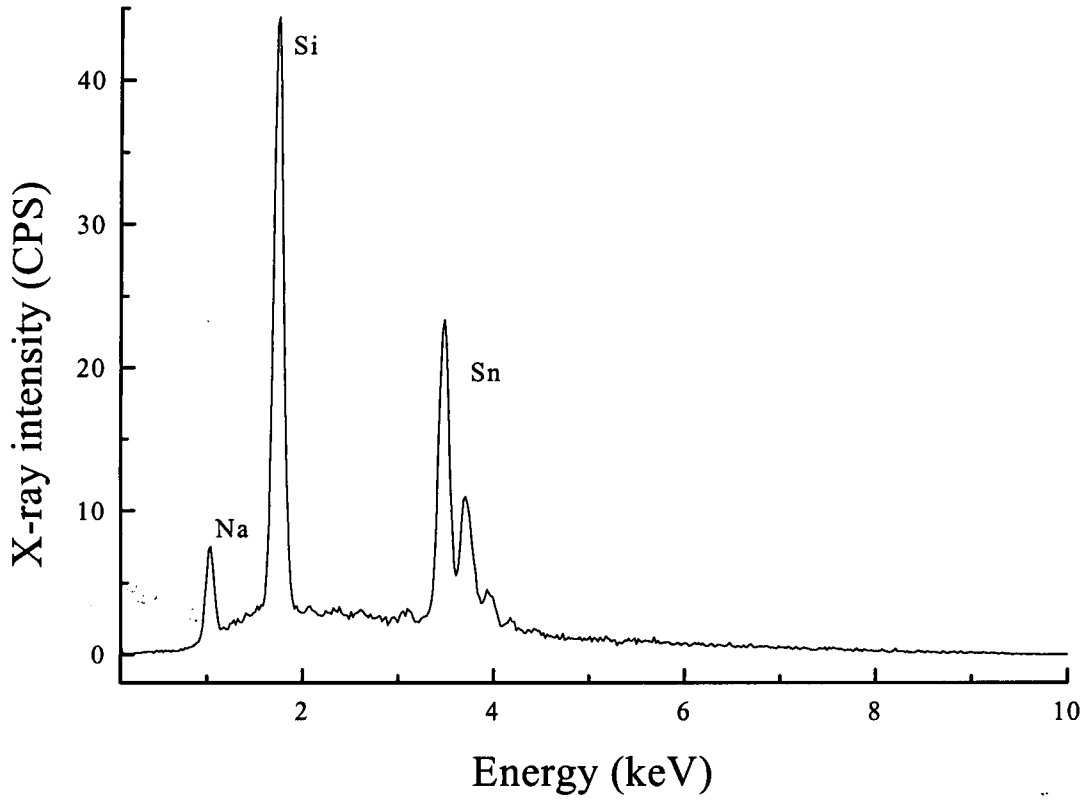

Figure 7.8 Typical EDX spectrum for pottinsil15.

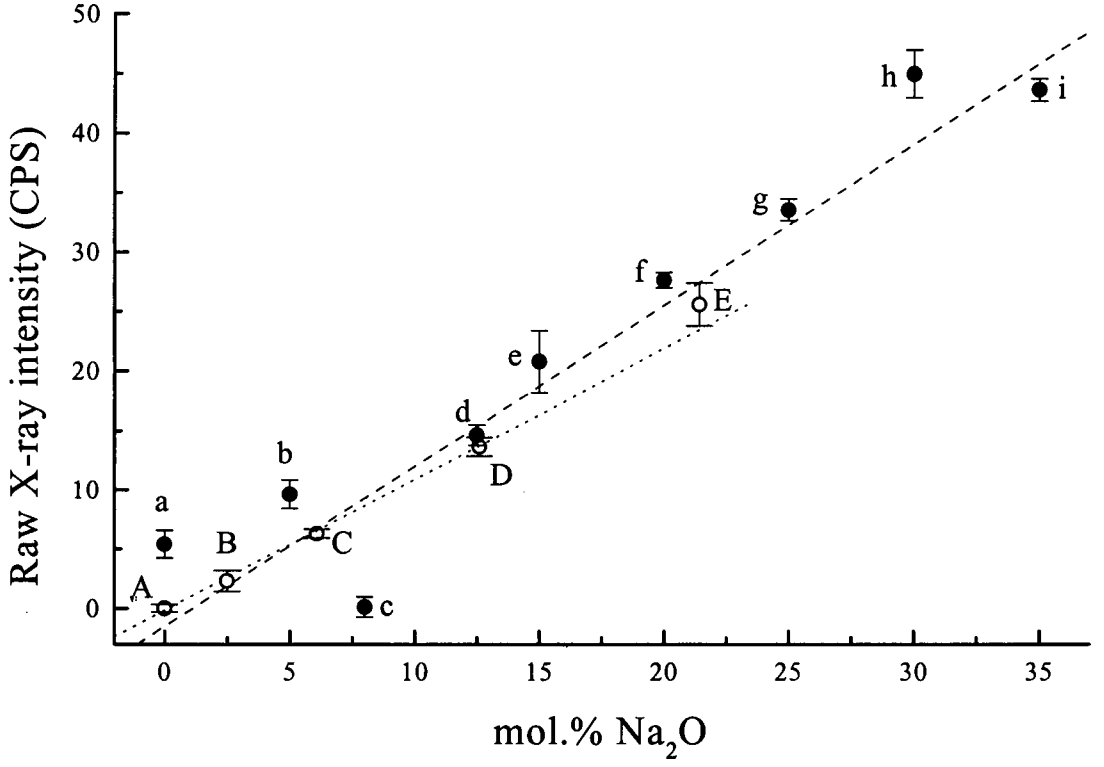

Figure 7.9 Raw Na-K_α Xray intensity vs mol% Na_2O for sodium tin silicate standards (circles) and samples (squares).

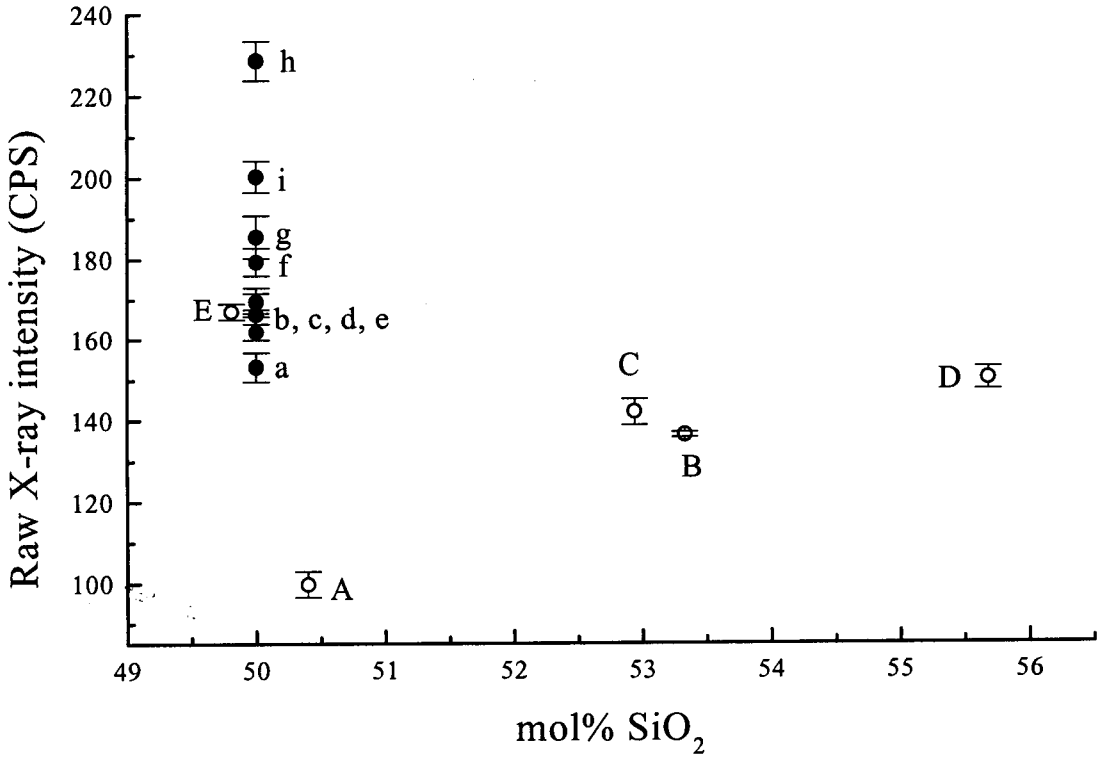

Figure 7.10 Raw Si-K_α Xray intensity vs mol% SiO_2 for sodium tin silicate standards (circles) and samples (squares).

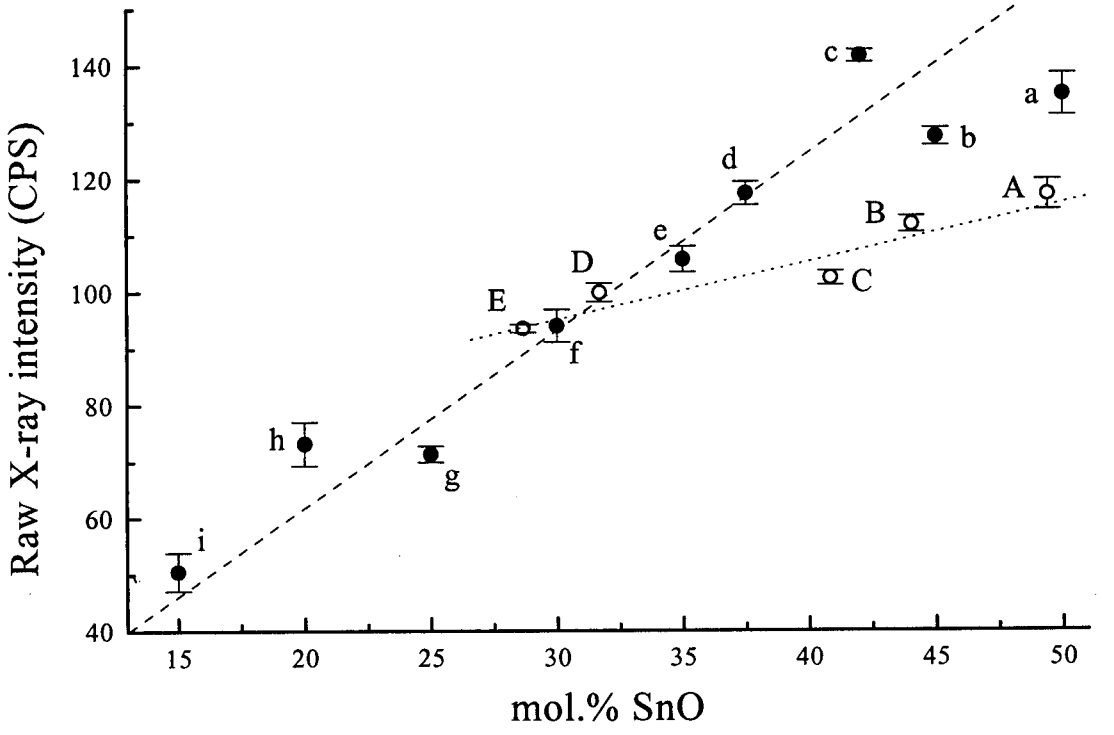

Figure 7.11 Raw Sn-L_α Xray intensity vs mol% SnO for sodium tin silicate standards (circles) and samples (squares).

Figures 7.9, 7.10 and 7.11 compare the raw sodium, tin and silicon X-ray intensities for sodium tin silicate glasses of known and unknown composition. The Na-K_α intensity increases at the same rate with sodium content for both sample and 'standard' measurements. However, there is an offset between the two series of results as all the sample measurements (including the sodium-free binary tin silicate sample) are larger than their corresponding 'standard' measurements. It could be argued that the 'standard' glasses are older, may have absorbed more atmospheric moisture and hence have a different matrix, which is slightly sodium deficient, at the surface. But this does not account for the offset at 0mol% Na_2O, so this approach is not taken any further.

The sample and 'standard' glass Sn-L_α X-ray intensities increase at a different rate with tin content. There is reasonable agreement between sample f and 'standard' E, which have similar reported compositions, see tables 7.2 and 7.3. However, there are no low tin content 'standards' and at high tin contents the sample intensities are larger than the 'standard' intensities. It should be noted that the high tin content glasses are the same samples for which the Na-K_α intensity was higher than in the 'standard' glasses of similar composition.

The high tin content glasses (samples a, b, d and e) Si-K_α intensities are in reasonable agreement with that for standard E. However the low tin content glasses (samples f, g, h and i) have larger Si-K_α intensities whilst the high tin content standards (B, C and D) have lesser Si-K_α intensities. This could be interpreted as the increasing absorption of the Si-K_α X-rays as a result of an increasing tin content. However, there are no high sodium (low tin) content 'standards' to confirm this supposition.

If this supposition is qualitatively correct then the sample i Si-K_α intensity should be greater than that for sample h. Sample i nominally contains less tin than sample h, see table 7.2. However the sample h Si-K_α intensity is greater than that for sample i. This is thought to indicate the uncertainty in the measured intensity, whilst the error bars in figures 7.9, 7.10 and 7.11 indicate the repeatability of each measurement.

The data corresponding to sodtinsil8 do not correspond to the trends outlined above and on repeating the measurement at a later date needles of silicon were found to have crystallised on the sample surface. On both occasions the Si-K_α and Na-K_α

intensities were found to be significantly less and the Sn-L_α intensity was found to be larger than in other samples of similar nominal composition. This would imply that cation migration and crystallisation had occured on both occasions, possibly due to the absorption of atmospheric moisture during the SEM-EDX sample preparation. This highlights a significant problem with SEM-EDX analysis of reactive samples since a flat, polished surface is necessary to make quantitative measurements.

The discrepancies between sample and standard glass X-ray intensities, as outlined above, for the low sodium (high tin) content glasses cannot relate to both the sodium and tin contents being larger in the samples than their nominal contents whilst the silicon content remains at ~50mol.%. This does not correspond to the problems associated with preparing these samples, as outlined in section 6.2, which would suggest that tin and sodium are more likely to be lost during the melt process than silicon.

The sample composition cannot be deduced from this data due to the limited number of 'standards' available and the large deviation in either X-ray intensity and/or composition that is required to ensure that the total molar fraction is 1. The expected sample compositions, predicting tin loss, and the 'standard' glass compositions are summarised in tables 7.2 and 7.3 respectively.

The SEM-EDX analysis detailed above also questions the reliability of the compositional analysis of the 'standards'. The ISIS software quantitative analysis (using the elemental internal standards) calculated the composition of the 'standard' sodium tin silicate glasses with a variance of ±5mol.% relative that reported by Sears [2]. This may largely be due to use of internal standards which do not account for the matrix effects of the glass structure. However, the internal standards used in the Pilkington analysis are similarly not likely to incorporate the matrix effects of the glass structure. The Pilkington Analytical Division used XRF to determine the sodium and tin content of these glasses and deduced the silicon content by difference. The XRF technique, outlined in section 4.3, is capable of measuring the fluorescent X-ray intensity of all three cations. It is thought that the deduction of the silicon content by difference is a deliberate manipulation to avoid the problem of scaling the proportion of each species so that the sum of the atomic fractions is 1. This questions the validity of the sample compositions as reported by Sears [2] and introduces uncertainty in comparing experimental results between glass systems.

		% Na_2O	% SnO	% SiO_2
a	sodtinsil0	-	50	50
b	sodtinsil5	5	45	50
c	sodtinsil8	8	42	50
d	sodtinsil125	12.5	37.5	50
e	sodtinsil15	15	35	50
f	sodtinsil20	20	30	50
g	sodtinsil25	25	25	50
h	sodtinsil30	30	20	50
i	sodtinsil35	35	15	50

Table 7.2 The estimated composition of the sodium tin silicate glasses.

		% Na_2O	% SnO	% SiO_2	% Fe_2O_3
A	TS7*	-	49.4	50.4	0.2 (Al_2O_3)
B	AJS26	2.5	44.05	53.33	≤0.12
C	AJS25	6.09	40.85	52.94	≤0.12
D	AJS8	12.60	31.69	55.68	0.03
E	AJS32	21.43	28.66	49.81	0.10

*Table 7.3 The composition of the 'standard' sodium tin silicate glasses used for EDX analysis, after Sears [2] and * Karim [11].*

7.3.2 RESULTS AND DISCUSSION OF NEUTRON DIFFRACTION DATA

The data were corrected using the ATLAS suite software, as outlined in chapter 2. The Plazcek calculations (assuming an ideal gas) were not sufficient to correct for proton contamination. The inelastic scattering was removed by fitting and subtracting a straight line to the high Q data from each detector bank ($20 \leq \theta \leq 150°$). It was not possible to accurately fit the low angle (5 and 10°) detector banks with a straight line, so this data was translated to agree with the higher angle detectors between 1.66 and 6.90$Å^{-1}$. The Q-ranges over which the data from different detectors could be combined were restricted to maintain good agreement between detector banks. The absorption and multiple scattering corrections were calculated using each sample composition and an additional water content. The water content of each glass, at the time of the neutron experiment, was estimated by adding a fraction of the H_2O cross section (available in the FORTRAN library at RAL as g_f:h2o.mut) to the theoretical cross section such that it agreed with the experimental transmission cross-section for each sample, see figure 7.12. The water content, see table 7.4, increased with alkali content.

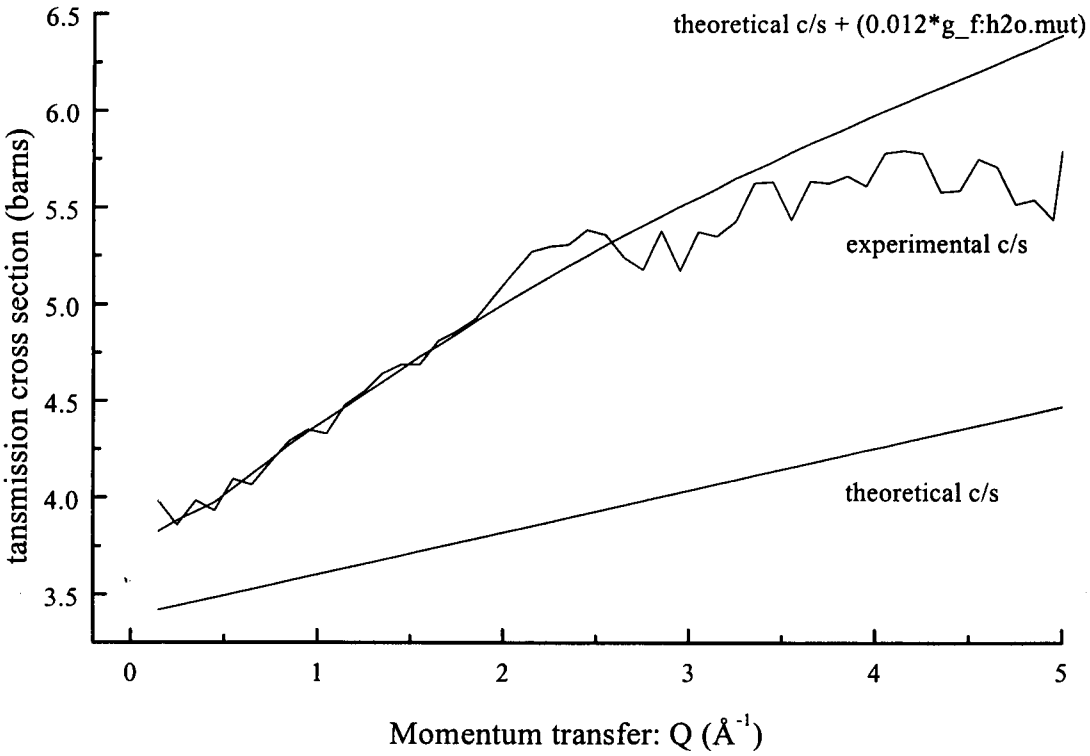

Figure 7.12 The experimental transmission cross section for pottinsil20, and its theoretical transmission cross section with and without adding 0.012 g_f:h2o.mut.

sample	pottinsil5	pottinsil10	pottinsil20
additional mol.% H_2O	0.5	0.75	1.2

Table 7.4 Additional mol.% H_2O contamination in potassium tin silicate glasses.

This approach was suitable for processing this data because the water content in these glasses was small. The differential correlation function, D(r), oscillated about $T^0(r)$, see equations 2.10 and 2.11. A similar approach has been reported by Rigden et al., who fitted and subtracted a Chebyshev polynomial to i(Q) to correct for a large proton content (~50atom%) in several TiO_2:SiO_2 mixed sol-gel glasses [14].

The increase in proton contamination with potassium content suggests that the potassium depolymerises the tin silicate network. Modified silicates are more susceptible to contamination by protons than non-modified silicates [10].

Several, very small Bragg peaks are evident in i(Q) for each of the potassium tin silicate glasses, see figure 7.13. The area associated with these Bragg peaks amounts to less than 2% of the scattering function. This crystallisation is thought to have occurred upon cooling as a result of variation in the quench rate due to uncertainties in the sample preparation [2]. The estimated volume fraction of crystallites is sufficiently small to consider the samples as amorphous. No evidence of crystallinity was found in either the ^{29}Si MAS NMR or T(r) data.

The detail in the scattering at low Q changes on replacing tin with potassium, see figure 7.13. The FSDP in pottinsil20 is sharp, like that in TS10 (see figure 6.5), whilst in pottinsil5 it is less defined, similar to that in TS7 (again, see figure 6.5). The FSDP shifts to lower Q on replacing tin with potassium, see table 7.5. This indicates an increase in the periodic length ($2\pi/Q$) [15] of the intermediate order, as reported for increasing tin content in ν-SnO-SiO_2, see table 6.5. It should be noted that the total (tin + potassium) content in these glasses remains constant (~50mol.%). This additional change in detail at low Q indicates that potassium has a greater effect on the intermediate order than tin.

	pottinsil5	pottinsil10	pottinsil20
Q-FSDP ($Å^{-1}$)	1.3 (1)	1.26 (2)	1.16 (1)
r-intermediate order (Å)	4.4 (3)	4.49 (7)	4.87 (4)

Table 7.5 The position of the FSDP in i(Q) for each potassium tin silicate. The experimental uncertainty is indicated in parenthesis.

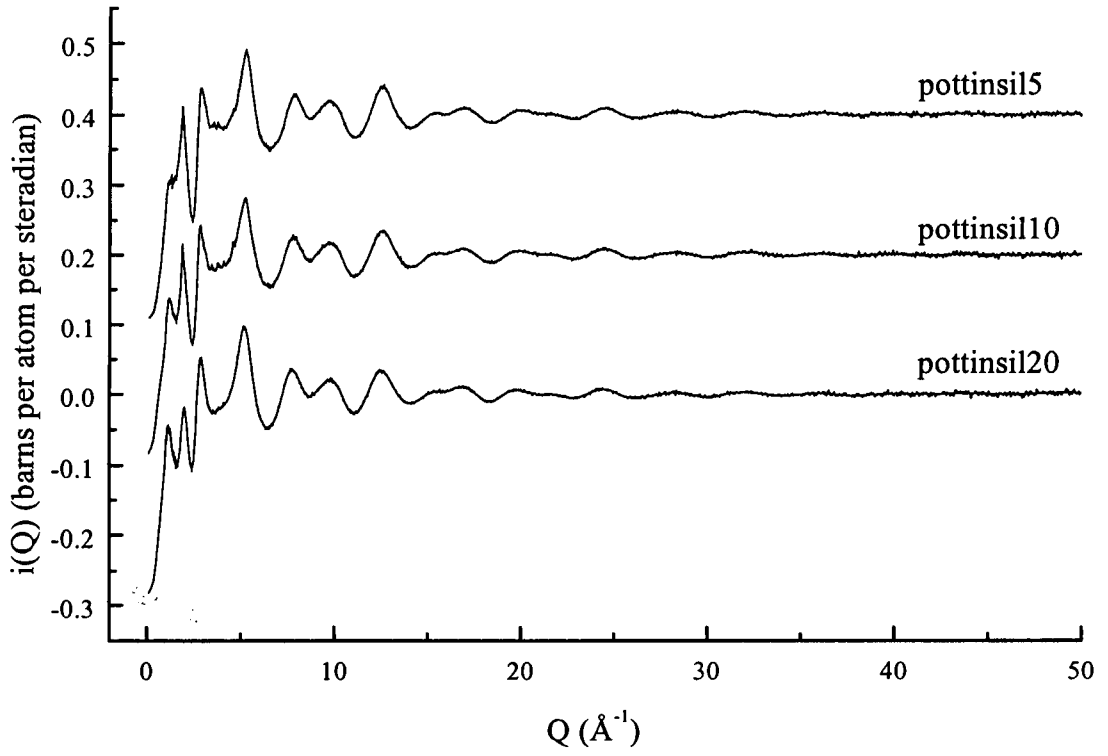

Figure 7.13 i(Q) for three potassium tin silicate glasses.

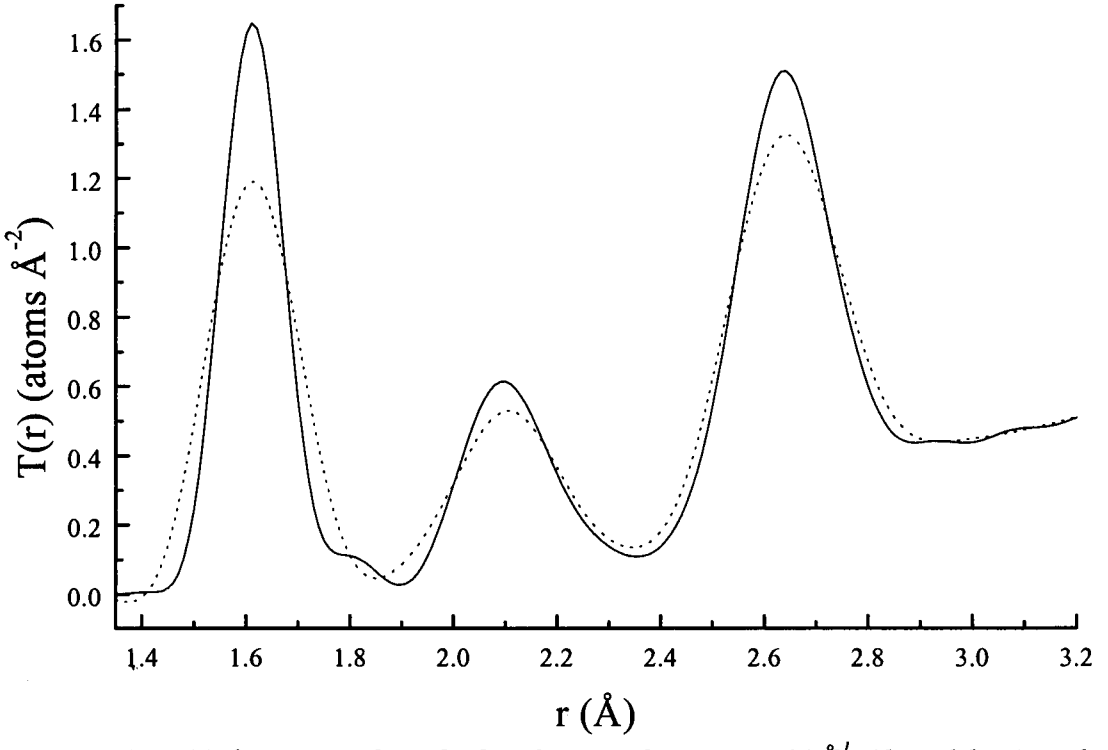

Figure 7.14 T(r) for pottinsil5 calculated using data up to 30Å^{-1} (dotted line) and 50Å^{-1} (solid line).

T(r) was calculated for pottinsil5 using data up to 30, 35, 40, 45 and 50Å^{-1}, see figure 7.14. The peak at 1.6Å narrowed with increasing Q-space resolution but revealed a systematic peak at 1.78Å, as outlined in chapter 6.

Several two peak fits were performed on T(r) for pottinsil20 between 1.44 and 1.88Å. The positions of each peak were held constant so that the fit reflected the Si-O correlation (at 1.61Å) and the systematic peak (at 1.78Å). Truncating i(Q) ≤ 30Å^{-1} included the systematic peak into the broadened Si-O correlation.

With reference to accepted bond lengths, the interatomic distances and the measured change in peak area with composition, the peak at ~1.6 can be assigned as Si-$O_{4/2}$, the peak at~2.1 as Sn-$O_{3/3}$ and the peak at ~2.6Å is thought to contain both the K-O and O-O correlations [16]. The data in the range 1.44 ≤ r ≤ 2.78Å were fitted by three peaks, each of which was described by the convolution of a Gaussian and P(r) as described in chapter 2. Figure 7.15 shows T(r) calculated using data up to 30Å^{-1}, the three peak fit and its residual for each potassium tin silicate glass. The fit parameters are summarised in table 7.6.

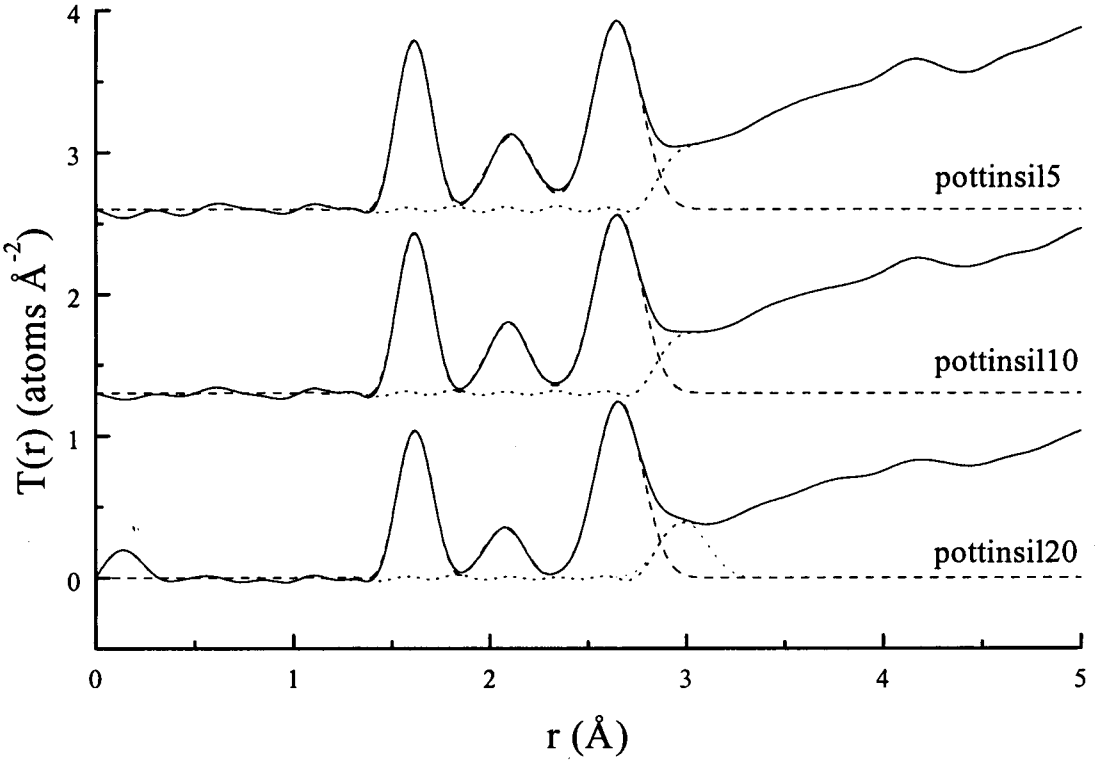

Figure 7.15 T(r) (solid line), a fit of the first three peaks in T(r) (dashed line) and the residual between the two (dotted line) for three potassium tin silicate glasses.

	Peak	$r_{ll'}$ (Å)	$\langle u_{ll'}^2 \rangle^{1/2}$ (Å)	Area
pottinsil5	Si-O	1.6152 (3)	0.0510 (6)	0.2516 (9)
	Sn-O	2.1106 (9)	0.095 (1)	0.148 (1)
	O-O	2.6462 (6)	0.1016 (7)	0.397 (2)
pottinsil10	Si-O	1.6168 (3)	0.0474 (6)	0.2351 (7)
	Sn-O	2.0928 (8)	0.078 (1)	0.1264 (9)
	O-O	2.6501 (4)	0.0984 (5)	0.3718 (9)
pottinsil20	Si-O	1.6206 (3)	0.0522 (1)	0.2210 (5)
	Sn-O	2.0739 (9)	0.071 (1)	0.0853 (8)
	O-O	2.6583 (5)	0.0998 (6)	0.370 (1)
	K-O	2.986 (3)	0.098 (3)	0.117 (3)

Table 7.6 Fit parameters (uncertainty of the fit in parenthesis) for the total correlation functions T(r) for each potassium tin silicate sample using data up to 30Å^{-1}.

The first three peaks in each T(r) are well resolved from each other and unlike the data presented for TS10 in chapter 6, the visual peak positions, see table 7.7, are in good agreement with the peak fit positions, see table 7.6.

	TS7	pottinsil5	pottinsil10	pottinsil20
r_{SiO}	1.621 (5)	1.615 (5)	1.617 (7)	1.621 (7)
r_{SnO}	2.123 (5)	2.11 (1)	2.09 (1)	2.07 (1)
r_{OO}	2.65 (1)	2.65 (1)	2.65 (1)	2.66 (1)
r_{KO}	-	-	-	2.98 (2)
r_{OO}/r_{SiO}	1.63 (1)	1.64 (1)	1.64 (1)	1.64 (1)

Table 7.7 Visual peak positions and the distance ratio r_{OO}/r_{SiO}. (estimated experimental uncertainty in parenthesis).

The errors reported in table 7.6 are the errors associated with each fit parameter and suggest a greater accuracy than can realistically be obtained from the data. The interatomic separations and r_{OO}/r_{SiO} distance ratio for each sample, with estimated associated uncertainties, are presented in table 7.7. The $SiO_{4/2}$ tetrahedra do not appear to be distorted on replacing tin with potassium. The distance ratio r_{OO}/r_{SiO} is slightly larger than that for an ideal tetrahedron (1.633) at all compositions.

Both the Si-O and O-O interatomic separations are larger in pottinsil20 than in the lower potassium content glasses. This is thought to be due to an increase in the depolymerisation of the network on replacing SnO with K_2O. A similar increase in the Si-O bond length with increasing alkali content has been reported for v-Na_2O-SiO_2 [17]. This was interpreted as being due to an increase in the bridging oxygen (BO) bond lengths on the addition of a non-bridging oxygen (NBO). An increase in Si-O peak width, corresponding to an increase in the distribution of correlations is not seen, see table 7.6. However, an increase in peak width with NBO content was not reported in v-Na_2O-SiO_2 either.

The increase in the O-O interatomic separation could correspond to the stretching of the $SiO_{4/2}$ described in the previous paragraph. Alternatively, this could be due to the inclusion of other high r correlations in the O-O peak. It should be noted that these changes in both the Si-O and O-O bond lengths are of the order the accuracy to which the distances can be measured.

The Sn-O interatomic separation and peak width decrease on replacing tin with potassium. The decrease in peak width is, on repeated fitting, of the order of the experimental uncertainty. The decrease in peak position is in excess of the experimental uncertainty.

The absolute interatomic distances reported here may not be correct, due to a TOF calibration problem on LAD. It is possible that this could be corrected by reprocessing the data using amended detector calibration parameters but this was not considered necessary as the offset is thought to be small and the data, as reported, is sufficiently accurate to obtain all the possible structural information. It is still considered accurate to compare the interatomic separations within the series of glasses measured on LAD. The possible error in interatomic separation was noticed by comparing the data presented in this study with the interatomic separations reported in lithium, sodium and rubidium tin silicate glasses, all of which were measured on GLAD at Argonne, USA. Figure 7.16 shows the Si-O interatomic separation for each series of alkali tin silicate glasses. The Sn-O and O-O interatomic separations in v-$(K_2O)_x(SnO)_{1-x}(SiO_2)$ are also slightly shorter than those reported for other alkali tin silicate glasses [1].

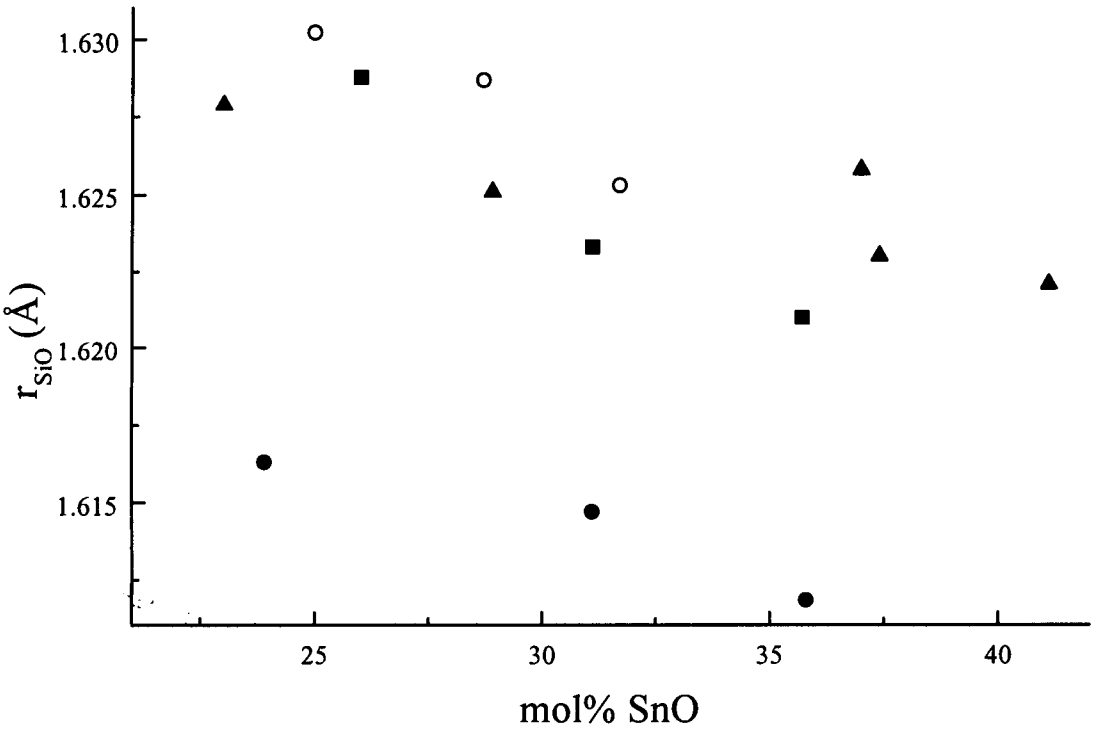

Figure 7.16 The Si-O bond lengths in ν-$(R_2O)_x(SnO)_{1-x}(SiO_2)$, where R is Li (triangle symbol), Na (hollow circle symbol), K (solid circle symbol) and Rb (square symbol).

	pottinsil5	pottinsil10	pottinsil20
N_{SiO} (atoms) (±0.3)	3.9	3.7	3.7
N_{SnO} (atoms) (±0.3)	3.1	3.1	2.8
N_{OO} (atoms) (±0.5)	5.2	5.0	5.2
N_{KO} (atoms) (±0.5)	-	-	5.8

Table 7.8 Co-ordination numbers $N_{ll'}$ calculated from the peak positions and areas in table 7.6 (uncertainty in parenthesis).

The uncertainty in the co-ordination numbers calculated from the peak position, area and $t_{ll'}(r)$ coefficient (see eq.2.19) is dominated by the uncertainty in composition, not bond lengths and areas. The Si-O co-ordination number (n_{SiO}) is just less than four, this is typical for $SiO_{4/2}$ units, see table 7.8.

The SnO co-ordination number (n_{SnO}) is about three for all potassium tin silicate glasses, as reported for ν-SnO-SiO_2 in the previous chapter. However, n_{SnO} is smaller in pottinsil20 than in the other potassium tin silicate glasses. This is coincident with a decrease in Sn-O interatomic separation on replacing SnO with K_2O, see table 7.7. This could be interpreted as a small proportion of the tin

becoming two co-ordinated on replacing tin with potassium. However, the width of the Sn-O peak also decreases with increasing potassium content. It is possible that the r_{SnO} distribution decreases on reducing the number of three co-ordinated tin (and oxygen) atoms, but it is thought that an increase in the number of sites would cause an increase in the peak width.

The O-O co-ordination number is calculated at about five for all the glasses. This is thought to include contributions from O-O correlation in and between the $SiO_{4/2}$ and $SnO_{3/3}$ polyhedra and the fit may include some of the K-O correlation.

$N_{II'}$ (atoms)	4	5	6	7	8
r_{KO} (Å)	2.64	2.73	2.79	2.85	2.90

Table 7.9 Bond valence calculations for several K-O interatomic separations.

A fourth peak has been fitted to the residual of the pottinsil20 T(r) data between $2.63 \leq r \leq 3.36$, see figure 7.15. A maximum in the residual at 2.98Å is only visible in the highest potassium content glass, pottinsil20. Pottinsil20 contains less tin than the other $(K_2O)_x(SnO)_{1-x}(SiO_2)$ glasses so this peak is thought to be due to K-O correlations rather than further O-O correlations between oxygen atoms within the $SnO_{3/3}$ polyhedra, as described in chapter 6. The peak fit width is slightly larger than that reported for Si-O and Sn-O, see table 7.6. This is considered reasonable by comparison with the width of the Na-O peak in v-Na_2O-SnO-SiO_2 [1]. The peak fit position and area correspond to a K-O co-ordination of 5.8±0.5, but the peak position does not correspond to the bond valence calculation for potassium co-ordinated to six oxygens, see table 7.9. This could highlight a problem in comparing the bond valence calculations [18] to the glass structure. Alternatively, the K-O fit may not be physically meaningful as the peak is not well resolved. T(r) contains several correlations at high r.

The K-O peak at 2.98Å increases with potassium content but is dominated by the O-O peak at 2.6Å and by next nearest neighbour interactions; Sn-Sn at 3.7Å [19] and Si-Si, at 3.2Å [20]. The K-O interatomic separation was not reported by Hannon et al. [16] as it was not resolvable from the O-O peak in v-$(K_2O)_{0.25}(SiO_2)_{0.75}$.

7.3.3 RESULTS AND DISCUSSION OF THE ^{29}Si MAS NMR DATA

All the ^{29}Si spectra contain a single, broad, featureless resonance which narrows and shifts downfield with increasing alkali content. The processed spectra for the potassium tin silicate glasses are shown in figure 7.17. The peak positions and Gaussian fit FWHM to all the spectra are summarised in table 7.10.

	^{29}Si δ (ppm) ± 0.5	^{29}Si fwhm (ppm) ± 1
litinsil5	-99	24
litinsil10	-95	23
litinsil15	-88	20
litinsil20	-86	18
sodtinsil0	-103.0	19
sodtinsil5	-96.4	18
sodtinsil8	-94.5	16
sodtinsil125	-91.0	17
sodtinsil15	-89.1	15
sodtinsil20	-87.0	14
sodtinsil25	-85.0	14
sodtinsil30	-84.8	14
sodtinsil35	-82.2	14
pottinsil0	-102.7	23
pottinsil06	-101.3	22
pottinsil5	-99.2	20
pottinsil10	-95.2	18
pottinsil15	-91.8	17
pottinsil20	-89.9	16

Table 7.10 Gaussian fit parameters to lithium tin silicate, sodium tin silicate and potassium tin silicate glass ^{29}Si MAS NMR spectra.

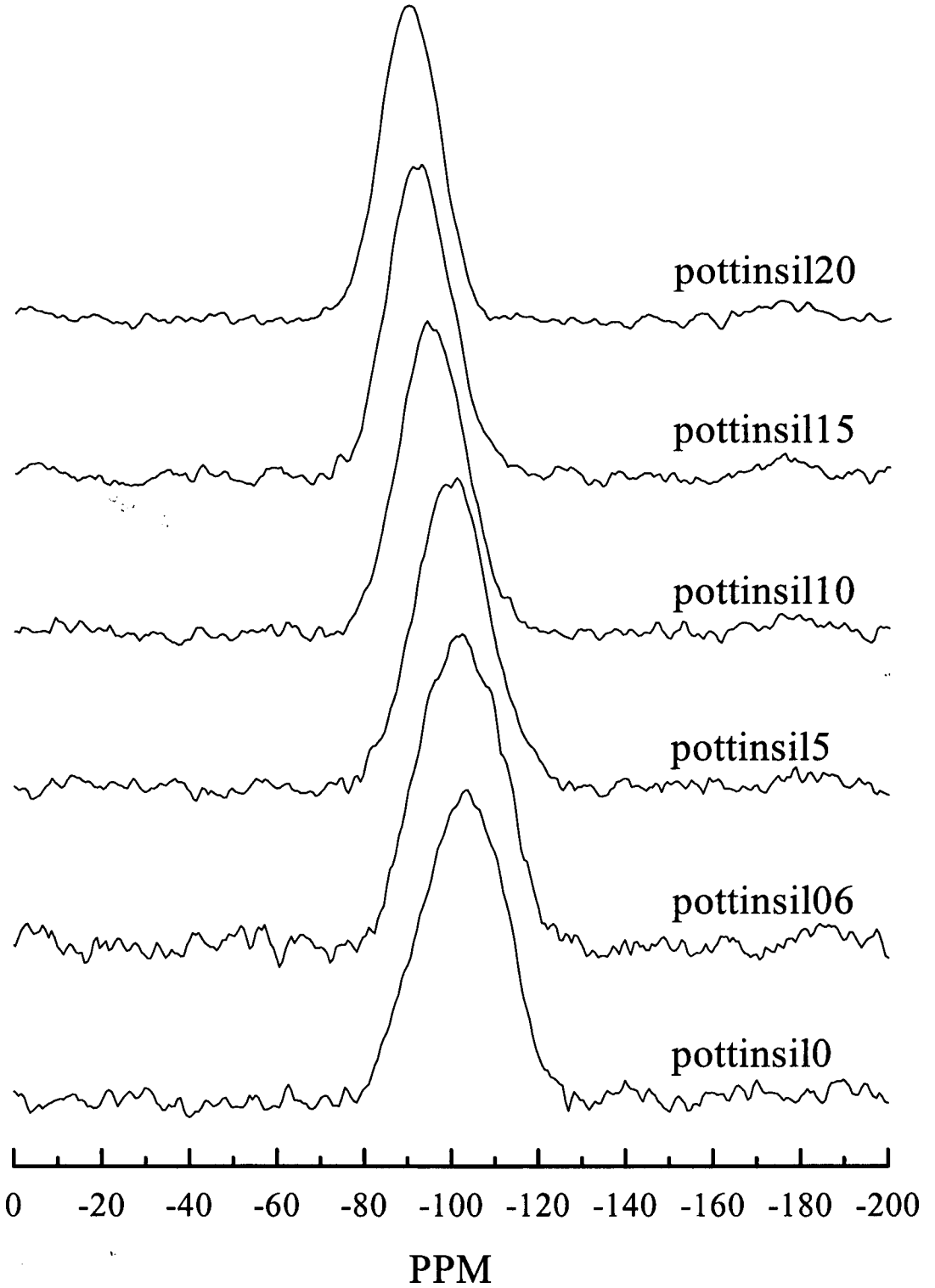

Figure 7.17 ^{29}Si MAS NMR spectra for potassium tin silicate glasses.

The single peak in each ^{29}Si MAS NMR spectrum is thought to contain contributions from several different silicon environments. However, without an accurate compositional analysis and knowledge of the role of each species then the number, type and weight of each contribution cannot be constrained to give a multiple Gaussian fit any physical significance. Each spectrum was fitted with a single Gaussian.

The ^{29}Si MAS NMR data reported here can be combined with data reported for a series of binary tin silicate glasses [11] and lithium tin silicate glasses [21]. Similar trends are observed in the data for each alkali tin silicate glass system whilst the v-SnO-SiO_2 data acts as a reference against which the effect of the alkali can be compared, see figures 7.18 and 7.19.

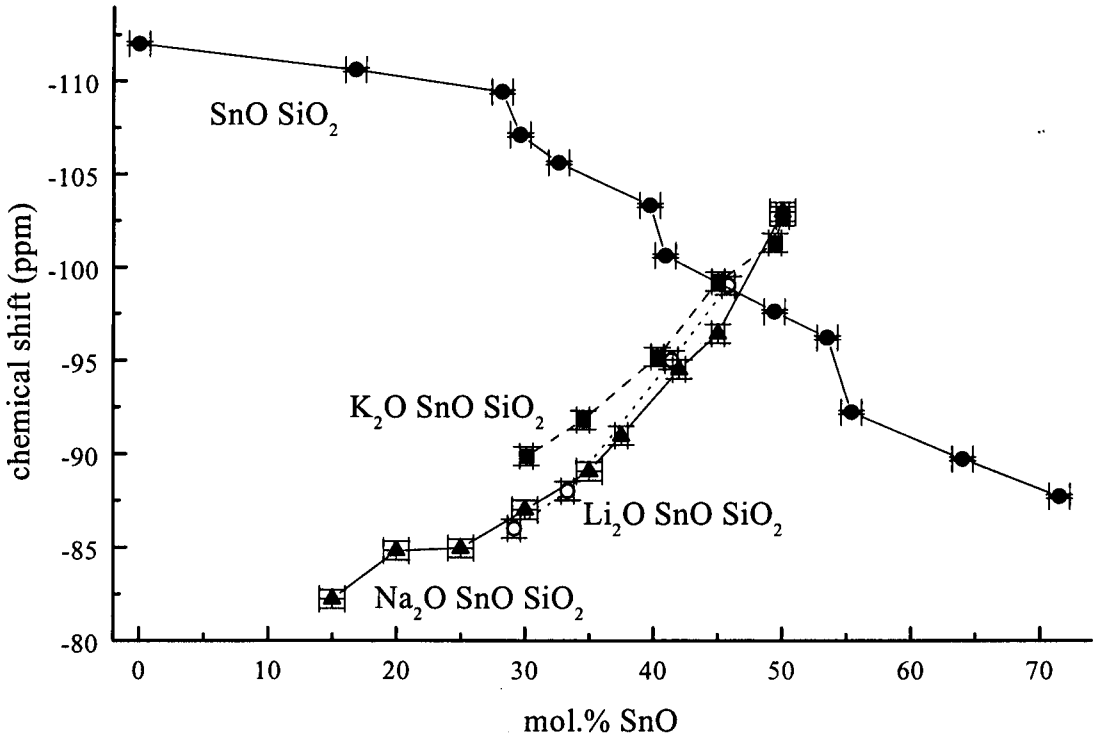

Figure 7.18 The ^{29}Si NMR chemical shift vs tin content for tin silicate glasses [11] (solid circles), potassium tin silicate glasses (squares), sodium tin silicate glasses (triangles) and lithium tin silicate glasses [21] (hollow circles).

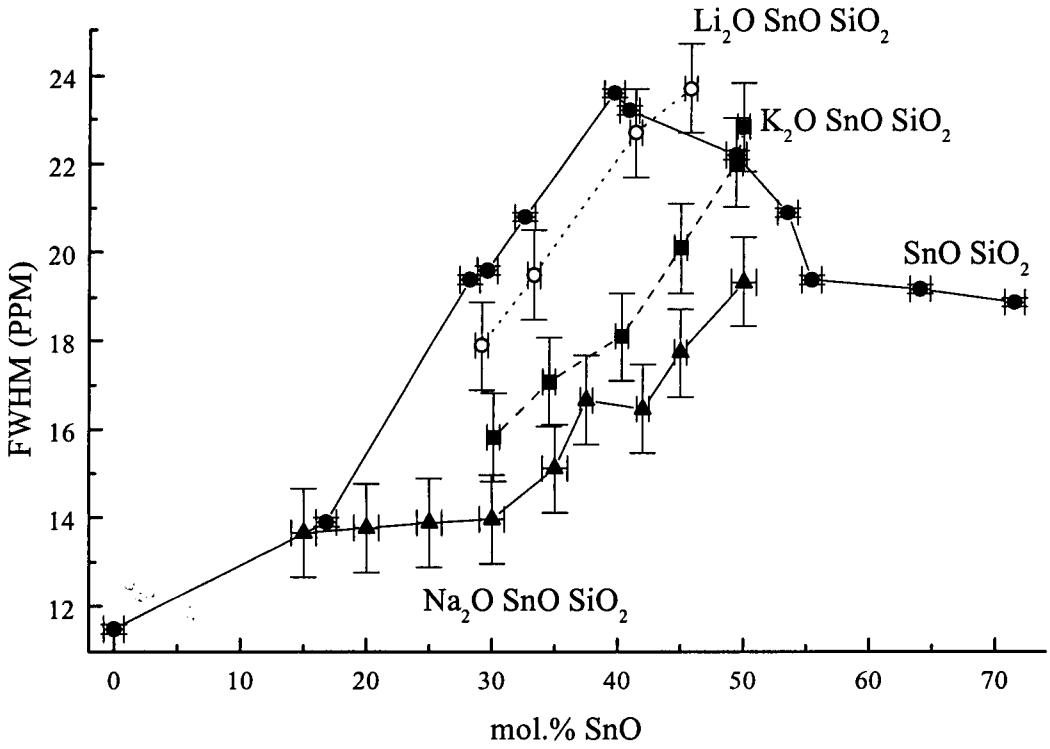

Figure 7.19 The FWHM of Gaussian fits to ^{29}Si NMR vs tin content for tin silicate glasses [11] (solid circles), potassium tin silicate glasses (squares), sodium tin silicate glasses (triangles) and lithium tin silicate glasses [21] (hollow circles).

The variation in isotropic chemical shift for sodtinsil0, pottinsil0 and TS7 (all of which contain ~50mol.% SiO_2) is thought to indicate the variation in sample composition. The isotropic ^{29}Si chemical shift suggests that sodtinsil0 and pottinsil0 contain a lower tin content than reported in table 7.1; approximately $(SnO)_4(SiO_2)_6$. However, this is not considered an accurate measure of sample composition as the SnO content of the binary tin silicate glasses was analysed by wet chemistry and the silicon by difference [11].

The chemical shift is a measure of the electronic shielding of the nucleus. On adding tin to the silicate network the silicon nuclei are increasingly deshielded (the shift becomes less negative). This rate of this deshielding with change in composition is not as dramatic as in alkali silicate glasses [22] but indicates that tin increases the ionicity of the bonding about the silicon. In alkali silicates these changes are described by an increase in the number of NBOs [23] but this terminology does not accurately describe the role of tin in these glasses. It is possible to prepare ν-$(SnO)_x(SiO_2)_{1-x}$ past the ortho-silicate composition and the tin

has a low co-ordination number, with a well defined local order. The Si-O-Sn bonding is more directional than that described by a NBO but is more ionic than Si-O-Si bonding.

The silicon nuclei are increasingly deshielded (the chemical shift becomes less negative) on replacing tin with an alkali oxide. This is interpreted as the alkali metal having a greater modifying effect than the tin.

The isotropic chemical shifts are similar, at a constant tin content, for each alkali oxide (Li_2O, Na_2O or K_2O). Such a similarity between alkali oxides had previously been reported for the average chemical shift in ν-R_2O-SiO_2, where R = Li, Na and K, [22].

The deshielding of the silicon nuclei in ν-SnO-SiO_2 is also accompanied by an increase in the peak fit FWHM up to tin contents of 40mol.%, above which composition the FWHM decreased. Karim [11] reported this change to represent a change in the nature of the distribution of Q^n-species, due to a change in the behaviour of the Sn^{2+}. The work reported in the previous chapter does not support a change in the behaviour of the Sn^{2+}, but this change in ^{29}Si NMR peak width can be interpreted in terms of static disorder of the network.

If ν-SnO-SiO_2 does contain Sn^{2+} pairs, as in figure 6.9, then at approximately the disilicate composition (33mol.% SnO) each silicon atom will have one Si-O-Sn bond. Beyond this composition each silicon will be involved in at least one Si-O-Sn bond. These linkages can be thought to make the network more flexible, have less static disorder and narrower resonances. On substituting tin with alkali oxide the network is disrupted further and the FWHM decreases further.

The FWHM decreases on substituting alkali for tin up to 20mol% alkali oxide, above which further substitution does not change the FWHM. This is only found in the sodium tin silicate glasses as high lithium and potassium content glasses were not studied.

7.6.4 GENERAL DISCUSSION AND PROPOSED STRUCTURAL MODEL

Sears et al. [9] proposed an average structural model for ν-R_2O-SnO-SiO_2 in which the tin is three co-ordinated, the silicon four co-ordinated and the alkali associates with and charge compensates the tin, see figure 7.20. The values for n_{SiO} and n_{SnO} were taken from this work and the role of the alkali was largely based on the interpretation of the increase in TCE and the decrease in T_g. Both these trends can be considered as a removal of the three co-ordinated oxygen (which crosslinks the network) by the alkali.

This proposed model of the glass structure is further supported by considering how the glass structure forms from the melt. As the melt cools the local structural units form and the positively charged alkali ions associate with the $(SnO_{3/3})^-$ groups, due to their electrostatic attraction. In the absence of an alkali cation; a three co-ordinated oxygen atom is required to charge balance each $(SnO_{3/3})^-$ group, as described in the previous chapter for binary $(SnO)_x(SiO_2)_{1-x}$ glasses.

The decrease in Sn-O interatomic separation, see table 7.7, with increasing potassium content, may also support the proposal that the alkali ion associates with the tin. The Sn-O bond length is dependent upon the strength of attraction between the tin and oxygen, their steric hindrance and that of the atoms about them. The open chain structure has more flexibility for the tin atoms to rotate and allow the oxygen atoms to get closer. The proximity of the potassium may also change the hybridisation of the non-bonding pair of electrons, which by their size and directionality affect the bond length.

The ^{29}Si NMR data for ν-Na_2O-SnO-SiO_2 may also be interpreted to support this model in which the alkali associates with the tin rather than depolymerising Si-O-Si bonds. The peaks shift downfield on replacing tin with alkali and the peak fit FWHM decreases until 20mol.% Na_2O. At alkali contents in excess of 20mol.% the FWHM remains approximately constant. This narrowing is interpreted as an increase in the ionic character of the network and a subsequent decrease in the static disorder. Then in glasses containing ≥25mol.% Na_2O the excess sodium depolymerises Si-O-Si bonds and does not influence the tin so strongly.

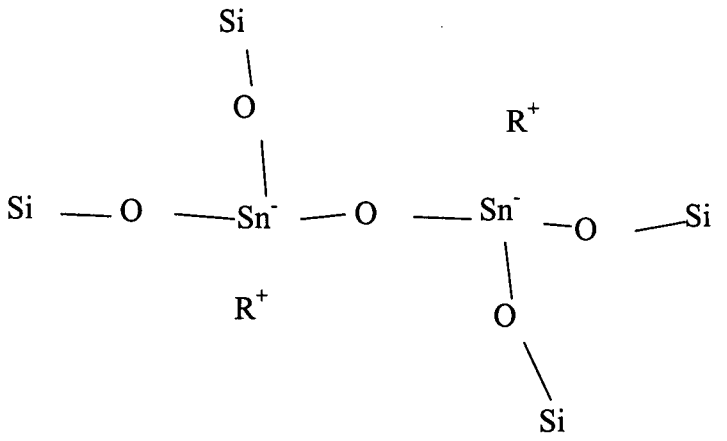

Figure 7.20 Proposed structure of R_2O-SnO-SiO_2 glass structure, after Sears [9].

The proposed structure in figure 7.20 is thought to be the most likely model of the average glass structure, considering the experimental data available. However, some of the experimental data could support alternative interpretations.

The decrease in Sn-O bond length could correspond to a decrease in n_{SnO}. This would remove the electrostatic attraction between the tin and alkali ions so the potassium could then depolymerise the silicate network even at low alkali contents.

It is also curious to note that the ^{29}Si MAS NMR chemical shift linearly tends to the alkali silicate value. This suggests that both Sn^{2+} and R^+ are modifying the silicate network, rather than clustering in K^+-$(SnO_{3/3})^-$ pairs.

7.4 CONCLUSIONS AND FUTURE WORK

The composition of the glasses used in this study can only be estimated from the trends observed in a previous study of v-$(SnO)_x(SiO_2)_{1-x}$ [11]. Quantitative XRF and SEM-EDX analysis both require reference materials for which the composition is known and in which the ZAF effects on the X-rays is similar to that in the samples studied. Suitable reference materials were not available for this SEM-EDX study and the XRF analysis by Pilkington [2]. This is considered to be a significant problem for the compositional analysis of glasses. The preparation of glasses within a sealed ampoule should be considered, to prevent the loss of volatile species from the melt, in future studies.

The SEM-EDX analysis also requires a flat surface to be quantitative. At least one of the ν-$(Na_2O)_{1-x}(SnO)_x(SiO_2)$ samples reacted with atmospheric moisture during the preparation of the flat surface.

Small quantities of proton contamination in each sample were quantified using the neutron diffraction transmission cross section. The additional inelastic scattering from the protons was removed during the data correction of the diffraction data, but the proton content is not considered to influence the average glass structure.

The scattering at $\leq 2Å^{-1}$ in pottinsil20 is similar to that in TS2. This is considered to indicate that the network is similar to that in a high silica content tin silicate glass, ie. that the potassium associates with the tin.

The total correlation function calculated using data up to $50Å^{-1}$ includes an offset to high r for some of the Si-O correlation. This is thought to be due to a systematic error in the calibration of the high angle detectors on LAD. The data presented in this study are truncated at $30Å^{-1}$. The peaks in T(r) are well resolved and do not reveal this systematic shoulder on the Si-O peak but the reported interatomic separations are less than those for lithium, sodium and rubidium tin silicate glasses, measured on GLAD. This discrepancy is thought to be due to errors in the calibration of LAD.

The glass is thought to consist of tetrahedral $SiO_{4/2}$ and triangular based $SnO_{3/3}$ pyramids. Both n_{SnO} and r_{SnO} decrease on replacing SnO with K_2O. This is thought to indicate a change in the hybridisation of the tin. The K-O correlation cannot be clearly distinguished from the O-O correlations. The intensity of the total correlation function increases at about 2.9Å, with increasing potassium content, but it is not clear that this is due to an increase in K-O correlation. A diffraction experiment on higher potassium content glasses and/or isotropic substitution between ^{39}K and ^{41}K could further study the potassium environment.

A single, broad peak in the ^{29}Si MAS NMR spectrum shifts downfield and narrows on replacing SnO with alkali oxide. The decrease in chemical shift is not as dramatic as in the binary alkali silicate glasses. This suggests that the alkali oxide has a greater modifying effect then the tin. In glasses containing $\geq$20mol% Na_2O the FWHM does not decrease any further. This is thought to indicate that the alkali cation associates with the tin and reduces the distribution of shielding about the

silicon nuclei, until most of the three co-ordinated oxygen atoms have been removed. The alkali cations then depolymerise the silicate network.

The average structural model for ν-R_2O-SnO-SiO_2 proposed by Sears et al. [9] is supported by the data presented here. The alkali cation is thought to associate with the $(SnO_{3/3})^-$ groups within a $SiO_{4/2}$ network.

This work could be continued by ;

- studying the physical properties of high alkali content glasses,
- a study of crystalline alkali tin silicates (by controlled crystallisation of the glass),
- correcting the neutron diffraction data using recalibrated LAD parameters.
- an isotopic substitution neutron diffraction [24] experiment using ^{41}K enriched $(K_2O)_x(SnO)_{1-x}(SiO_2)$ glasses.

REFERENCES

[1] J.Johnson, C.E.Johson, D.Holland, A.Sears, J.F.Bent, P.Appleyard, M.F.Thomas and A.C.Hannon in progess

[2] A.Sears, 'The characterisation of stannosilicate glasses', PhD thesis, Physics Department, Warwick University, in progress.

[3] P.G.Appleyard, '', PhD thesis, School of the Built Environment, John Moores University, Liverpool, in progress

[4] V.H.Danheim,H.J.Oel and G.T.Erlangen, *Glastechn.Ber.* **49** (1976) 170

[5] K.P.Mitrofanov and T.A.Sidorov, *Soviet Physics - Solid State* **9 #3** (1967) 693

[6] N.A.Eissa, E.E.Shaisha and A.L.Hussiun, *J.Non-Cryst.Solids* **16** (1974) 206

[7] K.F.E.Williams, C.E.Johnson, D.Holland, M.M.Karim, *J.Phys.Condensed Matter* **7** (1995) 9485

[8] Z.Zhang, *Phys.Chem.Glasses* **34** #3 (1993) 95

[9] A.Sears, D.Holland and M.G.Dowsett, *Phys.Chem.Glasses* (2000)

[10] J.E.Shelby, 'Introduction to glass science and technology', RSC Paperbacks 1997.

[11] M.M.A.Karim, 'A study of tin oxides in silicate based glasses', Phd thesis, Physics Department, Warwick University, March 1995.

[12] M.Fellows, Undergraduate project report, Physics Department, Warwick Univerity 1998

[13] 'The Oxford guide to Xray microanalysis', Oxford instruments plc 1997.

[14] J.S.Rigden, J.K.Walters, P.J.Dirken, M.E.Smith, G.Bushnell-Wye, W.S.Howells and R.J.Newport, *J.Phys.Condens.Matter* **9** (1997) 4001

[15] P.H.Gaskell and D.J.Wallis, *Phys.Rev.Letters* **76** #1 (1996) 66

[16] A.C.Hannon, J.M.Parker and B.Vessal, *Trans ACA* **27** (1991) 293

[17] A.G.Clare, B.Bachra, A.C.Wright and R.N.Sinclair, in 'The Physics of Non-Crystalline Solids' Taylor & Francis 1992

[18] N.E.Brese and M.O'Keeffe, *Acta Cryst.* **B47** (1991) 192

[19] T.Ishikawa and S.Akagi, *Phys.Chem.Glasses* **19 #5** (1978) 108

[20] R.L.Mozzi and B.E.Warren, *J.Appl.Crystalogr.* **2** (1969) 164

[21] M.Cao, Undergraduate project report, Physics Department, Warwick University 1998

[22] H.Maekawa, T.Maekawa, K.Kawamura and T.Yokokawa, *J.Non-Cryst.Solids* **127** (1991) 53

[23] R.Dupree and D.Holland in 'Glasses and Glass-Ceramics' Chapman and Hall 1989 pp1-40.

[24] L.Cormier, P.H.Gaskell, G.Calas, J.Zhao and A.K.Soper, *Physica B* **234** (1997) 393

CHAPTER 8

POTASSIUM PHOSPHOSILICATE

8.1. INTRODUCTION

Modified phosphosilicate glasses are of interest to glass science because they have been shown to contain 6 co-ordinated silicon, Si^{VI} [1]. This contradicts Zachariasen's observation that the cation co-ordination should be small (4 or less) in network oxide glasses [2]. It is also of geological interest as higher co-ordinated silica units (Si^{V} and Si^{VI}) are thermodynamically more stable than Si^{IV} at high pressures and are expected to be major constituents of the earth's mantle, [3]. Ion dynamics simulations of liquid and glassy silicates [4] suggest that Si^{V} and Si^{VI} populations should eventually dominate over Si^{IV} with increasing temperature and pressure. These results are analogous to density studies of crystalline silicates at high pressures [5,6] which claim that Si^{VI} should predominate over Si^{IV} at pressures between 8 and 24GPa. Several characterised high pressure silicate mineral phases contain high co-ordinated silicon. Stishovite (SiO_2), [7], wadeite ($K_2Si_4O_9$), [8], $MgSiO_3$ perovskite [9], ζ-$Na_2Si_2O_5$ [10] and silicon diphosphate (SiP_2O_7) [11] all contain Si^{VI} and calcium silicate, ($CaSi^{V}_2O_5$), [12], contains Si^{V}.

An in situ, high temperature NMR study of sodium aluminosilicate melts by Stebbins et al [13] found an increase in high co-ordinated silicon and aluminium (an analogue to silicon) species with temperature. However extending this to in situ high temperature and high pressure experimental studies of silicate melts has not yet been possible. To date, the silicon environment in high pressure, high temperature liquids has been probed by studying silicate glasses cooled rapidly at high pressure, assuming that the glass structure approximates the melt structure at T_f.

Xue et al [14] observed well defined tetrahedral and octahedral sites by MAS NMR in ^{29}Si enriched sodium silicate glass ($Na_2Si_2O_5$) quenched from 1500°C at 8GPa. The tetrahedral peak, centred at -87.5 ± 0.5 ppm, was shifted down-field by 1ppm and had more pronounced shoulders, on both sides of the main peak, relative to an identical composition glass quenched at ambient pressure. This was interpreted as a disproportionation from predominantly Q^3 species to a more random distribution of bridging and non-bridging oxygen with increasing pressure. A small

peak, estimated to contain ~1.5% of the total silicon, was also found in glass quenched at 8GPa but not at 5GPa or ambient pressure. It was 8ppm wide, centred at -197ppm and was assigned to amorphous Si^{VI} species with reference to shifts observed in high co-ordinated crystalline silicates [15-17]. A previously unknown high pressure polymorph of $Na_2Si_2O_5$ was also studied, quenched from 1150°C at 8GPa. The ^{29}Si MAS NMR spectra showed four distinct peaks at -94.4, -97.9, -199.8 and -200.4 ppm which were interpreted as two tetrahedral and two octahedral sites.

Stebbins et al. [18] observed both octahedral and pentahedral silicon sites in a $K_2Si_4O_9$ glass quenched at 1.9GPa. This was the first observation of Si^V species in silicates. The sample was isotopically enriched with 95% ^{29}Si such that the small proportion of high co-ordinated species 0.2% and 0.4% were observable at -200 and -150 ppm respectively. The peak assignments were made with reference to ^{27}Al MAS NMR spectra of minerals in which the increase from four to five to six co-ordinated aluminium produces a systematic increase in chemical shielding and hence more negative chemical shifts.

Xue et al [19] continued this study of alkali silicates with a combined MAS NMR, Raman and FTIR study of ^{29}Si enriched $Na_2Si_2O_5$, $Na_2Si_4O_9$ and $K_2Si_4O_9$ glasses quenched at a series of pressures up to 12 GPa. Distinct peaks in the NMR spectra centred about -100, -150 and -200ppm were assigned to Si^{IV}, Si^V and Si^{VI} respectively. The relative proportions of the higher co-ordinated species and the disproportionation of the Q-species increased with pressure. The Raman and FTIR spectra also changed with the proportion of silicon species, although the assignment of peaks in these spectra was acknowledged not to be unique.

No high co-ordinated silicon species were observed in a SiO_2 glass quenched at 6GPa, in which there was no spread in Q-species. Also, more Si^V and Si^{VI} were observed in $Na_2Si_4O_9$ glasses than $Na_2Si_2O_5$ at any specific quenched pressure and at a lower quenched pressure in $Na_2Si_4O_9$ than in $Na_2Si_2O_5$. The glasses were not chemically analysed but it is assumed that the $Na_2Si_4O_9$ glass has a greater spread in Q-species (Q^3 & Q^4) than $Na_2Si_2O_5$ (Q^3 only). They suggest a model, see figure 8.1, which requires both Q^3 and Q^4 species to form the Si^V and Si^{VI} species and their tetrahedral next nearest neighbours, Q^{4*}.

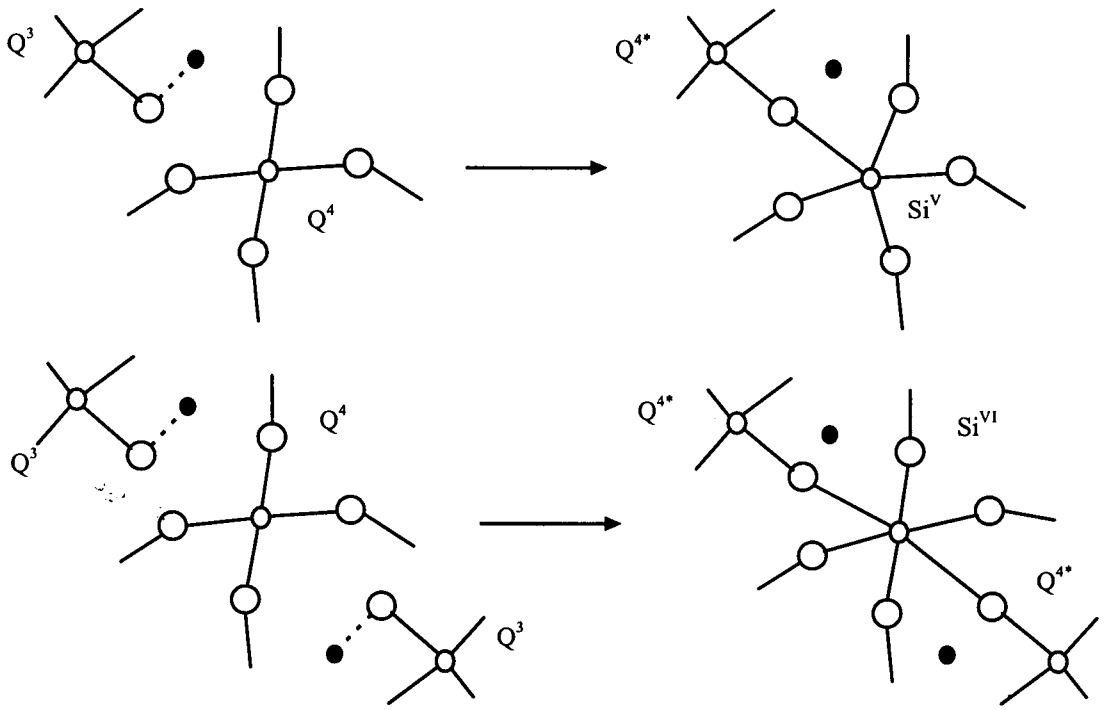

Figure 8.1 Schematic model of the formation of Si^{V} and Si^{VI} in silicate melts (after Xue[19]) in which are ●sodium, ○silicon and ○oxygen.

The formation of high co-ordinated species, according to this model, converts non-bridging oxygens to bridging oxygens and repolymerizes the melt. This could also explain the changes in germanium co-ordination seen in $R_2Ge_2O_5$-GeO_2 glasses, [20]. Several spectroscopic and diffraction techniques indicate an increase in the average germanium co-ordination with increasing alkali content, accompanied by fewer than might be expected non-bridging oxygens.

Stebbins has also observed five co-ordinated silicon in several ambient pressure alkali tetrasilicate glasses, [21]. Quenching the melt at ambient pressure simplified the sample preparation such that several samples were prepared with different quench rates. The abundance of Si^{V} was seen to increase with T_f, suggesting that it is more abundant at lower viscosity and supporting its role as an intermediate state in viscous flow and oxygen diffusion [22]. This requires Q^4 and Q^3 species to form pentavalent silicon which then returns either to its initial state or transforms to a different Q^3 and Q^4 configuration, see figure 8.2.

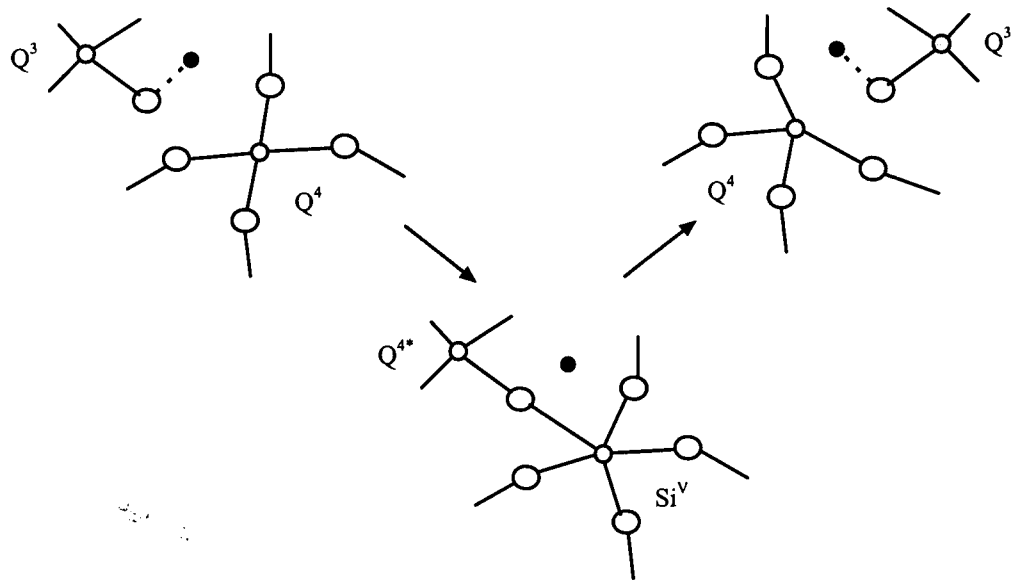

Figure 8.2 Schematic model of diffusion and viscous flow mechanisms via an intermediate Si^V state (after Xue [19]) in which are ● sodium, ○ silicon and ○ oxygen.

Higher co-ordinated silicon has also been observed in phosphosilicate glasses quenched at ambient pressure, [1]. This is geologically important as phosphorus is common in natural magmas and is thought to affect the thermodynamic properties of complex melts [23]. The observation of high co-ordinated species in glasses prepared at ambient pressure is also significant as other studies of silicate melts and glasses have found pressure induced co-ordination changes to relax on decompression [24].

Phosphosilicate glasses have not been extensively studied, largely because P_2O_5 is volatile at high temperatures and the glasses are often extremely hygroscopic. The interpretation of spectra from multi-component glasses is also more ambiguous than that from just a modified silicate network as there is an increased number of contributions to the lineshape. However, both ^{29}Si and ^{31}P are spin $^1/_2$ nuclei and can be probed by NMR. Crystalline and amorphous phosphates consist of tetrahedral $PO_{4/2}$ structural units which can be described with Q^n nomenclature, as described in chapter 1. ^{31}P MAS NMR can resolve different structural units by their typical chemical shifts, as described in chapter 3.

Hoppe et al. [25] measured two P-O bond lengths in ν-P_2O_5 using neutron diffraction with high real-space resolution (Q_{max}~50Å^{-1}). The two peaks; P-O_B

(bridging) at 1.58Å and P-O_T (terminal) at 1.43Å, had not been resolved in a previous study (Q_{max} ~ 22Å^{-1}) [26] which related the medium range structure of ν-P_2O_5 to that of ν-As_2O_3 (both are three-fold linked networks). The bond lengths are comparable with those in the three crystalline polymorphs of P_2O_5 [27-29] which have bond lengths in the ranges 1.432≤P-O_T≤1.445 and 1.57≤P-O_B≤1.59 Å. They also fit trends from previous ab initio calculations [30] and diffraction studies by Hoppe et al. [31-34] of the MeO-P_2O_5 series (where Me=Ca or Zn), considering P_2O_5 as an end point composition.

On increasing MeO content both the P-O_T and P-O_B bond lengths increase but the mean P-O bond length remains invariant. This is interpreted as the Q^3 network depolymerising to Q^2, Q^1 and possibly Q^0 species so that there are fewer (longer) bridging oxygens. The increase in P=O_T bond length is interpreted as the double bond becoming delocalised between increasing number of non-bridging oxygens. The non-bridging oxygens form Me-O-P bonds and increase the connectivity of the $PO_{4/2}$ tetrahedra. This change in structural unit is suggested to account for changes in glass properties. Further addition of modifier breaks P-O_B bonds and forms a modified random network. This change in Q-speciation has been confirmed by ^{31}P MAS NMR [35,36] and by XPS [36-38]. The widths of the P-O correlations in the modified glasses [34] are greater than in ν-P_2O_5 [25] which also suggests a more disordered modified network.

A visual splitting of the P-O correlation was not reported in a further neutron diffraction study of ν-P_2O_5 and alkali phosphate glasses using data up to a Q_{max} of 30Å^{-1} [39]. The scattering functions were compared with those for several models of intermediate range order. ν-P_2O_5 was described by a P_4O_{10} molecule packing model. The addition of alkali oxide was seen to depolymerise the local $PO_{4/2}$ network but introduce extended range order, the length scale of which increased with Me^+size.

A MAS NMR study [40] of alkali disilicate glasses containing up to 5mol.% P_2O_5 found that the two network forming species remain separate whilst the phosphate rich regions scavange the modifier cations. This partially repolymerises the silicate network, converting Q^3 to Q^4, whilst forming ortho- (Q^0) and pyro-phosphate (Q^1) units.

At higher P_2O_5 contents [41] meta-phosphate groups form and the silicate network is at first depolymerised and then repolymerised again. Between 8 and 12

mol.% P_2O_5 the silicate network depolymerises to a mixture of Q^4 and Q^3(P) species, where the Q^3(P) species are more shielded in Si-O-P linkages. Between 12 and 25 mol.% P_2O_5 the silicate network is repolymerised to contain just Q^4 species whilst the alkali cations associate with the increasing number of metaphosphate groups. At higher P_2O_5 contents (38, 46 and 57 mol.% P_2O_5) the proportion of Si^{VI} species increases relative to the Q^4 silicon whilst the proportion of Q^2, 'SiP_2O_7-like' phosphorus species, at -33ppm in the ^{31}P spectra, increases relative to the metaphosphate species. A further study observed Si^{VI}, by MAS NMR, in potassium tetrasilicate-P_2O_5 glassses containing more than 28mol.% P_2O_5 and by infra-red absorption spectroscopy, when the Si^{VI} content was greater than 10%, [42]. Similar trends in speciation and fictive temperature were observed as previously in the alkali disilicate-P_2O_5 glasses and an additional peak observed at -155ppm in the ^{29}Si MAS NMR spectra was assigned as a spinning sideband of axially symmetric Si^{IV} species.

An increase in Si^{VI} species with P_2O_5 content has also been seen in a recent NMR and Raman study of Na_2O-P_2O_5-SiO_2 glasses by Yamashita et al., [43]. Si^{VI} was only observed when the $[P_2O_5]/[Na_2O]$ ratio was greater than unity, below which only Q^4 silicon and Q^2 phosphorus (typical of $NaPO_3$) species were observed.

The onset of the formation of Si^{VI} species was also found to coincide with a discontinuity in T_g in a further study of the compositional dependence of the Si^{VI} species [44]. No Si^{VI} was found in $R_2O{\cdot}2SiO_2{\cdot}pP_2O_5$ glasses where $p \leq 1$ and the percentage of Si^{VI} species dropped rapidly on reducing the alkali content in $rR_2O{\cdot}2SiO_2{\cdot}3P_2O_5$ glasses (where $0 \leq r \leq 1$). No Si^{VI} was found in the base glass (when $r = 0$). The modifying cation was considered to charge balance the $[Si^{VI}]^{2-}$ species within an amorphous phosphosilicate network. This interpretation relates to a previous study by Weeding which failed to produce a Si^{VI} containing alkali-free silicon phosphate glass although on devitrification this produced $Si_5O(PO_4)_6$ and SiP_2O_7, (high co-ordinated crystalline phases), [16].

More recently the role of the modifying cation in stabilising the Si^{VI} species has been studied by replacing alkali cations with other modifying cations. Nogami reported MAS NMR evidence of Si^{VI} in SrO-P_2O_5-SiO_2 glasses containing more than 50% P_2O_5 [45]. The proportion of Si^{VI} species increased with $(P_2O_5\text{-SrO})/SiO_2$, which decreased T_g. Nogami also mentions a presently unpublished NMR study which observed Si^{VI} species in phosphosilicate glasses containing MgO, CaO and

BaO. Si^{VI} has also been observed in a series of lead phosphosilicate glasses [46]. Li et al. [47] identified Si^{IV} and Si^{VI} species in amorphous $0.75SiO_2$-$0.25P_2O_5$ and crystalline SiP_2O_7 using high resolution Si and P K- and L-edge XANES. Fleet et al. combined XANES, infrared, Raman and MAS NMR in a study of alkali- and alkali-CaO-phosphosilicate glasses [48]. The Si^{VI} content was greater in sodium disilicate-P_2O_5 glasses quenched at higher temperatures (ie. with a lower T_f) as found previously by Dupree et al. [44]. However, whilst Dupree suggested that the alkali cations were essential to stabilise the Si^{VI} species, Fleet concluded that the modifying cations were independent of the Si^{VI} species as the proportion of Si^{VI} species did not change on substituting $2R^+$ with Ca^{2+} cations. From this they suggest that the alkali and Ca^{2+} cations form metaphosphate groups which are interconnected with $SiO_{4/2}$ tetrahedra whilst the Si^{VI} species associate with pyrophosphate groups which may be independent of the alkali silicophosphate network. This relates to a 2-D ^{29}Si NMR study by Knight et al. who found no next nearest neighbour connectiviy between Si^{VI} and silicon Q^4 species in a nominal $20Na_2O$-$20SiO_2$-$60P_2O_5$ glass [49]. However this model requires an increase in the number of pyrophosphate groups with P_2O_5 content which was not seen in sodium disilicate-P_2O_5 glasses containing $57\%P_2O_5$ [44]. Lockyer observed two narrow resonances about 11.6 and 0ppm in potassium tetrasilicate-P_2O_5 glasses containing more than 40mol.% P_2O_5, [44]. These are typical shifts for ortho- and pyro-phosphate species but were seen to increase in intensity with no change in shift with deliberate exposure to atmospheric moisture, so were considered to be H_3PO_4 and $H_4P_2O_7$ and not part of the potassium phosphosilicate network.

Paper chromotography [50], a combined TEM and ^{31}P MAS NMR study [51] and the increase in ^{31}P fwhm with P_2O_5 content [44] in modified phosphosilicate glasses all suggest that silicon substitutes into phosphate chains (or rings), increasing the range of chain lengths. No evidence of phase separation was detected by the TEM study and the isotropic chemical shifts recorded by Vogel remained invariant with increasing silicon content. They suggest that the silicon substitutes within rather than between phosphate chains forming (-P-O-**P**-O-Si-) and/or (-Si-O-**P**-O-Si-) linkages. They considered these as phosphorus Q^{1+1Si} and/or Q^{0+2Si} respectively, the electronic environments of which are more similar to Q^2 metaphosphate chains than the branching Q^{2+Si} bridges. Evidence of Si-O-P linkages is also provided by an IR study

[52] and the strong increase in solubility, caused by the the low hydrolysis resistance of the Si-O-P bonds.

This present study applies natural abundance ^{31}P and ^{29}Si MAS NMR and neutron diffraction to several nominal potassium disilicate-P_2O_5, potassium tetrasilicate-P_2O_5 and alkali free phosphosilicate glasses with different thermal histories. The relative proportion of Si^{VI} species is dependent upon the rate at which the glass is quenched [53]. Several glasses of identical composition but with different proportions of species are studied. MAS NMR spectra have been reported for similar glasses but neutron diffraction has not previously been used to observe Si^{VI} in a glass. Bond valence calculations [54] suggest the different silicon co-ordinations have different bond lengths which should be resolvable on LAD. A further novelty of this study is that the glasses were prepared alumina-free. This is important as Al_2O_3 was found to have an impeding effect on the formation of Si^{VI} species [53].

8.2 EXPERIMENTAL DETAILS

8.2.1 SAMPLE PREPARATION

Eight samples, of three nominal compositions, were made using analytical grade potassium carbonate, Wacomsil quartz, ammonium dihydrogen phosphate and iron oxide. The reagents for each sample were first mixed for 12~16 hrs and then added to a silica crucible in a muffle furnace. Fused silica crucibles were used in preference to platinum or alumina crucibles because P_2O_5 attacks platinum [55] and aluminium replaces silicon in the octahedral sites, [53]. The premelt temperature was increased slowly to control the decomposition of ammonium di-hydrogen phosphate and potassium carbonate, evolving carbon dioxide, water and ammonia, equations 8.1 and 8.2, whilst minimising the loss of P_2O_5 and K_2O.

$$K_2CO_3 \rightarrow K_2O + CO_2 \qquad (8.1)$$

$$2NH_4H_2PO_4 \rightarrow P_2O_5 + 3H_2O + 2NH_3 \qquad (8.2)$$

The calcined reagents were then transferred to a melting furnace and heated at $10°min^{-1}$ to melting temperature, table 8.1.

	$(K_2O\text{-}4SiO_2)\text{-}P_2O_5$	$(K_2O\text{-}2SiO_2)\text{-}P_2O_5$	$SiO_2\text{-}P_2O_5$
premelt temp. range (°C)	400 → 600	350 → 600	350 → 600
melt temp. (°C)	1390	1500	1600
melt dwell (mins)	90	180	30

Table 8.1 Potassium phosphosilicate glass melting conditions.

8.2.1.a POTASSIUM TETRASILICATE - P_2O_5

Three potassium phosphotetrasilicate glasses were made with nominally identical compositions: $0.5(K_2O\ 4SiO_2)\ 0.5(P_2O_5)\ 0.0005(Fe_2O_3)$ but with different cooling rates. One melt, KPTSSC, was left in the furnace to cool from 1390°C to 750°C at approximately 2.5°Cmin^{-1}, then placed in a desiccator to cool to ambient. Only the central regions of the melt were used for later studies as the edges of the melt fused with the crucible. Two further melts were splat cooled between carbon coated steel plates; one with hot plates at 200°C , KPTS480, and one with liquid nitrogen cooled plates, KPTS77. All samples were immediately stored in a desiccator as they were known to be extremely hygroscopic, [53]. A small piece of each sample was used to check amorphicity by powder X-ray diffraction.

8.2.1.b POTASSIUM DISILICATE - P_2O_5

Four potassium phospho-disilicate glasses were made with nominally identical compositions: $0.4(K_2O.2SiO_2)\ 0.6(P_2O_5)\ 0.0005(Fe_2O_3)$ but with different cooling rates. One melt, KPDSSC, was left in the furnace to cool from 1500°C to 950°C at approximately 7°Cmin^{-1}, then placed in a desiccator to cool to ambient. As noted previously, only the central regions of the melt were used for later studies. Three further melts were splat cooled between carbon coated steel plates; one with hot plates at 200°C, KPDS480, one with room temperature plates, KPDS293, and one with liquid nitrogen cooled plates, KPDS77. All samples were immediately stored in a desiccator as solid lumps until required for study. A small piece of each sample was used to check amorphicity by powder X-ray diffraction.

8.2.1.c PHOSPHO-SILICATE

One phosphosilicate glass was made with a nominal composition $0.24(SiO_2)$ $0.76(P_2O_5)$ $0.0005(Fe_2O_3)$. An alumina crucible was used as the silica crucibles melted with the sample at the required higher melt temperature and alkali free phosphosilicate glasses were not found to exhibit Si^{VI} sites [53]. The melt was allowed to cool in a desiccator in the crucible since the high viscosity of the melt prevented pouring the melt. This indicates that the glass has a high silica content due to a significant loss of P_2O_5 during the melt process. The silica crucible shattered on cooling and the central region of the melt was used for this study. A small piece of sample was used to check amorphicity by powder X-ray diffraction.

8.2.2. SAMPLE COMPOSITION

X-ray fluorescence (XRF) measurements were made for each glass and several reference mixtures, using a Phillips PW1400 at the Geological Science Department, Durham University. It is assumed that the ZAF attenuation of the X-rays is comparable between the glasses and reference mixtures. The reference mixtures of analytical grade K_2CO_3, SiO_2 and P_2O_5 were weighed and mixed in a pestle and mortar under dry argon. The powdered samples and reference mixtures were kept dry in an evacuated glove box until use. Approximately 1g of each sample was irradiated and the intensity of the major fluorescent line was measured for each element. The fluorescent X-rays were selected by wavelength using a LiF crystal. The K, Si and P content of the glasses are determined by interpolating between the raw X-ray intensities of the reference mixtures. Further details of the XRF technique are given in section 4.3.

8.2.3 SAMPLE DENSITY

Sample volumes and related sample masses were measured using a micropycnometer and a digital balance, at RAL. The sample densities were calculated from these measurements, as described in section 4.4. The sample and sample cell were first purged with helium for ~10 minutes to flush air and moisture from pores in the sample surface. The volume was measured repeatedly until settling at a value within the uncertainty associated in measuring the sample cell pressure.

8.2.4 ^{29}Si MAS NMR

^{29}Si MAS NMR spectra were recorded for all phosphosilicate samples using a 1-pulse sequence with a 120 second delay between 2.5 μs (< $^{\pi}/_{2}$) pulses. The samples were packed into spinners in a dry box. Long acquisition times (~20hrs) were required for the nominal tetrasilicates and alkali free phosphosilicate, spinning at 11kHz in a 4mm diameter rotor. An even longer aquisition time (~85hrs) was used for KPTS77. The nominal disilicates required a larger sample volume due to the lower silicon content. These spectra were acquired, spinning at ~ 1.1kHz in a 9.5mm diameter rotor. 50Hz line broadening was applied to each FID.

8.2.5 ^{31}P MAS NMR

^{31}P MAS NMR spectra were recorded for all the phosphosilicate samples, using a 1-pulse sequence. The samples were packed into 4mm diameter spinners in a dry box. The samples were spun at 9kHz and the data acquired using a 10 second delay between 2μs (< $^{\pi}/_{2}$) pulses. These parameters did not saturate the magnetisation. 50Hz line broadening was applied to each FID.

8.2.6 ^{27}Al MAS NMR

A quantitative ^{27}Al MAS NMR spectrum was recorded for the alkali-free phosphosilicate glass sample. The alkali-free phosphosilicate sample was the only sample prepared in an alumina crucible because it required a higher melt temperature than the alkali phosphosilicate samples. The sample was packed into a 4mm diameter spinner in a dry box and the mass of the sample measured using a digital balance (accurate to ±0.001g). The sample was spun at 6kHz and the spectrum acquired using a 1-pulse sequence with a 5 second pulse delay between 2μs $^{\pi}/_{2}$ pulses. The sample intensity was measured relative to that for a known mass of a mixure of 90%SiO_2 10%Al_2O_3.

8.2.7 ^{1}H MAS NMR

^{1}H MAS NMR spectra were recorded for all phosphosilicate samples. Each sample was packed into a 4mm diameter spinner, in a dry box, and spun at ~6kHz. The data was acquired using a 1-pulse sequence with a 2 second pulse delay between 1μs pulses. This irradiation did not saturate the spin system.

8.2.8 NEUTRON DIFFRACTION

TOF neutron diffraction measurements were made for all phosphosilicate samples on the LAD at RAL. The samples were loaded into 8mm diameter cylindrical, vanadium cans in a dry box. The total scattering from each sample, a vanadium rod, an empty vanadium can and the empty spectrometer was measured in 300μAhr increments using a mechanical sample changer. Data was acquired for a total ~2400μAhrs for each sample, 1700μAhrs for the vanadium rod, 1300μAhrs for the empty can and 300μAhrs for the empty spectrometer.

8.3 RESULTS AND DISCUSSION

8.3.1 SAMPLE COMPOSITION

The sample cation concentrations were deduced by interpolating between the raw XRF intensity for each cation species in reference mixtures. However, the interpolated total mol.% composition was ~103% for the potassium disilicate-P_2O_5 glasses and ~94% for the potasium tetrasilicate-P_2O_5 glasses. This is crudely considered to be due to the powdered disilicates having a lower density than the standard mixtures; resulting in less absorption, and the reverse for the powdered tetrasilicates. The variation in the measured raw XRF intensity can be seen in the spread in X-ray intensity measured for several 50% SiO_2 reference mixtures, see figure 8.5.

The sample compositions were estimated by maintaining the total molar fraction to be unity. The estimated concentration of each cation is within the experimental uncertainty of this technique for these samples, see figures 8.3, 8.4 and 8.5. The estimated sample compositions are summarised in table 8.2.

	mol.% K_2O	mol.% P_2O_5	mol.% SiO_2
KPTS77, KPTS480	12 (±1)	37 (±1)	51 (±1)
KPTSSC	10 (±1)	33 (±1)	57 (±1)
KPDS77, KPDS293, KPDS480	18.5 (±1)	38.5 (±1)	43 (±1)
KPDSSC	18 (±1)	38 (±1)	44 (±1)
PS	-	11 (±1)	89 (±1)

Table 8.2 Sample compositions deduced from XRF measurements.

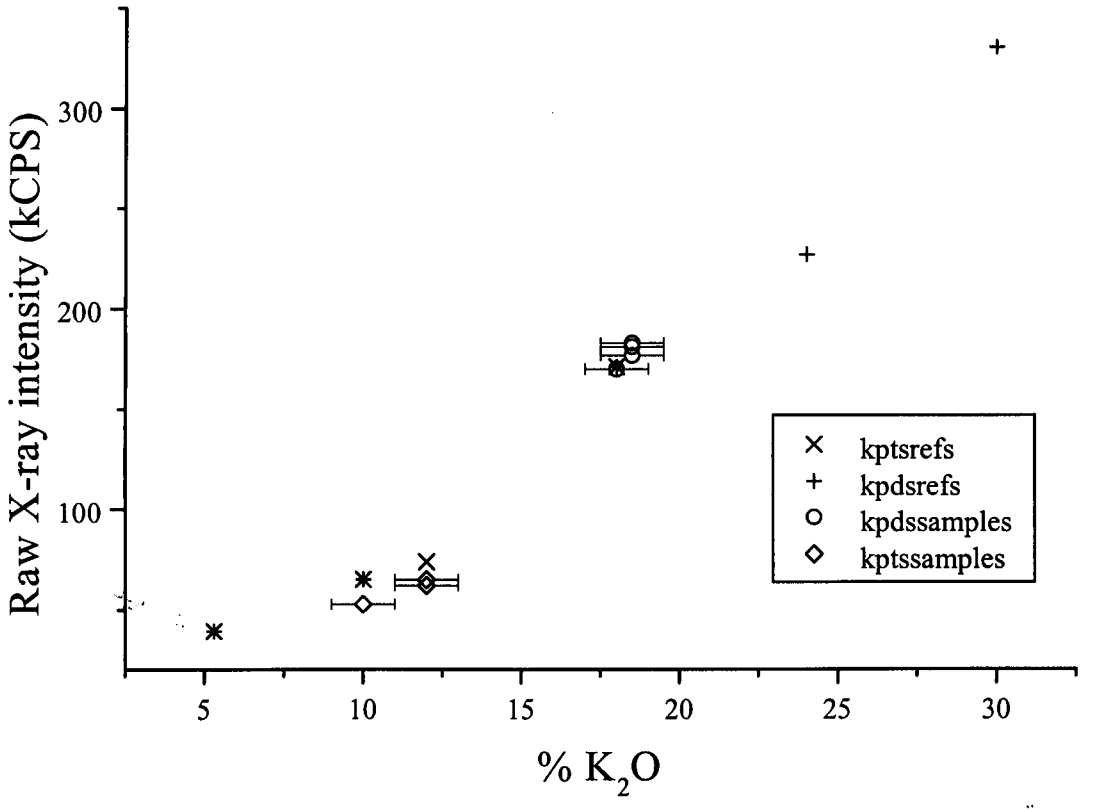

Figure 8.3 K (K^{α}) XRF intensity @136° (2θ) vs composition for mixed reference powders and powdered phosphosilicate glasses.

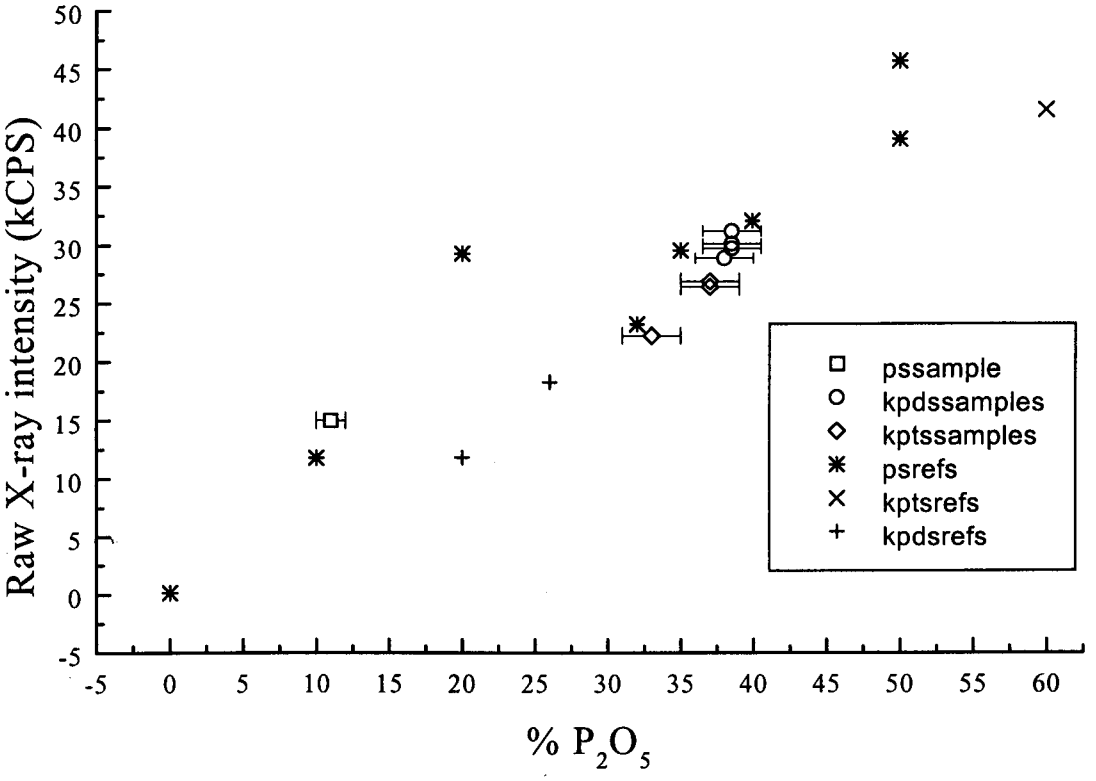

Figure 8.4 P (K^{α}) XRF intensity @140° (2θ) vs composition for mixed reference powders and powdered phosphosilicate glasses.

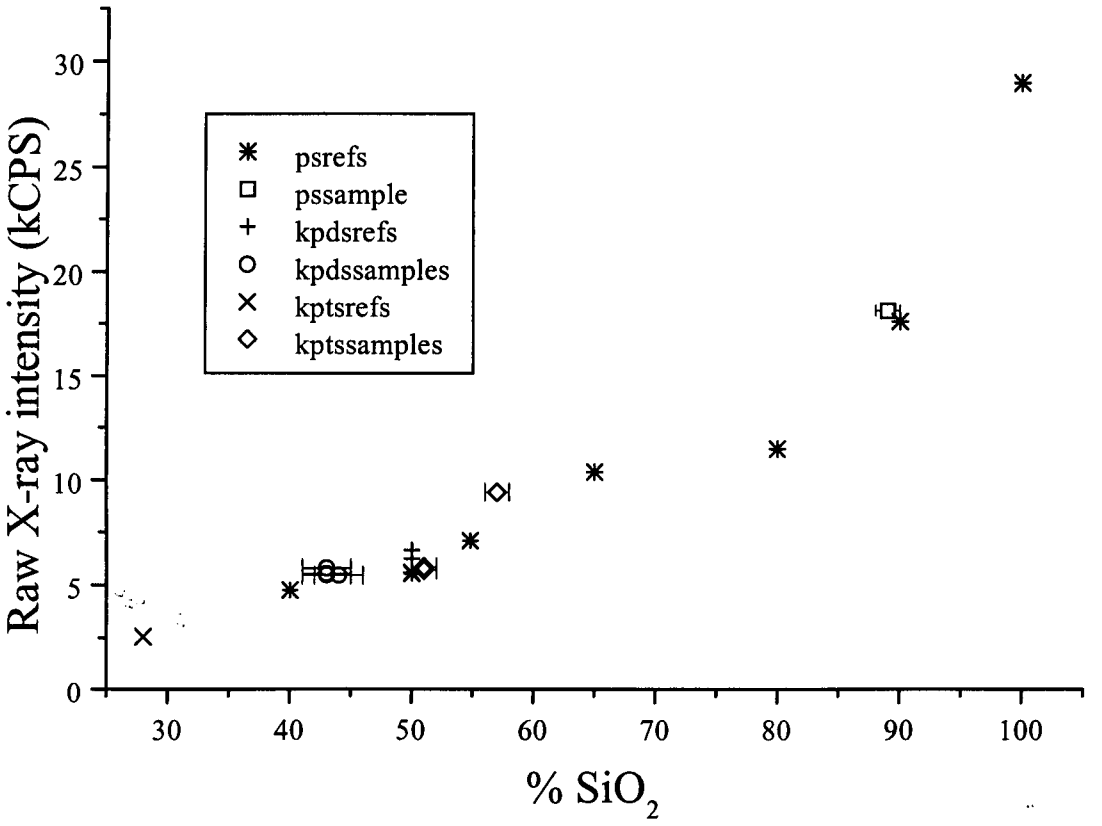

Figure 8.5 Si (K^{α}) XRF intensity @109° (2θ) vs composition for mixed reference powders and powdered phosphosilicate glasses.

9.3.2 SAMPLE DENSITY

The measured sample volume (and sample density) settled to an equilibrium value after approximately five measurements for each sample, see figure 8.6. This is considered to be due to an outgassing of moisture from the sample surface. The sample densities, see table 8.3, reflect changes in the sample composition but not the structural changes between samples of the same composition. The values obtained were used in correcting the neutron diffraction data.

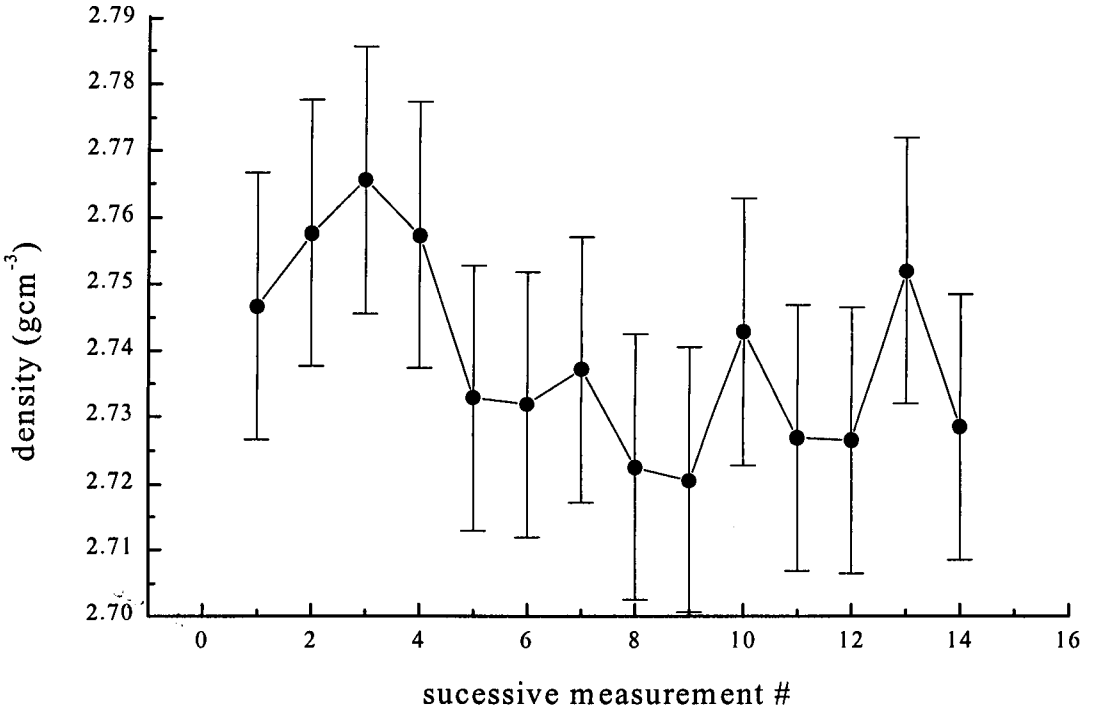

Figure 8.6 The measured density of KPTSSC settled at 2.73±0.02gcm^{-3} after purging with helium and several measurements.

	KPTS77	KPTS480	KPTSSC	KPDS77	KPDS293	KPDS480	KPDSSC	PS
ρ (gcm^{-3}) (±0.02)	2.86	2.86	2.73	2.46	2.44	2.44	2.48	2.50

Table 8.3 The measured density of the phosphosilicate glasses.

8.3.3 ^{29}Si NMR

Each ^{29}Si MAS NMR spectrum clearly distinguishes sites with different Si-O co-ordination. The spectra for glasses of the same nominal composition are similar but the relative intensities of the peaks change with thermal history. The processed spectra are shown in figure 8.7 and the peak parameters of Gaussian fits to these spectra are summarised in table 8.4.

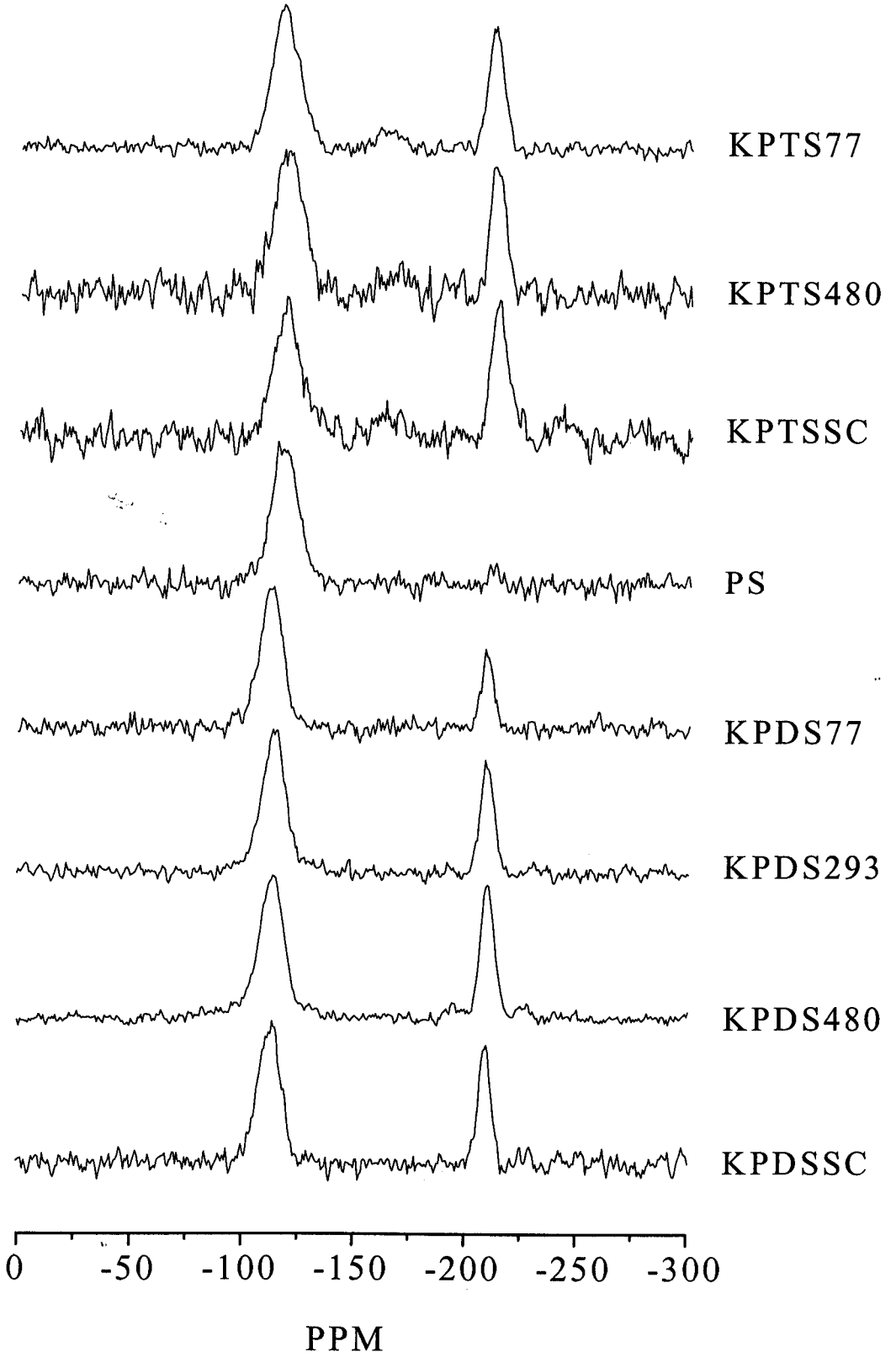

Figure 8.7 ^{29}Si MAS NMR spectra for all phosphosilicate samples.

	^{29}Si δ (ppm) ± 0.5	^{29}Si fwhm (ppm) ± 1	relative intensity (%) ± 1.5
KPTS77	-117.0	12.4	62.3
	-163.6	10.6	6.7
	-211.6	6.8	31.0
KPTS480	-118.8	13.1	61.5
	-167.6	12.7	8.8
	-212.8	6.8	29.7
KPTSSC	-118.6	13.0	54.6
	-164.3	14.1	10.6
	-214.1	7.9	34.8
PSSC	-117.8	12.2	95.4
	-212.3	4.2	4.6
KPDS77	-112.5	10.3	78.2
	-209.7	5.4	21.8
KPDS293	-113.7	11.0	69.2
	-209.7	6.2	30.8
KPDS480	-113.1	11.5	65.3
	-209.9	6.4	34.7
KPDSSC	-112.7	10.3	68.4
	-209.3	5.5	31.6

Table 8.4 Gaussian fit parameters to phosphosilicate ^{29}Si MAS NMR spectra.

The ^{29}Si MAS NMR spectra for the potassium tetrasilicate-P_2O_5 glasses are similar to those reported by Lockyer [53]. Each spectrum contains three peaks centred about -118, -164 and -212ppm. These peaks can be assigned as Si^{IV}, Si^{V} and Si^{VI} with reference to crystalline silicates [15-17] and previous NMR studies of silicate glasses [17].

There is no evidence for an increase in the distribution of Q-species with the number of higher co-ordinated silicon species, as previously reported for alkali silicates [19]. Instead the phosphate and/or potassium species are thought to accommodate and charge balance the Si^{V} and Si^{VI} species.

A static spectrum and MAS spectra, at several spinning speeds, were obtained for KPTS77. The peak at -164 is not a spinning sideband. This contradicts the interpretation given by Lockyer et al. [42]. The peak at -164ppm is invariant with spinning speed in the MAS spectra and the static widths of the peaks at -118 and -212ppm are not sufficiently broad to include the peak at -164ppm as a spinning sideband, see figure 8.8.

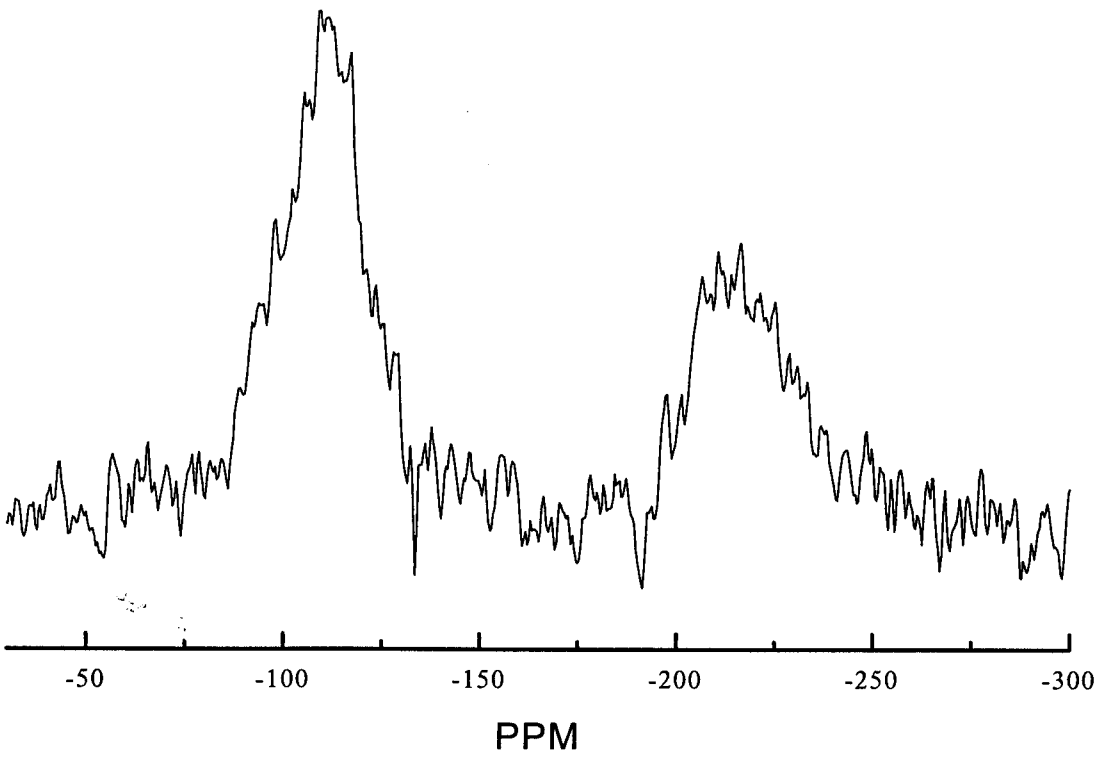

Figure 8.8 Static ^{29}Si NMR spectrum for KPTS77, shift relative to TMS.

The peak positions are up-field from those observed in phosphate-free potassium silicate glasses; $Si(OSi)_4$ in ν-K_2O $4SiO_2$ (-105ppm) [56], $Si(OSi)_5$ in ν-$K_2Si_4O_9$ (-150ppm) [19] and $Si(OSi)_6$ also in ν-$K_2Si_4O_9$ (-200ppm) [19]. This suggests that each silicon atom has phosphorus atoms as next nearest neighbours.

The Si^{IV} resonance at -118ppm is thought to be due to $Si(OSi)(OP)_3$ groups by comparison with the tetrahedral species at -120ppm in $Si_5O(PO_4)_6$ [16]. Likewise, the Si^{VI} resonance, at -213ppm, is thought to be due to $Si(OP)_6$ groups by comparison with the octahedral sites in $Si_5O(PO_4)_6$. The Si^{V} resonance at -165ppm is shifted upfield relative to that seen at -150ppm in $K_2Si_4O_9$ [18] and is thought to be due to $Si(OP)_5$.

The peak positions and widths in the alkali-free phosphosilicate spectrum are similar to those observed for the potassium tetrasilicate-P_2O_5 glasses. It contains a large, broad resonance centred about -118ppm and a small (~ 4% by area) peak centred about -212ppm. These peaks can be assigned as $Si(OSi)(OP)_3$ and $Si(OP)_6$ respectively. This result is of significance because Si^{VI} had not previously been observed in an alkali-free phosphosilicate glass [16].

The nominal potassium phospho-disilicates spectra are similar to those reported by Dupree et al. [41]. Each spectrum contains two peaks centred about -112 and -209ppm which can be assigned as Si^{IV} and Si^{VI} respectively. Both peaks are narrower than those in the potassium tetrasilicate-P_2O_5 and alkali-free phosphosilicate glass spectra, despite being acquired at a slower spinning speed. This suggests that the silicon sites in the potassium disilicate-P_2O_5 glasses have less static disorder (variation in next nearest neighbours and bond angles) than in the potassium tetrasilicate-P_2O_5 glasses.

The type and number of next nearest neighbours can be inferred from the isotropic chemical shift. Si^{IV} in quartz, in which silicon has four silicon next nearest neighbours, resonates at -107ppm [15]. The resonance shifts upfield on introducing phosphorus next nearest neighbours. The Si^{IV} peak in $Si_5O(PO_4)_6$ is reported at -120ppm [16]. $Si_5O(PO_4)_6$ contains both octahedral and tetrahedral silicon species which are linked by tetrahedral phosphate groups [57]. Each Si^{IV} has 3 phosphorus and 1 Si^{IV} next nearest neighbours.

By crude interpolation, neglecting the effects of variation in bond angle and the presence of other cations on the isotropic shift, the Si^{IV} species in the potassium disilicate-P_2O_5 glasses which resonate at -113ppm have one (or two) phosphorus next nearest neighbours.

A similar arguement can be made for the octahedral silicon environment. Stishovite has six silicon next nearest neighbours, $Si(OSi)_6$, and an isotropic shift of -191ppm [15], whilst $Si_5O(PO_4)_6$ has two nonequivalent $Si(OP)_6$ octahedra with isotropic shifts at -213.9 and -217.9ppm [58]. Two polymorphs of SiP_2O_7 which contain $Si(OP)_6$ octahedra, interconnected by PO_4 and P_2O_7 species at differing bond angles, have isotropic shifts reported at -213.7 and -220.6ppm [58].

A crude interpolation between $Si(OSi)_6$ at -191ppm and an average $Si(OP)_6$ site at -216ppm suggests that the Si^{VI} species in the potassium disilicate-P_2O_5 glasses which resonate at -210ppm have four (or five) phosphorus next nearest neighbours.

The 3mol.% increase in Si^{VI} content between KPDS77 and KPDS480 is the most significant change in speciation, between samples of the same compostion but different thermal history. This increase in Si^{VI} content with decreasing quench rate is not as dramatic as previously reported in $Na_2O.2SiO_2.3P_2O_5$ glasses [41].

8.3.4 ^{31}P MAS NMR

The ^{31}P MAS NMR peak positions, widths and relative intensities vary with composition but not significantly with thermal history. The processed spectra are shown in figure 8.9, and the fit parameters summarised in table 8.5.

	^{31}P δ (ppm) ± 0.5	^{31}P fwhm (ppm) ± 1	relative intensity (%) ± 1.5
KPTS77	-39.7	18.0	67.5
	-11.4	5.5	8.2
	0.0	4.2	24.3
KPTS480	-39.7	16.6	93.3
	-11.2	8.2	3.2
	0.0	3.4	3.5
KPTSSC	-39.9	17.2	94.7
	-11.1	3.6	1.6
	0.0	2.7	3.7
PSSC	-43.0	15.2	98.2
	-11.1	5.8	0.80
	-0.2	2.7	1.0
KPDS77	-32.5	12.1	43.9
	-21.8	8.1	56.1
KPDS293	-32.3	12.5	45.6
	-21.9	7.9	54.4
KPDS480	-32.4	11.4	41.0
	-21.8	8.1	59.0
KPDSSC	-32.0	10.8	41.2
	-21.8	8.3	58.8

Table 8.5 Gaussian fit parameters to phosphosilicate ^{31}P MAS NMR spectra.

The potassium-tetrasilicate-P_2O_5 glasses and the alkali free phosphosilicate glass spectra all contain a broad peak centred about -40ppm and two narrow peaks centred about-11 and 0ppm. The spinning sidebands are well removed from the isotropic peaks. The isotropic peak positions and widths remain constant (within the estimated experimental error) whilst the intensity of the two narrow peaks increase relative to the broad peak with quench rate.

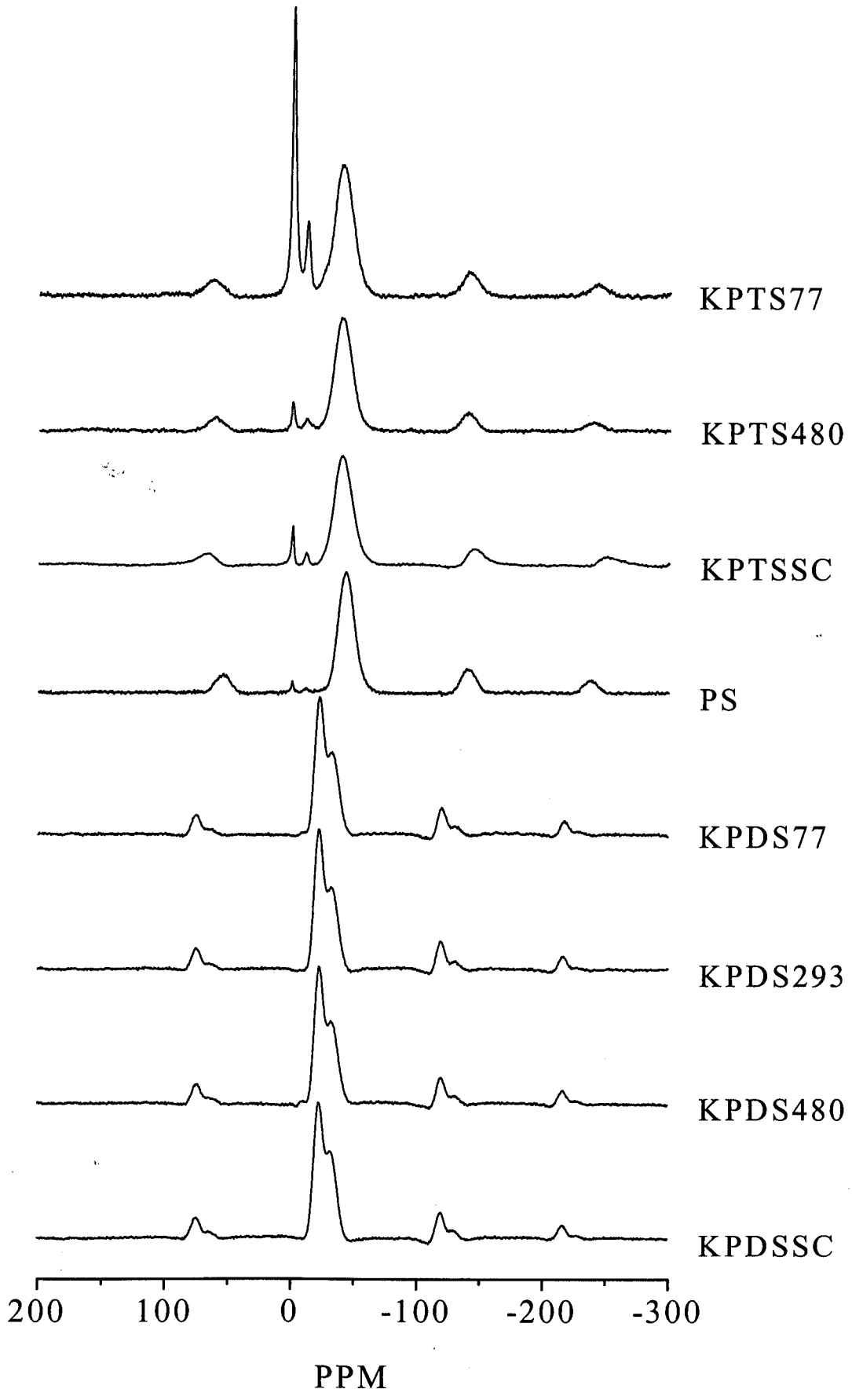

Figure 8.9 ^{31}P MAS NMR spectra for all phosphosilicate samples relative to H_3PO_4.

The intensity of the spinning sidebands of the resonance at -40ppm indicates that the peak is symmetric with a large chemical shift anisotropy. The isotropic shift is similar to but the chemical shift anisotropy is much larger than that reported for silicon monophosphate [59]. No ^{29}Si NMR data nor structural characterisation of $Si_3(PO_4)_4$ could be found in the literature, other than a powder diffraction pattern (JCPDS 22-1380) [60]. It is not considered possible to conclusively assign this peak, although further discussion is given in section 8.3.8.

The two peaks centred about 0 and -11ppm are considered to be due to hydrated ortho ($P\text{-}Q^0$) and pyro ($P\text{-}Q^1$) phosphate groups. The widths of these peaks (FWHM ~ 5ppm) are typical of terminal phosphate groups within an amorphous network [44] and the shifts are up-field of those measured in crystalline $K_4P_2O_7$ and K_3PO_4 [61].

^{31}P MAS NMR spectra were acquired for KPTS480 after several minutes exposure to atmospheric moisture, see figure 8.10. The relative intensity of the two narrow peaks centred about 0 and -11ppm increase relative to the broad peak at -40ppm with no change in the observed chemical shifts. These peaks at 0 and -11ppm are considered to be due to H_3PO_4 and $H_4P_2O_7$ respectively. The potassium cations are not thought to associate with the terminal phosphate groups. A third narrow peak at -24ppm is also observed after 30 minutes exposure to moisture. The peak fit parameters are summarised in table 8.6.

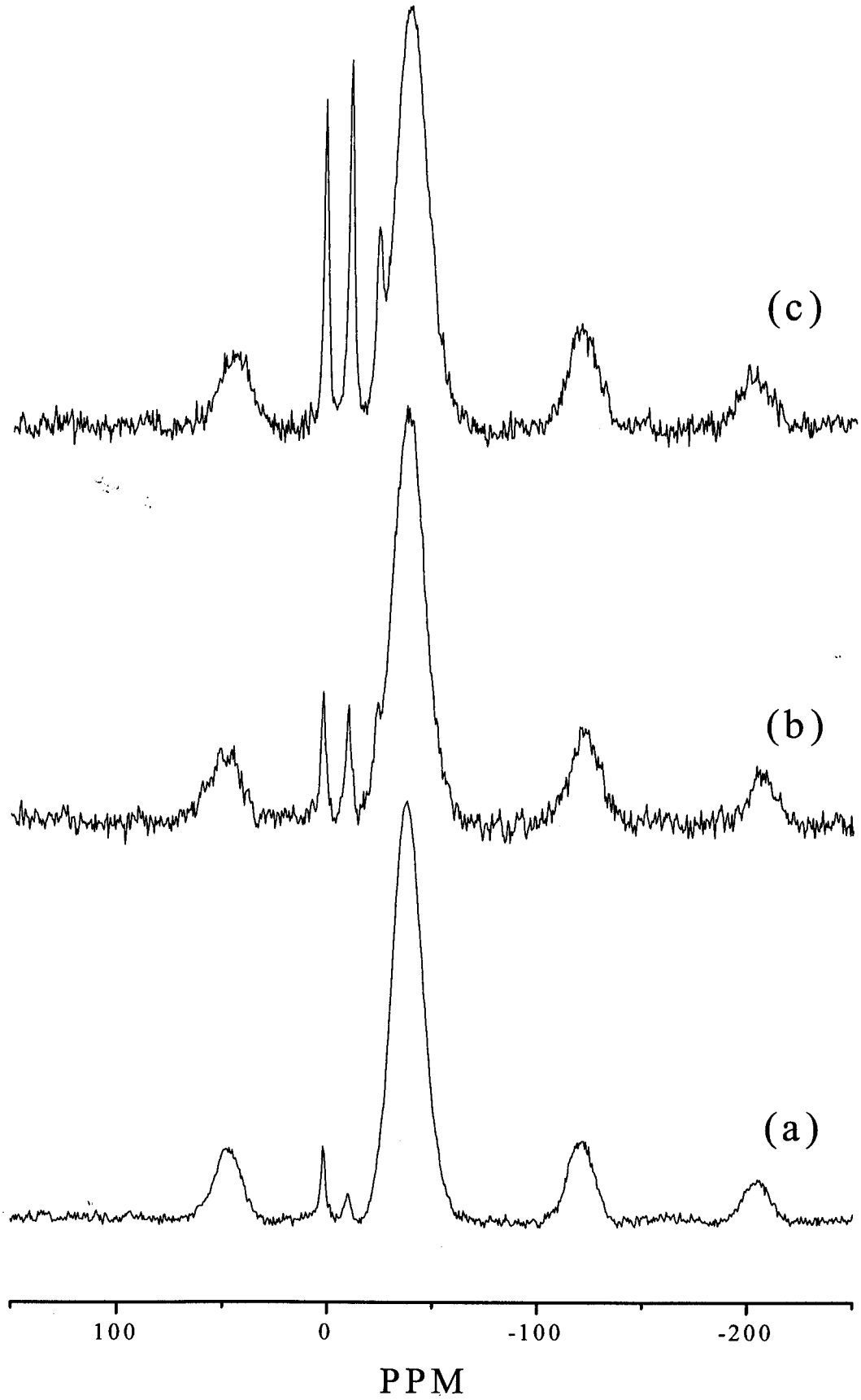

Figure 8.10 ^{31}P MAS NMR spectra relaive to H_3PO_4 for KPTS480 exposed to atmospheric moisture for (a) 0, (b) 5 and (c) 30 minutes.

	^{31}P δ (ppm) ± 0.5	^{31}P fwhm (ppm) ± 1	relative intensity (%) ± 1.5
KPTS480 fresh powder	-37.9	17.2	98.2
	-10.7	2.5	0.5
	1.3	0.3	1.3
KPTS480 5 minutes exposure	-37.6	18.3	92.3
	-22.7	2.6	1.1
	-9.4	3.9	3.3
	2.5	3.4	3.3
KPTS480 30 minutes exposure	-37.9	18.7	82.5
	-22.8	3.0	2.8
	-9.6	3.4	8.2
	2.4	3.1	6.5

Table 8.6 Gaussian fit parameters to ^{31}P MAS NMR spectra for hydrated KPTS480.

The alkali free phosphosilicate ^{31}P MAS NMR spectrum is similar to those for the potassium tetrasilicate-P_2O_5 glasses. It contains two small, narrow peaks at 0 and -11ppm, which are thought to be due to hydrated terminal phosphate groups, and a broad peak at -43ppm which is slightly narrower and shifted up-field relative to that in the nominal potassium-tetrasilicate-P_2O_5 spectra due to the absence of K^+.

The nature of the phosphate species in these glasses can be implied from the absorption of atmospheric moisture. Ultra-phosphate glasses are susceptible to deliquescence because the protons attack the double bond in the $PO_{4/2}$ groups. Alkali phosphates are less susceptible to attack from protons because the depolymerised phosphate groups do not have this double bond. Therefore the observation of terminal phosphate groups suggests that the phosphate species in the potassium tetrasilicate-P_2O_5 and alkali-free phosphosilicate glasses contain a double bond. No terminal phosphate groups are observed in the potassium disilicate-P_2O_5 glass spectra, which are considered not to contain P-Q^3 species.

The potassium disilicate-P_2O_5 ^{31}P MAS NMR spectra contain two overlapping peaks centred about -22 and -32ppm and well removed spinning sidebands. The shifts, widths and relative intensities all remain constant, within the estimated experimental error, for various quench rates. The intensity of both sets of spinning sidebands show that both peaks have a large asymmetric chemical shift anisotropy. This suggests that both species have low symmetry, ie. P-Q^2, or P-Q^4 with different next nearest neighbours. The resonance at -22ppm is comparable to that predicted for potassium metaphosphate, KPO_4, at -18.5ppm [62]. The resonance at -32ppm is thought to be due to P-Q^4 species, although it is noted that it is downfield from and has a much larger chemical shift anisotropy than the P-Q^4 species in SiP_2O_7 [59].

8.3.5 ^{27}Al MAS NMR

No aluminium was found in PS1 above the aluminium impurity in the SiN spinner used to make the ^{27}Al NMR measurements.

8.3.6 ^{1}H MAS NMR

The ^{1}H MAS NMR data were acquired several months after the neutron diffraction, ^{31}P and ^{29}Si MAS NMR data. The samples are thought to have absorbed atmospheric moisture during this time, so quantitative results are not reported. Each spectrum contains an isotropic peak centred about 11 ± 1 ppm with spinning sidebands on either side. The processed spectra are shown in figure 8.11 and Gaussian fit parameters to each spectra are summarised in table 8.7.

	KPTS77	KPTS480	KPTSSC	PS	KPDS77	KPDS293	KPDS480	KPDSSC
δ (ppm) ± 2	12	12	12	11	13	13	13	13
fwhm (ppm) ± 1	6.7	7.4	7.5	2.2	4.6	6.9	7.8	4.9

Table 8.7 Guassian fit parameters to ^{1}H MAS NMR spectra.

All the samples used in this study were stored under vacuum in a desiccator and the sample holders; vanadium cans and MAS NMR rotors were packed in a dry box. However the samples were exposed to atmospheric moisture on cooling from the melt, and the dry box was later found not to be very dry. The proton content increased with the time after the sample was powdered. The signal to noise ratio is significantly worse in the ^{1}H MAS NMR spectra for freshly powdered KPDS77 and KPDSC.

Each of the ^{1}H spectra contain a single resonance centred about 12ppm in the potassium tetrasilicate-P_2O_5 samples, 13ppm in the potassium disilicate-P_2O_5 samples and 11ppm in the alkali-free phosphosilicate. These shifts are comparable to the resonance at 13ppm assigned as weakly bonded P-O-H sites in a combined infra-red and NMR study of -OH containing ultaphosphate glasses [63].

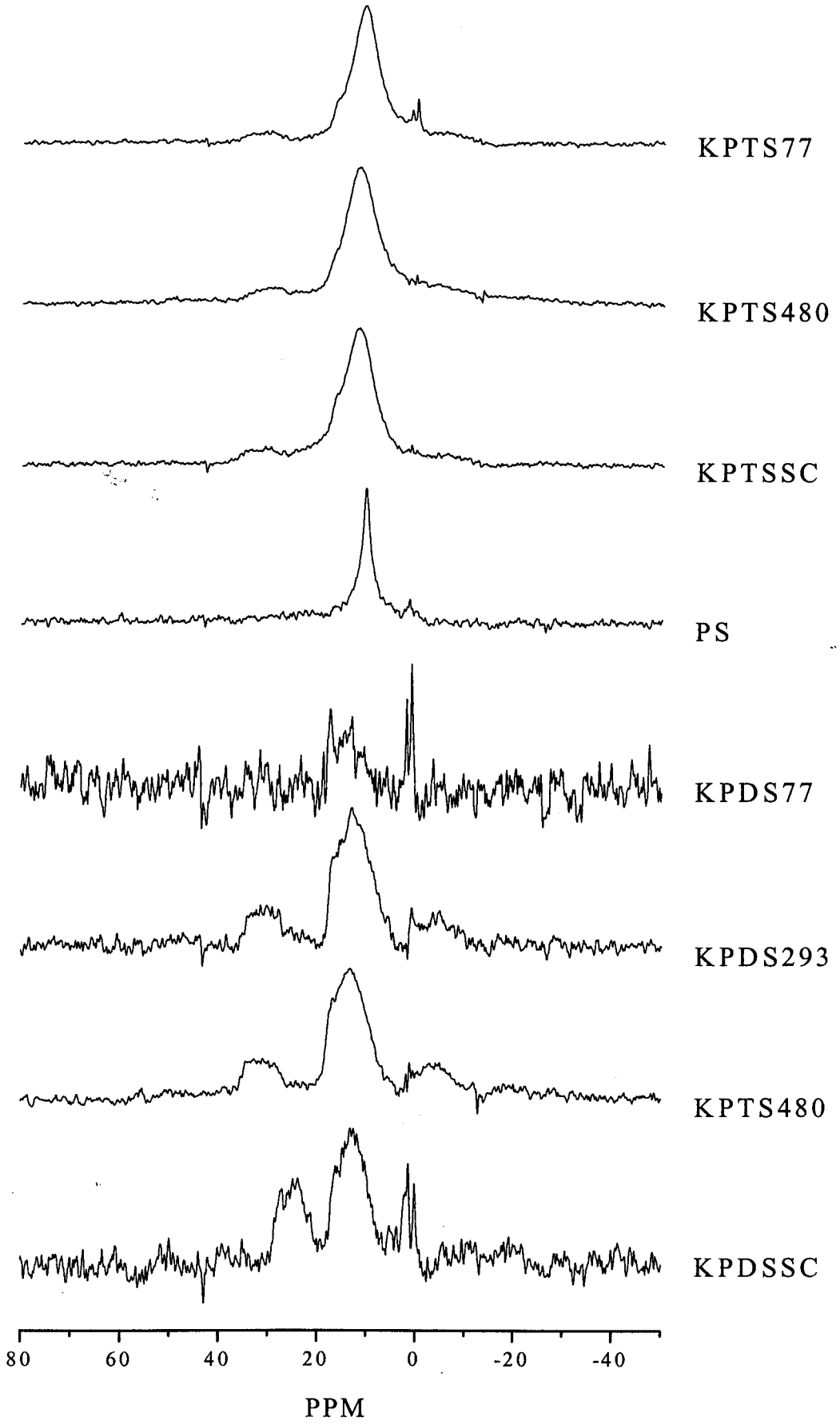

Figure 8.11 ^{1}H MAS NMR spectra for all phosphosilicate samples relative to TMS.

8.3.7 NEUTRON DIFFRACTION

The data were corrected using the ATLAS suite software, as outlined in chapter 2. No additional corrections were made for proton contamination. The experimental and theoretical transmission cross-sections were in good agreement for each sample, suggesting less than 1mol.% H_2O.

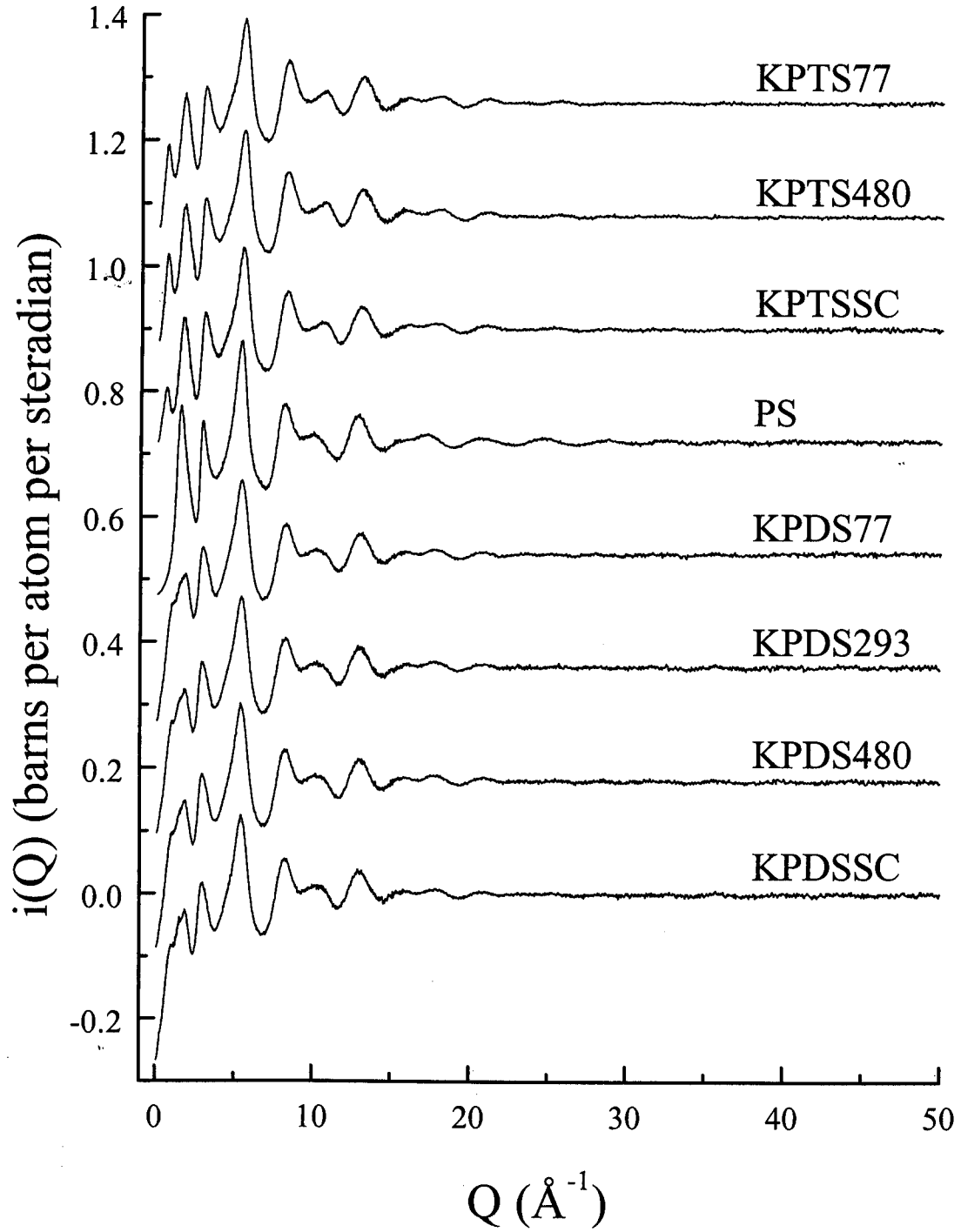

Figure 8.12 i(Q) for all phosphosilicate samples.

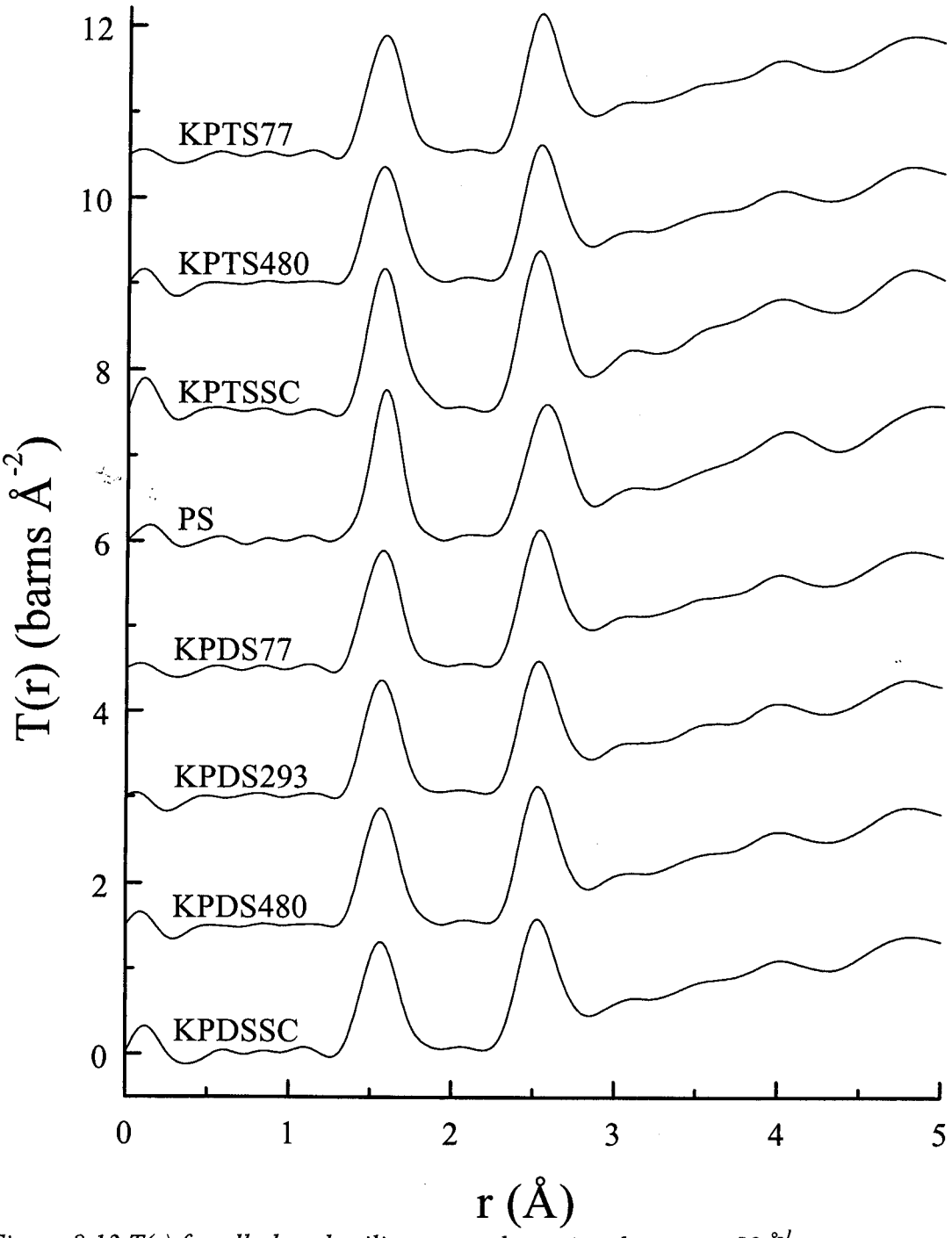

Figure 8.13 T(r) for all phosphosilicate samples, using data up to 50Å^{-1}.

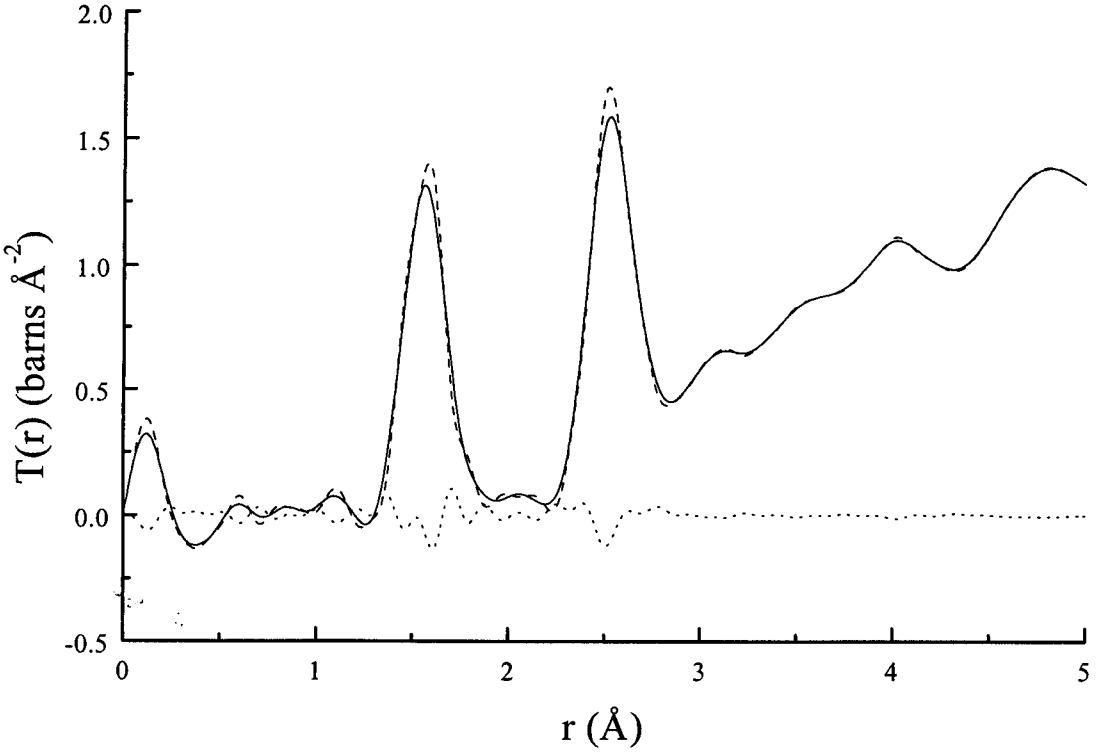

Figure 8.14 KPDSSC T(r) transformed to Q_{max} = 35Å (dashed line), 50Å (solid line) and the residual between the two (dotted line).

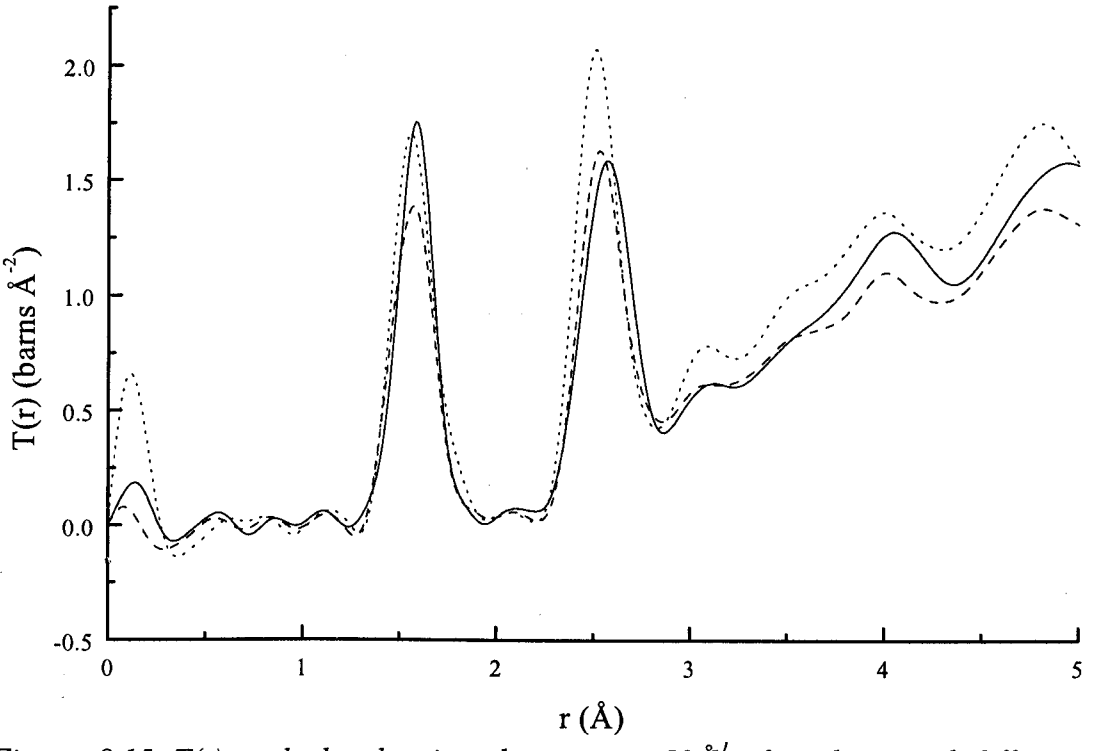

Figure 8.15 T(r), calculated using data up to 50Å^{-1}, for glasses of different composition KPDS77 (dashed line), KPTS77 (dotted line) and PS (solid line).

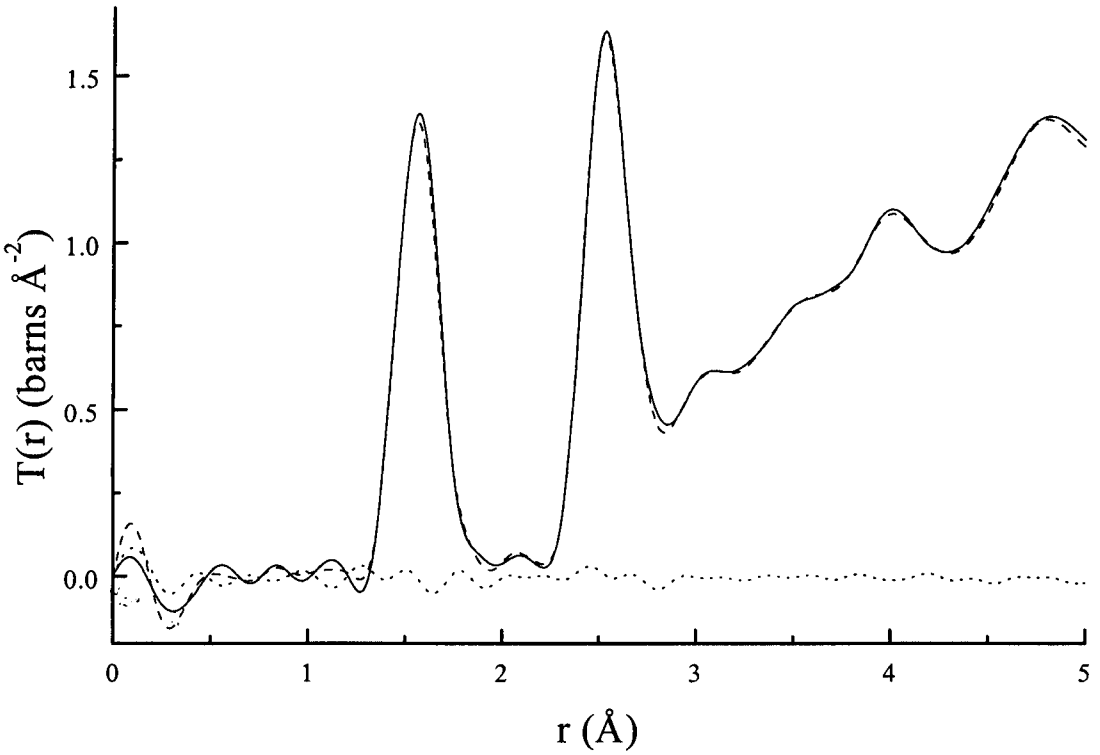

Figure 8.16 T(r) calculated using data up to 50Å^{-1} for glasses of identical composition but different proportions of higher co-ordinated silicon species; KPDS77 (solid line) and KPDS480 (dotted line).

The distinct scattering for each sample are shown in figure 8.12. The alkali-free phosphosilicate, which contains only 11mol.%P_2O_5, gives an i(Q) which is very similar to that for silica [64] with a strong first sharp diffraction peak (FSDP) at 1.56Å^{-1}. The potassium tetrasilicate-P_2O_5 glass i(Q)s are also similar to that for silica but contain a further peak at 0.65±0.01Å^{-1}. This relates to intermediate and extended range range structure of the order of 9Å. The FSDP is not so clear in the potassium disilicate-P_2O_5 glasses, similar to those reported for small cation alkali silicates [39].

The sample scattering function at high Q (above 35Å^{-1}) is very weak but does contribute to an improvement in the resolution, see figure 8.14. When T(r) is calculated using data up to 50Å^{-1}, compared with T(r) calculated using data up to 35Å^{-1}, the first peak is shifted to 1.58Å from 1.57Å. This improved resolution reveals a slight shoulder on the low r side and a more significant shoulder at 1.78Å. The shoulder at 1.78Å is not thought to be due to the systematic problem outlined in chapters 6 and 7, because data for the partially crystallised tin silicate (chapter 6) and other data [25, 33 & 34] recorded on LAD at about the time of this experiment do

not appear to have this systematic problem. It is assumed that this data is accurate to high Q and is presented up to 50Å^{-1}.

The total correlation functions shown in figure 8.13 have been calculated using data up to 50Å^{-1}. It is possible to distinguish between the T(r)s for glasses of different composition, see figure 8.15, but not between those for glasses of identical composition which have different proportions of silicon species, see figure 8.16. This is because the change in speciation between glasses of identical composition are very small and several Si-O and P-O correlations overlap, see table 8.8.

	K^{VI}	Si^{IV}	Si^{V}	Si^{VI}	$P\text{-}Q^2$	$P\text{-}Q^3$	$P\text{-}Q^4$
R-O bond length (Å)	2.79	1.62	1.71	1.77	1.52	1.52	1.52

Table 8.8 First shell interatomic separation, calculated according to bond valence considerations [54].

The large widths of the Si^{IV} and $P\text{-}Q^n$ resonances in the ^{29}Si and ^{31}P NMR spectra, see figures 8.7 and 8.9, indicate a large variation in the type of next nearest neighbours and/or bond angle distribution. Hence, the Si^{IV}-O and ($P\text{-}Q^n$)-O correlations in T(r) are also expected to be broad.

The experimental T(r)s are not fitted nor simulated to obtain structural information because the uncertainty in sample composition introduces significant uncertainty in the area of each $t_{ij}(r)$. The potassium tetrasilicate-P_2O_5 glass T(r)s are thought to contain Si^{IV}-O, Si^{V}-O, Si^{VI}-O and ($P\text{-}Q^n$)-O correlations between 1.4 and 1.9Å. K-O and various O-O correlations are thought to overlap between 2.3 and 3.5Å. The potassium disilicate-P_2O_5 glass T(r)s are thought to contain Si^{IV}-O, Si^{VI}-O ($P\text{-}Q^2$)-O and ($P\text{-}Q^4$)-O correlations between 1.4 and 1.9Å. This combination of peaks can be simulated for an average potassium disilicate-P_2O_5 structure using typical widths and positions for each contribution.

For the purpose of this simulation the two silicon species, Si^{IV}, Si^{VI}, are assumed to have bond lengths similar to those in c-$K_2Si_4O_9$ [8] and FWHMs as reported for $Si\text{-}Q^2$ species in v-K_2O-SiO_2 using data up to Q_{max}= 40Å^{-1} [65]. This width is considered typical of the static disorder because the ^{29}Si MAS NMR FWHMs, see table 8.4, are comparable to those reported for alkali silicates by Maekawa [56]. The areas associated with both Si-O peaks were calculated from the sample composition and the ratio of the two areas from the ^{29}Si NMR data.

The P-Q^2 bond lengths are assumed to be similar to that in ν-KPO_3 [66] and the P-Q^4 correlation similar to that in c-SiP_2O_7 [11]. The area associated with the P-Q^2 and P-Q^4 peaks was calculated from the sample composition. Hoppe reported two distinguishable P-Q^2 correlations in KPO_3 using data measured up to 50$Å^{-1}$ on LAD [66]. The simulation shown below, see figure 8.17, uses these bond lengths and widths, see table 8.9, in the ratio 1(P-O_T):1(P-O_B). The P-Q^4 species in c-SiP_2O_7 also has two distinguishable bond lengths associated with P-O-Si^{VI} and P-O-P bonds. In c-SiP_2O_7 these two P-Q^4 peaks are in the ratio 3(P-O-Si^{VI}):1(P-O-P) but this simulation uses a 1(P-O-Si^{VI}):1(P-O-P) ratio to represent the charge balancing considerations detailed in section 8.3.9.

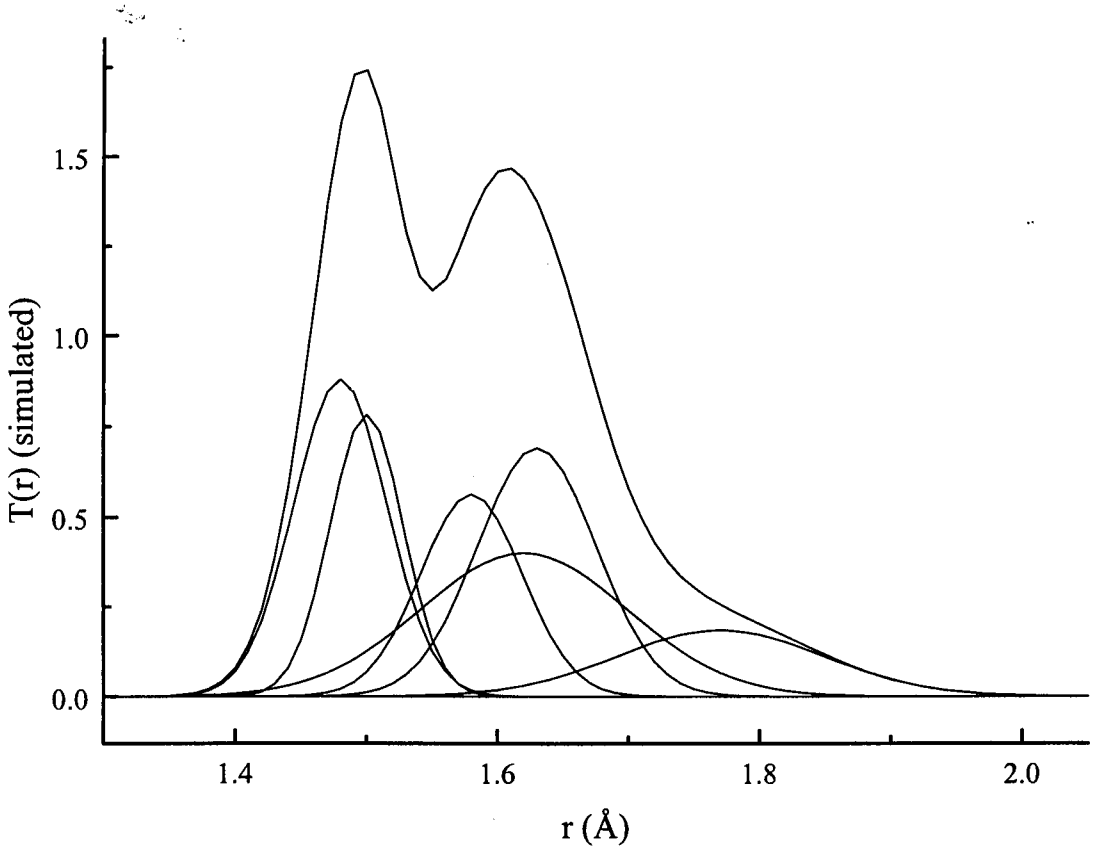

Figure 8.17 Simulated T(r) for the average potassium disilicate-P_2O_5 glass composition.

	Si^{IV}-O	Si^{VI}-O	$(P-Q^2)$-O		$(P-Q^4)$-O	
reference	c-$K_2Si_4O_9$ [11]	c-$K_2Si_4O_9$ [11]	v-KPO_3 [Hoppe]		c-SiP_2O_7 [Till.]	
bond length (Å)	1.62	1.77	1.48	1.63	1.50	1.58
$\langle u^2\rangle^{1/2}$	0.079^{+}	0.079^{+}	0.0356	0.0454	0.028^{*}	0.039^{*}

Table 8.9 Summary of bond lengths and widths ($\langle u^2\rangle^{1/2}$) of species in an average potassium disilicate-P_2O_5 structure, as reported from diffraction studies of related materials. Superscripts indicate that the widths are taken from: $^{+}$v-K_2O-SiO_2 [65] and *v-P_2O_5 [66].

The simulated T(r) for the proposed average disilicate structure, shown in figure 8.17, consists of five overlapping peaks which contribute to a broad asymmetric peak centred about with two shoulders at 1.50 and 1.61Å. The experimental correlation functions do not reveal the detail shown in figure 8.17. This indicates that the phosphosilicate network in these glasses is more disordered than in either modified silicate or modified phosphate networks. As noted previously, this is also apparent from the broad peaks in the ^{29}Si and ^{31}P NMR spectra.

8.3.8 POTASSIUM TETRASILICATE-P_2O_5 AND ALKALI-FREE PHOSPHOSILICATE GLASS SRUCTURE

It is evident from the ^{29}Si and ^{31}P NMR spectra that the potassium tetrasilicate-P_2O_5 and the alkali-free phosphosilicate glasses consist of similar structural units. The ^{29}Si and ^{31}P MAS NMR spectra are in good agreement with those reported by Lockyer [42] for glasses of a similar composition with the exception of the terminal phosphate peak positions.

The relative proportion of terminal phosphate groups in the potassium tetrasilicate-P_2O_5 samples increases with quench rate. However, it is not clear from this study whether this is due to the amount of exposure to atmospheric moisture during cooling or the hydrophilic nature of the resulting glasses. The splat cooled glasses were exposed to more atmospheric moisture on cooling than the slow cooled glasses because their surface area was large and it was difficult to completely remove condensation on the two liquid nitrogen cooled plates. The slow cooled glasses were left to cool in their crucible with a smaller exposed surface area. The alkali free phosphosilicate was also left to cool in its crucible and also has a small proportion of terminal phosphate groups. However the neutron diffraction data

(which was the first experimental data collected on these glasses) does not indicate the large proton content observed in the ^{31}P MAS NMR spectra.

The protons detected indirectly by the ^{31}P NMR are considered independent of the network. There are insufficient protons to charge balance the high co-ordinated silicon species, the proton content does not increase with the Si^{V} and Si^{VI} contents and the ^{31}P isotropic shift remains invariant on further exposure to moisture. However, the time dependence of the proton contamination complicates the study of glass structure. The samples may have been attacked by moisture during sample preparation but they are considered most susceptible during storage, particularly as powders. Each technique studied a slightly different series of glasses because proton content, which increases with time, removes $P\text{-}Q^{n}$ phosphate groups from the network.

	K	Si^{IV}	Si^{V}	Si^{VI}	H_3PO_4	$H_4P_2O_7$	$P\text{-}Q^{n}$
KPTS77	16	21	2	11	12	4	34
KPTS480	16	21	3	10	2	2	46
KPTSSC	14	22	4	14	2	1	43
PS	-	76	-	4	0.5	0.5	19

Table 8.10 Proportion of cations (mol.% ± 1) in potassium tetrasilicates-P_2O_5.

The small variations in the distribution of cation species, see table 8.10, cannot be interpreted either as a function of thermal history or composition. No two samples have identical compositions, due to the loss of volatiles on cooling and phosphate groups being removed by protons. It is also not possible to interpret the proportion of cations in terms of composition as this is dependent upon the thermal history [53].

	K	Si^{IV}	Si^{V}	Si^{VI}	$P\text{-}Q^{n}$
mol.% (±1)	16	23	3	13	45
δ (ppm) (±1)	-	-118	-165	-213	-40
fwhm (ppm) (±1)	-	13	13	7	17

Table 8.11 Average isotropic chemical shifts and relative proportions of cations in the potassium tetrasilicate-P_2O_5 samples.

It is possible to consider an average distribution of cation species, see table 8.11. The ^{29}Si resonances at -118, -164 and -212ppm are considered to be due to $Si(OP)_4$, $Si(OP)_5$ and $Si(OP)_6$ species, as described in section 8. It is not possible to assign a single phosphate species which contributes to the charge neutrality of the network.

The phosphate species in the potassium tetrasilicate-P_2O_5 glasses are thought to have silicon next nearest neighbours, $P(OSi)_n$ because the ^{31}P MAS NMR spectra are similar to that for the alkali-free phosphosilicate glass. The alkali-free phosphosilicate glass contains only 11mol.% P_2O_5, so each phosphorus is likely to have silicon next nearest neighbours. The single, broad peak at -43ppm is shifted up-field of the potassium tetrasilicate-P_2O_5 glasses, due to the absence of K^+, but the P-Q^n species is assumed to be the same.

The ^{31}P NMR spectra all consist of a single broad but symmetric resonance. This suggests that the glasses contain a single phosphate species with a spread in sites. This single phosphate species must also contribute to charge balance the high co-ordinated silicon species because the potassium tetrasilicate-P_2O_5 glasses contain less K^+ than total $(SiO_5)^-$ and $(SiO_6)^{2-}$ and the alkali-free phosphosilicate also contains 4mol.% Si^{VI}. A single phosphate species with a fractional net positive charge; P-Q^n (where $3<n<4$), could not be found in the literature.

It is not possible to suggest a possible structure for the potassium tetrasilicate-P_2O_5 glasses because it is not possible to define the nature of the network phosphate species. However, the distribution of species obtained from this study do contradict the interpretation given by Lockyer [42]. Lockyer assigned the broad resonance at -40ppm to metaphosphate chains. However, the proportion of cations calculated from the relative intensities in the NMR spectra and the sample compositions, see table 8.11, show that the potassium tetrasilicate-P_2O_5 glasses have insufficient K^+ to charge balance either metaphosphate chains, $(P\text{-}Q^2)^-$, and/or the high co-ordinated silicon species, $(SiO_5)^-$ and $(SiO_6)^{2-}$.

8.3.9 POTASSIUM DISILICATE-P_2O_5 GLASS STRUCTURE

The proportion of cation species can be calculated from the relative intensities in the NMR spectra and the sample composition, see table 8.12.

	K	Si^{IV}	Si^{VI}	$P\text{-}Q^2$	$P\text{-}Q^4$
KPDS77	24	21	6	27	22
KPDS293	24	19	8	27	22
KPDS480	24	18	9	29	20
KPDSSC	23	19	9	29	20

Table 8.12 The proportion of cations (mol.% ± 1) in each potassium disilicate-P_2O_5 glass.

The potassium disilicate-P_2O_5 glasses were prepared and stored in a similar manner to the potassium tetrasilicate-P_2O_5 glasses and the ^1H MAS NMR data indicate similar proton contents and environments in all the glasses but the ^{31}P MAS NMR spectra for the potassium disilicate-P_2O_5 glasses do not contain narrow peaks at 0 and -11ppm. The protons are thought to modify the phosphate in preference to the silicate species, as in all the glasses, but the P-O-H linkages may contribute to the broad peaks at -22 and/or -32ppm rather than remove phosphate groups from the network. Alternatively the proton content measured by ^1H MAS NMR may have been absorbed during storage and not present when the ^{31}P MAS NMR data was acquired. This cannot be resolved by this study.

The changes in speciation content with thermal history, are sufficiently small to consider the average experimental results, see table 8.13 and to interpret these in terms of an average glass structure. It is possible to suggest a model structure linking these cation species in these proportions and maintain an overall charge neutrality.

	K	Si^{IV}	Si^{VI}	$P\text{-}Q^2$	$P\text{-}Q^4$
mol.% (±1)	24	19	8	28	21
δ (ppm) (±1)	-	-113	-210	-22	-32
fwhm (ppm) (±1)	-	11	6	8	12

Table 8.13 Average isotropic chemical shift, FWHM and relative proportion of each cation species in the potassium disilicate-P_2O_5 glasses.

To maintain local charge neutrality each $(P\text{-}Q^4)^+$ species requires $(n/2)Si^{VI}$ next nearest neighbours, where n is the number of $(P\text{-}Q^4)^+$ next nearest neighbours to each Si^{VI} species. The Si^{VI} MAS NMR isotropic chemical shift suggests that n is

four, in which case each $(P\text{-}Q^4)^+$ group has two Si^{VI} next nearest neighbours. The remaining two Si^{VI} linkages are thought to be bridging to either tetrahedral silicon or potassium metaphosphate chains. A further COSY MAS NMR experiment, similar to that used by Knight [49], is necessary to differentiate between Si^{VI} with four $P\text{-}Q^4$ and two $Si\text{-}Q^4$ and Si^{VI} with four $P\text{-}Q^4$ and two $P\text{-}Q^2$ next nearest neighbours.

A possible potassium disilicate-P_2O_5 glass structure, assuming $Si^{VI}\text{-}Si\text{-}Q^4$ linkages, is illustrated in figure 8.18. The $(PO_4)^+$ species, on average, bridge to two Si^{VI}, one $P\text{-}Q^2$ and one $(PO_4)^+$ species. The excess $(PO_4)^+$ species can be considered to form a third link in the P_2O_7 groups between the Si^{VI} species. This charge balances neighbouring potassium deficient metaphosphate chains which form, on average, three membered chains.

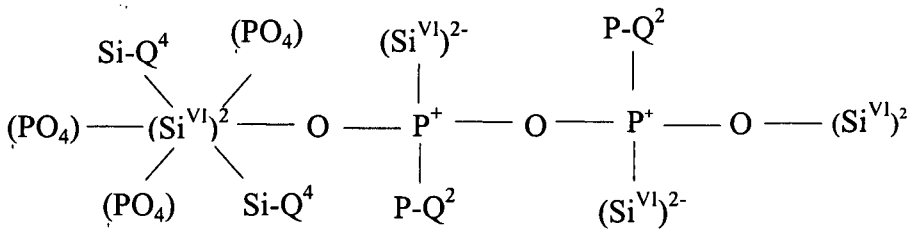

Figure 8.18 Proposed model of potassium disilicate-P_2O_5 glass structure.

The glass structure proposed above is one of several models which interconnect the Si^{VI}, $Si\text{-}Q^4$, $P\text{-}Q^2$ and $P\text{-}Q^4$ species in an amorphous potassium disilicate-P_2O_5 network. The type and number of next nearest neighbours is not clear from this data but the association of the potassium with metaphosphate chains relates to the work by Nogami [45] in which replacing the modifier cation with a different modifying cation had no effect on the number of Si^{VI} species. The KPO_3 chains introduce disorder into the amorphous network and are necessary in forming a network which accommodates Si^{VI} species without directly charge balancing the Si^{VI}, as previously thought [41].

8.4 CONCLUSIONS AND FUTURE WORK

All the samples are considered alumina-free and the water contents in each sample are not considered to influence the average glass structure. Each glass is thought to consist of a modified phosphosilicate network possibly with silica and phosphate rich regions but not phase separated.

The discussion of trends in experimental results with respect to glass structure is greatly dependent upon the accuracy with which the sample composition can be determined. Without reference materials of the same composition with the same matrix and the same density as the samples then the XRF analysis can only be used to estimate the sample compositions. The deduced composition for each glass in this study are considered accurate to ±1mol.%.

The neutron diffraction study of these glasses does not provide much structural information. The detail in scattering at low Q changes with composition. The total correlation functions, calculated using data up to $50Å^{-1}$, also distinguishes the glasses of different composition. However, the changes in the distribution of species between glasses of the same composition are not observed by neutron diffraction. Each total correlation function contains a broad peak about 1.6Å, which is thought to contain several Si-O and P-O correlations, and a second broad peak about 2.7Å which is thought to contain O-O and K-O correlations. These peaks in T(r) were not fitted or simulated to obtain structural information because of the uncertainty in the assignment and distribution of species. The experimental total correlation functions are not as well resolved as that simulated for an average potassium disilicate-P_2O_5 glass. This suggests that the phosphosilicate network is more disordered than that in modified phosphate and silicate glasses (which were used to define the simulated peak positions and widths).

The distribution of and type of structural units in each glass were determined by ^{29}Si and ^{31}P MAS NMR. The proportion of high co-ordinated silicon species changed with thermal history but this is thought to be partially due to the changes in composition with thermal history. Si^{VI} species were observed in an alkali-free phosphosilicate glass, unlike in previous studies [16 & 44]. The resonance observed at -164ppm in the ^{29}Si NMR spectra for the potassium tetrasilicate-P_2O_5 glasses is thought to be due to Si^{V} species, unlike previously reported [42].

The phosphate species are thought to accommodate the higher co-ordinated silicon species within a phosphosilicate network. There is no evidence that the tetrahedral silicon repolymerise with increasing high co-ordinated silicon content, as described by Xue et al. for high pressure alkali silicate glasses [19].

The potassium tetrasilicates-P_2O_5 and alkali-free phosphosilicate glasses are thought to contain similar structural units. The shifts and widths of the peaks in the ^{29}Si and ^{31}P NMR spectra are considered to be due to $Si(OP)_4$, $Si(OP)_5$, $Si(OP)_6$ and $P(OSi)_n$ species. The tetrahedral silicon and single phosphate species are thought to have significant variation in either the type of next nearest neighbour and/or the bond angle between them. The glasses are susceptible to attack from atmospheric moisture. This is typical of $P\text{-}Q^3$ phosphate species. However, it is not possible to assign the type of phosphate species from the ^{31}P NMR data and maintain charge neutrality.

A possible average potassium disilicate-P_2O_5 glass structure can be proposed in terms of the proportion and type of network forming and network modifying species. These can be deduced from the ^{29}Si and ^{31}P MAS NMR spectra with reference to shifts reported for similar crystalline and amorphous systems and the speciation necessary to maintain net zero charge. The potassium disilicate-P_2O_5 glasses are thought to consist of $Si(OP)_3(OSi)$, $Si(OP)_4(OSi)_2$, $(P\text{-}Q^2)^-$ and $(P\text{-}Q^4)^+$ species. It is not possible to define the manner in which the structural units interconnect. No crystalline alkali-silicate-P_2O_5 has been found in the literature.

This study could be continued by;

- recording ^{29}Si NMR for $CaSiO_3$ to obtain a characterised Si^V shift
- recording ^{29}Si and ^{31}P NMR data and characterising $Si_3(PO_4)_4$
- 2D COSY ^{29}Si NMR to distinguish the type and number of next nearest neighbours
- crystallising and characterising potassium phosphosilicate crystal structures
- studying the effect of the hygroscopicity of the glasses on the glass structure

9.11 REFERENCES

[1] R.Dupree, D.Holland and M.G.Mortuza, *Nature* **328** (1987) 416-417

[2] W.Zachariasen, *J.Am.Chem.Soc.* **54** (1932) 3841

[3] J.F.Stebbins and M.Kanzaki, *Science* **251** (1991) 294-298

[4] C.A.Angell, C.A.Scamehorn, C.C.Phifer, R.R.Kadiyala and P.A.Cheeseman, *Phys. Chem. Min.* **15** (1988) 221-227

[5] S.M.Ridgen, T.J.Ahrens and E.M.Stolper, *J.Geophys.Res.* **93** (1988) 367

[6] E.Knittle and R.Jeanloz, *Science* **235** (1987) 668

[7] W.Sinclair and A.E.Ringwood, *Nature* **272** (1978) 715

[8] D.K.Swanson and C.T.Prewitt, *Am. Mineral.* **68** (1983) 581

[9] L.Strixrude and R.E.Cohen, *Nature* **364** (1993) 613-615

[10] B.D.Santarsiero, X.Xue and M.Kanzaki, *Trans.ACA* **27** (1991) 279-283

[11] E.Tillmans, W.Gerbert and W.H.Baur, *J.S.S.Chem.*, **7** (1973) 69-84

[12] R.J.Angel, N.L.Ross, F.Seifert and T.F.Fliervoet, *Nature* **384** (1996) 441-444

[13] J.F.Stebbins and I.Farnan, *Science* **255** (1992) 586-589

[14] X.Xue, J.F.Stebbins, M.Kanzaki and R.G.Trønnes, *Science* **245** (1989) 962-964

[15] J.V.Smith and C.S.Blackwell, *Nature* **303** (1983) 223-225

[16] T.L.Weeding, B.H.W.S.de Jong, W.S.Veeman and B.G.Aitken, *Nature* **318** (1985) 352

[17] R.Dupree and D.Holland in 'Glasses and Glass-Ceramics' ed. M.H.Lewis Chapman and Hall (1989) pp1-40

[18] J.F.Stebbins and P.McMillan, *Am. Min.* **74** (1989) 965-968

[19] X.Xue, J.F.Stebbins, M.Kanzaki, P.F.McMillan and B.Poe, *Am. Min.* **76** (1991) 8-26

[20] M.Ueno, M.Misawa and K.Suzuki, *Physica* **120B** (1983) 347-351

[21] J.F.Stebbins and P.McMillan, *J.Non-Cryst.Solids* **160** (1993) 116-125

[22] M.F.Hochella and G.E.Brown, *Geochimica et Cosmochimica Acta* **49** (1985) 1137

[23] H.Gan and P.C.Hess, *Am.Mineral.* **77** (1992) 495-

[24] Q.Williams and R.Jeanloz, *Science* **239** (1988) 902

[25] U.Hoppe, G.Walter, A.Barz, D.Stachel and A.C.Hannon, *J.Phys.Cond.Matt.* **10** #2 (1998) 261-270

[26] A.C.Wright, R.A.Hulme, D.I.Grimly, R.N.Sinclair, S.W.Martin, D.L.Price and F.L.Galeener, *J.Non-Cryst.Solids* **129** (1991) 213

[27] M.Jansen and B.Luer, *Z.Kristallogra.* **177** (1986) 149

[28] H.El.Arbib,B.Elouadi, J.P.Chaminade and J.Dariet, *J.Solid State Chem.* **127** (1996) 350

[29] D.Stachel, I.Svoboda and H.Fuess, *Acta Crystallogra.* **C51** (1995) 1049

[30] T.Uchino and Y.Y.Ogata, *J.Non-Cryst.Solids* **181** (1995) 175

[31] U.Hoppe, G.Walter, R.Kranold, D.Stachel and A.Barz, *J.Non-Cryst.Solids* **192-193** (1995) 28

[32] U.Hoppe, D.Stachel and D.Beyer, *Physica Scripta* **T57** (1995) 122-126

[33] U.Hoppe, G.Walter, D.Stachel, A.Barz and A.C.Hannon, *Z.Naturforsch* **52a** (1997) 259

[34] U.Hoppe, G.Walter, R.Kranold, C.Stachel, A.Barz and A.C.Hannon, *Physica B* **234-236** (1997) 388

[35] P.Losso, B.Schnabel, C.Jäger, U.Sternberg, D.Stachel and D.O.Smith, *J.Non-Cryst.Solids* **143** (1992) 265

[36] R.K.Brow, D.R.Tallant, J.J.Hudgens, S.W.Martin and A.D.Irwin, *J.Non-Cryst.Solids* **177** (1994) 221

[37] R.Brückner, H.U.Chun, H.Goretzki and M.Sammet, *J.Non-Cryst.Solids* **42** (1980) 49

[38] R.Gresch, W.Müller-Warmuth and H.Dutz, *J.Non-Cryst.Solids* **34** (1979) 127

[39] K.Suzuya, D.L.Price, C.K.Loong and S.W.Martin, *J.Non-Cryst.Solids* **232-234** (1998) 650

[40] R.Dupree, D.Holland and M.G.Motuza, *Phys.Chem.Glasses* **29** #1 (1988) 18

[41] R.Dupree, D.Holland, M.G.Mortuza, J.A.Collins and M.W.G.Lockyer, *J.Non-Cryst.Solids* **106** (1988) 403

[42] M.W.G.Lockyer, D.Holland and R.Dupree, *Phys.Chem.Glasses* **36** #1 (1995) 22

[43] H.Yamashita, H.Yoshino, K.Nagata, I.Yamaguchi, M.Ookawa and T.Maekawa *J.Ceram.Soc.Japan* **106** #6 (1988) 539

[44] R.Dupree, D.Holland, M.G.Mortuza, J.A.Collins and M.W.G.Lockyer, *J.Non-Cryst.Solids* **112** (1989) 111

[45] M.Nogami, K.Miyamura, Y.Kawasaki and Y.Abe, *J.Non-Cryst.Solids* **211** (1997) 208

[46] S.Prabaker, K.J.Rao and C.N.R.Rao, *Mat.Res.Bull.* **26** (1991) 285

[47] D.Li, G.M.Bancroft, M.Kasrai, M.E.Fleet, X.H.Feng and K.H.Tan, *Am.Mineral.* **79** (1994) 785

[48] M.E.Fleet, S.Muthupari, M.Kasrai and S.Prabakar, *J.Non-Cryst.Solids* **220** (1997) 85

[49] C.T.G.Knight, R.J.Kirkpatrick and E.Oldfield, *J.Non-Cryst.Solids* **116** (1990) 140

[50] S.Ohashi and F.Oshima, *Bull.Chem.Soc.Jpn.* **36** #11 (1963) 1489

[51] J.Vogel, C.Jana and P.Hartmann, *Glasstech.Ber.Glass Sci.Technol.* **71** #4 (1998) 97

[52] J.Wong, *J.Non-Cryst.Solids* **20** (1976) 83

[53] M.W.G.Lockyer, 'High resolution multinuclear nuclear magnetic resonance studies of oxide glasses', PhD thesis, Department of Physics, University of Warwick, September 1993

[54] N.E.Brese and M.O'Keeffe, *Acta Cryst.* **B47** (1991) 192

[55] P.Volf, 'Technical Glasses', Pitman & Sons (1961)

[56] H.Maekawa, T.Maekawa, K.Kawamura and T.Yokokawa, *J.Non-Cryst.Solids* **127** (1991) 53-64

[57] D.M.Poojary, R.B.Borade and A.Clearfield, *Inorg.Chim.Acta* **208** (1993) 23

[58] A.R.Grimmer, F.Von Lampe and M.Mägi, *Chem.Phys.Lett.* **132** #6 (1986)549

[59] P.Hartmann, C.Jana, J.Vogel and C.Jäger, *Chem.Phys.Letts.* **258** (1996) 107

[60] H.Makart, *Helvetica Chimica Acta* **50** #47 (1967) 399

[61] I.L.Mudrakovskii, V.P.Shmakkova and N.S.Kotsarenko, *J.Phys.Chem.Solids* **47** (1986) 335

[62] R.K.Brow, C.C.Phifer, G.L.Turner and R.J.Kirkpatrick, *J.Am.Ceram.Soc.* **74** #6 (1991) 1287

[63] C.Mercier, L.Montagne, H.Sfihi, G.Palavit, J.C.Boivin and A.P.Legrand, *J.Non-Cryst.Solids* **224** #2 (1998) 163

[64] D.I.Grimley, A.C.Wright and R.N.Sinclair, *J.Non-Cryst.Solids* **119** (1990) 49

[65] A.C.Hannon, B.Vessal and J.M.Parker, *J.Non-Cryst.Solids* **150** (1992) 97

[66] U.Hoppe, G.Walter, D.Stachel and A.C.Hannon, *Z.Naturforch.* **51a** (1996) 179

CHAPTER 9

CONCLUSIONS AND FURTHER WORK

9.1 GENERAL CONCLUSIONS

This study primarily combines neutron diffraction and NMR data to probe the local order in several silicate based glasses. Both techniques are considered powerful probes of glass structure. It has been possible to define the structural units for most cation species in most of the glasses studied. However further experiments are required to define the interconnection of these structural units.

A one dimensional correlation function, T(r), has been calculated from the neutron diffraction data for each sample. It has been possible to fit the first few peaks in each T(r) to directly obtain structural information (ie. bond lengths, rms variation in the bond lengths and co-ordination numbers). The neutron diffraction data has been particularly useful in this study of tin silicate and alkali tin silicate glasses, as the different correlations are generally well removed from each other. However, at high r (≥3Å) and in multicomponent glasses the sum of the different correlations overlap such that it is often not possible to extract structural information. It is important to consider the probable interatomic separations by comparison to related crystal structures when designing the experiment.

Multinuclear MAS NMR data has been acquired for each glass system. It has been possible to assign the peaks in most spectra by comparison to previous NMR studies of related glasses and crystal structures. It has been useful to study several glasses of varying composition within the same glass forming system. This comparative approach has been useful in making the peak assignments and also in suggesting the structural role of the species within the glass.

The interpretation of experimental data in terms of glass structure requires an accurate knowledge of the sample composition. It is apparent from this study that the compositional analysis of oxide glasses requires considerable attention. All the analytical techniques considered in this study require several assumptions to determine each sample composition: X-ray spectroscopic methods require 'standards' of similar composition and ZAF characteristics, NMR requires ideal experimental conditions and wet chemistry assumes that all the sample has dissolved

and reacted. It is considered important that each technique or combination of techniques should be used to determine the proportion of all the atom species present. This is thought to self regulate the values obtained and it also indicates the accuracy of the analysis.

It may be possible to avoid the problems associated with determining the sample composition by preparing each glass in a sealed ampoule. The glass composition could then reasonably be assumed to be the same as the nominal composition. This would be of little use for glasses such as the tin silicates, for which not all the reagents form a melt, and may be problematic when heating volatile reagents. However, the development of a sealed ampoule melt-quench technique would significantly improve the quantification of experimental data.

The interatomic separations measured on LAD may include a systematic error. This is thought to be associated with an error in the calibration of the high angle detectors. Most of the neutron diffraction data presented in this study is truncated at $30Å^{-1}$. This reduces the reciprocal space resolution but is not considered to prevent accurate fits to the data. The error in the calibration of the high angle detectors on LAD is thought to effect data acquired between 1994 and 1997. Data acquired during this period can be corrected in retrospect, if necessary.

9.2 THE EFFECTS OF EXPERIMENTAL RESOLUTION ON THE STRUCTURAL PARAMETERS OBTAINED BY NEUTRON DIFFRACTION

The effects of real and reciprocal space broadening of the peaks in T(r) have been considered for TOF neutron diffraction data. The simulations used in this study considered each broadening effect independently. It is not proposed that this accurately describes the combination of resolution effects on neutron diffraction data but it greatly simplifies the necessary simulations. The results presented in this study could be used to correct the structural parameters obtained from neutron diffraction data. However, the general conclusion of this work is that the magnitude of any such corrections would be small for typical TOF neutron diffraction data.

The real space resolution study considers the effects of fitting the peaks in T(r) with the analytically incorrect function. The peaks in T(r) are described by the cosine Fourier transform of the modification function broadened by a Gaussian function. This describes the scattering from and the thermal motion of the nuclei in

the sample. The thermal broadening dominates the peak shape when the scattering is measured up to a high Q_{max}. A Gaussian function can be used to accurately fit such data. However, the Gaussian peak fit width and area is not found to be accurate for data acquired up to less than $30Å^{-1}$. The correct structural parameters can be extracted by fitting with the analytically correct function or the accuracy of a Gaussian fit can be improved by truncating the data with a step modifiaction function.

The reciprocal space broadening, ΔQ, of TOF data is proportional to Q at a constant scattering angle but is assumed to be approximately constant for data measured at several scattering angles. Both broadening effects are considered because scattering up to $15\sim20Å^{-1}$ is measured and combined from detectors at several scattering angles whilst the scattering at high Q is only measured by the high angle detectors.

The ΔQ = constant resolution broadening transfers some of the scattering intensity to a tail on the low r side of the peak in T(r). This may be removed by scaling D(r) to $T^0(r)$. The effect of this on the structural parameters obtained from either the renormalised or pre-low r correction data is small for realistic values of ΔQ.

The $\Delta Q/Q$ = constant resolution broadening increases the peak width and shifts the peak position to low r. The area reported by fitting with a broadened peak function is also reduced for large values of $\Delta Q/Q$. However, these effects are very small for the reciprocal space resolution reported for the high angle detectors on LAD.

This simulation study simplifies the combined effects of resolution broadening. However, it is not anticipated that further work is necessary to consider a more realistic and more complicated model. The effects of resolution broadening on the structural parameters obtained from these simulations of neutron diffraction data are small for realistic values of ΔQ. The experimental resolution is expected to be improved with the replacement of LAD with GEM. This may allow measurements to be made to higher Q, which according to these simulation results further reduces the effect of fitting with a Gaussian function. It is, however, suggested that the broadened peak function is used to fit the peaks in T(r). A routine is available to users to do this on the computers at RAL.

9.3 TIN SILICATE GLASSES

The neutron diffraction data suggest that the tin silicate glasses consist of a tin silicate network within which the tin is three co-ordinated and the silicon sits at the centre of regular $SiO_{4/2}$ tetrahedra. The tin is bivalent (Sn^{2+}) such that a three co-ordinated oxygen atom is required for every three co-ordinated tin atom, to maintain charge neutrality within a continuous network. This does not explicitly contravene one of Zachariasen's rules for glass formation, which states that the majority of oxygen atoms should be bonded to only two cations.

The three co-ordinated oxygen atoms are thought to increase the cross linking and strengthen the network, such that it is possible to form tin silicate glasses with a high tin content. This interpretation is also given by Sears to explain the physical properties of these glasses.

The ^{29}Si MAS NMR data reported by Karim suggest that the tin modifies the silicate network. The width of the peaks in the neutron diffraction data suggest that the SnO structural unit is more ordered than that of a typical modifier, such as an alkali metal. The ^{119}Sn NMR data reported by Karim suggests that the tin environment is asymmetric. Tin is thought to sit at the apex of a well defined trigonal based pyramid, within a tin silicate network, at all compositions. Only one O-O peak is fitted at 2.65Å. A correlation on the high r side of this peak does increase with tin content. It is possible that this is due to O-O correlations within the $SnO_{3/3}$ structural unit, but it is not possible to fit this peak. As a result, it is not considered possible to accurately obtain the O-Sn-O bond angle from this data.

It is possible to interconnect $SnO_{3/3}$ and $SiO_{4/2}$ groups into a continuous three dimensional network by forming pairs or chains of $SnO_{3/3}$ pyramids. It is thought that the chains may join ends to form rings, in which case the pair model could be considered to be a two membered chain. These two models differ in the magnitude and definition of the Sn-Sn separation. This could be further studied by NMR relaxation studies of the ^{119}Sn dipolar broadening and/or by XAFS.

The relative intensity of the peaks in the ^{17}O MAS NMR data do not fit the proportion of species predicted by either models. It is considered possible that the ^{17}O did not diffuse homogenously during melting. A further sample could be melted for a longer period, although this would increase the amount of tin lost from the melt.

The metastable crystalline phase is thought to have a higher tin content than previously reported. The positions and relative intensities of the peaks in the ^{29}Si NMR spectrum suggest that the composition is of the order of $(SnO)_4(SiO_2)$.

The peak positions in T(r) are similar for the glasses and the partially crystallised sample. The local order in the crystalline phase is thought to be similar to that in the glasses.

The ^{29}Si and ^{119}Sn NMR spectra suggest that the crystalline phase contains two tin and two silicon sites but it has not been possible to characterise the crystal structure from a polycrystalline diffraction pattern. This is thought to be an important aspect of this work which should be continued in the future.

9.4 ALKALI TIN SILICATE GLASSES

The potassium tin silicate glasses are considered as modified tin silicate glasses. The potassium is thought to depolymerise the tin silicate network. The tin silicate network is thought to consist of regular $SiO_{4/2}$ tetrahedra and trigonal based $SnO_{3/3}$ pyramids, like in the binary tin silicate glasses.

It has not been possible to define the local environment about the potassium cations because the K-O correlation in T(r) overlaps the O-O correlations. The intensity on the high r side of the O-O correlation increases with potassium content. The best fit to this suggests that the K-O correlation is six co-ordinated whilst the position of the fit at 2.9Å suggests that it is eight co-ordinated. This could be further probed by a ^{39}K MAS NMR study or by an isotopic substitution neutron diffraction technique.

The ^{29}Si MAS NMR chemical shift decreases on replacing tin by potassium. This is considered to indicate that the potassium cations have a greater modifying effect than the tin cations. This supports the model proposed by Sears to explain the physical properties of these glasses. The potassium is thought to associate with the $SnO_{3/3}$ groups and depolymerise the network by removing the associated three co-ordinated oxygen species. This model could be tested further by extending the physical property study and/or by a ^{17}O NMR study of high alkali content glasses.

9.5 POTASSIUM PHOSPHOSILICATE GLASSES

The phosphosilicate glasses used in this study are thought to consist of a phosphosilicate network and not phase separated regions. It is thought that this would be difficult to confirm by electron microscopy because the glasses are extremely hygrocopic but it may be possible by a small angle scattering experiment.

It did not prove possible to distinguish the different silicate and phosphate species by neutron diffraction because all the P-O and Si-O correlations overlap each other in the range $1.4 \leq r \leq 1.8$Å. It was also not possible to determine the potassium environment because the K-O correlation overlaps the O-O correlation.

^{29}Si and ^{31}P MAS NMR was used to identify the various silicate and phosphate species. Si^{VI} was observed, for the first time, in an alkali-free phosphosilicate glass. The potassium tetrasilicate-P_2O_5 glasses were found to contain a higher proportion of high co-ordinated silicate species than the potassium disilicate-P_2O_5 glasses. Both Si^{V} and Si^{VI} species were identified in the potassium tetrasilicate-P_2O_5 glasses. The phosphate species are thought to accommodate the high co-ordinated silicate species.

The proportion of species was found to change with thermal history, but the data was interpreted in terms of an average glass structure. A model structure of the potassium disilicate-P_2O_5 glasses was proposed to interconnect Si^{IV}, Si^{VI} , P-Q^2 and P-Q^4 species. It is necessary to perform a two dimensional ^{29}Si NMR experiment to test this model. It was not possible to suggest a model structure for the potassium tetrasilicate-P_2O_5 glasses because it was not possible to maintain charge neutrality with a single phosphate species.

The samples were found to be hygroscopic. The structural role of the absorbed protons could be considered in future work. It would be interesting to acquire both ^{29}Si and ^{31}P MAS NMR data at same time (without unloading the spinner), particularly for a dry potassium tetrasilicate-P_2O_5 glass.

These glasses are of particular interest because phosphorus and high co-ordinated silicate species occur in the earth's mantle. A study of the physical properties of these glasses would be necessary to ascertain their geological significance, but this may be problematic because of their hygroscopicity.